Study of ink release from gravure cells using neural networks and CFD simulations.

Deganello, Davide

Swansea University
Prifysgol Abertawe

Study of ink release from gravure cells using Neural Networks and CFD simulations

By
Davide Deganello

Thesis submitted to the Swansea University in fulfilment of the requirements for the Degree of Doctor of Philosophy

Swansea University
October 2007

Summary

In rotogravure printing, engraved cells collect ink from a bath and then release it onto the substrate forming a series of printed dots that comprise the printed image. The purpose of this work was to explore the ink release in the rotogravure process to improve its predictability and scientific understanding. Two complimentary approaches have been investigated, an empirical approach embodied into Artificial Neural Network models and a numerical physical approach based on Computational Fluid Dynamics modelling.

The Artificial Neural Network approach was based on a statistical correlation of experimental data on cell geometry with optical properties of the resulting print. The developed A.N.N. models were able to accurately predict the effect of cell geometry on ink release, outperforming traditional modelling techniques such as polynomial regression fitting techniques. The models were found to be practical and suitable to integration into manufacturing environments.

The A.N.N. modelling highlighted the need for improved cell geometry data; to facilitate this, new software was developed for the automatic and accurate geometric characterisation of the engraved cells from interferometric profiles.

A Computational Fluid Dynamic model of the ink release was successfully developed; the process was described as the evacuation of a Newtonian liquid from an axi-symmetric cavity, showing the progressive splitting of the ink and retention of ink in the cell. This model is the first that takes into consideration the dynamic contact angle in the analysis of ink release from a cavity. The reliability of the numerical method and of its dynamic contact angle model was verified by comparing specifically designed models with experimental and literature data. The developed evacuation model shows the importance of the evacuation speed on the dynamics of the process and the critical importance of dynamic contact angle.

Declaration and Statements

DECLARATION

This work has not been previously been accepted in substance for any degree and is not being concurrently submitted in candidature for any degree.

Signed .....(candidate)
Date .....3/4/2008.....

STATEMENT 1

This thesis is the result of my own investigations, except where otherwise stated. Other sources are acknowledged giving explicit references. A bibliography is appended.

Signed .....(candidate)
Date .....3/4/2008.....

STATEMENT 2

I hereby give my consent for my thesis, if accepted, to be available for photocopying and for inter-library loan, and for the title and summary to be made available to outside organisations

Signed .....(candidate)
Date .....3/4/2008.....

Acknowledgements

I would like to give my thanks to all who have supported me through the completion of this thesis, particularly Dr Tim Claypole and Prof David Gethin for giving me the opportunity and supporting me throughout.

I would like to thank all my colleagues and students at the WCPC for their help, advice and indulgence towards me. Thank you. Special thanks to Chris Phillips, for his prompt English, to John Cherry, David Beynon, Simon Hamblyn, Alex Lubansky for their assistance and interest towards my work.

Thanks to Alison Williams, Nick Croft and Prof Mark Cross for the continuous development of a remarkable computational software, and in particular for their interest to my questions and requests.

Thank you to all my friends in Swansea for their encouragements and the lunch time discussions, always challenging and refreshing, in particular thank you to Mauro, Fausto, Wulf and Fabio.

Thank you to my family for the great and irreplaceable support

Thank you to my fiancée Caroline, for your patience, support and love

Table of contents

List of figures

List of tables

1 Introduction

1.1 Introduction

Rotogravure is a major industrial printing process. In the gravure process, microscopic engraved cells collect ink from a bath and then release it onto the substrate forming series of printed dots that comprise the printed image, Figure 1-1.

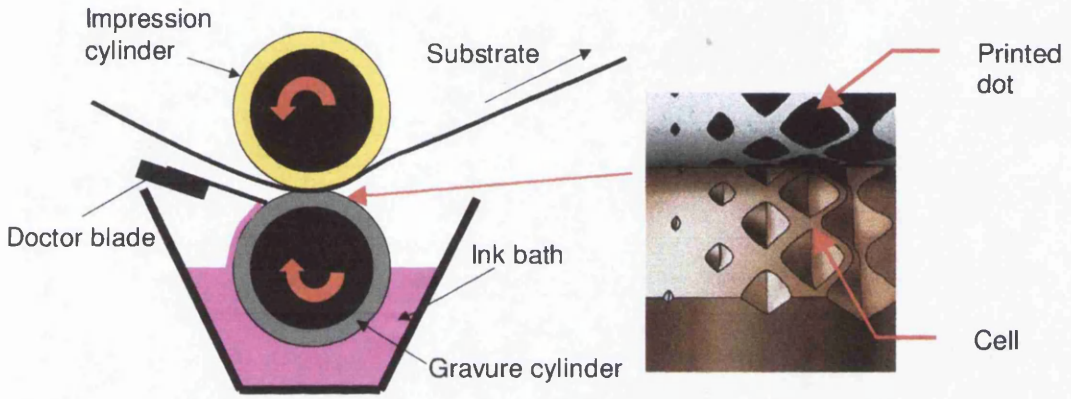

Figure 1-1: The gravure process

The size and shape of the engraved cells influence the process and quantity of ink released from the engraved cells, generating a range of different dots. Different press settings (such as speed, pressures, doctor blades) inks, substrates also affect the release. The combination of these factors determines the final outcome of the gravure printing.

Difficulties arise since the actual knowledge of the process, of its factors and of the interactions among them is limited; gravure printing, as other printing processes, has therefore been regarded as a skilful art, to be mastered by experience. This approach induces high costs in waste material, long set-up time and quality issues. There is a need to improve the scientific understanding of the process and to develop and improve methods for the prediction and estimation of the process.

The objective of this thesis is the understanding of the physics of the ink release during the gravure printing process through experimental evaluations and modelling with a view to improving the predictability of the process. This requires the

development of techniques to quantify the gravure cell geometry as well as modelling techniques.

1.2 Modelling techniques

Modelling of the gravure printing presents several difficulties due to the complexity of the process characterised by a large number of interrelated factors and complex physical phenomena. Two different approaches are examined for the modelling of the gravure printing process: an Artificial Neural Network statistical approach and a Computational Fluid Dynamic one. These two approaches are complementary; the first is experimental, based on a statistical analysis of data gathered during print trials and the analysis of print samples; the second is theoretical, based on the analysis of the physical laws underlining the process of the ink release.

1.2.1 Neural Networks

Neural Network modelling is based on a statistical analysis of experimental trials. The aim of this modelling technique is the definition of correlations between the inputs of a process and its outputs. These correlations or patterns are determined by a statistical analysis of the experimental data. Artificial neural networks are particularly interesting statistical modelling tool, due to their recognised ability to deal with complex processes and interactions.

Major requirement for the development of this type of model is the definition of measurable numerical parameters for the correct characterisation of the inputs and outputs of the process. On the basis of an extensive experimental collection of these parameters, it is therefore possible to develop a Neural Network model of the process.

Parameters commonly used in the industry could be integrated in the modelling, leading to a possible direct application in manufacturing environments. On the basis of parameters known to the engraver or printer the model could be able to estimate the printed results.

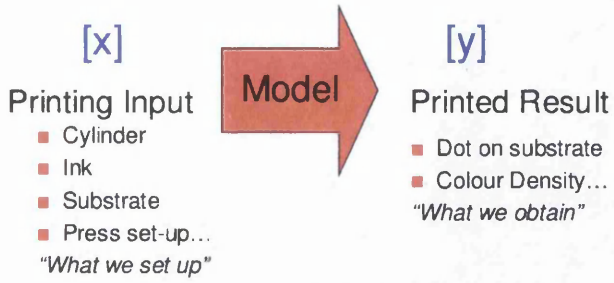

Figure 1-2: Modelling of the Gravure Printing: N.N. approach

1.2.2 Computational Fluid Dynamic

The computational fluid dynamic modelling is based on the discretisation of the physical domain. The aim of this modelling is the actual simulation of the fluid flow. In the case of the analysis of the ink release from an engraved cell, the model should simulate the physical flow and evacuation of the ink during the progressive separation of the engraved cell from the substrate.

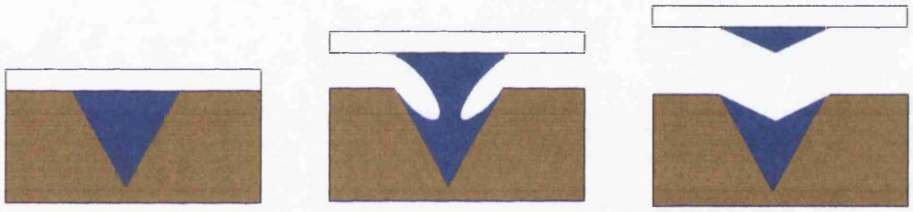

Figure 1-3: ink released from an engraved cell

This model would allow the preliminary analysis of a large range of conditions, without the necessity to run expensive trials. Experimental tests would concentrate in the one-time physical characterisation of inks and substrates.

The development of this model presents several challenges; from a mathematical side the analysis of free-surface flows presents several difficulties in its discretisation; from a physical side, current models of some physical phenomena such as complex rheological behaviours and dynamic contact angles present several limitations.

1.3 Closure and thesis layout

The object of this thesis is the development and study of models of ink release in the gravure printing process, in order to improve its predictability and the scientific understanding of the process itself. Neural Networks and CFD modelling techniques will be investigated. The thesis is composed of 10 chapters:

Chapter 1: Introduction

Chapter 2: The gravure printing process: an overview

Chapter 3: Engraved cell geometric characterisation

A list of parameters is discussed for the correct geometric characterisation of the engraved cells.

Chapter 4: Development of a software for the cell geometric characterisation

A specially developed software is presented to automatically measure relevant geometric parameters from cell interferometric profiles, achieving an accurate geometric characterisation of engraved cells.

Chapter 5: Experimental trial and data collection

The measurement and collection of experimental data from an extensive printing trial is presented. The trial was carried out on an industrial press. The collected data include parameters characterising the engraved cell geometry, ink viscosity and the output achieved colour densities.

Chapter 6: Artificial Neural Networks

The theory of Artificial Neural Networks as statistical modelling method is presented

Chapter 7: Development of ANN models for the gravure printing process

Neural Network models of the gravure printing process were developed on the base of the experimental data collected in Chapter 5 to verify the feasibility of Neural Networks for the modelling of the gravure process. Neural Networks are compared with other statistical modelling methods. Models are examined for application in the industry.

Chapter 8: Computational Fluid Dynamics for Gravure printing

Introduction to Computational Fluid Dynamic and to the software PHYSICA and its Level-set Finite Volume method.

Chapter 9: CFD modelling for ink release in gravure printing

An enhancement to the PHYSICA Level-set Finite Volume method is presented. The reliability of the numerical method is verified by comparison of models with experimental and literature data. A CFD model of ink release from an engraved cell is developed and analysed.

Chapter 10: Conclusions & further work

2 The gravure printing process: an overview

2.1 Introduction

Gravure is a major volume printing process; it is the favourite choice for the production of long run, high quality multicoloured printed materials over a large range of substrates, [1][2]. This process is characterised by relative high setting up costs per job, due to the high cost per image; as for each colour of an image, a cylinder has to be engraved, an expensive process. However, the simplicity of the process in itself allows an extremely high quality and robust product at low running cost. Therefore, the use of rotogravure has been traditionally limited to relatively long run jobs in order to spread the set-up cost, or when the highest quality is critical.

A 2005 survey [3] shows that gravure represents around the 10-15 % of the global market with a relative constant share in the last decades, Figure 2-1.

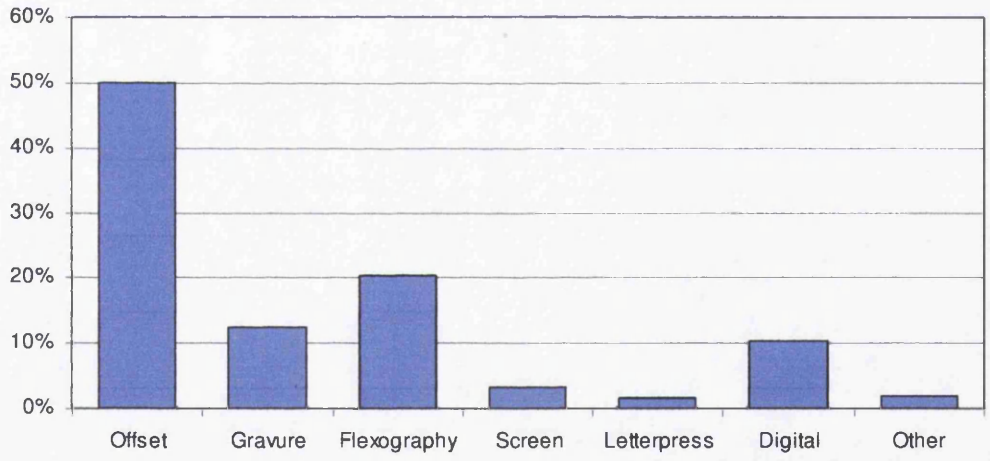

Figure 2-1:Global market share in printing industry [3]

Its application can be classified in three main categories: publication, packaging and decorative gravure. In the publication industry [4], more than the 50% of magazines (e.g. Glamour, National Geographic) and catalogues (e.g. Argos, Ikea) are printed with gravure presses, while in packaging it has 25% of the European market (80% in Japan). Decorative gravure includes prints on textile, wallboard, wallpaper, gift-wrapping paper and laminates. This sector has witnessed a worldwide production

increase of 55% in the last decade reaching around 6 billion m^2, with Europe leading as the major manufacturer.

2.2 Historical background of rotogravure process

The gravure process is one of the oldest volume printing processes. There are indications of its use with wood carved plates in China as far back as 100AD. Modern gravure derives from the "intaglio" printing process commonly used for art and illustration purposes as early as the 1300s during the period of Italian pre-Renaissance [1]. In general, for any intaglio process, the image to be printed is recessed below the non-printing surface on a plate, in fact the Italian word "in-taglio" means "cut in". In the early stages wood plates were used but they were unsuitable for large numbers of copies. In 1446 in Germany the first copper metal plate was engraved with a representation of a religious picture of "the flagellation". In the early 16^{th} century the chemical etching process was introduced; an artist could now draw on a soft "resist" coating instead of painstakingly carving the copper, the image was than fixed on the metal surface by the etching action of a mordant, usually an acid. Another advance in the 16^{th} century was the introduction of a full metallic printing press, which allowed a more even distribution of the pressure. In the 18^{th} century engraved cylinders where introduced in the textile industry. In the 19^{th} century several advances transformed gravure in to a mass-production manufacturing process. The major advance was the halftone screen integrated with photo resists. In particular Karel Klic developed an engraving process by which a carbon tissue was first exposed to a screen, hardening a fine grid, and then to a positive image. This caused the cells between the grid to harden relative to the density of the image. Several magazines started to adopt this new method of gravure printing as it became apparent that gravure offered the most vivid tonal reproduction.

In the 1960s electromechanical engraving was introduced. The first machines were developed by Hell corporation. The machines used either an electronic scanner or a direct digital input, driving a diamond cutting tool, engraving mechanically, rather than etching, the material on the cylinder. Also in 1960 electrostatic assist printing was introduced, improving by electrostatic means the amount of ink released from the engraved cells. In the 1980s Crosfield introduced direct laser engraving using a high-

powered laser on a roller coated with epoxy. The project was abandoned due to problems with the material; in the meanwhile the Hell corporation developed an electron beam engraving process, lately abandoned due to cost of capital investment for high vacuum technology. In 1995 Daetwyler AG developed a new laser engraving system using direct laser engraving onto zinc coating on top of the normal copper surface of the gravure cylinder. This process allows a much faster engraving reaching up to 140000 cells/s compared to the 9000 of mechanical engraving.

Meanwhile the cylinders were also evolving with the development of copper plated small sized (up to 1 m length) cylinders with a plastic core, which are extremely lightweight (in comparison to the steel core ones) and therefore easy to handle.

2.3 Technical overview of the gravure printing process

The basic working principle of the gravure printing process is very simple Figure 2-2.

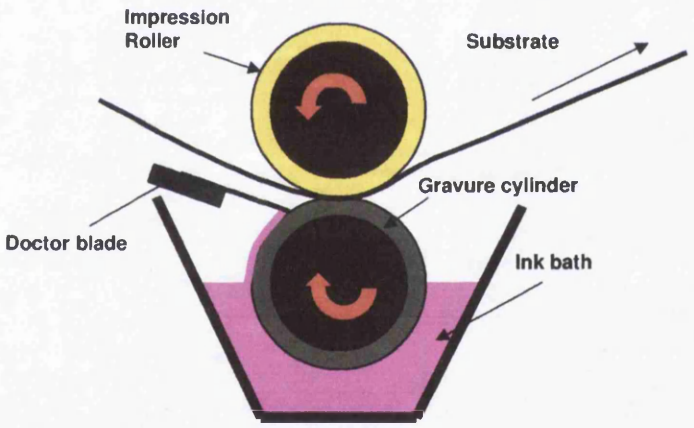

Figure 2-2: Schematic of the gravure process and of the nip contact

The image to be printed is engraved on a cylinder in the form of thousands/ millions of recesses or cells. This engraved cylinder rotates in an ink bath where each cell is flooded with ink. A metering system, called "doctor blade", is angled against the cylinder wiping away the excess of ink from the cylinder surface, leaving the ink only inside the cell wells. Subsequently, the cylinder enters into contact with the printing substrate, while an impression roller presses the substrate against the cylinder. This area of contact is called nip, here part of the ink is drawn out of the cell cavities and transferred to the substrate, forming printed dots. Larger cells, which will have previously collected more ink, will release more ink onto the substrate, generating

larger printed dots than smaller cells, Figure 2-3. Finally the printed substrate passes through dryers that dry and fix the ink on it.

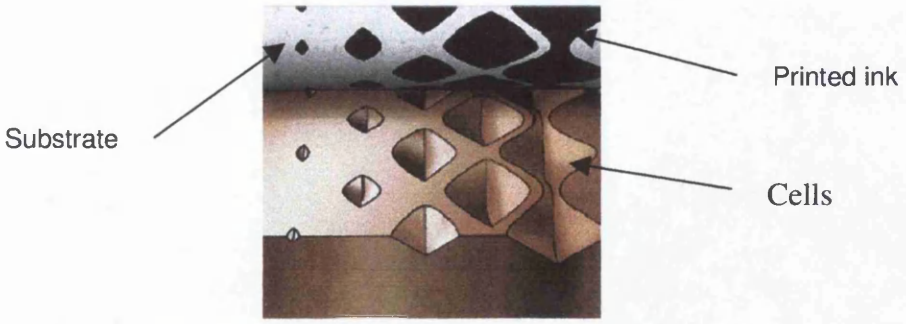

Figure 2-3: Different cells will print different dots [4]

This process has to be repeated for each colour separately; therefore a typical gravure press is composed by several units, each one with its own ink bath, gravure cylinder, doctor blade, impression roller and dryer.

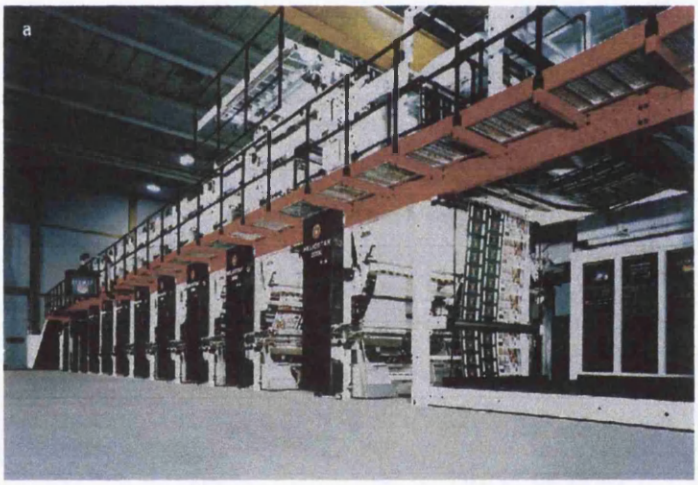

Figure 2-4 Gravure press with 10 printing units [2]

In the next sections the different elements that characterise the printing will be discussed in detail:

1) Gravure cylinders
2) Doctor Blade
3) Impression roller and nip contact
4) Ink bath
5) Dryers
6) Inks
7) Substrates

2.4 Gravure Cylinder

At the heart of the gravure process there is the gravure cylinder engraved with the image to be printed. The gravure cylinder acts as the image and ink carrier in the process. Their size ranges from a length of around 50 cm up to 3-4 m and diameters from 10 cm up to 50 cm. The production of a cylinder can be divided in several stages. At the core there is a well-balanced accurate machined cylinder, this is usually made of steel, and more recently, in the case of small size presses, of plastic. This cylinder is electroplated with an engravable soft material (copper) and then the image is engraved on it in the shape of small cavities, cells. The cylinder is then again electroplated with a harder material (usually chrome) and is ready for printing. At each stage proper polishing and milling processes assure to achieve uniform smooth surfaces and the removal of imperfections. After printing, the cylinder can be recycled by de-chroming the surface, milling away the used engraved layer and then repeating the plating and engraving process. The images are engraved in the cylinder in the shape of small cavities, or cells. The different size and shape of cells will be able to carry and release a different quantity of ink, being able therefore to release a large tonal range of densities of colour. Three engraving processes are, nowadays, available for the imaging of the gravure cylinder on a production scale: electromechanical engraving, chemical etching and laser engraving. Each of these processes produces distinctive types of cells.

2.4.1 Electro-mechanical engraving

Electro-mechanical engraving is, currently, the dominant engraving process. This is a metal cutting process and it is accomplished in lathe style machines. While the cylinder rotates, a diamond triangular face tool, called *stylus*, moves, with a specific vibration speed, in and out of the cylinder surface. The cutting process will happen along the cylinder circumferential direction.

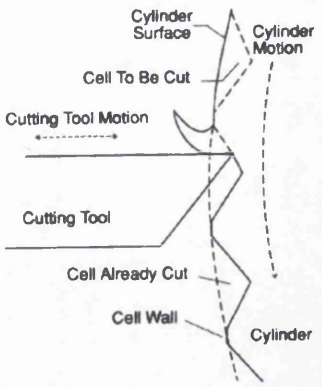

Figure 2-5: Electro-mechanical engraving process

The generated cells have a specific diamond shape with a specific depth/opening ratio (depending on the stylus used) between the width of the cell and the obtained depth. This process generates cells of different size and shape depending on the depth of cut and on the contact length between the tool and the cylinders, which is regulated by the rotational speed of the cylinder. A faster rotating cylinder will generate elongated cells, while lower speed will generate compressed cells. After the primary engraving, a scraper removes the burrs on the copper, induced by the cutting action. Due to its importance in the development of this work, this type of engraved cell has a specific section in 3.2.1 describing its geometric characterisation. A modern engraving head can reach frequencies of 9000 cells per sec; in order to achieve higher speed of engraving multi-head machines can be used.

Figure 2-6: Electro-engraving machine with 16 stylus heads (HELL Gravure Systems)

2.4.2 Laser engraving

Laser engraving is an engraving process recently introducted ("Laserstar", 1995 , Daetwayler). Here a solid–state laser engraves a zinc layer, which coats the cylinder. This non-contact method of engraving avoids the risk of wear and damage connected to the stylus, while highly increasing the speed of engraving. A modern laser machine can operate at up to 70KHz per laser head; laser cells typically have an oval shape, round dot cells are supposed to give a better ink release than diamond shape cells. Furthermore, the laser permits the cell depth and area to vary independently from each other, allowing a larger variability of shapes than the mechanical engraving.

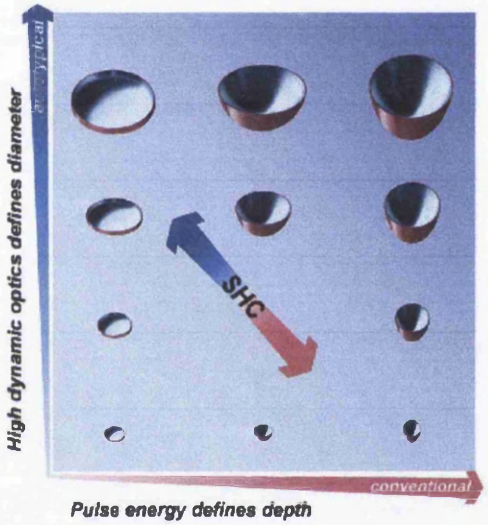

Figure 2-7: Laser engraving allows to define area and depth independently (Daetwayler)

For a comparable printing density, the depth is only two thirds of that of an electromechanically engraved cell. Less cell depth of course means thinner galvanic plating, and less plating time.

2.4.3 Chemical etching

Chemical etching was the first mass-production engraving process and was dominant until the 1960s. In this case the copper cylinder is etched on the basis of a positive mask carrying the image. The imaging of the cylinder with etchant is a quick process and it allows the generation of a large range of cells, but noticeable time and care has to be placed in the preparation stages with the development of all the necessary masks. Furthermore since the etchants are acids, there are environmental concerns.

2.5 Doctor blades

The doctoring process is essential in metering the ink in to the cells. The doctor blade wipes off the excess of ink from the surface of the cylinder, leaving the ink only inside the cell. In order to effectively wipe the ink with minimum wear, the edge of the blade is carefully prepared, different types of edges are available, Figure 2-8 , most common is the lamella blade, where the thickness of the edge (typically 90 μm) remains constant throughout the progressive wear of the blade. The other type of blade is the traditional bevel type, where the contact area of the blade with the cylinder will increase with the wear.

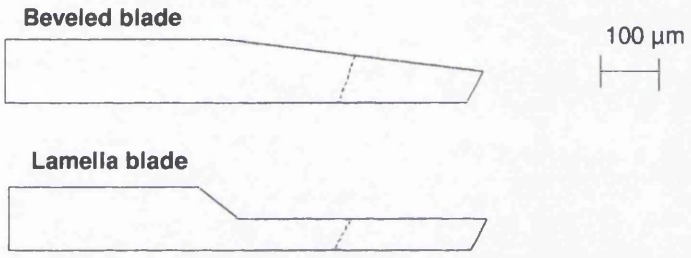

Figure 2-8: Blade edges

The blade is usually made of high carbon steel, cold rolled, steel strip, hardened and tempered. This material is chosen due to its high resistance to wear and good wiping capabilities, for specific tasks (like coating rolls) plastic blades can be used. The blade is hold by a doctor blade holder, a rigid mechanism that allows precise positioning and orientation of the blade. In order to increase the stiffness of the blade, at a short distance from the contact edge, a back-up blade can be used to increase the thickness and therefore the rigidity of the system. In placing the blade in contact with the cylinder, three elements are of primary importance: nip distance, contact angle, and contact pressure. The blade is usually placed at a relativly short distance from the nip in order to avoid the risk of evaporation of the solvents inside the ink with consequent clogging on the cell with dried ink. The contact angle is defined as the angle formed by the blade and the tangent to the gravure cylinder in the point of contact, Figure 2-9. The contact angle is defined by setting the blade holder at a specific angle, called set angle, taking in account that during the press motion the doctor blade will be deflected by the forces (friction, hydrodynamic pressure) acting in the system, changing the contact angle.

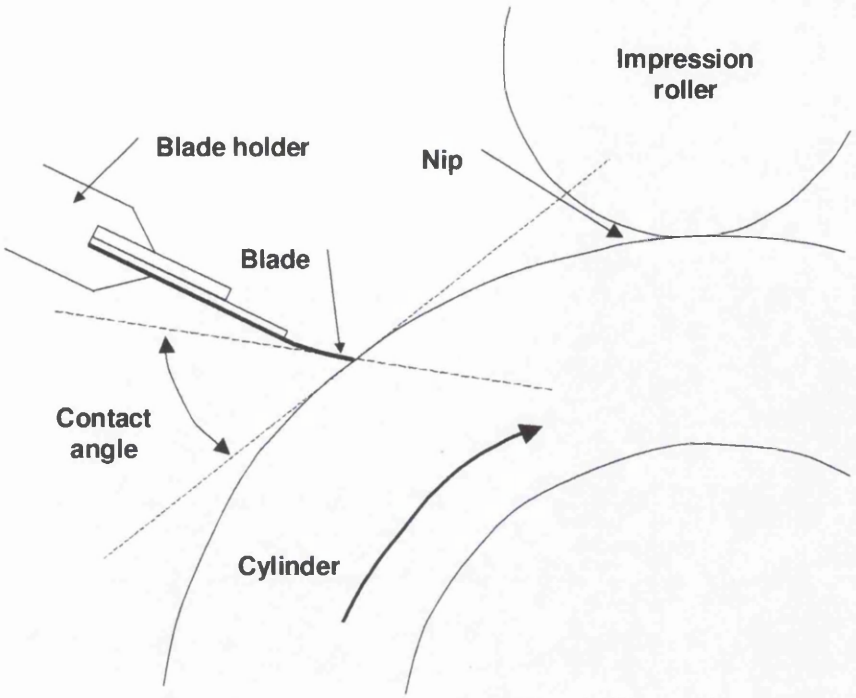

Figure 2-9: Doctor blade system

The contact angle is usually between 55°-65°; moving outside of this range induces a variety of problems; lower angles are less effective in wiping, while higher angles are more prone to bounce or chatter. In practice, however, doctor blades are often operated outside optimum angle range in an attempt to counteract cylinder or ink problems [2]. The final parameter is the contact pressure, this will influence the deflection of the doctor blade and therefore the contact angle itself, too low pressure will result in a loose contact and therefore hazing or scumming, too high pressure will excessively bend the doctor blade reducing its angle, this will also induce hazing. Several studies show that a cell will be full for around the 95% of its volume after a proper doctor blade process.

2.6 Impression roller and nip contact

In order to achieve a good transfer of ink from the cylinder to the substrate, it is important to ensure a good contact between the two. This is achieved at the nip contact by the action of the impression roller. This is a cylinder that compresses the substrate against the gravure cylinder, ensuring a proper ink transfer, while propelling the substrate through the press. Its cover is made from a variety of synthetic rubber elastomers. Covers with different hardness are available, softer ones will deform more

in the contact generating a higher surface of contact with lower pressure (for same force applied). In order to ensure an easy changing of the covers, sleeve systems are commonly used. Impression rolls are smaller then the engraved ones (usual ratio 2:1) in order to achieve high contact pressures; these pressures tend to bend the impression roller in the middle. These would induce a non-uniform distribution of pressure and therefore problems in the ink transfer. In order to counteract this phenomenon, back-up rollers have been used to increase the rigidity of the system; a major limitation of this method is the high heat generation due to the friction, which limits the maximum speed. A common modern solution is the use of deflection-compensated impression rollers (developed from the 1960s). In this roller the pressure is kept constant throughout the contact "line", adapting the shape of the impression roller by the action of localised forces (NIPCO roller, K2 KBA roller).

2.6.1 ESA: Electrostatic assist

In order to improve the ink release on the substrates (especially paper) an electrostatic charge can be applied on the impression roller in order to generate an electromagnetic field between the impression roller and the gravure cylinder; this field will tend to concentrate on the edges of the engraved cells (behaving like "spikes"). The partially polarised ink will therefore tend to move towards the areas with higher charge, this will push the ink around the edges of the cell to slightly rise above the surface of the cylinder, where it could be easily picked up by the substrate helping the ink transfer. This method, introduced in the 1960s, enabled rougher substrates to be used successfully.

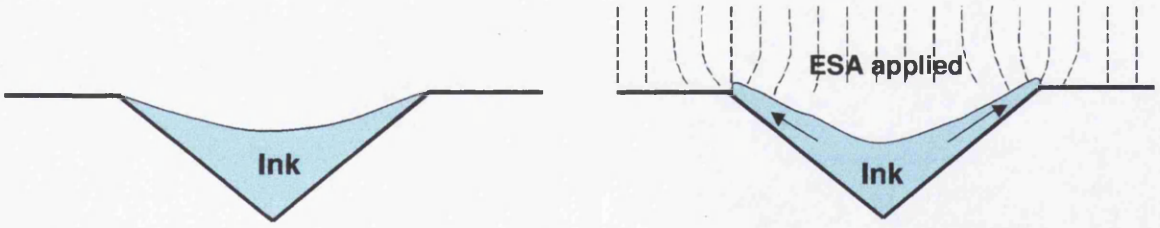

Figure 2-10: Effect of ESA on ink in engraved cell

2.7 Ink bath

The ink bath or ink fountain has the role of filling the engraved cell with ink. In a traditional bath system, the engraved cylinder is partially immersed in a bath full of ink; the depth of immersion is around a quarter of the diameter. During the rotation of the cylinder, the ink in the bath wets the surface of the cylinder, filling the cells on its surface, excess ink being removed by the doctor blade. In recent solutions an ink fountain roller is applied; this cloth covered roll is positioned underneath the cylinder, touching its surface. It is also partially immersed in the ink. During the printing it also rotates picking up ink and squeezing the ink into the cells of the cylinder.

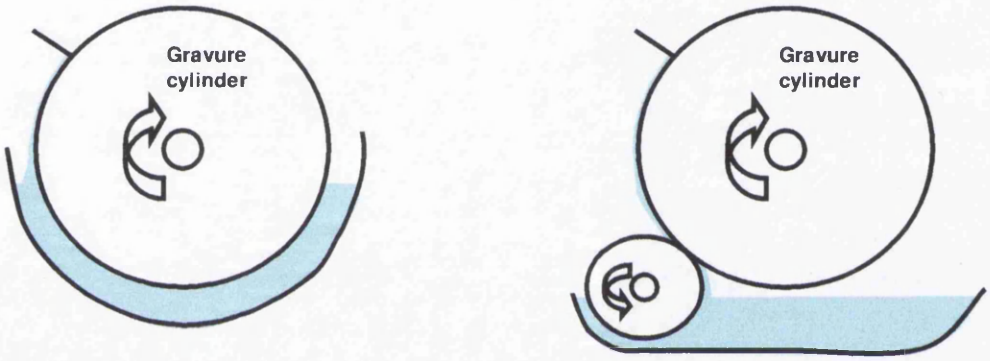

Figure 2-11: Ink bath (left) and ink fountain roll system

In order to achieve filling of the cells it is essential to guarantee a high fluidity of the ink; it is essential to constantly monitor the viscosity of the ink in the bath correcting for the loss of solvents whenever necessary. Several ink baths are equipped with automatic viscometer systems, which add the solvent to the ink bath as required. A common manual technique is the use of flow cups (Zahn, Shell) , in which the time taken for the ink to empty from the cup is used to measure the viscosity.

2.8 Ink dryer

After the ink has been deposited over the substrate, it has to be cured. Commonly used inks are based on highly volatile solvents. The ink is dried by blowing hot air against the printed substrate to evaporate the solvent. Due to the time necessary for evaporation and the high speed of the printing presses, a substrate has to cover a long length in the dryer before the ink is fully cured; the air dryers are therefore the largest

size single piece of equipment; furthermore since the solvents are often toxic, their pollution has to be minimised, this is achieved with solvent recovery systems and fume incinerators. An alternative (regarded as more eco-friendly) is the use of water-based inks. These inks, due to the high boiling point of the water and the atmospheric humidity, require larger drying systems with more length, air supply, and consequently a larger energy input. Another type of ink, that is recently emerging, is UV curing gravure inks; this ink cures by the cross linking of polymers instigated by the exposure to UV light. Their main advantage is the much more compact driers and the lack of production of solvent pollution. Its main limitation is the ink itself, which is very viscous due its polymeric composition and it is not generally suitable for high-speed printing.

2.9 Substrates

A large range of substrate can be used in gravure printing. An advantage of gravure printing is its capability to use cheap substrates yet to give a high quality finished product. The major requirement is that the substrate has to be thin and flexible enough to pass between the gravure cylinder and the impression roller. Papers are a commonly used substrate. Most kinds of papers and paperboards can be used in gravure. These substrates can be coated in order to achieve a higher printability. In the case of rough substrate ESA can be used to improve the ink transfer. Other important substrates are plastic films; all types of plastic film can be printed in gravure, providing that the surface energy level of the film is higher than that of the ink; examples are polyethylene, PVC, PET, cellophane. An important issue with these substrates is their non-porous surface that is a critical factor in the drying process. Another problem is friction: during printing this generates high surface charges on the plastic films (which are insulators), these could influence the drawing of the ink from the cell and generate dangerous sparks (many solvents are inflammable); it is therefore essential to eliminate these charges by the use of static eliminators and antistatic additives. Other substrates include textiles and laminates.

2.10 Inks

Gravure inks are characterised by a relative low viscosity in a range of 0.05-0.5 Pa·s in order to guarantee a good filling of the cells. Inks are essentially composed of pigments or dyes, extender base, solvents and additives. Pigments are coloured particles insoluble and dispersed in the ink liquid to give the required colour. For some applications, pigments are added for functionality; for example, in the case of printing electronics, conductive pigments are used (e.g. silver particles). Dyes are an alternative colorant, soluble in the medium and solvents; dyes are more expensive and used less in the gravure industry, while dominant in other printing sectors like inkjet printing. The extender base has two primary roles: carrying the ink through the printing process and then providing binding agent between the pigments particles and between the pigments and the substrate. The binding action takes place by polymerisation; this is a mechanism where short-chained molecular organic compounds combine forming long chains. Common extender bases are acrylics, nitrocellulose, vinyl resins; these are thermosetting polymers; their process of polymerisation happens in the dryers where as the hot air leads to the evaporation of the solvents, the polymers close together and combine. The solvents are liquids capable of dissolving another substance without undergoing a change in the chemical state or physical properties. They are the liquid medium in which all the other constituents are dispersed in and it guarantees the adequate rheological properties required by the printing process. Essentially the solvent has to be able to dissolve the resins without affecting the pigments. During the drying process the solvents will have to easily evaporate, solvents have therefore a low boiling point; Common solvents are esters (Ethyl acetate), alcohols (Methyl alcohol), glycol esters (Propylene glycol). Several solvents show levels of toxicity: Toluene, a common solvent few years ago, is forbidden in several countries since it is a carcinogen. Additives are modifiers, which are added to the ink formulation in order to achieve specific physical properties or effects like surfactants (to improve wetting), bactericides (to avoid mould growth), optical brighteners, wax and silicone oils (to reduce friction). In order to guarantee the high fluidity needed for the process, the pigment content is limited in the ink to only 10-30% of the total. The remainder is mainly solvent. Due to the high solvent content, gravure ink often shows a nearly Newtonian behaviour, i.e. the

viscosity is constant with strain rate. In other cases the shear-thinning becomes noticeable, i.e. viscosity decrease with strain rate.

Modern trends with the increase of environmental concerns have lead to the development and application of relative new inks: UV curing inks and Water-based inks. In the case of UV inks, the polymerisation process of the extender base is triggered by the action of UV light, which cures and solidifies the liquid medium of the pigments. Due to the total solidification of the ink and the lack of evaporation, the obtained ink film thickness is particularly high. Due to the high polymeric content of the ink, UV-curing ink usually shows a shear-thinning behaviour and a higher viscosity. Conversion from standard solvent-based inks to UV-ink requires a total modification of the curing drying system. It is therefore preferred to use UV-curing ink in specifically designed presses. Water based inks have the water as major solvent; they have been extensively developed and applied due to the increase of environmental concerns. Water-based inks usually rely on a group attached to the extender base (often an amine –NH2) to allow the inks to become soluble in water, this induces a typical strong ammonia odour. Conversion from standard solvent-based inks to water-based ink is a feasible option; Major limits are that, since water is characterised by the high boiling point, they require improved drying facilities, and that they are more difficult to clean and therefore to manage (inks are cleaned using their typical solvents, but several water-based inks are purposely non-resoluble after drying).

2.11 Current issues and future of rotogravure

The application of gravure has been constantly limited by the high cost per image of the process. For each colour of an image a cylinder has to be engraved; this is a more expensive set-up process in comparison with offset and flexography, where relatively "cheap" and easy-to-manufacture image plates are required. However, the simplicity of the process in itself allows the delivery of an extremely high quality and robust product at low running cost. A decade ago, with the continuous decrease of the average job run, the gravure printing industry seemed fated to heavy decline. The industry reacted by improving the management of the cylinders and the relationship between the engraver companies and the printing ones, while introducing new

products like lightweight plastic core cylinders, which are much easier to manage (even if less durable). All these induce reductions in the set-up cost, which anyway remains extremely high. The future of the rotogravure printing industry relies on a continuous improvement of the understanding of the process, of its physics and of the affecting parameters; this is the only way for a further advance of the gravure process with a reduction in its set-up cost, while improving consistency and quality. From an industrial point of view reduction of the set-up cost can be achieved by a cheaper engraving process but especially by a reduction of waste (time and materials) by "getting it right first time"; This can be obtained only from a better ability to predict the practical behaviour of the ink release from the engraved cylinders during the printing process. The development of models for an accurate prediction of the process is therefore a necessity in view of continuous market competition and increasing demands.

2.12 Closure

In this chapter an overview of the gravure printing process has been presented. Its technology and market position has been discussed; gravure printing is a major printing process, concentrated into the production of high volume and high quality products. Individual elements that compose the process, such as the engraved cylinder, the press, the inks, the substrate, have been discussed in detail. Recent history shows that reduction of waste and time-to-delivery is a current necessity in evermore competing market. Development of models of the process becomes an important step towards this objective.

3 Engraved cell geometric characterisation

3.1 Introduction

Engraved cells have an essential role in the gravure printing process; they are at the same time the ink and image carrier of the process. They collect the ink from the ink bath or ink fountain and then release it directly onto the substrate. Depending on their shape and size, different quantities of ink will be released onto the substrate generating unique printed dots. Furthermore, depending on the area density of the engraved cells on the cylinder, different densities per area of dots will be generated obtaining different range of colour densities.

A correct characterisation of the cells is essential for any accurate analysis of the gravure process, especially for the study of the effect of the cell shapes and size in the ink release process, for the assessment of the engraving process accuracy and variability, for the evaluation of wear phenomena during the cylinder manufacturing and the printing. An accurate geometric cell characterisation would be therefore a vital quality assessment tool.

This chapter defines geometric parameters for the characterisation of the engraved cells. Methodologies and techniques for the measurement of these parameters are then presented and discussed.

3.2 Parameters for geometric characterisation of gravure cells

The characterisation of engraved cells is achieved by the identification and measurement of geometric parameters, which completely identify the cell shape and size. No detailed review is present in literature concerning the geometric characterisation of cell geometry, although partial reviews can be found in [1],[2],[5],[7]. Geometric parameters that characterise the cells are:

- **Cell dimensions**: width, length, depth. The width and the length are measured on the open area at the top the cell. The depth of a cell is the measure of the

depth of deepest point of the cell assuming as zero level the land area of the cylinder surface surrounding the cell. The engraved cells can present typically lengths and widths in the range of 20-200 µm and depths of 5-50 µm. An example of an engraved cell is presented in Figure 3-1, dimensions are highlighted.

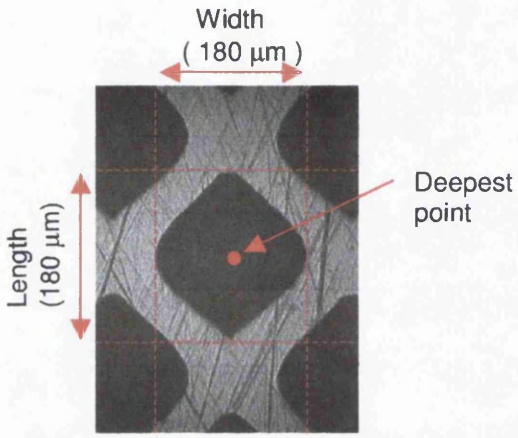

Figure 3-1: Microscope picture of an engraved cell with highlighted dimensions and deepest point

- **Open area**: the open area at the top of the cells; it is the "first" area of contact between the ink and substrate. It can be indicated as a value in cm^2 or as percentage of the total surface
- **Engraved volume**: the engraved volume can be defined as the quantity of fluid that can be placed inside the cell. It is an important factor in the estimation of the achievable ink release. It is usually expressed in the ratio volume over area [ml/m^2]. Its measurement presents several challenges in both its definition and measurement technique. The land area roughness surrounding the cells will have an effect on the possible conveyable fluid, different approaches to the land area roughness will determine different volumes (Figure 3-2).

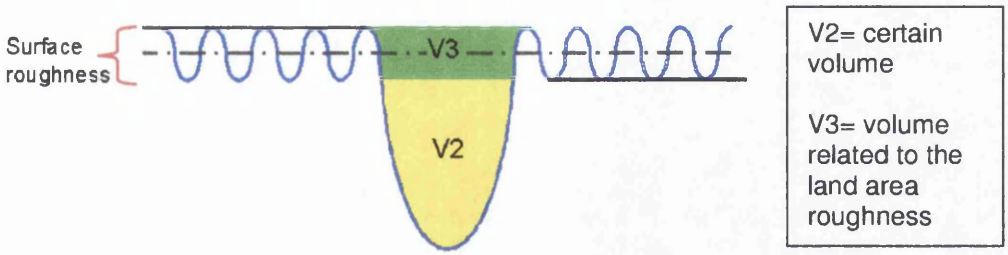

Figure 3-2: Volume of engraved cells

- **Screen ruling**: the number of cells per area; usually expressed in lines/cm or lines/inch; the square of its value represents the quantity of cells present in a cm^2 or an $inch^2$. Increasing the screen ruling allows finer prints.
- **Compression ratio:** this parameter represents the ratio between the length and the width of a cell
- **Land area roughness**: the land area surrounding the cells is smooth with Ra, i.e. average roughness, of the order of 0.2-0.3 µm. High level of roughness would badly influence the printing, the land would start to carry too much ink producing a "scumming" or dirty image. Certain amounts of roughness are considered useful for the lubrication and wear-reduction of the doctor blade.
- **Theoretical area coverage**: although not a geometric parameter, it is commonly used. For a specific set of ink and substrate, this value represents the optical colour area coverage achievable by the engraved cell pattern. This value is achieved by filtering the open area by known "**compensation curves**" specific for the set of inks and substrate. These curves, often referred to as gamma curves, are usually determined by experience and personal judgment of the printer and of the engraver.

These parameters are valid for any generic engraved cell. Different engraving techniques generate cells with different shapes and will therefore determine special relationships and require specific parameters. In the rotogravure industry, three main technologies are available to engrave cells on cylinders: electro-mechanical engraving, laser engraving and (historically) chemical etching. Electro-mechanical engraving is by far the most common production method.

3.2.1. Electro-mechanical engraved cells

A three dimensional profile of an electromechanical engraved cell obtained using interferometry is presented in Figure 3-3.

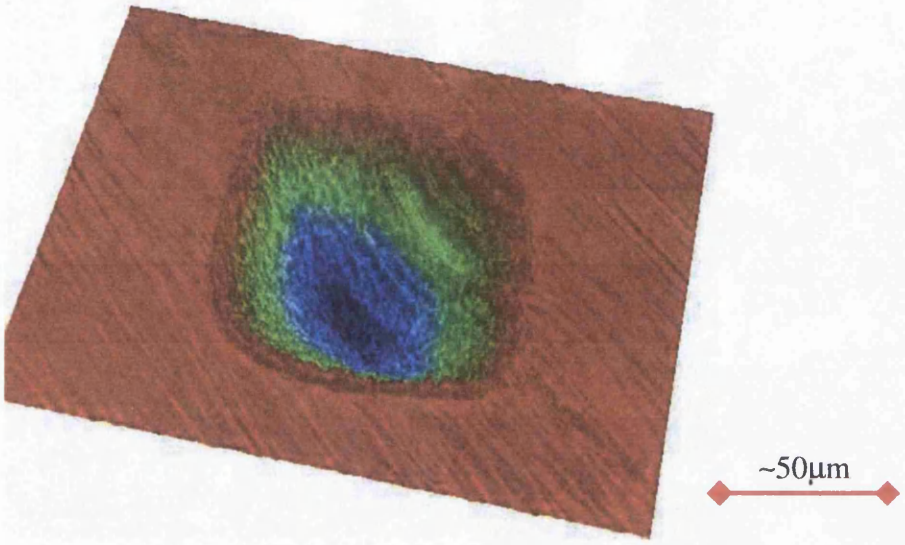

Figure 3-3: 3D profile of a mechanical engraved cell

Due to the cutting action of the diamond stylus the cell is characterised by a specific shape typically referred to as a "diamond", with a sharp triangular cross section profile, due to the triangular shape of the stylus face, and a more rounded profile in the direction of the cut, due to the progressive entering and exiting of the stylus from the copper.

In the case of small area coverage, where the engraved area is small in comparison to the total surface, the cells are separated from each other, while at high area coverage channels are engraved between the cells in order to increase the volume and supposedly help the ink release.

Specific geometric parameters used for the identification and characterisations of electromechanical engraved cells comprise:

- **Screen angle**: during the engraving process cells are engraved at a specific angle vs. the cutting direction, [1]; this determines the shape of the cell and the **compression ratio** of the cell. The value of screen angle is set up on the engraving equipment, controlling the lateral motion and rotational speed; it is not measured. Values of screen angle vary typically in the range of 30 to 60 degrees. In colour printing, variation of screen angle allows to avoid the risk of

Moiré patterns. Screen angle is typically a referable parameter since errors or inaccuracy in the engraving could be easily spotted in the cyclical engraving of the successive cells. Determining the shape of the cell, the value of the screen angle is correlated to the value of compression ratio of the cell. This correlation is not exclusive, since the width of an engraved cell is affected by the roundness of cell edges, see Figure 3-1, and this roundness is affected by different engraving parameters, such as frequency of engraving.

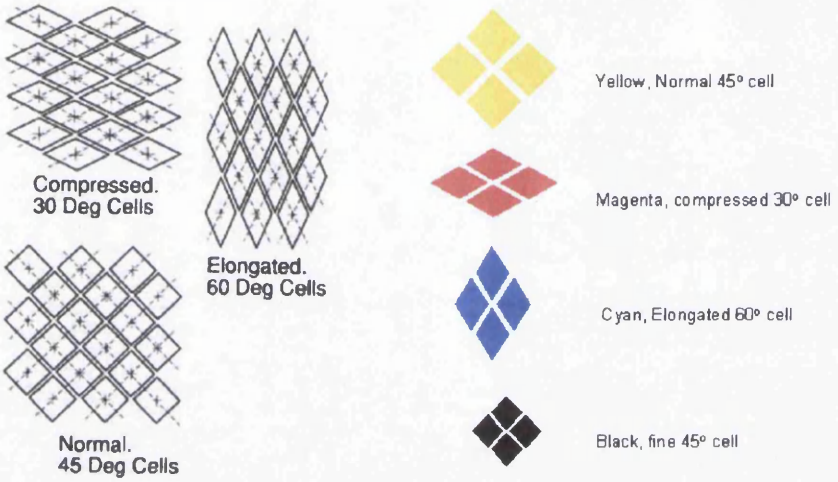

Figure 3-4 Screen angles and colours

- **Screen ruling**: Typical range of screen ruling is between 60 l/cm to 100 l/cm. In 4 colour printing, black has typically a higher screen ruling (for the text)
- **Stylus angle**: This parameter indicates the angle of the diamond stylus; the cut achieved will clearly have a similar angle. The stylus angle is a major issue in the engraving process since it is not possible to verify if the correct angle has been used with a simple picture of the engraved cell and verify the progressive wear of the stylus. New equipment for engraving can be equipped with a camera for the analysis of the stylus tool (Datwayler). Steeper stylus angles will engrave a deeper cell for the same width.

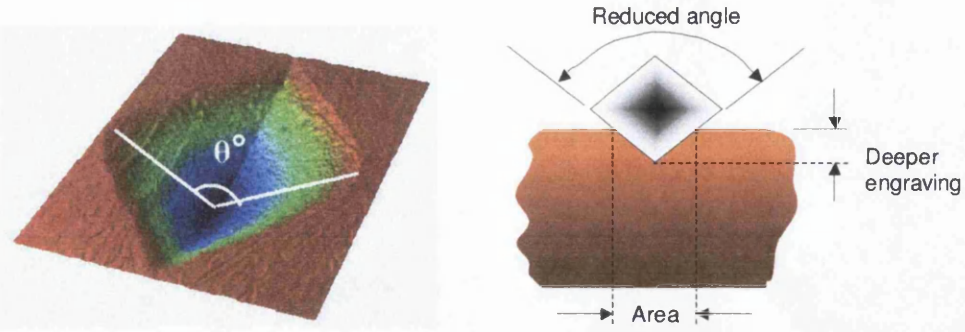

Figure 3-5: Stylus angle

- **Cell width**: The cell width has a particular importance in mechanical engraving since is the most common (and often the only one) measured parameter. A specific combination of stylus angle, screen ruling, screen angle will define the shape of the achieved cells, a single dimension parameter would therefore determine the size. Due to the simplicity in identification and measurement the cell width is commonly used.

- **Channel width**: This is the width of the channels that connect the cells at high area coverage.

3.2.2. Laser engraved cells

Laser engraving allows much more freedom, allowing independent ratios between the width and the depth and the possibility to create random stochastic screen rulings.

Specific parameters are:

- **Depth to opening ratio**: ratio between the cell width and depth

- **Cell wall inclination**: the cell walls will have a different inclination depending on the laser technique applied and the depth-opening ratio. YAG lasers tend to generate steeper surfaces.

- **Inner cell roughness**: Impurities and different rates of evaporation will heavily influence the inner roughness of the cells

Laser engraved cylinders are the **anilox** used in flexography for the transfer of ink from the bath to the plates; these cylinders are uniformly engraved with large open area percentage.

3.3 Conventional measurement techniques & limits

Different measurement equipment is available for the characterisation of the engraved cells. Most of the measuring equipment currently used in the industry is not able to fully characterise the engraved cells. A major factor in a production environment is speed and this comes at the expense of quality.

Optical microscopes are the most common measurement equipment. Most engraving machines are equipped with one of them. They are fast but from the obtained picture only top view parameters are measurable such as width, length, open area. Through focusing first at land area and then at the bottom of the cell, special microscopes allow estimation of the depth of engraved cells. This process is imprecise and requires a certain time (the bottom of the cell has to be found and focused on). Knowing the top surface and the depth of a cell, its volume can be theoretically deduced but with a large uncertainty (wear of stylus, variation in shape, roughness).

A simple method for the measurement of the volume is the **liquid patch**. This method allows a rudimentary estimation of the engraved volume without any indication of the cell geometry or screen rulings. A liquid patch is squeezed over the engraved surface of the cylinder, from the spreading of liquid the volume / area is estimated. This method is fast and can be carried out on site, but it is not accurate; with the increase of screen ruling and the reduction of cell size errors derived from liquid remaining outside the cells and by air bubbles becomes excessive.

Another method is based on the **replica tape**. With a plastic material, a mould of the cylinder surface is taken on site, to be subsequently measured. This method allows taking a fast cast of the engraved cells with little interference with the production line. The cast has then to be measured off-line: different equipment can be used: an optical microscope can be used to observe the cast from different angles giving a more complete characterisation than in the direct measurement counterpart. Otherwise the cast can be measured through the application of three-dimensional profiling techniques, such as white light interferometry (discussed below).

A limitation of the replica tape is that with deep cells or low stylus angles the plastic material is not able to sufficiently deform to follow the cell profile. The experience of the user is important in the correct application of this method: users have great

influence in deciding the level of pressure to apply, at the time of application; this makes this methodology strongly user dependent.

As shown in [8] all these presented techniques have been shown to be inaccurate and user dependent; in order to achieve an accurate characterisation of the engraved cell an accurate direct three-dimensional analysis of the engraved cells is necessary. White light interferometry is one of the few techniques able to achieve the desired three-dimensional profiling.

3.4 White light inteferometry

White light interferometry is a non-contact method of measurement that generates a 3D topographic image of surface. White light interferometry is based on the analysis of the interference patterns, or fringes, of light. The fringes can be analysed following two different techniques: **vertical scanning interferometry** and **phase shifting.**

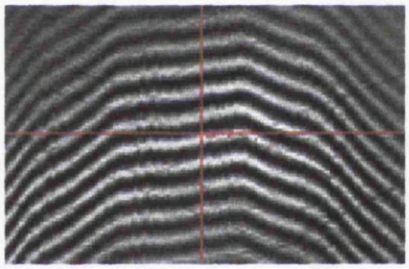

Figure 3-6: Interference light fringes

In vertical scanning interferometry, a white light beam passes through a microscope objective to the sample surface. A beam splitter reflects half of the incident light to a reference reflective surface. The beams reflected from both the sample and the reference surface recombine at the beam splitter, causing interference fringes.

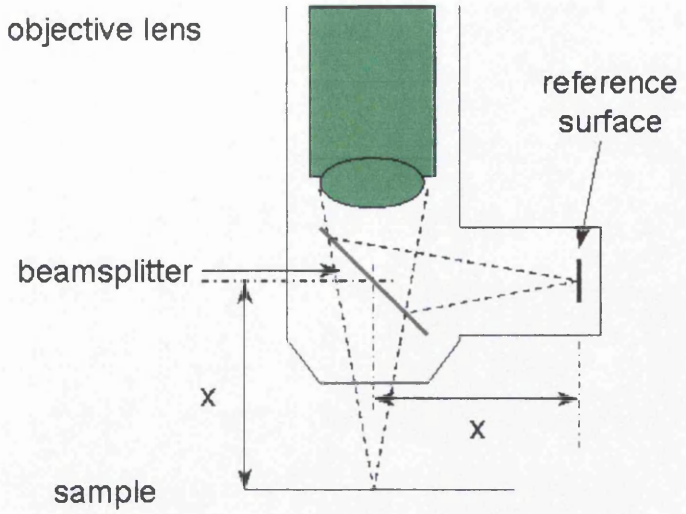

Figure 3-7:The optics assembly of an interferometer

The system scans vertically through focus at evenly spaced intervals. A CCD camera catches frames of interference data at regular intervals during the vertical movement, which is accurately controlled using a piezoelectric motion transducer. If the surface of the sample is uneven, different parts of it will come into focus at different heights. The fringe contrast (intensity of interference) increases as the sample comes into focus, and decreases as the sample falls out of focus. By recording the vertical position at which maximum contrast occurs, the interferometer software can determine the height of each point on the profile.

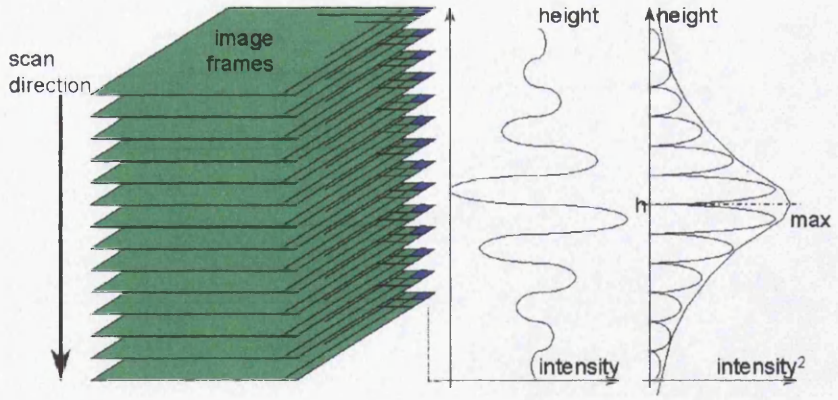

Figure 3-8: Fringe contrast and focus

Vertical scanning is very flexible technique allowing large scan areas limited only by the magnification lens used, and depth limited by the movement of the objective versus the reference mirror (1 mm depth is easily achievable).

Its specifications are perfectly adequate for most of the surfaces used in printing and the characterisation of engraved cells, which have a depth ranging from few microns to around hundred microns.

Phase shifting differs from the vertical scanning since is based on the analysis of the phase transition of the fringes; this method has a measurement range limited to 200 nanometers and is therefore limited to very smooth surfaces such as a polished mirror. It is unsuitable for most surfaces found in the printing industry

3.4.1. White light interferometers for cell characterisation

The most appropriate interferometer for the characterisation of the engraved cells is the rollscope. This compact portable equipment is connected to a computer, Figure 3-9; it can be placed directly on the cylinders for profiling of the engraved surfaces. The profile can be stored on the computer for detailed analysed.

Figure 3-9: Rollscope

At the Welsh Centre for Printing and Coating, two rollscopes are available, by WYKO-VEECO, one with an internal magnification lens of 0.5x and the other of 0.9x. A wide range of external lenses is available: 5x, 10x, 20x, 50x. The combination of the internal lenses with the external ones allows a large choice of different area coverage, ranging from 0.12x0.09 mm^2 to 1.5x1 mm^2. The range of measurement on the vertical axis is around 1 mm with an estimated accuracy of 0.05-0.1 µm depending on the sample material.

For smaller rolls or for substrates, a fixed interferometer workstation is available, the WYKO NT2000. The NT2000 incorporates a table mounted on air bearings to reduce vibrations. The instrument is fitted with 3 internal microscope objective lenses

providing the magnification of 0.5x, 1.0x, 2.0x, while the external lenses are exchangeable with the ones of the rollscopes. The sample has to be placed onto a measurement table that can be adjusted and tilted in the three planes. Its accuracy is higher than rollscopes thanks to higher focal distances and less vibration; depending on the sample surface the accuracy (in VSI mode) can be estimated around 0.02-0.04 μm.

3.4.2. Advantages and limits of current White light interferometers

White Light interferometry presents several advantages:

- Accurate 3-D profiling of surface
- Non-contact method
- Fast in comparison to Atomic Force Microscopes

Limitations of White light interferometry are:

- Slow in comparison to microscopy: a scan requires around 30-60 seconds much slower than the fraction of second for a picture
- Surface gradient: if a surface is too steep, insufficient light is reflected back, the local height can not be determined but has to be interpolated

New generations of interferometers are dealing with these limitations improving the speed of scanning and the coherency of the light source.

3.5 Data processing of the WLI 3-D profiles of engraved cells

The three-dimensional profile, obtained by the White light interferometer, is not a measurement by itself but a virtual representation of the cell. The data require processing and analysing to extract the relevant geometric parameters.

The WYKO-VEECO interferometers are equipped with software that allows observing the scanned profiles, carrying out some basic geometric transformations, such as sectioning and alignment towards a discretional plane. The software allows measuring of the linear distance between two discretional points of the profile and the volume of a selected section, integrating the depth of the pixels. These measurement processes requires user interaction and decisions, being therefore highly subjective.

In order to avoid this, the VEECO software has automatic modules for the calculation of some geometric parameters in relation to specific scanned objects. A particular interesting module is devised for the measurement of the engraved volumes of anilox rolls. In order to operate, a large number of cells have to be present within the same scanned profile and they have to be aligned to a sixty-degree screen angle. This module has proven to be highly unreliable giving a wide range of results for the same set of cells; this could be related to issues in distinction of the cells on the contour of scanned profile and to the reduction of resolution per cell when too many cells are within the same single scanned profile.

Based on these experiences, the best solution for an accurate characterisation of the engraved cells is a single cell analysis method. For each different engraved patch, a series of engraved cells are individually characterised, giving an accurate view of the geometry of the cells and, also, of their variability.

Lists of step-by-step manual procedures have been previously developed for the extrapolation of the geometric parameters from the profile using the basic tools provided by the VEECO software [5][7]. The step-by-step approach allows these procedures to be robust and to a large extent user-independent but time consuming.

3.5.1. Manual procedure for the measurement of the volume

The procedure for the measurement of the engraved cell volume is a valuable example of step-by-step approach in the analysis of the profile, using the software tools provided with WYKO interferometers. This procedure has been previously presented in [5][7].

The correct definition of the cell engraved volume is influenced by the land area roughness surrounding the cell. The volume can be considered as composed by two parts: a minimum certain volume (V2) and a volume determined by consideration of the land area roughness (V3); the total volume is the sum of the two, Figure 3-10.

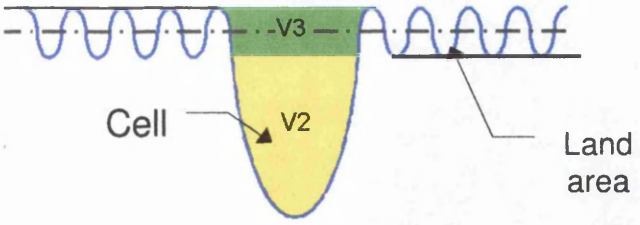

Figure 3-10: Volume of a cell: V2 and V3

The list of instructions of the manual procedure:

1. **The cell to be measured is scanned**

   A single scan can cover several cells and can not be properly horizontally aligned.

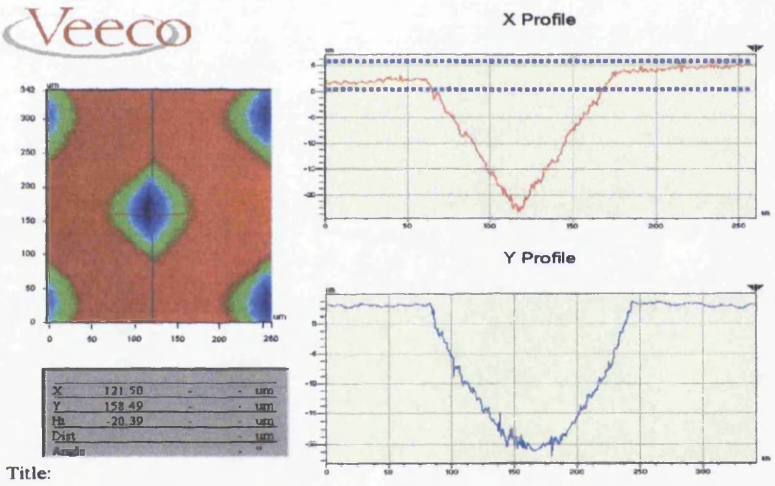

Figure 3-11: Scan of a cell: VEECO software display

2. **Selection** of the cell of interest and of a ring surrounding it

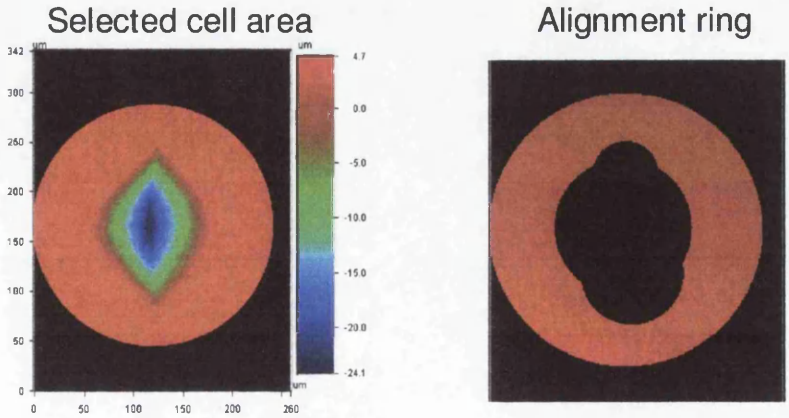

Figure 3-12: Selection of the cell and of surrounding ring

3. **Alignment** of the cell with reference to the alignment ring

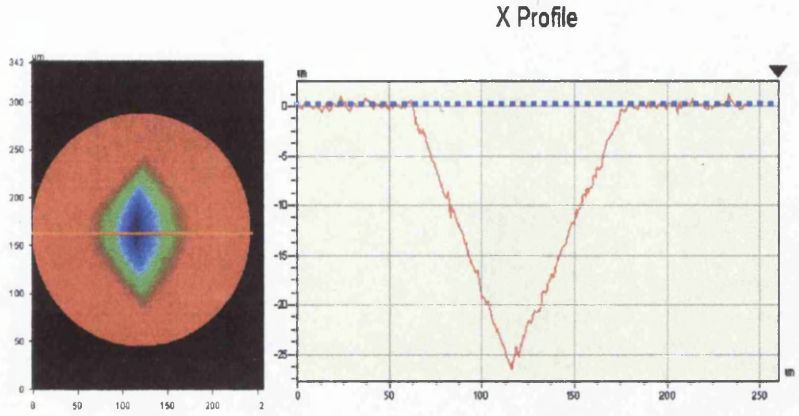

Figure 3-13: Top view and cross section of aligned cell

4. **Call the histogram** of the surface points per height

5. **Mask the land area:** the cursor is moved on the histogram to a value equal to ½ Rz of the land area from the top of the peak to the left and then the right side is masked. Rz is defined as the average value of the ten greatest peak-to-valley separations on the selected land area. The mask is carried out in order to eliminate the volume affected by the land area (V3) **The cell is masked** and volumeV2 is identified.

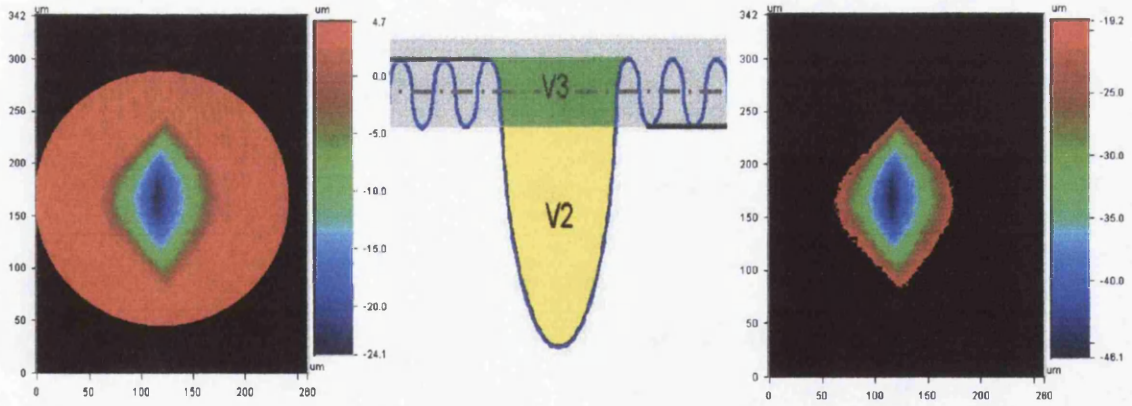

Figure 3-14: Masking process: top views and diagram

6. **Calculate the volume V2** using the software utility provided with VEECO software

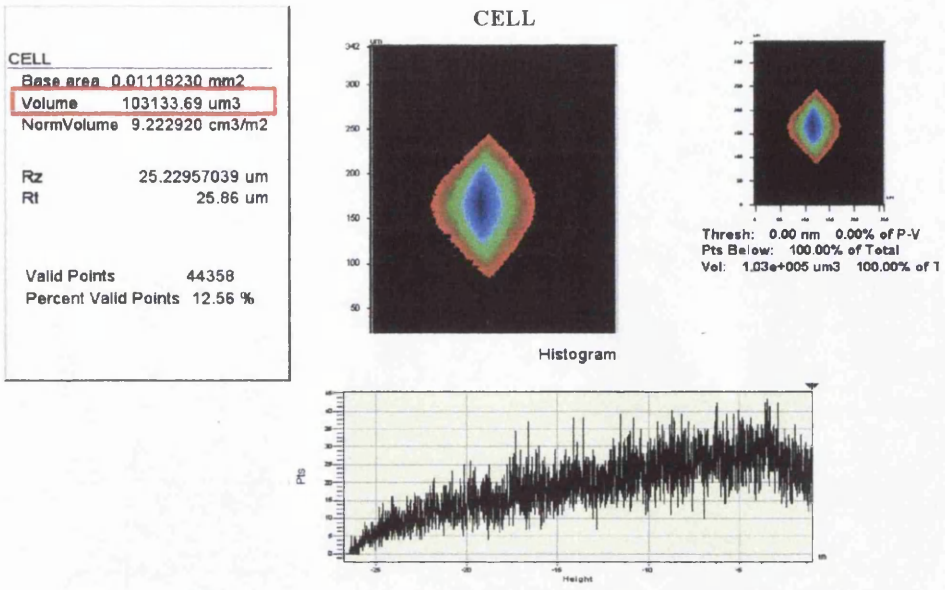

Figure 3-15: VEECO software display: measurement of volume V2

7. **Estimate volume V3:** This volume related to the land area roughness is calculated as a cylinder with a base area equal to the top area of the volume V2 and a height connected to the roughness.

   The surface roughness is defined by two parameters: Ra and Rz. Ra is the average roughness calculated over the entire selected land area and defined by the ANSI B46.1 standard, while Rz is the average value of the ten greatest peak-to-valley separations on the selected land area. Different approaches to roughness will generate different values of V3, Figure 3-16:

   - 1: Minimum volume = Area × ½Rz

     This volume reaches the land area zero level

   - 2: Maximum volume =Area × Rz

     This volume reaches the highest peaks of land area surrounding the cell

   - 3: Average volume =Area × (½Rz+Ra)

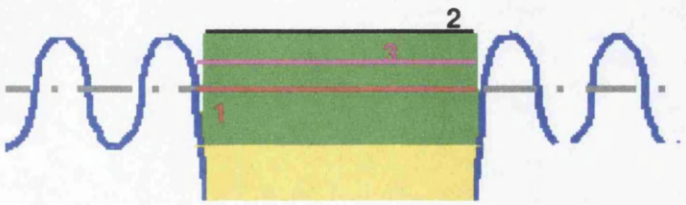

Figure 3-16: Different land area roughness volumes

On the gravure cylinder, the land area surface is relatively smooth; in the case of large cells, the volume V3 will be much smaller than the volume V2, indicatively less then 1-2%; the effect of the land area roughness becomes more significant with the reduction in size of the cells. Land area roughness will be also critical in the case of anilox cylinders, which are fully engraved cylinders typically used for coating operation or in other printing process as flexography. Anilox cylinders present high roughness to increment the quantity of ink carried.

8. **Calculate total volume**: the total volume will be obtained by the sum of the two volumes: V1=V2+V3.

3.5.2. Additional geometric feature characterisation

The accurate characterisation of the engraved cells through White Light Interferometry allows the identification and the measurement of new geometric features, extending the list of parameters previously presented, see section 3.2.

In the case of mechanical engraved cells, a more compressive list of parameters will include:

- **Chromed stylus angle**: following the chromium deposition, the cross sectioned profile of the cell can be slightly different to the stylus angle of the cell due to the unevenness of the electric charge during the galvanic process. White light interferometry allows the actual measurement of the engraved angle, important in the determination the real shape of the cells and of the effect of the chromium deposition.
- **Cell offset**: the deepest point in a cell is often not centred with respect to the cell width; this distance is called offset. Offset is due to the movement of the stylus, whose movement is not perpendicular to the cylinder being pinned on one side. The pivot point of the stylus head is at a distance of several centimetres, the offset value is therefore limited to a few microns in relation to cell depths of few tens of microns

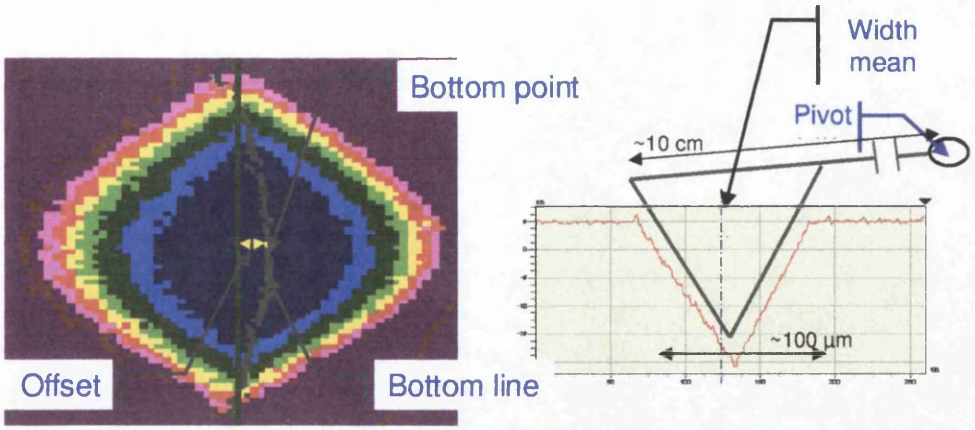

Figure 3-17: Top view of a cell with highlighted offset and scheme

- **Asymmetry**: The movement of the stylus during the engraving process can result in the cell having an asymmetric "rhomboid" shape with semi axis of different length

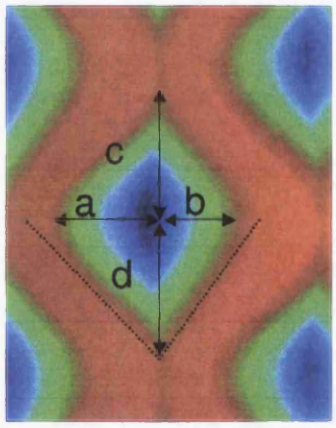

Figure 3-18: Cell top view with asymettric semi-axis highlighted

- **Border angle**: this is the actual angle of the edge of the cells, its value is usually very close to the screen angle

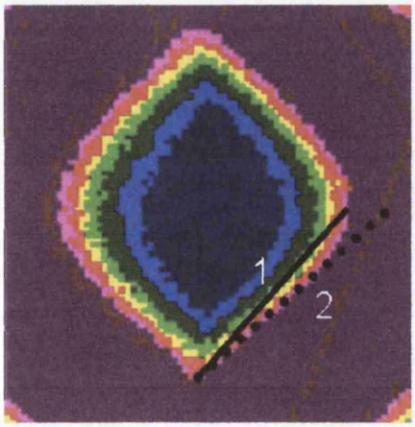

Figure 3-19: Length/width (1) and border edge angle (2)

- **Thickness of the cell extremes:** at the two extremes, where the tool enters and exits the copper, the cut is not a clean point but shows some "thickness". This is induced by the hardness of the copper and by progressive wear of the stylus. An accurate characterisation of these extremes could be useful for the monitoring of the quality of machining and the wear of the stylus tool.

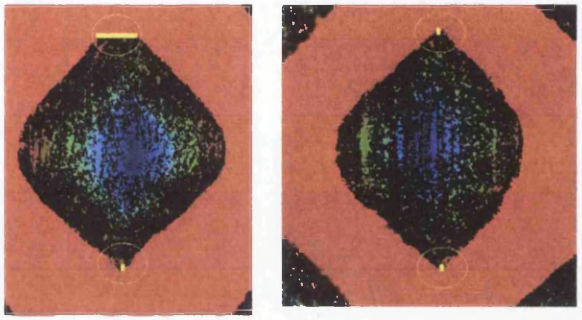

Figure 3-20: Different thickness of the cell extremes for different cells

3.5.3. Disadvantages of manual procedures

The ability to manually measure the profiles obtained from white light interferometry allows a great flexibility to the user; any parameter can be deduced once it has been identified and a procedure has been established.

On the other hand, the great importance attributed to the human user creates disadvantages, which limit the application of white light interferometry on large scale characterisation:

1. Manual procedures are **time consuming**; while the scanning of a cell requires around 30-60 seconds, its analysis can require several minutes: each parameters has to be measured individually, following adequate step-by-step procedures, as shown in 3.5.1 for the volumes, especially when a longer list of geometric parameters area required. This is a clear bottle-neck which limits large scale applications
2. **User training**: the user has to be adequately trained to carry out the analysis of the profile. Different users must follow similar training in order to consistently apply the procedure in the same manner for reference.
3. **Human error** in the analysis; the user has to measure and record the geometric parameters, errors during the process are possible due to

distractions. It is important therefore verify the results, but this implies more procedures, resources and time.

3.6 Conclusion

In this chapter, a compressive list of geometric parameters has been defined for a complete characterisation of the engraved cells. Measuring techniques have been presented stating their limits. White light interferometry is capable of a full characterisation of the engraved cells. Application on a large scale of this technique is limited by the time required for the profiling and by the time and expertise required for the analysis and measurement of relevant geometric parameters from the profile. In the next chapter, the development of an automated technique for cell analysis and its validation is described. This enables the operator to rapidly analyse many cells confident in the consistency of the measurements.

4 Development of software for cell geometry characterisation

4.1 Introduction

In order to study the ink transfer in the gravure printing process there is the need for an accurate, reliable method for the geometric characterisation of the engraved cells.

White light interferometry provides the required accuracy, but before the development of this thesis, its application on a large-scale investigation was severely limited by the long time required for the profile data analysis, as discussed in 3.5. A special software was created during the development of this thesis to overcome this limitation, speeding up the analysis of the data profiles. The software, named "CellWCPC", fully implements measuring procedures allowing a fast and accurate complete geometric characterisations of the individual engraved cells from the scanned profiles. The software carries out this measuring process automatically with minimal intervention; necessary user actions are the selection of the profile file and the click of the "start button". In this chapter, the development of the software will be discussed, its theoretical background and its procedures.

4.2 Development history

The software has been coded by the author in Microsoft Visual Basic with the specific development of all the necessary algorithms. Its coding follows a modular structure allowing a great flexibility in the development and implementation of measuring procedures for different geometric parameters. Its development has been progressive, spanning two years, with continuous implementations of new procedures and improvement of others. The use of Visual Basic allowed the easy creation of a practical user-friendly interface, with the creation of visual representations of the analysed profiles. Originally developed for the geometric characterisation mechanical engraved gravure cells, its application has been successfully extended to laser engraved cells in anilox rolls.

4.3 Measurement methodology

The software carries out an individual geometric characterisation of the engraved cells present on the profile completely automatically. A key point for the development of the automatic process is the ability to identify and delimit the engraved cells over the scanned profile; this is achieved with the development of a *watershed algorithm.*

The intuitive concept underlining this method comes from geography [6]: it is that of a landscape being flooded from beneath with a flow of water. Holes are pierced in local minima on the landscape. Basins will fill up with water flowing through these holes; the water level will rise uniformly with respect to the sea level. At points where water coming from different basins would meet, damns are built. As a result, the area will be portioned into regions separated by damns or *watersheds.* For this software, a watershed algorithm has been written by the author: starting from the profile of the scan, source points of "liquid" are placed at the bottom of the cells and at the edges of the scan image; the source point at the bottom of the cell to be analysed is distinguished from the others with a different "liquid". This cell can be identified as being around the centre of the image, Figure 4-1.

The scanned profile is constituted by a grid of pixels, each one presenting values indicating its X and Y spatial locations on the grid and the local height of the profile. Each depth value will be the multiple of a discrete unit, the depth resolution of the white interferometer; it is therefore possible to step from one plane to another, progressively flooding the levels.

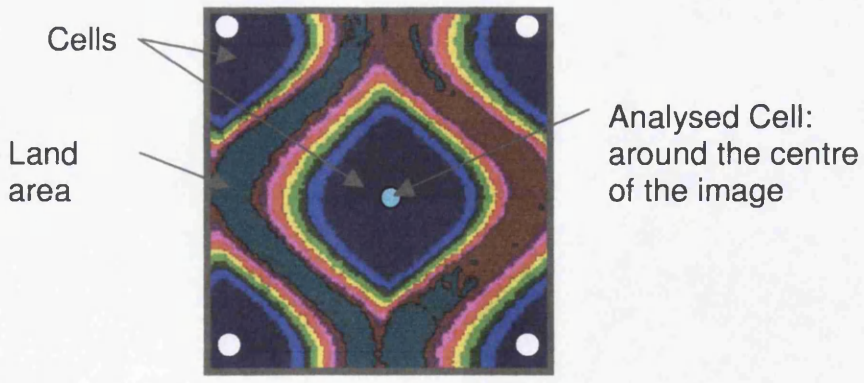

Figure 4-1: Scanned profile as loaded on the software with indication of source points (white and light blue circles)

The flooding starts at the lowest point of the profile, i.e. the bottom of the cells, continuously filling the cells and eventually flooding the land area where the liquids

from different cells meet up defining the watershed points. A graphical representation of the execution of a watershed algorithm is presented in Figure 4-2.

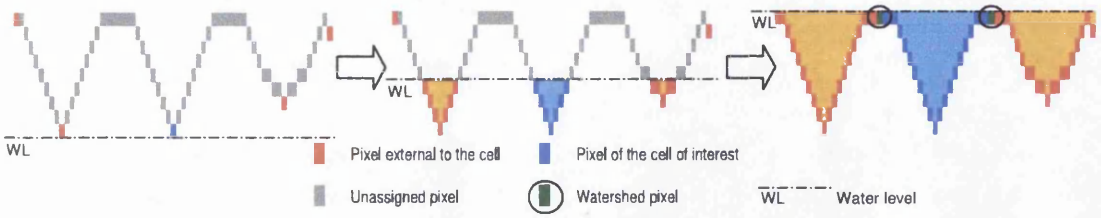

Figure 4-2 Watershed algorithm execution

On a flat area the water, coming from the two sides, would meet in the middle; following this algorithm, a ring is determined surrounding the engraved cell shown in Figure 4-3. The scanned profile is horizontally aligned on the base of this ring. Possible channels between cells are identified with a statistical analysis of the ring and excluded from the alignment.

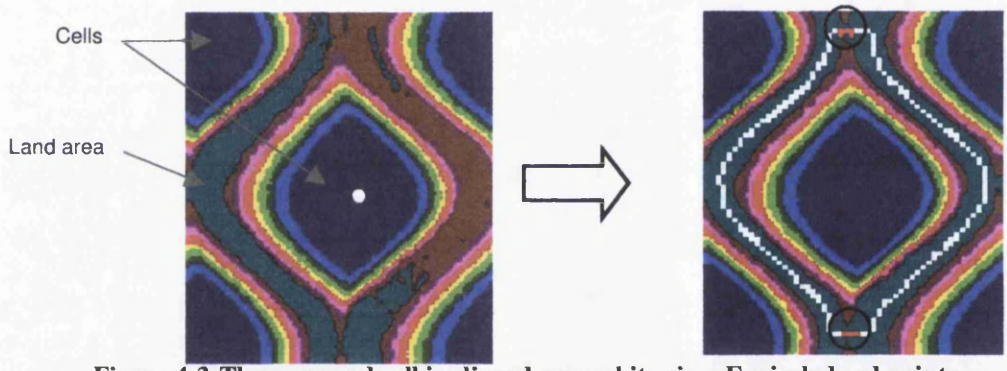

Figure 4-3:The engraved cell is aligned over white ring. Encircled red points on channel, not used for alignment

In this phase targeted to the identification of an alignment ring, the profile can be "smoothed" decreasing, by averaging methods, the pixel resolution in the three dimensions (X,Y and depth) of the scanned profile; this leads to a reduced number of pixels composing the scan profile and to a lower number of discrete levels in the Z direction. This methodology has the double advantage of decreasing the necessary computing power, and obtaining an alignment ring of significant thickness, avoiding the influence of the land area roughness. Analysing the related pixels on the raw profile, the roughness of the land area can be studied.

For the identification of cell edges, the watershed algorithm was appropriately modified. Giving priority to the liquid external to the cell with respect to the liquid

inside the analysed cell, the watershed point will be exactly on the edge of the cell; A graphical representation of the application of this modified watershed algorithm is presented in Figure 4-4. In order to achieve the most accurate delimitation of the border of the cell, this modified algorithm is applied to the scanned profile at its full resolution (or in any case at a finer stepping than the related alignment one).

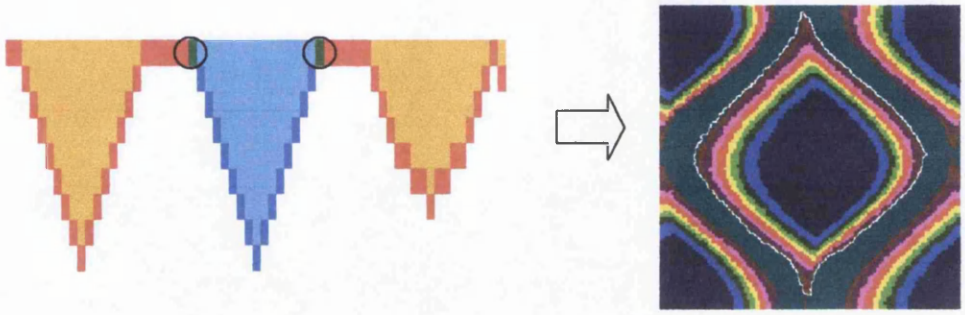

Figure 4-4: Edge definition through modified watershed algorithm

Due to the presence of the surface roughness, this method is subject to a high variability with possible large errors, Figure 4-5. Integrating the watershed algorithm with a gradient analysis of the top surface solved the problem, allowing the definition of a reliable and referable cell edge, Figure 4-6. The gradient analysis consist of analysing the local gradient or slope on the edges of the engraved cells as defined by the modified watershed algorithm for a depth equivalent to the roughness of the land area surounding the cells. Through the imposition of a threshold value for the gradient related to the local roughness, it is possible to distiguish the slope of the cell from the natural variability of the land area roughness obtaining a more accurate and less jagged border of the cells.

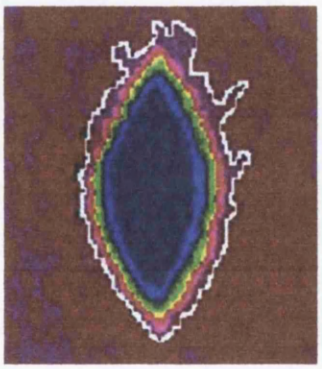

Figure 4-5:Limits of watershed algorithm in the definition of the border

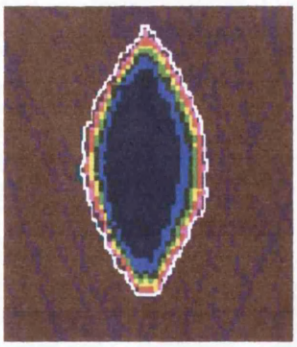

Figure 4-6: Same cell but here the watershed algorithm is integrated with gradient analysis

Once the cell and its edges has been identified and delimited, the geometric parameters, which characterise the engraved cells, can be easily measured, as presented in the next section. Together with their numerical values CellWCPC can generate pictures of the engraved cells highlighting geometrical parameters of interest, this pictures can be stored for reference and rapid visual verification, Figure 4-7.

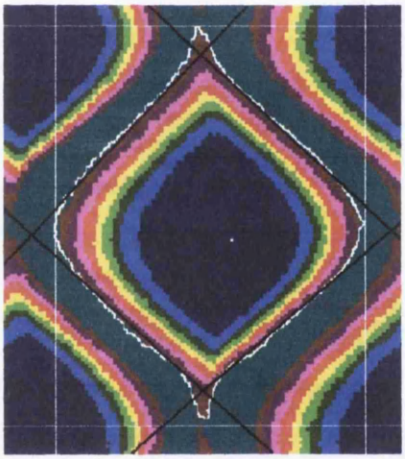

Figure 4-7: Visual output of the software highlighting some geometric parameters

4.4 Calculated geometric parameters

From the measurement of the profile, CellWCPC measures a list of parameters, which characterise the engraved cells.

a. **Cell dimensions**: width, length, depth, easily calculated by the analysis of the defined top border profile, Figure 4-6

b. **Compression ratio**: ratio between the width and the length

c. **Top open area** is obtained by counting the pixels included within the defined border

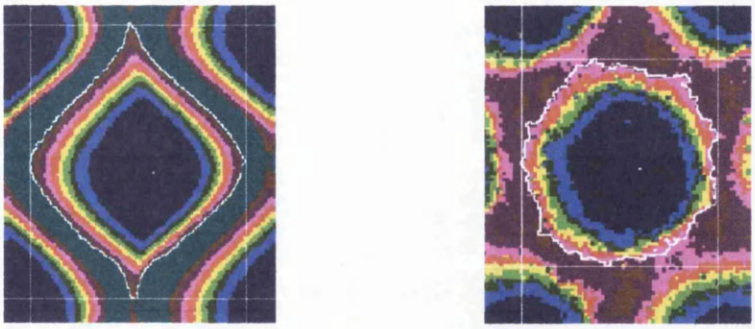

Figure 4-8: Picture of a mechanical engraved gravure cell and a laser anilox cell highlighting dimensions, position of deepest point, area within the border

d. **Land area roughness** surrounding the cell. The roughness can be calculated from the alignment ring. The ring surrounds the cell and lies on the surrounding land area; the ring is obtained on a smoothed and reduced profile; Roughness values can be calculated by analysing the data points on the original (raw) profile related to the alignment ring. CellWCPC is able to calculate the roughness parameters Ra, Rz (described in 3.5.1) and the Rt, i.e. the maximum peak-to-valley difference on the alignment ring.

e. **Volume of engraved cells**: the volume is obtained by integration of the depth of the pixel data within the border. The volume is defined as the quantity of liquid that can be placed inside the cell. The exact quantity of liquid is influenced by the land area roughness surrounding the cell. Different approaches to the land area roughness lead to different values of volume, as discussed in section 3.2; the software implements these different approaches, calculating different alternative values for the volume. The data pixels can be, in fact, integrated up to different reference planes. The volume is typically integrated up to the land area mean height. CellWCPC does calculate other values of the volume determining a reference plane in relation to the surface roughness or border profile. Reference level values, usually examined together with the mean height level one, are the ones related to the Ra and the Rz of the land area. In engraved gravure cells the difference among these values is very little due to the relatively low roughness levels of the land area; this is not the case for other engraved cells such as on anilox rollers.

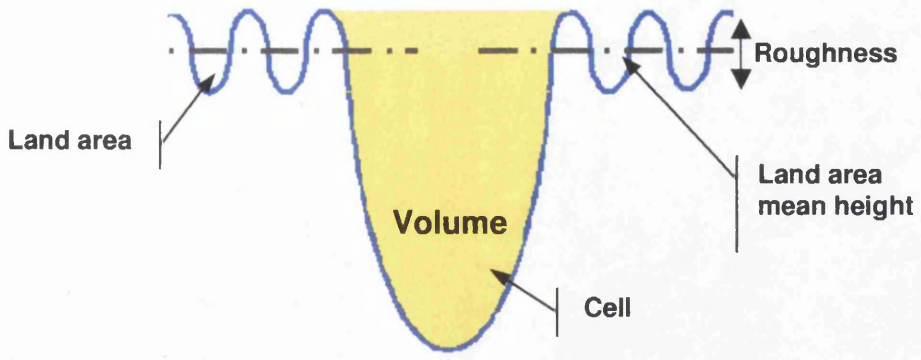

Figure 4-9: Cross section schematic for the measurement of the volume

In addition to these reference parameters, CellWCPC is also able to define other parameters, often previously omitted due to the complexity of measurement process.

For **mechanical engraved cells** it is able to measure:

a. **Stylus angle:** The stylus angle is calculated from the cell wall angles in the cross sectional profile through the cell. The software does not simply calculate the value of the stylus angle but it can examine its variation with the cell depth, allowing examination of the straightness of the engraving tool cut. Furthermore it can compare an extrapolated theoretical depth in the presence of a perfectly sharp stylus engraving tool with the related actual real depth; this comparison is useful for the analysis of engraving tool wear or of residual ink deposit, Figure 4-10

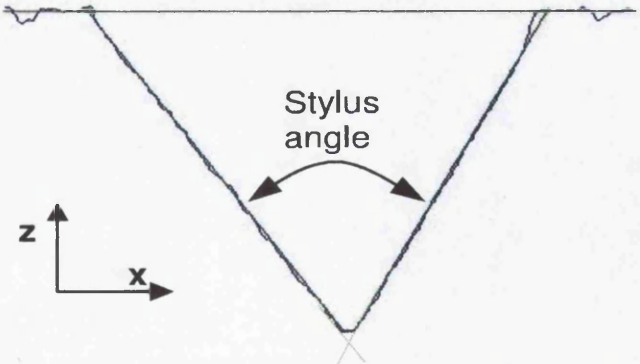

Figure 4-10: Cross section profile of the cell, stylus angle

b. **Offset** between the bottom of the cell and its median axis, Figure 4-11, see section 3.5.2.

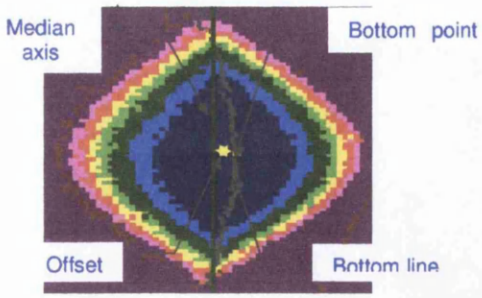

Figure 4-11: Offset between the bottom of the cell and its median axis

c. **Cell edge angles**: the actual angle of the outline edges of the cell is different from the compression ratio (i.e. width over length). From an analysis of the cell edges of the four sides of a mechanical engraved cell top area, the theoretical pyramidal shape of the top area is determined, Figure 4-12, Figure 4-13. This gives the opportunity to notice any possible **asymmetry** in the cell shape. Asymmetry of the engraved is related to the alignment of the stylus tool with the surface of the cylinder, see section 3.5.2.

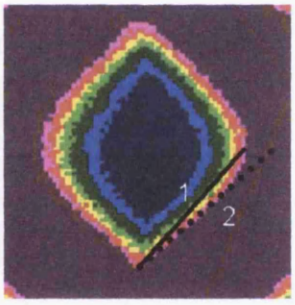

Figure 4-12: Compression ratio (1), Cell edge angle (2)

Figure 4-13: Highlighted shape of an asymmetric cell

d. **Thickness of cell length extremes:** the cell length extremes are the points of input and output of the engraving tool with the cylinder. The two extremes show, sometimes, a different thickness due to the machining process. The analysis of the thickness of these extremes could be useful for an analysis of the engraving process and of the wear of the tool; more worn tools should generate more rough exit edges due to a less clear cut with a rougher edge finish

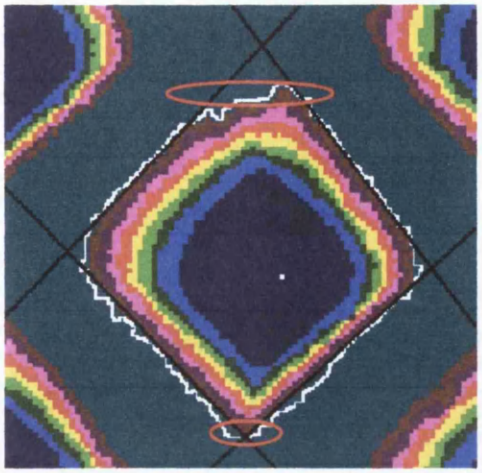

Figure 4-14:The two extremes of the cell length show a different thickness

e. **Perimeter of the border:** perimeter of the outline of the cell on the top area

f. **Inter-cell channel thickness**: during the analysis of the alignment ring, CellWCPC is able to recognise the channels, whose thickness can be then calculated. These inter-cell channels are typically present in electromechanical cells at high area coverage.

Laser engraved cells are less common in the gravure printing industry. They are the standard in flexography in the production of ceramic anilox rolls. Taking into account the needs of this sector, in the case of laser engraved cells, CellWCPC is able to calculate:

a. **Inclination of the cell walls:** this is important for understanding the shape of the engraved cells, depending on the ratio of this inclination with the depth the cell will present more V or U shape.

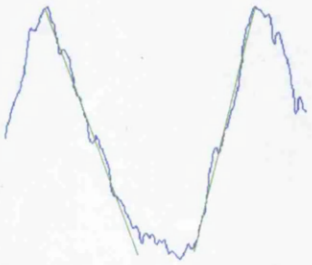

Figure 4-15: Cross section profile of the laser engraced

b. **Perimeter of the border:** perimeter of the outline of the cell on the top area

c. **Circularity of the cell top area:** in case of oval laser engraved cell this parameter can be related to the effect of the screen angle of the electromechanical cells.

d. **Depth to opening ratio**, the ratio between the depth and the width, parameter commonly used in anilox rolls.

e. **Depth to open area ratio :** ratio between the depth of the cell and its top open area

The software can also execute a sectioning of the profile of the engraved cells at a specific depth, measuring the area and the dimensions of the obtained section. This gives an **alternative volume measurement method,** derived by a strict implementation of the manual method explained in section 3.5.1. Following this alternative method, the cell is sectioned at a depth depending on the land area roughness, Figure 4-16. The volume is then calculated in two parts; the first part is the actual volume below the sectioning plane obtained by integration of pixel data (V1 in Figure 4-16). The depth of this sectioning plane is equivalent to half the Rz value of the land area roughness. The second one represents the volume of cell over the sectioning plane and it is based upon consideration of the land area roughness (V2 in Figure 4-16); the sum of these two parts gives the volume of the cell based on its geometry. This method has been developed in order to have the opportunity to compare with measurements obtained by the manual step by step procedure presented in [5] and section 3.5.1.

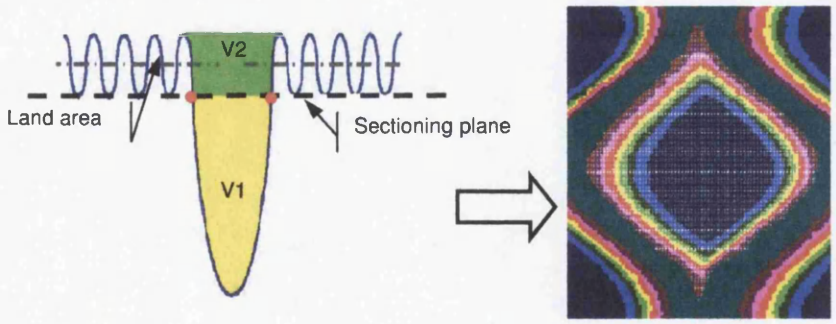

Figure 4-16: Sectioning of the image; Cross section schematic and planar view with defined bordered cell highlighted

CellWCPC is able to give an accurate characterisation of a single cell; this has to be used in combination with the **screen ruling** and the **screen angle** to give the engraved volume per unit area and a complete view of the roll layout. The screen angle and

screen ruling can be accurately determined by simple image capture and analysis of the engraved surfaces or of the printed web.

4.5 Verification of the software

In order to verify the validity and accuracy of the developed software, different experiments were carried out

4.5.1. Comparison with optical microscope

Results from the software were compared with results obtained with a microscope to evaluate the performance of the cell edge definition algorithm. Engraved patches of a gravure cylinder were measured with a microscope and with white light interferometry. From the two-dimensional pictures of the cells obtained from the microscope the width, the length and the top open area were measured; the high contrast between the engraved areas and the land area allowed an easy manual determination of the cell dimensions, Figure 4-17. The 2D picture had a pixel resolution of 0.615 μm, calibrated on a reference.

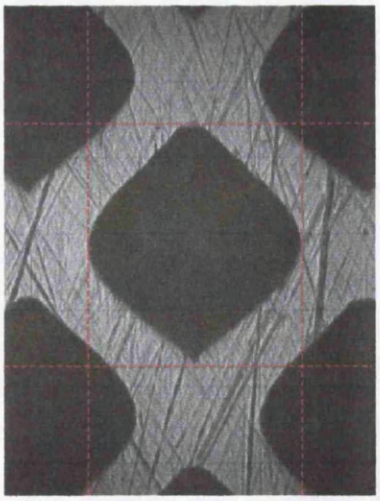

Figure 4-17: 2D Optical microscope picture highlighting dimensions

Corresponding three-dimensional cell profiles were obtained with white light interferometry and analysed using CellWCPC; the obtained width, length and top open area were then compared with the ones obtained with the optical measurement. The lateral resolution for the scanned profile was 0.542x0.464 μm; this value is very close to the camera resolution allowing a good comparison of the eventual results.

The analysed patches were engraved with a 130° stylus and a screen ruling of 60 l/cm in two sets, one with a nominal compression ratio of 45° and one of 60°. For each set, there were four levels of nominal area coverage (10%, 40%,70%,100%), giving a total of 8 engraved patches. For each patch, 5 white light interferometer cell measurements and 5 optical cell measurements were carried out.

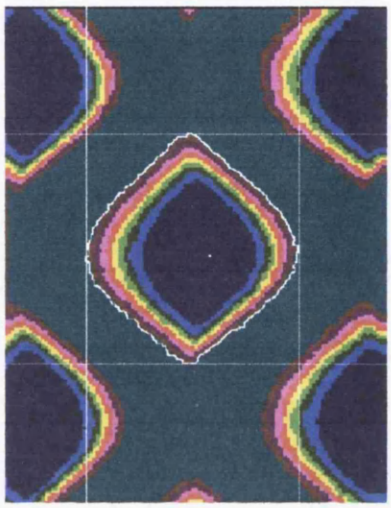

Figure 4-18: Top view of 3D profile, highlighting dimensions calculated by the software

In Figure 4-19, Figure 4-20, Figure 4-21, the results are plotted against each other for the 45° Compression ratio cells; the same trends were observed for the 60° Compression ratio cells.

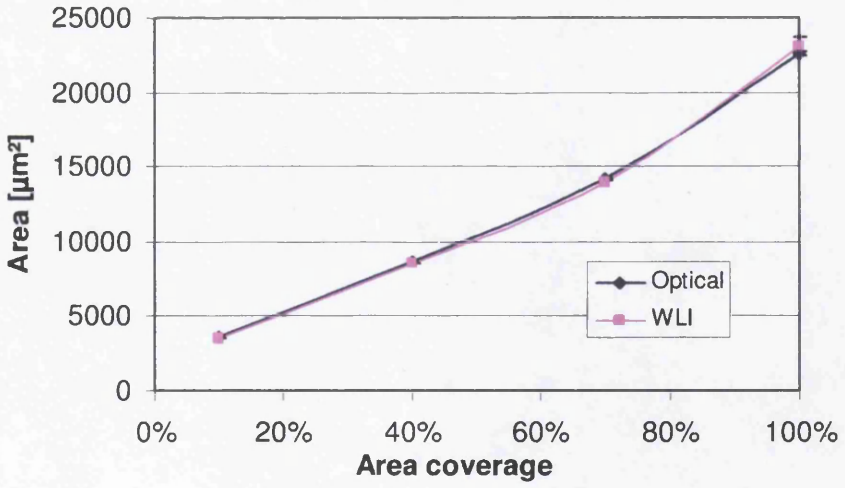

Figure 4-19: Cell top open area vs. nominal area coverage

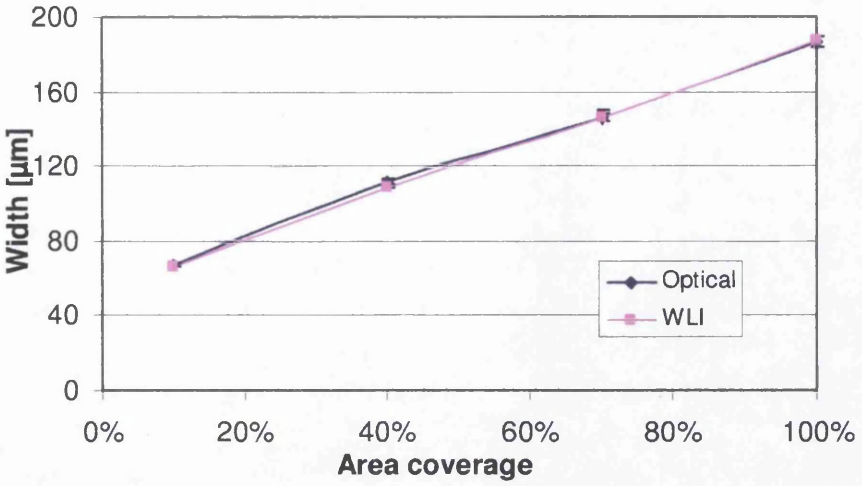

Figure 4-20: Width vs. nominal area coverage

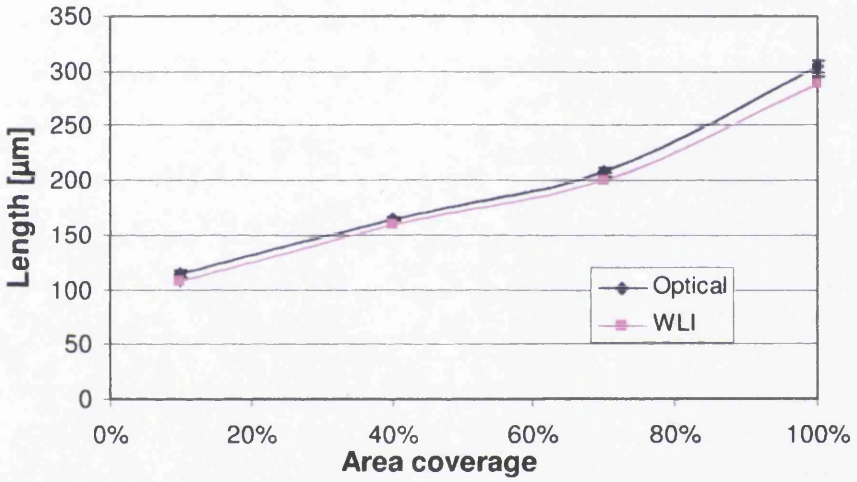

Figure 4-21: Length vs. nominal area coverage

The comparison shows an extremely good compatibility. For the comparison the overlapping of the band of errors was verified. Error bands used for the comparison were equivalent to 99% interval confidence of the mean.

The confidence interval of the mean is calculated using the standard formula:

$$\bar{x} \pm \left(c * \frac{s}{\sqrt{N}} \right)$$

where X is the average of the sample, s the standard deviation of the sample, N the size of the sample and c the coefficient derived by the T-student distribution. In the case of 99% confidence interval for a sample size 5 (4 degree of freedom) c is 4.604.

The error bands overlap, meaning a complete compatibility in the results. In the charts the bands are rarely visible, meaning an elevated precision in the engraving and in the measurement methods. The only clearly "visible" band is in Figure 4-21at high area coverage, this is due to the presence of inter-cell channels, which increase the variability of the measurement.

Being able to reach the same results using two completly different methods of measurement proves the capability of the developed watershed algorithm in the identification of the cell and in the definition of its border.

4.5.2. Evaluation of precision and repeatability

The volumes of four different engraved bands on a anilox roll were characterised by three different operators in a "blind test", [9].

Anilox rolls are characterised by typically a higher screen ruling and much higher degree of surface roughness than their gravure counterpart; this induces a much larger variability on the measurement of volumes, amplifying any problem related to the repeatability.

Each operator had to carry out independently the profiling of the anilox rolls with white light interferometry and then the measurements with the developed software. The purpose of the experiment was to verify the repeatability of the measuring method independently from the user and its precision.

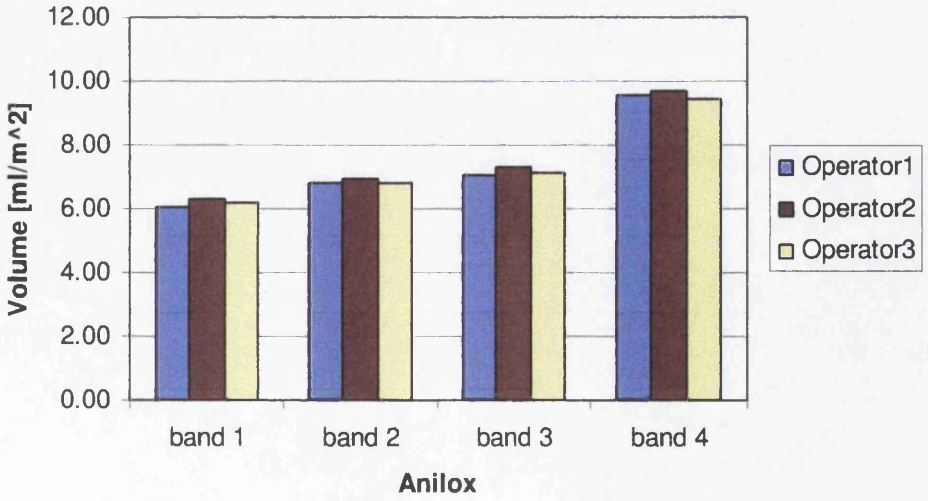

Figure 4-22: Comparison of operators

The results show that the calculated values of volume were very close to each over: the average difference is less than 2% of the mean values. These differences are minimal, considering the effect of the land area roughness on the variability of the engraving, with a Ra of the order of 1-2 um. The process of measuring has been shown, therefore, to be repeatable and precise.

4.6 Examples of applications of the software

The developed software can analyse previously stored profile data files or it can be placed in-line with the white light interferometer giving immediately the characterisation of the profiled engraved cell. In Figure 4-23, Figure 4-24, examples are presented to visually show the ability of CellWCPC to recognise and characterise a large range of engraved cells. In Figure 4-23 mechanical by engraved cells are presented, the cells range in dimensions and inter-cell channel is present in the larger ones. In Figure 4-24 CellWCPC is used in the characterisation of anilox rolls cells with different configurations; CellWCPC was shown to be robust, being able to deal also with cells roughly engraved, far right Figure 4-24 .

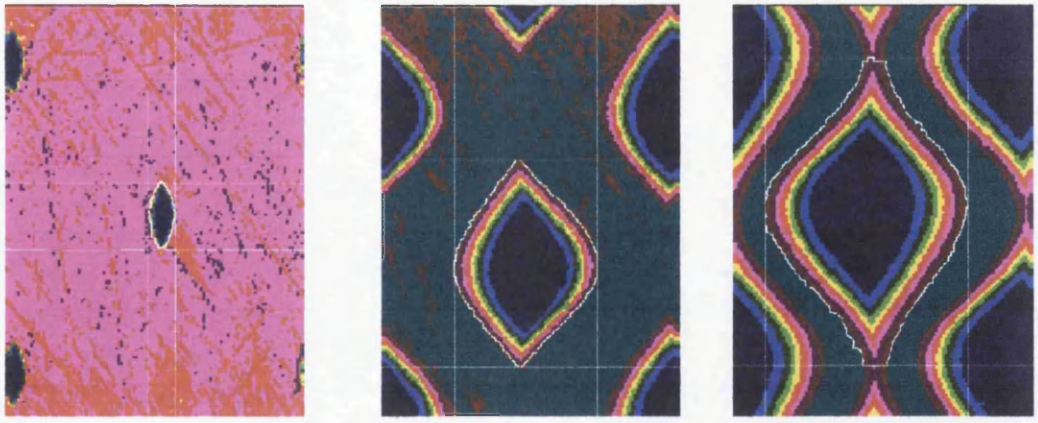

Figure 4-23: Examples of results from mechanical engraved cells with different area coverage

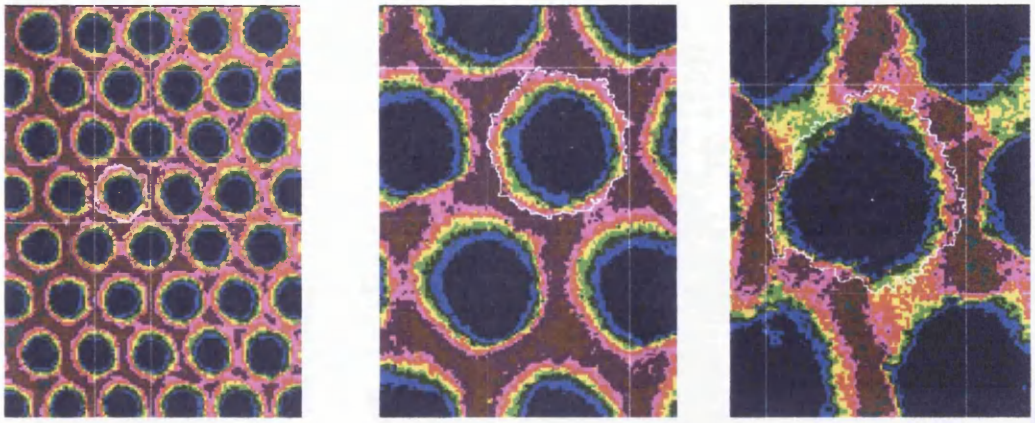

Figure 4-24: Anilox cells with different screen ruling, on the far right a poorly engraved cell.

CellWCPC has completely changed the scale size of possible analysis explorations; before the application of the software, few hundreds analysis, carried manually step by step, required weeks of work, now the software is able to automatically carry out thousands of analyses in less than a day giving more accurate and extensive results.

An example of the capabilities and possible applications of the software is a study of the effect of chromium plating over the size and shape of the engraved cells. In Figure 4-25 and Figure 4-26 the effect of a chromium plating process over cells is shown. The cells were engraved with 55 l/cm screen ruling, 45° compression ratio at 12 nominal area coverage levels (3,5,10,20,30,40,50,60,70,80,90,100%)

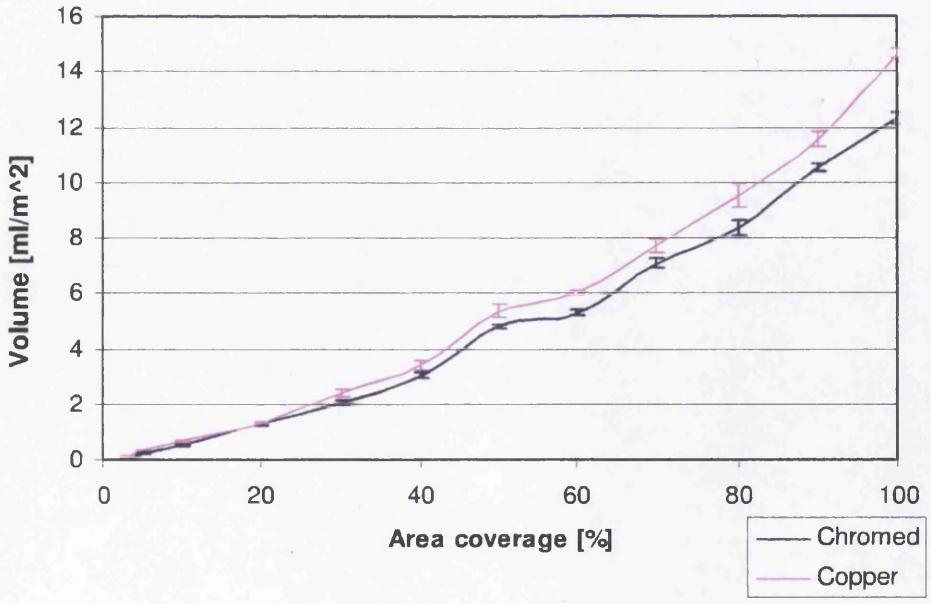

Figure 4-25:Volume variation due to chromium plating

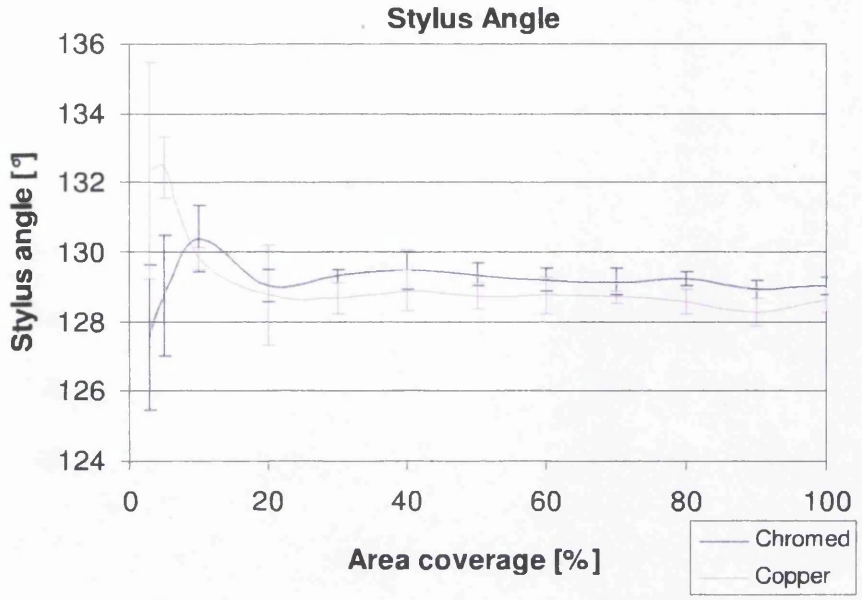

Figure 4-26:Stylus angle variation due to chromium plating

In this analysis the software showed great accuracy; average cell volumes were measured with 1 % accuracy. The software was able to assess very small variations of volumes between cells in the same patch, estimating standard deviation as small as less than 0.01 ml/m² for some patches. In the measurement of stylus angle showed great accuracy being able to assess a standard deviation value of < 1° among a range of cells of same patch.

4.7 Closure

In this chapter, CellWCPC software for accurate characterisations of engraved cells has been presented. Analysing each engraved cell separately, the software is able to automatically identify the cell and its border over a three-dimensional profile using a newly developed watershed algorithm; it then calculates a large number of geometric parameters, which completely identify the cell.

The list of geometric parameters is: volume, width, length, depth, top area; for mechanical engraved cell: stylus angles, offset, cell edge angles, thickness of cell length extremes; for laser engraved cells: circularity of the open area, depth to opening ratio.

The software was shown to be robust and accurate, able to deal with a large range of cells, independently from the engraving technique, the quality of engraving and the operator. The software has greatly increased the speed of the process of analysis of the engraved cells allowing large-scale extensive characterisations of gravure cylinders and anilox rolls, a process previously too time consuming and trained-labour intensive. This software is able to provide the geometric parameters that are essential for a successful analysis of the gravure process and its modelling.

5 Experimental printing trial and data collection

5.1 Introduction

The development of the gravure printing model is based on experimental data that characterise the different aspects of the process. In this chapter the execution of an extensive press trial, its related collection and analysis of experimental data are presented. The collected data pertained to the engraved cylinder, the press set-up and the printed results. The data from this trial will be used in the development of the model, presented later in chapter 7. The data were collected in a controlled manner in order to achieve valid and usable data, being able to account for different sources of inaccuracy.

5.2 Experimental trial

A printing trial was carried out during the development of the thesis of [7]. During this trial an extensive range of conditions and geometric parameters were explored, within in a controlled environment. The test was carried out on a commercial press at BASF. The use of a commercial press allows a more reliable study of industrial printing applications than the use simulation presses.

The experimental trial can be split into four variable parameters: the engraved cylinder, the press settings, the substrate and the ink. A limited and partial analysis of these elements was carried out in [7] and [10]. The scale and size of the trial did not allow the previous authors to carry a complete characterisation of the trial. During the development of this thesis, the analysis of the trial was largely extended, most notably in regards to the characterisation of the cylinder. Data derived by previous work is referenced when recalled.

5.2.1 The gravure cylinder and its image

A single cylinder was used for the trial; the cylinder was expressly designed for the analysis of the effect of different cell shapes and cell configurations, Figure 5-1.

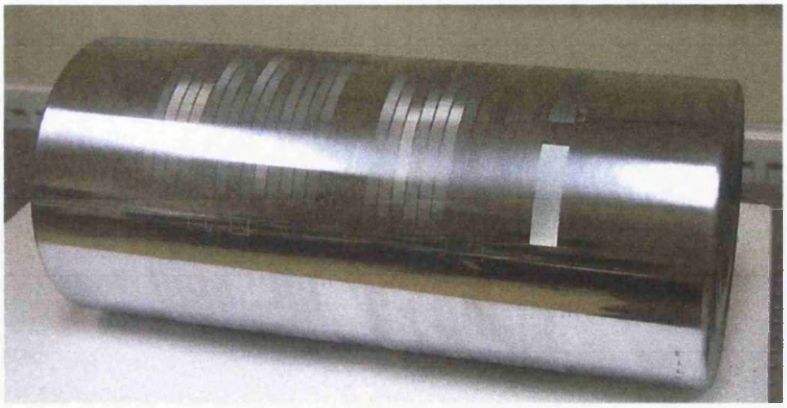

Figure 5-1: The gravure cylinder

The cylinder was engraved on an Ohio Electronic Engravers electro-mechanical engraving machine, the pre-engraving copper layer was prepared on a Daetwayler Polishmaster and the final chromed layer was finished on a Daetwayler Finishmaster. The cylinder has a diameter of 21 cm and a length of 50cm, its test image is shown in Figure 5-2.

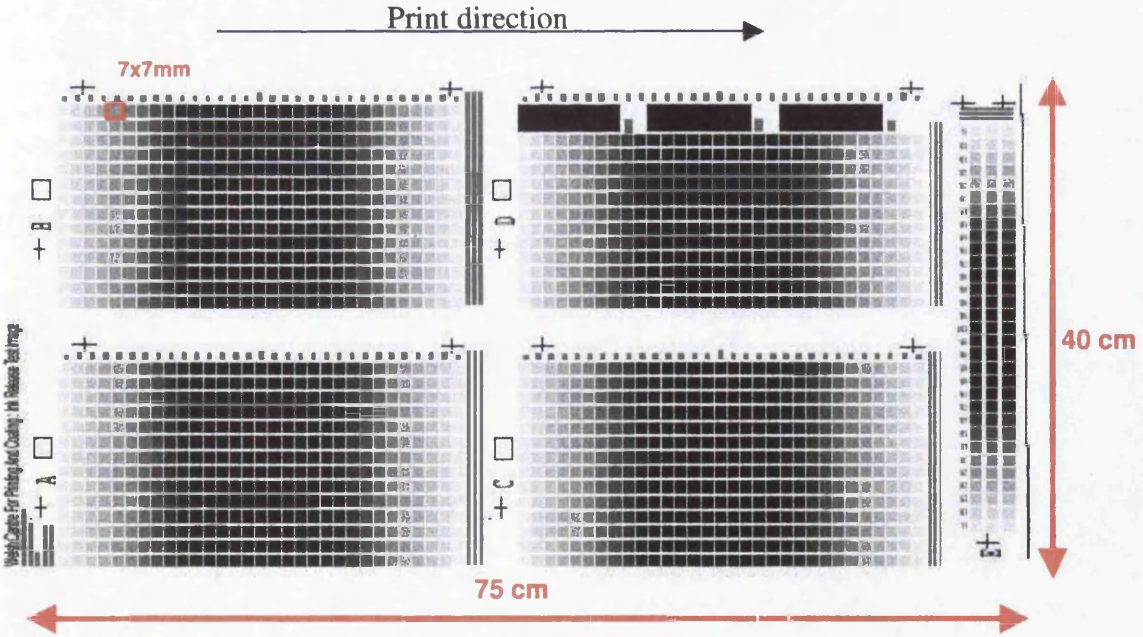

Figure 5-2: Test image of gravure cylinder

The test image is constituted by 57 graduation scales, organised in 5 major areas, identified as A to E; Each graduation scale was expressly engraved with a specific

combination of screen ruling, screen angle and stylus angle. During the engraving process, at the end of each graduation line, the engraving machine had to be stopped and recalibrated; furthermore, the machining of the cylinder required the use of 4 different diamond stylus tools. The preparation of this cylinder took several days, the engraving alone took 30 machine-hours; this allowed an extensive range of engraving parameters to be explored.

Each graduation scale was composed of 31 patches, each one engraved with cells of different volume; the volumes were chosen to obtain a full printed density range, expressed in nominal area coverage. The nominal area coverage indicates the theoretical optical area coverage attainable on the print as estimated by the engraver. Each scale was engraved so that each patch had a specific value of nominal area coverage increasing from 5% to 100 % and than reducing to 5%. In the aiming for the same optical area coverage across the combinations for the same nominal area coverage, the engraver established the engraved volume for each patch based on previous experience.

The size of each patch is 7x7 mm, large enough for the optical measurements under the spectrometer. The 31 analysed area coverages are for each graduation line as follows:

- Area coverage levels: 5%, 10%, 15%, 20%, 25%, 30%, 40%, 50%, 60%, 70%, 75%, 80%, 85%, 90%, 95%, 100%, 95%, 90% ... 0%

On the cylinder, the engraving parameters for each one of the 54 graduation lines were chosen as combination of

- Screen angle range: 30°, 37°, 40°, 45°, 50°, 51°, 57°, 60°
- Screen ruling range: 50, 60, 70, 80, 90, 100 lines/cm
- Stylus angles: 110°, 120°,130°,140°

These values of engraving parameters were chosen to cover the standard ranges typical of industrial applications. A complete factorial analysis of these parameters would require a total of 192 graduation lines, the cost of such an experiment would be excessive; the number of graduation lines was therefore decreased to the 57 significant combinations analysed. The absence of a complete spectrum of data can be limiting for several modelling methods, while neural networks deal well with

randomly proposed data patterns, assuming they cover enough of the region of interest. The complete list of specifications of the engraved cylinder is presented in Appendix A.

5.2.2 Press settings, substrate and inks

In order to achieve a greater control in the production and environmental conditions, the necessary data were obtained during a single print trial on a small commercial gravure press at BASF Company on the 13^{th}-14^{th} February 2001 [7]. This trial was carried out during the development of the thesis of Clist [7].

The prints were made on a standard Oriented Poly-Propylene substrate, Mobil 247; this was chosen since it would not absorb the ink, avoiding capillarity effects.

During the press trial, the appropriate ink was loaded into the ink tray, and the press was run up to speed (100m/min). Prints were made for 60s producing around 100 m of print / 160 repeats. The speed of the press was confirmed using a handheld tachometer; temperature was monitored by a series of thermocouples within to the ink tray, the frame of the press and for monitoring the ambient temperatures. Strain gauges were attached to the doctor blade to verify the load and angle, which were kept constant through out the trials. All these sensors helped to monitor and to keep constant the printing conditions, in order to reduce the number of affecting variables. It has been previously shown that blade angle and load have as significant impact on the printed colour density [11][12].

The trial was carried out using nitrocellulose resin solvent-based inks. In the original plan of the trial 4 different inks were used: one standard magenta, one standard cyan, a specially modified magenta and modified cyan inks which should be characterised by a constant colour strength independently from the viscosity. The inks were printed at different viscosity.

For the study carried out in this thesis, a specific set of ink was selected and analysed: namely the **magenta standard ink**. The press trial was carried out at three different viscosity levels, with the viscosity modified with by addiction of solvent. The viscosity of the ink was measured using Zahn2 Cups (see section 2.7), giving viscosity values of 20s 24s and 17s, respectively for the three viscosity levels. The pigment and solvent composition of the trial ink is presented in Table 5-1for the three

levels of viscosity. The solvent blend used in all cases is 50/50 Ethanol / n-Propyl Acetate [7].

Table 5-1:Composition of the magenta inks

		20"Zahn 2	24"Zahn 2	17"Zahn 2
Neat ink	PR 57/1 Base(20% Pigment)	35%	33%	40%
	Medium	45%	47%	40%
	Additive	20%	20%	20%
Reduction		100 ink:80 solvent =20"Zahn 2	100 ink:65 solvent =24"Zahn 2	100 ink:130 solvent =17"Zahn 2

5.3 Data collection

The gravure cylinder and the printed material were measured to collect data for the successive analysis and modelling of the gravure process.

5.3.1 Geometric characterisation of the engraved cylinder

The engraved cylinder was geometrically characterised using white light interferometry. A white light interferometer rollscope, described in section 3.4, was used for the scanning of the profile of the engraved cells. All the engraved patches of interest present on gravure roll were scanned, typically carrying out 5-6 scans per each engraved patch for accuracy and repeatability. Each scan comprises a single cell, Figure 5-3.

The scanned profiles were then automatically analysed using CellWCPC software, described in Chapter 4. Thanks to the use of the software, it was possible to carry out an extensive, rapid and accurate characterisation of the gravure cylinder, collecting a large range of geometric parameters of interest, as explained in Section 4.4.

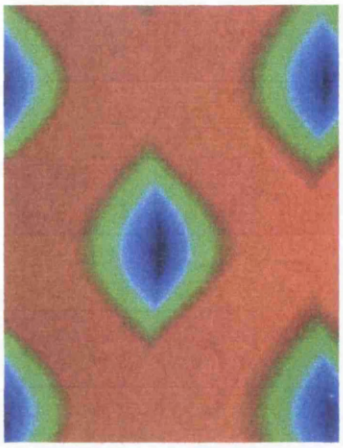

Figure 5-3: Example of a engraved cell scan

The scans were processed in order to calculate all the following **measured parameters** of interest from the profile:

- **Engraved Volume [ml/m^2]**
- **Open area [m^2/m^2]**
- **Width [μm]**
- **Length [μm]**
- **Depth [μm]**

For each patch, the measured parameters are obtained by averaging the data measured by the software for 5 measured cells of the specific patch. The engraved volume and the open area are then calculated in relation to the surface of the cylinder, with:

- Engraved volume= average volume of a cell x screen ruling^2 [ml/m^2]
- Open area = average open cell area x screen ruling^2 [m^2/m^2]

All the 57 different graduation lines were characterised, each one with its own specific combination of **engraving parameters**:

- **Screen ruling**
- **Screen angle**
- **Stylus angle**

These values of screen rulings, screen angles and stylus angles were given by the documentation provided with the engraved cylinder and verified by image processing. These values could be compared with the values measured by the software of border

angle (vs. screen angle) and the measured stylus angle (vs. provided stylus angle, it could differ due to chroming) to verify the correct association.

For each graduation scale, only half of the patches were measured, giving a total of 16 patches per line, as highlighted in Figure 5-4, providing a complete overview of the effect of cell size from 5% to 100%;

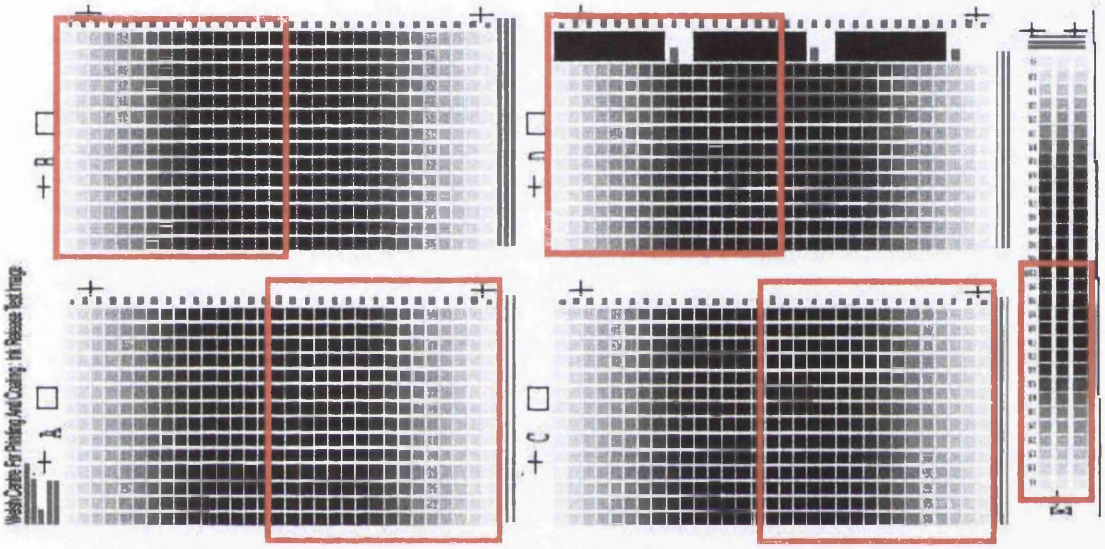

Figure 5-4: Measured engraved patches

Nearly 5000 scans were measured and characterised, equivalent to around 30 workdays using CellWCPC software. If the cells were characterised by using the manual techniques (see 3.5), it can be estimated that this characterisation would have required probably more than 150 workdays. The list of results is contained in Appendix A

5.3.2 Optical measurement of printed samples

The printed samples were measured using spectrophotometric techniques. These measurements were carried out by D.James [10]. The **optical density** of each patch was measured using a Gretag Spectrolino spectrophotometer. Optical density is used as an indication of the ink thickness. It is a measure of the spectral wavelengths absorbed by the ink film, and is defined as:

$$Optical\ Density = \log_{10} \frac{1}{reflectance}$$

For the optical density, only a narrow portion of the reflectance spectrum is used. This can be achieved by coloured filters or by computational filtering.

From the optical density, the optical area coverage can be determined using the Murray-Davies equation:

$$Optical\ dot\ area = \frac{1-10^{-D_t}}{1-10^{-D_s}}$$

Where D_s and D_t are the ink densities of the solid measurement area and of the analysed halftone patch.

The Spectrolino is a programmable spectrophotometer, which once programmed with the location of each colour patch on a printed samples will take the measurements at these locations on each printed sample provided. All the measurements were taken using a D50 illuminant, D65 filter, ANSI T standard. For each one of the 3 levels of viscosity, 32 samples were measured, measuring each patch on the image plus a no-printed patch of the substrate; a total of around 160000 measurements (54 graduation lines plus, 31 patches for graduation line, 32 repetitions) were carried out. The values of the measured density were normalised by subtracting the colour density of the substrate. The complete results are contained in Appendix A.

5.3.3 Data collection conclusions

A large range of experimental data was collected to accurately describe the geometric characteristics of engraved cells on a specially created roll and the optical characteristics of the relative obtained printed substrate in different conditions for a specific set of ink and substrate.

The engraved roll comprises a total 912 engraved patches in 57 graduation scales, each one characterised by its own combination of screen ruling, stylus angle and screen angle. For each scale, 16 patches were measured with different nominal area coverage levels in order to cover the all tone reproduction. Since the obtained optical density has been characterised at 3 different levels of viscosity, the experimental data comprised a total of 2736 measured datasets (912×3).

In order to integrate the land area in the data collection, "theoretical" datasets were added having a zero volume cell with a zero density (substrate has been normalised to zero). One of these theoretical zero patches was added for each graduation scale at each viscosity level, giving a final extensive collection of data of 2907 datasets, 969 per each viscosity. Each complete dataset includes 10 values (Table 5-2). The complete list is presented in Appendix A.

Table 5-2: List of parameters composing a dataset

Engraving parameters	Measured parameters	Viscosity	Colour density
Stylus angle [°]	Volume [ml/m^2]	Viscosity [Zahn2]	Colour density
Screen ruling [l/cm]	Open Area [m^2/m^2]		
Screen angle [°]	Width [µm]		
	Length [µm]		
	Depth [µm]		

5.4 Analysis of the engraved roll

In this section, the engraved cylinder is characterised with particular reference to the accuracy of the measurements and the consistency of the engraving. The verification of the quality of the data is a basis for any modelling and analysis.

5.4.1 Accuracy of the geometric characterisation

The accuracy is determined by the variability and the confidence in the mean of the measured parameters.

5.4.1.1 Standard deviation of the sample and Confidence of the mean

The variability of the results can measured with the standard deviation of the sample s

$$s = \sqrt{\frac{1}{N-1}\sum_{i=1}^{N}(x_i - \bar{x})}$$

With N number of datasets composing the sample, $\bar{x}$ the average of the datasets, x_i the value of a dataset, [13]. The achievable standard deviation is influenced mainly by two factors: inaccuracy in the measurements and the variability of the sample itself. In a normal distribution, 95% of the data lie between the average $\pm 2\times s$, 68% within $\pm s$. The confidence interval of the mean is calculated following the equation:

$$\bar{x} \pm \left(c * \frac{s}{\sqrt{N}} \right)$$

Where is c is a coefficient, s the standard deviation of the sample, N the size of the sample. It represents the confidence interval within which lies the mean of the population, it can be considered as the error in the estimate of the average. The coefficient c derives from the student T distribution and is related to the size of the sample and to the selected probability range. A 95 % confidence mean for a set of 5 data, assumes a c value of 2.571 (student t distribution) so that a 95% confidence is equivalent to $\pm 1.15 \times s$, very close to s.

5.4.1.2 Accuracy results

The statistical analysis of the measured data regarded two measured parameters, the volume and the width. The standard deviations were calculated over a size of 5 samples per cell. Results are presented for each level of nominal area coverage, averaged throughout the different graduation lines, Figure 5-5, Figure 5-7. For the volume, the 95% confidence interval of the mean is also presented, Figure 5-6. Data are presented as percentage of the average measured value of the parameter.

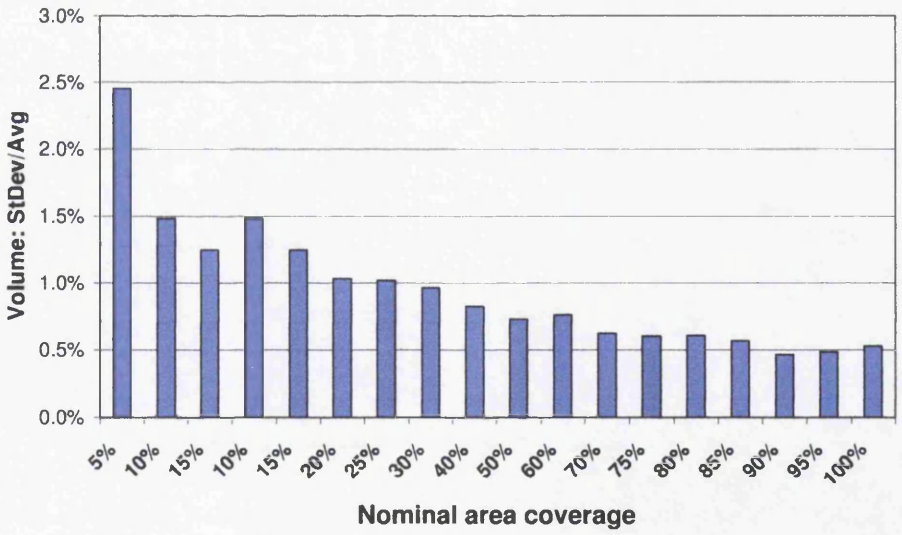

Figure 5-5: Standard deviation on the measurements of volume

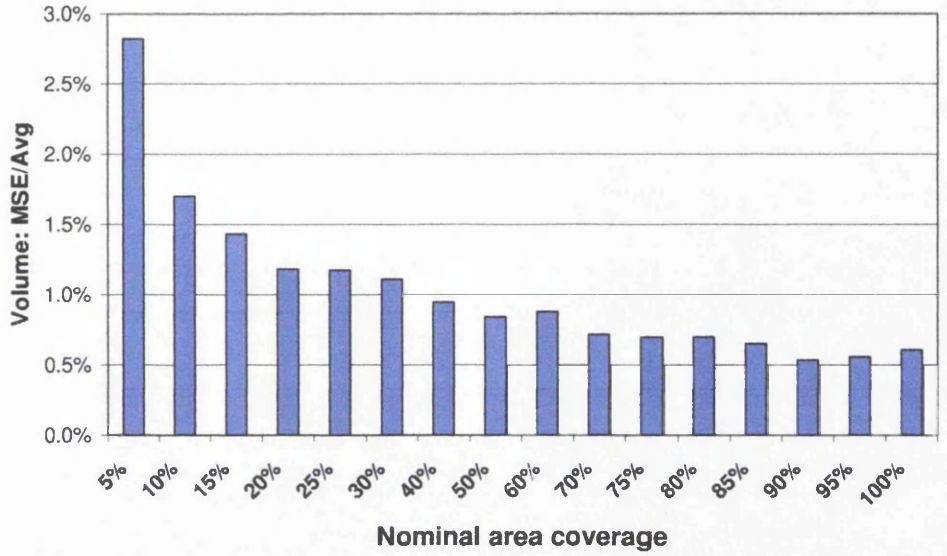

Figure 5-6: 95% Confidence interval on the measurements of volume

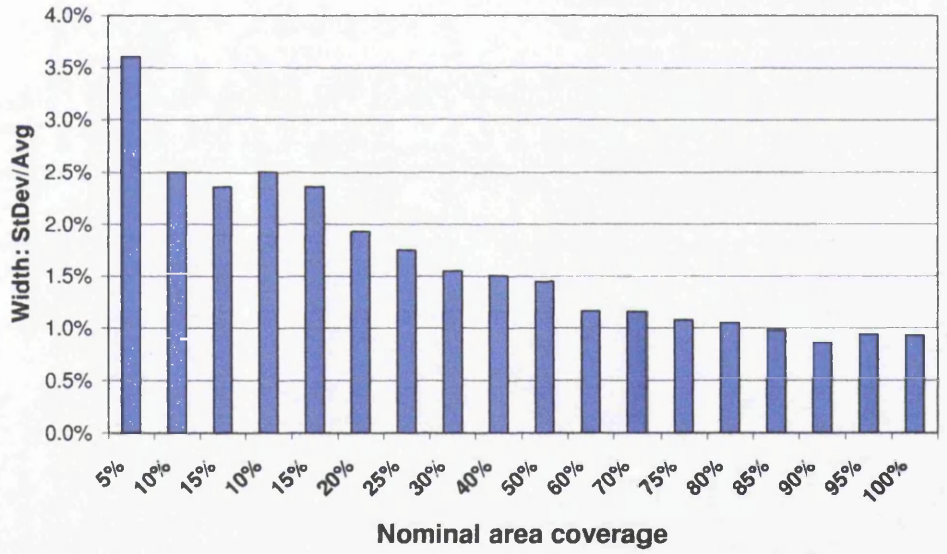

Figure 5-7: Standard deviation of the measurements of width

The results indicate a low variability and small confidence interval, with values of standard deviation of less than 1% in the volume and 1.5% in the width. In the smaller cells, variations of the surface roughness would have a larger impact in the measure of the cell volumes; hence, smaller cells present larger standard deviations.

The results indicate the cells are consistent within the patches and have a good level of accuracy in their geometric characterisation.

5.4.2 Repeatability of the engraved patches

The accuracy and repeatability of the engraving in the test cylinder were assessed. Each graduation line was independently engraved. Four of these were engraved nominally with the same values. These lines are identified as *An, Ba, Bn, Eb* and are highlighted in Figure 5-8. These graduation lines were engraved with a nominal compression ratio of 45°, a line ruling of 70 l/cm and a stylus angle of 130°. The four strips are located across the web. The strip An is vertically orientated and has been studied with a descending area coverage in the direction of printing. The strips *Ba, Bn* are both vertically orientated and have been studied with ascending area coverage in the direction of printing. The strip *Eb* is instead horizontally oriented.

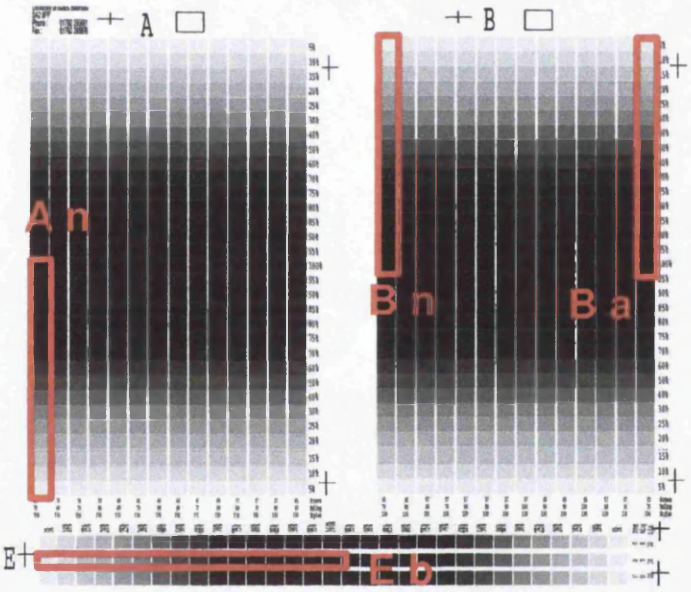

Figure 5-8: Analysed graduation lines

The different values of volume for each graduation patch can be compared with each other. Assuming a average values of confidence interval related to Figure 5-5 , the difference between equal patches should be within two times these values (one per side). In Figure 5-9, the volumes are plotted in relationship to the values of the volume of the graduation patch Bn, placed in the middle of the cylinder. On the chart the 2x 95% confidence interval line is indicated, derived from Figure 5-5.

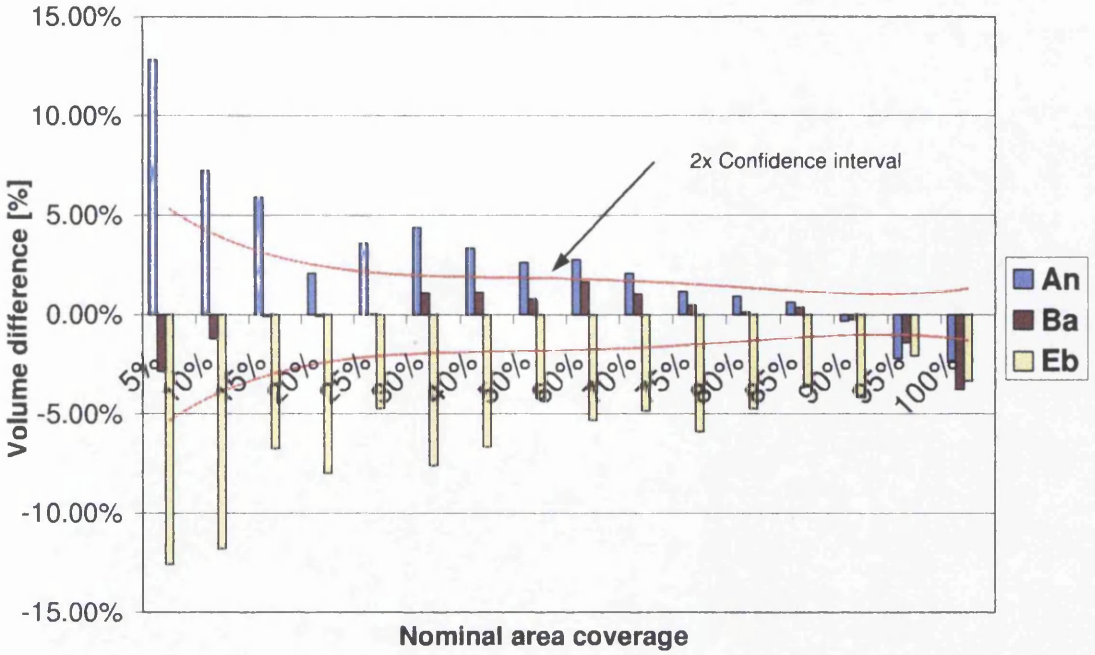

Figure 5-9: Volume difference from patches of lines Bn

The plotted confidence interval is double the values presented in Figure 5-6, because in Figure 5-9 one line is compared with another; assuming for each line the 95% confidence interval derived from Figure 5-6, on one side there will be the confidence interval of the reference line *Bn,* on the other the 95% confidence interval of the compared line; adding the two confidence intervals the 2×95% confidence interval is obtained and can be used for comparing the agreement of the mean values of engraved volume.

There is agreement between the engraved patches of line *Bn* and *Ba*; the results of line *An* are also close, while *Eb* has a low agreement. There is a good consistency between the "vertically" engraved patches, consistency not entirely kept during the engraving of the horizontal lines.

5.4.3 Conclusion

The gravure cylinder has been accurately engraved; the variability of the results within a patch is extremely limited. The engraving of the cylinder shows a good consistency: there is significant agreement between patches engraved with the same nominal values.

5.5 Preliminary analysis of collected optical data

A preliminary analysis of the collected data was undertaken to identify critical areas for further in depth analysis and also to establish the limitations of the data set. In Figure 5-10, the nominal area coverage is plotted against the measured densities with a viscosity of Zahn2 20s. There was a conspicuous spreading of the data, indication of a limited correlation.

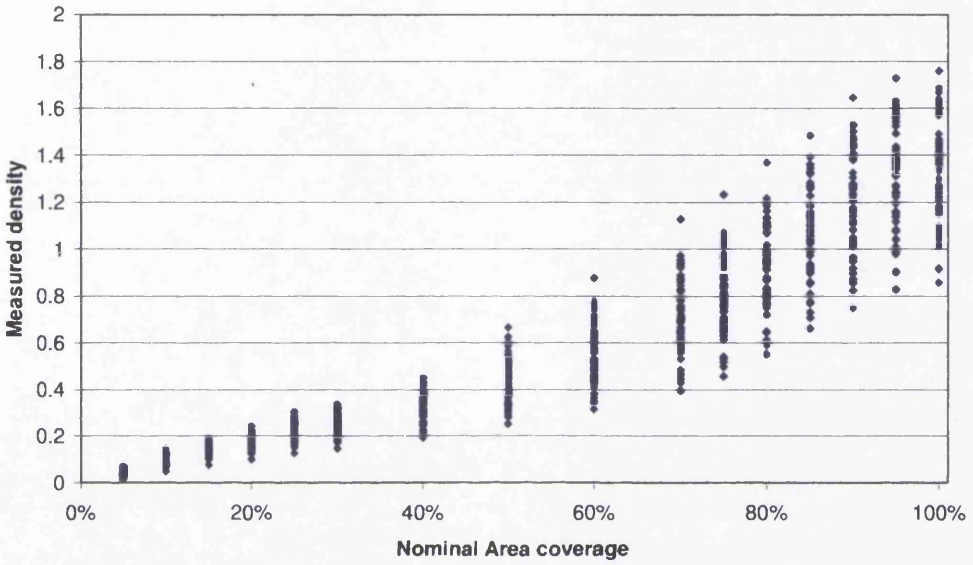

Figure 5-10: Nominal area coverage vs. measured density

This is also visible in Figure 5-11, where the nominal area coverage is plotted against the measured optical area coverage. In ideal situations, the nominal areas, as indicated by the engraver, should match the optical areas.

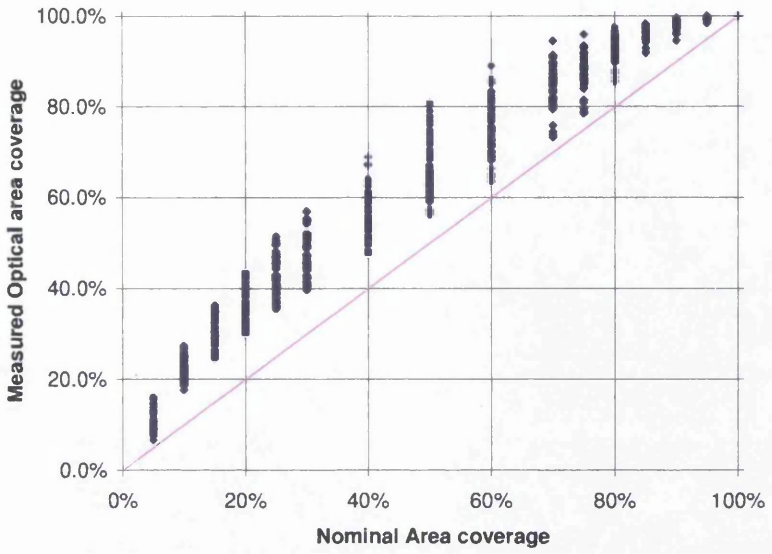

Figure 5-11: Nominal vs. measured optical area coverage

These results show the inaccuracy of the gamma or correction curves used by the engraver in estimating the nominal area coverage; a better method to define these gamma curves would allow a reduction in difference between the nominal and actual optical area coverage improving the quality and reliability.

5.5.1 Analysis of the engraved volume

On the basis of the geometric characterisation of the engraved cells, the colour density can be plotted against the measured values of volume, Figure 5-12; there is a much better correlation of the data than in the case of the nominal area coverage

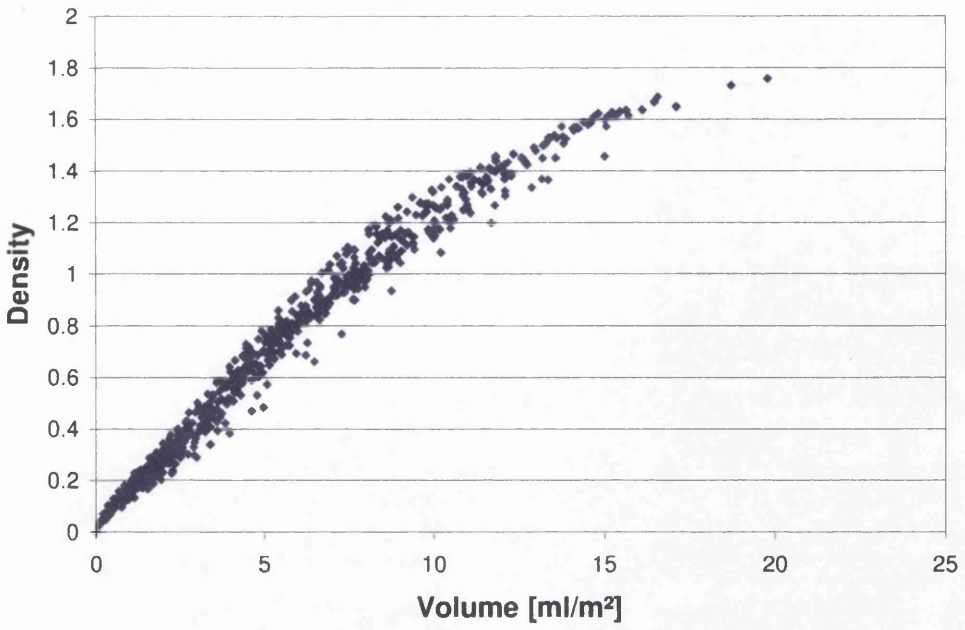

Figure 5-12 Colour density vs. Volume over area

A statistical analysis of the correlation between the engraved volume and the achieved density was carried out. A linear polynomial fitting analysis was carried out; this follows the equation:

$$y = n * x^n + .. + c * x^2 + b * x^1 + a$$

Where x represents the volume and y the obtained density.

Since a zero volume gives a zero density, the coefficient *a* could be imposed equal to zero. However, the colour variability of the substrate can give rise to small variations in densities. Therefore, an alternative approach was adopted: the value of *a* was not imposed to 0, but theoretical patches were added with value (0,0), as explained in 5.3.3. These patches represent the 0% area coverage for each strip. This alternative approach allowed the partial verification of the quality of the model and of the data collected: if *a* did not have a negligible value, then the model is clearly incorrect.

The analysis of the data shows a quadratic fit with equation:

$$y = -0.0032x^2 + 0.1538x + 0.0059$$

and is overlaid with the data in Figure 5-13

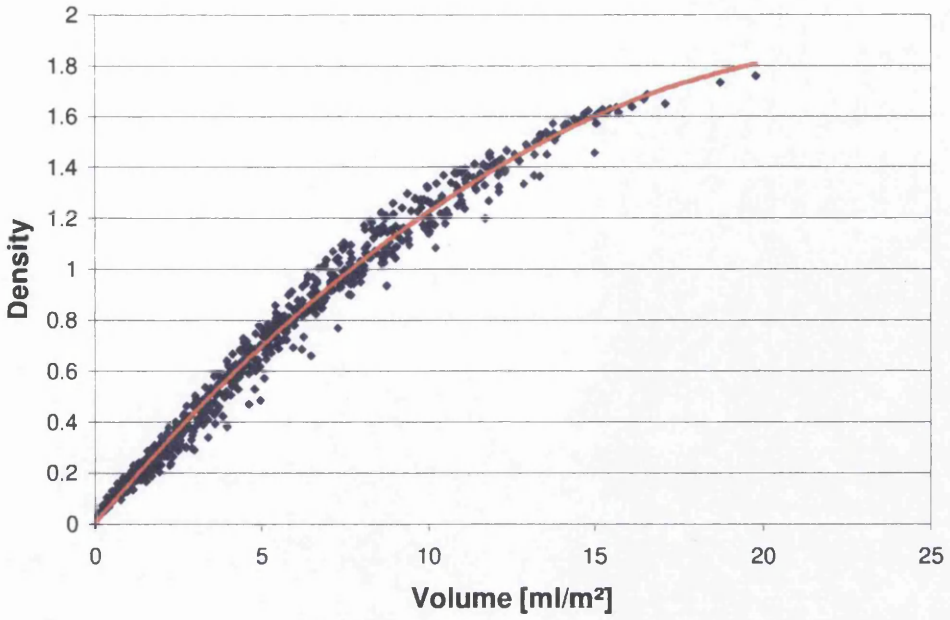

Figure 5-13: Polynomial fitting of volume vs. density

This equation gives a sparse residual error (Figure 5-14), indicating good fitting.

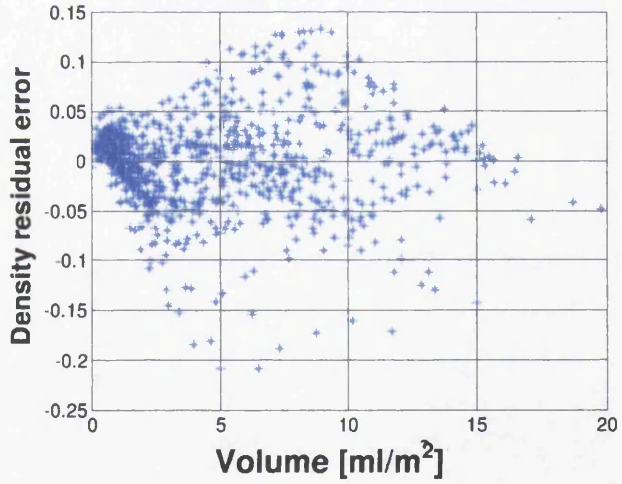

Figure 5-14: residual chart for 2nd grade fitting

5.5.1.1 Evaluation of the model quality: Root Mean Square

A common parameter for the evaluation of the quality of a generic model towards specific datasets is the Root Mean Square Error. The RMSE is the square root of the average squared difference between the estimated values and the actual ones; it is a measure of the typical size of the prediction error.

$$\mathrm{RMSD} = \sqrt{\frac{\sum_{i=1}^{n}(x_{1,i} - x_{2,i})^2}{n}}$$

Where n is the number of samples and and x_1 the predicted value and x_2 the measured one. This error has the same dimensionality as the actual and predicted values; it gives therefore a usable estimate of an average error. In a normal distribution of the errors, a 2×RMSE gives a 95% confidence of the estimate, i.e. 95 % of the actual data will fit in the interval of the estimated values ±2×RMSE. It is important to underline that this is a global error; the specific accuracy at a given point of the model could differ. The Root Mean Square between the measured values of densities and the estimated ones by the polynomial model gives a value of 0.0460. In Figure 5-15, the results are plotted with 2×RMSE confidence bands of value 0.92. This error value is noticeable; by experience, a human eye is able to distinguish colours with a density difference of around 0.03-0.04 with higher sensitivity towards the low tone and colours closer to the green.

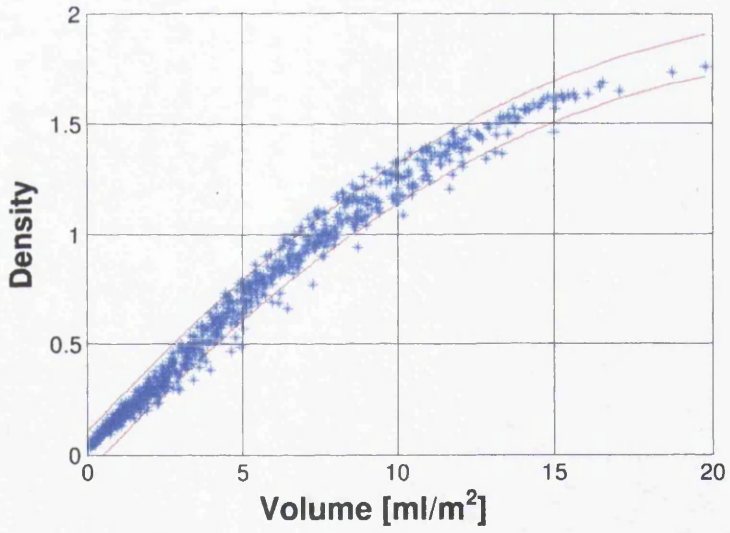

Figure 5-15: Volume vs. Density with 2×RMSE confidence band

5.5.2 Analysis of the engraved open area

A comparison of the obtained density versus the measured cell open area on the gravure cylinder shows a much poorer correlation (Figure 5-16) with a much larger spreading of the data. A polynomial analysis of the data shows a second order polynomial fitting with a resulting value of RMSE of 0.121 and equation:

$y = 0.986x^2 + 1.0706x - 0.0269$

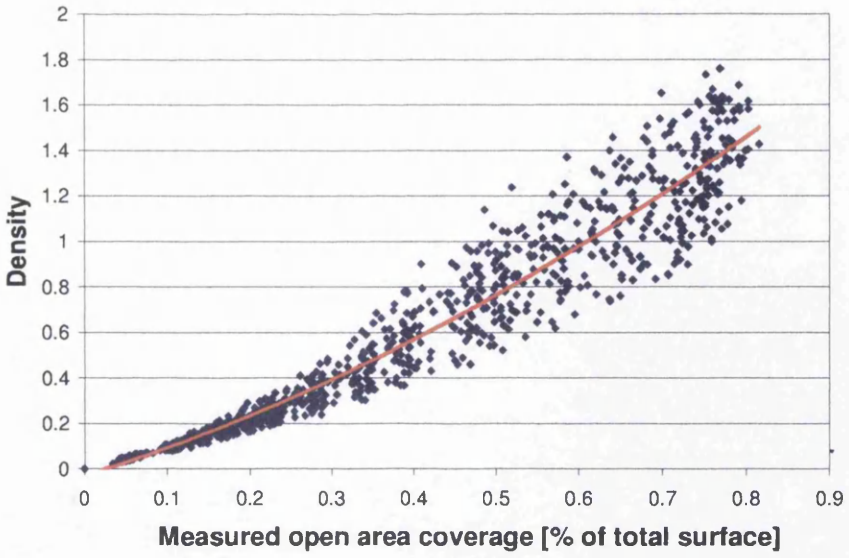

Figure 5-16: Colour Density vs. cell open area

Plotting the measured cell open area versus the nominal area coverage, which indicates the achievable colour area coverage as estimated by the engraver, shows a much better correlation (Figure 5-17) with a low spreading of data. This indicated that the cell open area was probably used as reference by the engraver for the estimation of the nominal area coverage. The correlation is not linear but follows a curve: the engravers, in their estimates, assume that at high open areas the ink will spread further more hence the non-linear relation. At the mid tone levels, the curve shows a saddle, indicating that the engraver was expecting a transition point.

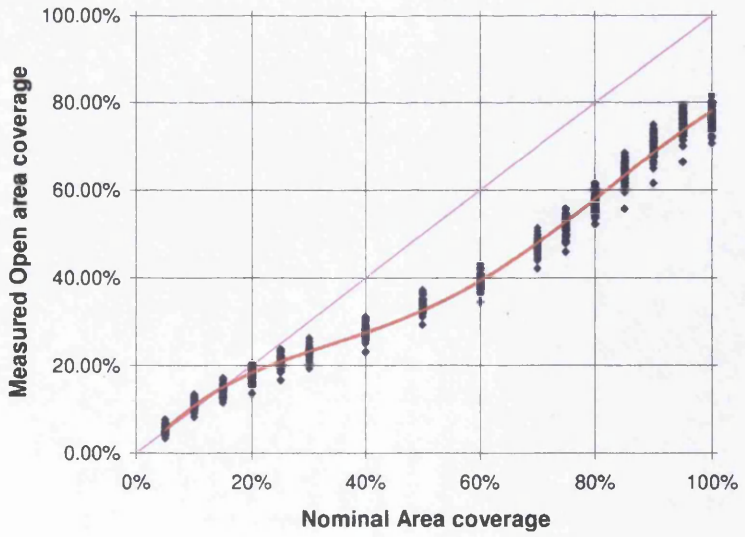

Figure 5-17: Nominal area coverage vs. measured cell open area

5.5.3 Conclusions of the preliminary analysis

The analysis of the data collected shows the limits in the current estimation of achievable colour density: patches engraved with the same nominal area coverage were supposed to give similar values of measured optical area coverage, in practice the results markedly differed. This confirms the issue of inaccuracy of the gamma or correction curves applied in standard industrial applications. Improvement of the estimation abilities is clearly a necessity.

Analysis of the data shows a strong correlation (quadratic) between the achieved densities and the engraved volume, which is visibly the most important parameter in the estimation of density. Models based on this single parameter are anyway insufficient, giving high errors, visible to the human eye.

5.6 Conclusions

An extensive press trial was analysed. The engraved cylinder and the printed output of the trial were accurately measured and characterised. An extensive database, regarding cell shapes, sizes and relative optical density, was created.

The gravure cylinder resulted to have been accurately engraved: the variability of the results within a patch was extremely low. Preliminary analysis indicated a strong correlation between the engraved volume and the achieved density. It also confirmed the unreliability of the gamma, or correction curves, currently applied in standard industrial applications, pointing out the need for better models.

6 Artificial Neural Networks

6.1 Introduction

Artificial neural networks have been widely used for the analysis of the experimental data and for the development of models. As an engineering tool, ANNs can be defined as non-linear mapping functions that seek to evaluate any relationship between some input and uncorrelated output data using statistical pattern recognition [15]. Originally inspired by biological studies of the neurons, ANNs have seen an explosion of interest over the last few years, being applied in a large range of areas, as diverse as finance, engineering and medicine. ANNs are being introduced in several fields in order to deal with problems of prediction, classification or control [16].

ANNs "learn from experience"; meaning they adapt on the basis of the statistical data provided, improving their mapping accuracy with the increase of data presented. They have proved to be robust to noisy, occasional incorrect data points and able to deal with complex relationships between the inputs and the outputs [15],[17]. Due to its inherent non-linearity, the ANNs can overcome the limitations of the traditional linear modelling techniques.

ANNs require a relatively limited user intervention; the user does need a heuristic knowledge of how to select and screen the data, how to select an adequate neural network structure and how to interpret the results. Neural network development requires a lower level of mathematical understanding in comparison with more traditional non-linear statistical methods. Furthermore, since ANNs work by defining the best statistical link between the input and the output, the theoretical understanding of the problem is necessary only for an appropriate selection of inputs and outputs. On the other hand, ANNs will not provide any explanation of the system behaviour and can provide a reliable estimation only within the range of provided data.

6.2 ANN background

Artificial Neural Networks were originally developed in the field of Artificial Intelligence (AI). From the 1950s' up to the 1970s', mainstream AI concentrated on

the development of expert systems, which, through the implementation of "Aristotelian" logic, attempted to create independent intelligence. This approach, even if successful in some specific cases, clearly failed to reach the primary goal. According to one line of speculation, this was due to their failure to mimic the underlying structure of the brain.

The brain contains around 10^{10} to 10^{12} neurons. A neuron is a specialised cell that can propagate an electrochemical signal. At the centre of the neuron there is the cell body around which there are the dendrites and the axon. Dendrites look like short branches or spikes extending from the main body and they are the input structure of the neuron. The axon is another extension stretching out from the main body, it has a cable-like appearance and it can be particularly long (up to a 1 metre). Neurons have only a single axon, whose ending usually undergoes extensive branching having several axon terminals. The axon is the output structure of the neuron. The axon terminal of a neuron is connected to the dendrites of another neuron by synapses. An average brain neuron has around 10^4-10^5 connections to other neurons. When a neuron is activated, it sends a signal through its axon to other neurons, which, in turn, may or not be activated. A neuron is activated if the signal coming through the dendrites exceeds a certain threshold level.

The strength of the signal coming to the neurons depends on the efficacy of the synapses. It has been proposed that the learning process of the human brain is merely a continuous modification of the strength of these synapses. These alterations would be based on the frequency of neuron-signal coming from our senses. A classic example is the Pavlovian conditioning experiment. During this experiment dogs were trained to associate the sound of the bell to the food. The synaptic connections between the auditory cortex and the salivation glands got strengthened, in other words dogs developed the tendency to increase the saliva production at the sound of the bell, independently from the presence of food [16].

In comparison with a standard CPU processor, a single neuron has an extremely limited capability and works at extremely low speed (100Hz). The greatness of the neurons appears in their ability to connect into an extremely complex network creating a massive parallel robust information processing system: the brain. In the case of the biological brain, the bottom-up emergence behaviour is clearly evident: the union of simple elements (neurons) is more powerful than their simple sum: totally

new abilities emerge. We can on a daily basis think, recognise, observe, reason, deal with new and complex problems; all actions external to the field of "experience" of a single neuron alone. Furthermore, biological brains can easily accept noisy data and even partial damage, thanks to the redundancy of the connections.

Biological neurological studies have led to the extensive development, starting from the early 1980s', of an approach to AI called Connectivism, whose aim is the modelling of mental or behavioural phenomena as the emergent processes of interconnected networks of simple units. A major development in this field was the creation of the Artificial Neural Network, where mathematical functions called neurons had to mimic the behaviour of the biological neurons. These artificial neurons could be connected to each other forming networks. On the basis of the data provided to the network the coefficients of the input within the artificial neurons would increase or decrease, behaving like synapses. With continuous training the ANN would acquire the ability to deal with more complex problems. The first artificial neurons were based on threshold functions, like the biological neurons, later advances led to the development of a list of different functions (linear sigmoid) applicable as artificial neurons.

Even if no truly independent intelligence has been developed until now through the connectivism approach, its development had a great influence in more practical fields. Artificial neural network are currently widely used and researched for several practical low-intelligence applications like the modelling, control and simulation of processes (manufacturing processes, financial trends), pattern recognition (recognition faces, handwriting) and pattern classification (risk assessments).

Among the different types of neural network, one of particular interest for the development of models is the Multilayer Perceptron Neural Network, which has been demonstrated to be able to approximate any function, with a finite number of discontinuities [18].

6.3 The artificial neuron

The first artificial neurons were originally developed in the 1950s' [17] in order to capture the essence of the biological neurons.

6.3.1 The perceptron

This first neuron was called the *perceptron.* Its behaviour strictly resembles the biological neurons and is described in [18]

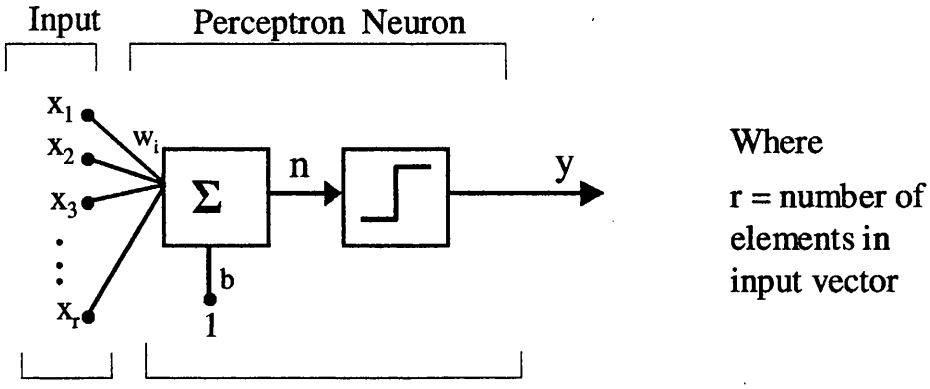

Figure 6-1: Schematic of a perceptron[18]

The perceptron neuron will receive R number of external inputs *x*, which could come from other neurons or from external data. Each input p will be weighted with an appropriate weight (*w*); these weights correspond to the synaptic efficacy in a biological neuron. The neuron has also a constant input of 1 which is weighted by the bias (*b*). The sum of the weighted inputs (n) will be sent through a threshold transfer function or hard limit transfer function, shown in Figure 6-2

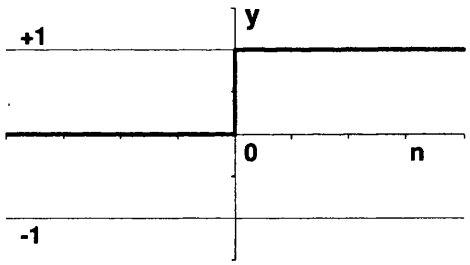

Figure 6-2: Step threshold function or hard limit function: y=Step(n)={1,0}

If the summation of the weighted inputs (n=**Wp**+b) is higher than the threshold value of the transfer function (i.e. n > 0 in Figure 6-2), the artificial neuron will be activated sending an output with value 1, otherwise the artificial neuron will send an output with value 0 . With its dual output, the perceptron resembles the activation of the biological neuron.

Mathematically, the perceptron can be described by (6-1)

$$y_j = f_{hl}\left(\sum_{i=1}^{n} w_{ji}x_i + b_j\right) \qquad (6\text{-}1)$$

Where

j = Considered neuron

n = Number of inputs for the j-neuron. A neuron can have any number of inputs.

x = Inputs (scalar values)

y = Output of j-neuron (1 or 0)

f_{hl} = hard limit transfer function (Figure 6-2)

w = Weight coefficients

b = Bias coefficient

Due to dual possible output (0 or 1) of the perceptron was originally applied as a pattern classifier. Perceptron shows great capabilities in logic; it can in fact act as AND, NOT, OR logical operators depending on the values of the weights and bias.

6.3.2 Linear and non-linear neuron

While the perceptron was created in order to closely emulate biological neurons, other artificial neurons have been developed in order to deal with specific tasks. Two of the most common are key-elements of this thesis and are the linear neuron and the non-linear neuron. The linear neuron is obtained by substituting the threshold transfer function present in the perceptron with a linear function (Figure 6-3).

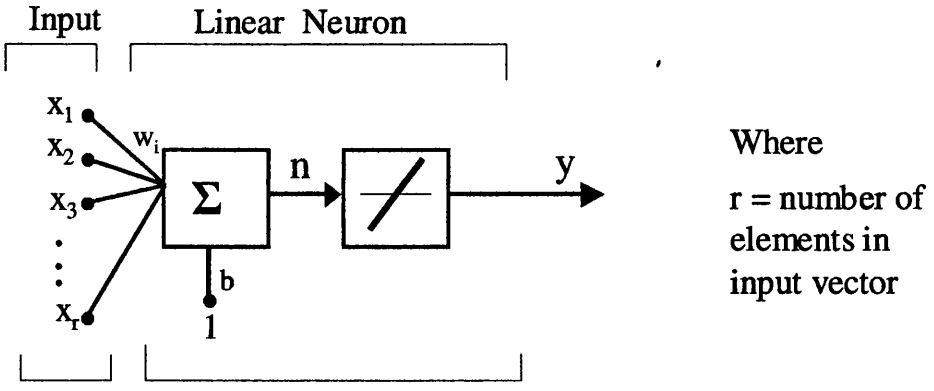

Figure 6-3: Linear neuron with diagram of its transfer function, [18]

The linear transfer function used in the linear neuron is an identity function where the input equals the output or y =1×n as in Figure 6-4

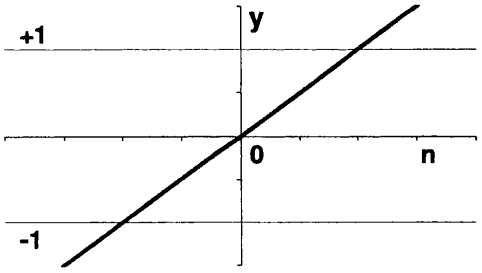

Figure 6-4: Linear transfer function: a=n

Mathematically, therefore, the linear neuron is a continuous function that can be described by the equation:

$$y_j = \left(\sum_{i=1}^{n} w_{ji} x_i + b_j \right) \tag{6-2}$$

Where

j = Considered linear neuron

n = Number of inputs for the j-neuron. A linear neuron can have any number of inputs.

x = Inputs (scalar values)

y = Output of j-neuron (scalar value)

w = Weight coefficients

b = Bias coefficient

The output of the linear neuron is a scalar value of any size (not limited to 0-1).

The non-linear neurons are obtained by substituting the threshold transfer function present in the perceptron with a non-linear transfer function. Very popular and useful non-linear neurons are the neurons with sigmoid transfer function, Figure 6-5

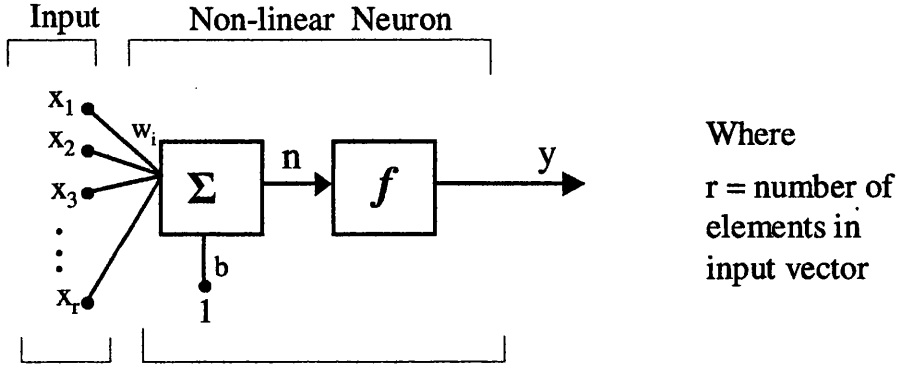

Figure 6-5: Non-linear neuron, [18]

Typical sigmoid transfer functions are in Figure 6-6

$$y = \frac{1}{1+e^{-n}} \quad (a) \qquad y = \tanh(n) = \frac{2}{1+e^{-2*n}} - 1 \quad (b)$$

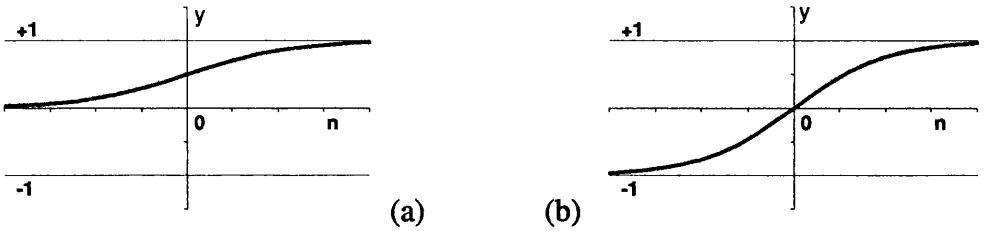

Figure 6-6: Sigmoid transfer functions

Their peculiarity is that their output is mapped in the range of [0,1] (a) or [-1,1] (b)

Mathematically, therefore, the linear neuron is a continuous function that can be described by the equation:

$$y_j = S\left(\sum_{i=1}^{n} w_{ji} x_i + b_j\right) \qquad (6\text{-}3)$$

Where

j = Considered linear neuron

n = Number of inputs for the j-neuron. A linear neuron can have any number of inputs.

x = Inputs (scalar values)

y = Output of j-neuron (scalar value [-1,1] or [0,1])

S = Sigmoid transfer function (Figure 6-6)

w = Weight coefficients

b = Bias coefficient

6.4 Multi-layer perceptrons

Networks of neurons are obtained by linking the local inputs and outputs of neurons among themselves and with external inputs and final outputs, Figure 6-7

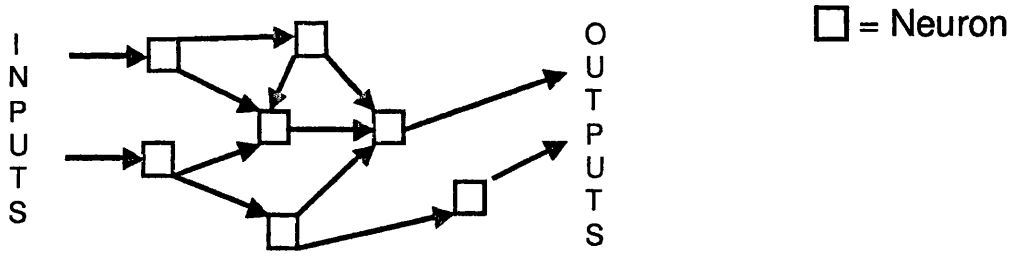

Figure 6-7: Example of a generic neural network

Different configurations of A.N.N will deal with different objectives. The most common architecture in use today is perhaps the **Multilayer perceptron,** Figure 6-8 .

Its design is originally due to Rumelhart and McClelland (1986) and is discussed at length in most neural network textbooks, such as Bishop [15].

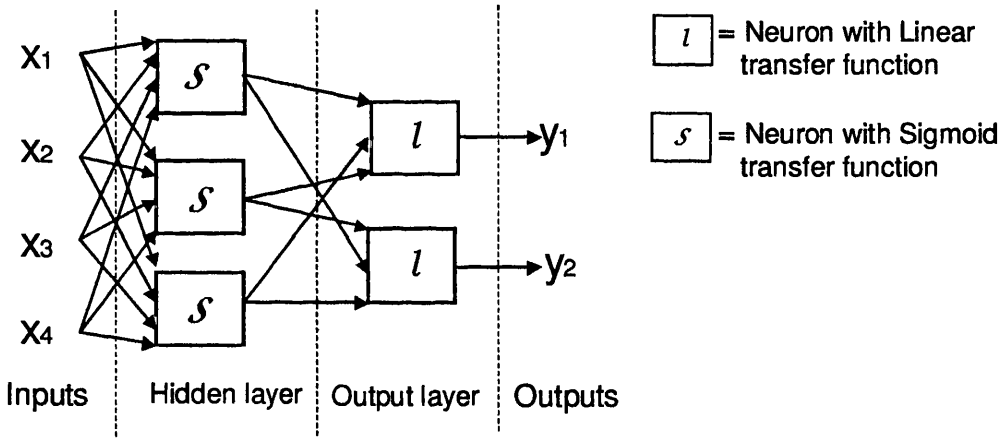

Figure 6-8: Scheme of the M.L.P. ANN

The multi-layer perceptron has a feed-forward layout, i.e. the connections among neurons don't form loops but feed forwards from inputs towards outputs. The neurons are organised in two separate layers between the main inputs and the main outputs. Neurons belonging to one layer do not connect among each other but feed all the neurons belonging to the next layer. The external inputs of the ANN will be connected to all the neurons belonging to the so-called hidden layer, these neurons are characterised by a sigmoid transfer function. The outputs of the hidden layer are then fed to all the neurons of the output layer; these are linear neurons and they generate the final external outputs of the ANN. In a M.L.P. ANN, there will be as many linear

neurons in the output layer as final outputs, while in the hidden layer the number of sigmoid neurons is independent from the number of inputs.

The Multi-layer perceptron is of primary interest for the development of the work of this thesis; this layout is, in fact, particularly useful for the development of models that aim to estimate the value of a (usually) continuous variable; this layout has indeed proven to be able to approximate any continuous function with a finite number of discontinuities [18]. A brief mathematical proof of this ability is demonstrated in the Appendix B.2

6.5 Training of a Multi layer Perceptron

The purpose of the training is the determination of the weights and biases that minimise the error function associated with the artificial neural network. The error function establishes the performance of the network, i.e. the difference between the outputs obtained by the network and the output data. The minimisation of the error function is obtained by an iterative modification of the weights and bias of the ANN until the optimum is reached.

6.5.1 Incremental and batch training

In the training of the neural networks, two different training styles are possible: the incremental training and the batch training.

The **incremental training** has been previously shown in the training of a single perceptron. In this style, the error of the network is calculated each time a pattern is presented and the weights are accordingly updated each time. The training process would continue until all the patterns give a zero error. This means that if the reference data are composed by n patterns and these patterns are proposed for c cycles (usually called epochs) to the network before convergence is achieved, the weights inside the net will be updated c*n times. This process is adequate when carrying out theoretical classifications of data like implementing absolute logic operators or the development of dynamic neural networks (whose response vary in time).

For the development of models based on real-world data, the **batch training** is more interesting. In this style the weights are updated only once every cycle, after all the patterns have been presented to the neural network. The update of the weights is based

on a *global error* obtained by the network; this global error is function of all the individual errors achieved by the different patterns. This method allows taking in account for possible noisy data, where it is not possible to achieve an absolute zero error due to the overlapping of the data provided. This is clearly the condition of most real-world collected data; batch training is therefore the most widely used style of training and will be the style of training that will be referred to in the next sections and throughout the thesis.

6.5.2 Error functions

Error functions establish the performance of the network, i.e. how well the neural network fits the data patterns proposed. The aim of the training will be the reduction of this error to a minimum. Different error functions are available [18][19] or can be constructed as needed. In batch training, the most common and widely used error function is the mean sum-of-squares of errors *(mse)*, (6-4)

$$E = \frac{1}{P}\sum_{p=1}^{P}(y^p - t^p)^2 \qquad (6\text{-}4)$$

Where y^p is the calculated output of the ANN and t^p the corresponding target value for the pattern p and P is the total number of patterns presented for training.

6.5.3 Training algorithms

The purpose of the training algorithms is the identification of the weights and biases that minimise the error function associated with the artificial neural network for a specific set of data patterns. They are so called *optimisation algorithms*; a list of different algorithms have been developed to solve ANNs.

These algorithm works in an iterative way cyclically modifying the weights of the ANN until the optimum is reached ([15]).

$$w_{i+1} = w_i + \Delta w_i \qquad \text{Where i is the iteration} \qquad (6\text{-}5)$$

The problem of minimisation of the weights has been a limitation for decades in the development of multi-layer ANNs. In the 1980s', the back propagation algorithm was developed for MLP networks.

$$w_{i+1} = w_i + \Delta w_i = w_i - \eta \frac{\partial E}{\partial w_i} \tag{6-6}$$

Where E is the function error, and η a small parameter that sets the step size, usually called *learning rate.* Other common optimisation algorithms are the conjugate gradient algorithms or the quasi-Newton algorithms [18]. Among those of particular interest is the Levenberg-Marquardt algorithm. This algorithm was particularly designed for efficiently resolving Multi-layer perceptron networks, integrating quasi-Newton solving techniques with gradient descent techniques.

$$\mathbf{w}_{i+1} = \mathbf{w}_i + \Delta \mathbf{w}_i = \mathbf{w}_i - \left[\mathbf{J}^T \mathbf{J} + \mu \mathbf{I}\right]^{-1} \mathbf{J}^T \mathbf{e} \tag{6-7}$$

Where J is the Jacobean matrix (first derivatives) of the error function with respect to the weights and e the vector of errors (the bold characters indicate the matrix form). In Appendix B.3.1 a mathematical explanation of the working mechanism is presented for the Back propagation algorithm and briefly in A.3.2 for the Levenberg-Marquardt algorithm.

6.5.4 Batch Training process of a MLP

For a specific set of data patterns and with a selected error function and training algorithm, the process of batch training of a MLP neural network can be described as follow:

1. Epochs (i.e. cycle) counter: i=0
2. Randomly initialise all the weights of the ANN: w_i
3. Propose the patterns of the training set to the network, calculating the outputs
4. Calculate the error function *E* of the network, (6-4)
5. If the error *E* is less than the goal (≈ 0) then go to 9
6. Through *training algorithm* calculate Δw_i
7. $\Delta w_{i+1} = w_i + \Delta w_i$
8. Go to 3
9. Stop: the Neural Network is trained

Through this process the network is trained and at the end able to estimate an output on the basis of its "experience" of the training set of data patterns provided. A

possible risk in the training of the neural network is the definition of a local minimum of the error function and not of its absolute minimum. In order to avoid this risk it is common practice to repeat the process of training several times, starting with different initial weights in order to explore a larger space of solutions.

6.6 Over-fitting and generalisation

In the training of a neural network with a series of data patterns, a major risk is the over-fitting of the data: the neural network fits "too well" to noisy data as shown in Figure 6-9

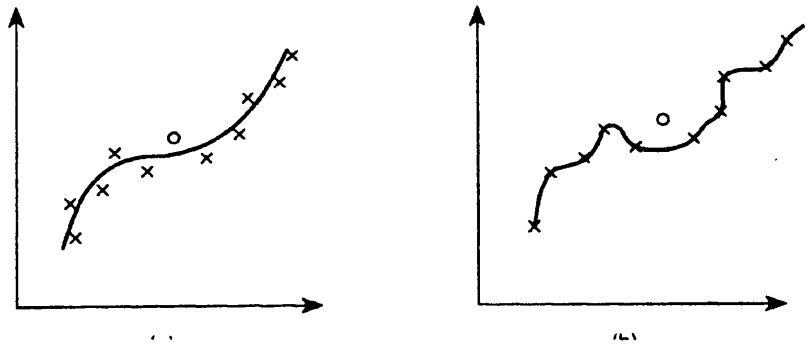

Figure 6-9: Noisy data are over-fitted on the right, correct fitting on the left, [17]

It is therefore important to improve the **generalisation** ability of the ANN, i.e. its ability to filter the noise and the incorrect data; obtaining more "visually smooth" functions. Different solutions are available to verify or reach a generalised training of the neural network:

6.6.1 Test set of data

Some data can be kept out of the training process in order to verify the quality of the obtained neural network; this set of data is usually called **test set**, while the set of data used in the training by the training algorithms for the determinations of the weights is called **training set**. Once the network has been developed and trained, the input data patterns of the test set can be inserted into the neural network; the estimates of the ANN can be then compared with the related test set results. The test set of data does not improve the training but it can verify its quality.

6.6.2 Hidden layer dimension

The complexity of the function that the MLP ANN can approximate can increase with the number of neurons present in the hidden layer. Reducing the number of neurons in the hidden layer would decrease the risk of over-fitting the data. Furthermore the required number of data patterns to adequately train a neural network increases with the number of neurons present in the hidden layer. On the other hand, insufficient neurons could lead to an inadequate fitting of the data and therefore poor modelling.

6.6.3 Early-stopping technique

The early stopping technique can improve the training by reducing the risk of over-fitting the data. A **validation set** of data patterns is introduced, which is different from the test set. The validation set of data is not used for the updating of the weights, but its error is monitored throughout the training process at each iteration. The validation error normally decreases during the initial phase of the training, as does the error of the training set. However, when the network starts to overfit the data, while the error of the training set keeps reducing, the error of the validation set will rise. At this point the training process is stopped, even if the error of the training set is still reducing, and the obtained weights will be returned. Unlike the test set, the validation set does interact with the training, improving its generalisation. In the application of this technique it is important to select a training algorithm that converges smoothly and not too fast.

6.6.4 Regularisation

The regularisation method improves the generalisation ability of the network by modifying the error function. The typical error function of mean sum-of-squares of errors can be modified by adding a term that consists of the mean of the sum of squares of all the weights and biases [18]:

$$E = \gamma\left(\frac{1}{P}\sum_{p=1}^{P}(y^p - t^p)^2\right) + (1-\gamma)\left(\frac{1}{n}\sum_{j=1}^{n} w_j^{\,2}\right) \tag{6-8}$$

Where γ is a coefficient between 0 and 1 called *performance ratio.*

This error function will drive the network to have smaller weights; this has proven to lead to a smoother response of the network [15]. This can be empirically explained by the fact that, in the presence of small weights, the weighted sum of the inputs would be small and it would lie in the range where its sigmoid function has almost a linear approximation.

The estimation of the correct performance ratio, which would give the best regularisation, can be quite difficult. For this purpose, Bayesian techniques can be used. This is a statistical approach, which, through an analysis of probability distribution of the weights, allows estimation of the performance ratios that give the best regularisation. In addition, during the training of the network, the Bayesian analysis will define and use only the number of weights, and therefore neurons, necessary for a correct generalisation; applying Bayesian regularisation techniques. It is therefore possible to define networks with a more numerous hidden layer without risk of over-fitting. Finally, thanks to its statistical analysis, the Bayesian technique is able to calculate the local variance of a prediction, providing an error for each of the outputs instead of just a single average value [19]. In the Appendix B.4 a mathematical description of the application of a Bayesian framework for the estimate of the performance of the network is given.

Bayesian regularisation is supposed to generally give a better generalisation of the early-stopping technique [18]. This is particularly noticeable in the presence of small data sets, where the definition of a validation set would heavily reduce the quality of the training.

6.7 Data selection

Data patterns are an essential element in the development of a neural network, being the basis of any training; a valid selection of data is therefore of primary importance; basic rules that have to be followed are:

1. For correct training it is important to have **enough experimental data** patterns; the quantity of data patterns necessary will steeply increase with the number of parameters (main inputs and outputs) under analysis; a rule of thumb is 10 dataset for each connection (the lines in Figure 6-8). If not enough data are present, it is possible to use smaller networks or to use other statistical

methods to generate virtual data to close the gap, this anyway would decrease the reliability of the obtained network. A better practice is to accept smaller networks that study the effect of a smaller number of parameters.

2. The neural network will be reliable only within the range of the data provided within the training; it is therefore important the experimental data covers all the range of interest. Neural networks will give estimates also outside this range but their reliability will decrease with their distance from it.

3. Finally it is important to ensure a balanced distribution of data over the range. Since the training algorithm will minimise the error function, if too much data belongs to a specific sub-range the network will particularly optimise its estimate for that subsection. Regularisation techniques can help to reduce irregularities but they cannot substitute a homogeneous distribution of a training data set.

6.8 Review of application of neural networks in gravure

Neural networks have been successfully applied in several manufacturing processes, so their application in the gravure process is of primary interest. Very few works have been published about the subject, not only regarding the gravure process but the printing industry as a whole.

In the review by Holub of TAGA proceedings of 1988 a first mention was made to the possible use of neural architectures in printing [20] At the time the applications of neural network was still in its infancy, the author concentrates its discussion on the development of parallel and neural processors.

An article about the application of the neural network in the printing production process was presented by Al-Mutawa and Moon in 1994[21] . In this article a neural network was presented for the management of the ink keys on an offset press. On the basis of the density deviations between the sample print and the match–print, the neural network corrects their opening.

Verikas et al. [22] presented another interesting application of the neural networks in the printing industry: a new method for the measurement of colours where algorithms based on ANN were used to transform colour components RGB to CMYK.

Publications about the application of ANN in gravure printing are even more limited. One paper was presented in 2004 by Ding et al, [23]; the paper was about the development of a demonstrative fuzzy neural network for the adjustment of a gravure press on the basis of the output obtained. In this case the ANN are used not for modelling the process but for controlling it on the base of experience. Parameters under control were the press speed, the impression pressure and ink viscosity, while the print quality was established on the basis of the characteristics of the printed dot (size, haze, streaking...). This network follows an iterative process where there is a "feed-back" loop of the process parameters, which are present both as the output of the network as well at the input, together with the quality parameters. Fuzzy logic is applied to decide when the quality of the print is too low and therefore the network must intervene on the process parameters. Even if interesting from a theoretical point of view, the experimental part in this work was limited; very few indications were given about the training set provided and this control system was analysed only at a simulation level on a computer.

6.9 Matlab and Artificial Neural Network

Matlab is an advanced programming language, published by Mathworks©, that quickly and efficiently implements algorithms and analyses data. It is recently becoming a sort of reference standard for the development of engineering applications, it was therefore chosen as language for the study of neural networks. Two collections of sub-routines are readily available for the development of Artificial neural networks. The first collection, referred as "neural toolbox" [18], is commercially provided by Mathwork©; a second package, called "Netlab" [19], have been instead developed at a university level as an implementation of the routines presented by Bishop [15] .

Among the two, "Neural toolbox" presents some advantages being already heavily tested and applied in several fields [18]. It also comprises complex and established routines for a complete training of neural networks. Netlab, due to its development as an algorithm implementation, shows more interest in the mathematical issues behind the development of artificial neural networks than on the practical development of an ANN. It comprises all the single elements for the development of the neural network

but at a lower degree of implementation. On the other hand, Netlab offers more flexibility and functions; an example is the estimation of the variance of the prediction in the Bayesian training, which is not implemented in the "Neural toolbox".

Taking in account these factors for the work of this thesis the collections have been used conjunctly, using primarily the more established "neural toolbox" but integrating it with functions of the Netlab collections. In order to achieve this integration the two collections needed to be observed and studied at the source level.

6.10 Closure

In this chapter the mathematical theory behind artificial neural networks has been discussed with reference to their application as non-linear mapping functions that seek to evaluate any relationship between some input and uncorrelated output data using statistical pattern recognition. Among different ANN configurations, the Multi-layer perceptron layout is of particular interest being proven to be able to approximate any continuous function with a finite number of discontinuities. The different phases of construction, training and verifications of ANN models have been discussed; these are the foundations for the development of artificial neural networks for the gravure printing process on the basis of the experimental data presented in Chapter 4. For the development of Artificial Neural Networks, Matlab software shows the capability to provide the adequate tools (Matlab Neural Network toolbox, Netlab) for the development and analysis of the ANNs .

7 Development of ANN models for the gravure printing process

7.1 Introduction

The development of a model through the application of Artificial Neural Networks is a progressive process. Neural Networks grow with experience, with the increase of the data provided and the complexity of the model created. This process is exemplified in the diagram of the life cycle of an artificial neural network presented in Figure 7-1, showing a recursive growth and development of a neural network from a preliminary stage, where its feasibility is assessed, up to being ready for application.

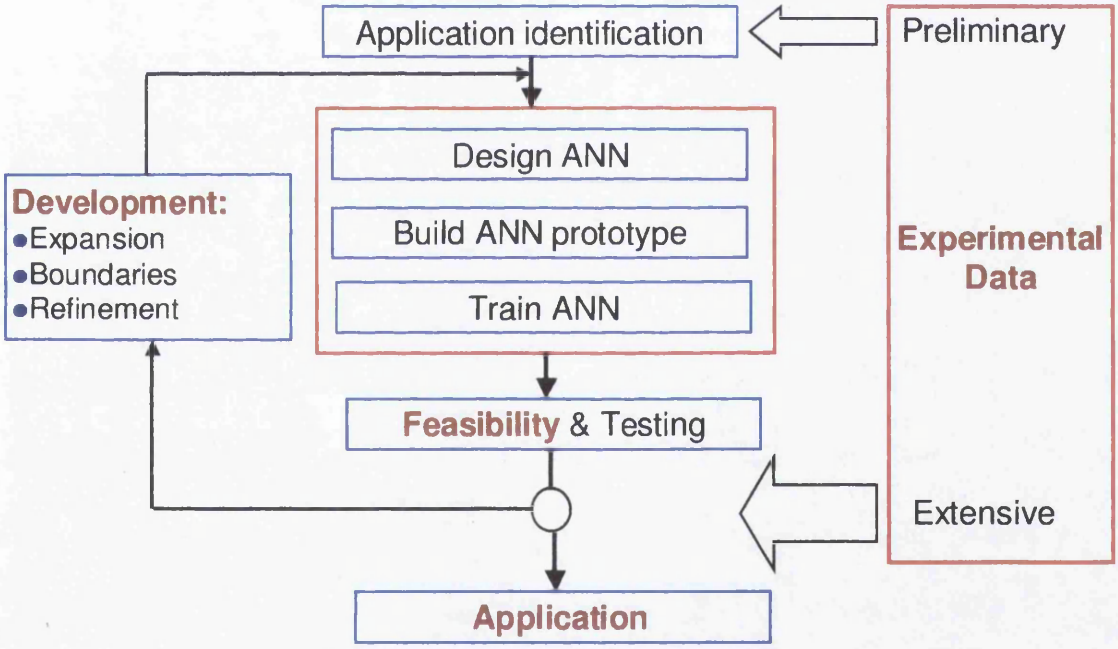

Figure 7-1: Life cycle of an Artificial Neural Network

The development of a neural network for the modelling of the gravure printing process for the estimation of the achievable colour density will follow this lifecycle. For the development of the Neural Networks, the software package Matlab was used integrated with its Neural Network toolbox, see section 6.9.

7.2 Identification of the model

The development of the model of the gravure printing process consists of the development of a function that correlates the influencing factors with the obtainable results, Figure 7-2. In the case of gravure, printing, influencing factors are the cell geometry, the ink, the substrate, the process set-up and the environmental conditions; these are the elements of the printing process selected and set up by the printer. The results are the printed samples.

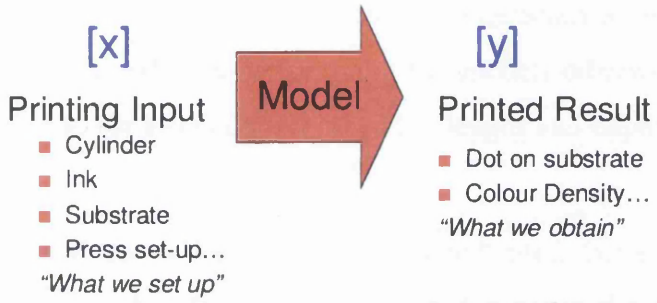

Figure 7-2: Gravure model

The development of a model requires the parameterisation of these factors and results, since only numbers are includable in functions. Adequate parameters have to be defined numerically for each factor. The printed samples, for example, could be described by the colour density, or the shape of the printed dots.

The development of models able to completely simulate the gravure process would require large resources and time; this work will concentrate, therefore, on the development of a practical model as feasible as possible given the means and time available. On the basis of these considerations, the development of the model was primarily focused on the analysis of the effect of engraved cell shape on the ink release and in particular on the achieved colour density. Important printing parameters such as substrate and the type of ink were kept constant, in order to limit the number of variables. In Figure 7-3, the model of interest is presented with the indication of all the parameters usable for the characterisation of the explored factors.

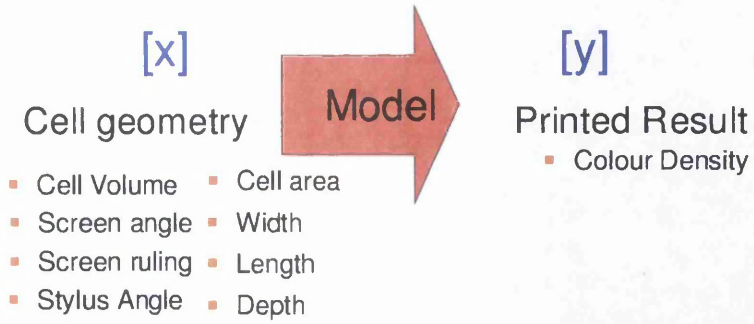

Figure 7-3: Reference parameters

Not all the parameters are necessary for a complete characterisation of the geometry, it is also important to avoid over-constraining the model, otherwise infeasible data could be proposed: e.g. for a specific set of width, length and depth there is only one possible volume.

Preliminary analysis of the collected data clearly indicated that the most important geometric parameter for the identification of the density is the engraved volume. During the engraving process engraved patches were identified by the engraving parameters used: screen ruling, screen angle, screen ruling. These four parameters together identify the cell shape (engraving parameters) and its size (volume). As first proposal, an Artificial Neural Network modelling of the cell geometry effect on the ink release based on these parameters would be therefore of great interest (Figure 7-4).

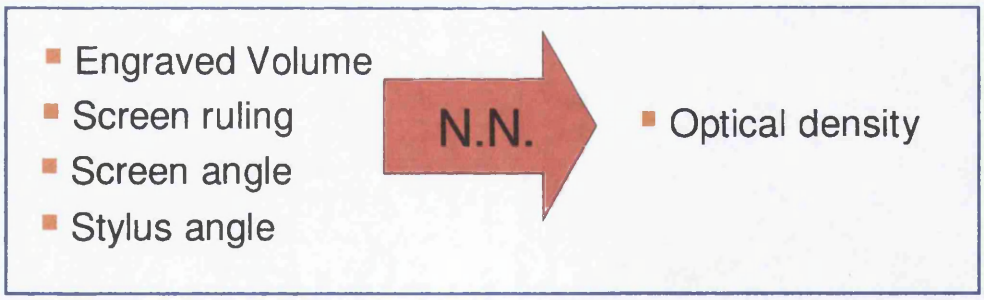

Figure 7-4: First proposed ANN model

7.3 Development of the Artificial Neural Network model

A neural network model was developed on the base of the model proposed in Figure 7-4. Four parameters were identified as input parameters: engraved volume, screen ruling, screen angle, stylus angle. The colour density was used as reference output, Figure 7-4. Source of experimental data was the extensive collection of data presented in section 5.3, taken at the single viscosity value of Zahn2 20s.

For the development of this model, the capability of different designs of ANNs was explored. Different layouts were proposed, whose training was carried out on the basis of the experimental data collected.

7.3.1 Network designs and development

For the development of the neural network model of the ink release of the gravure process three different network designs were assessed. In all of them, the selected structure is the Multilayer Perceptron feed forward layout having the screen ruling, screen angle, stylus angle and the volume as input parameters and the density as output to be estimated.

7.3.1.1 Levenberg-Marquardt MLP design

The first design uses a Multilayer Perceptron feed forward layout, adopting the Levenberg-Marquardt back-propagation algorithm in the training and the mean square error as convergence performance factor. This design is well established and extensively used in several fields [17] . In this case, the design was characterised by 8 neurons with a hyperbolic tangent transfer function in the hidden layer. This low number was chosen to reduce the complexity of the ANNs, reducing the need for large data samples and the risk of over-fitting [18]. This network is prepared for an early-stopping training technique. Its schematic is shown in Figure 7-5. This design is characterised by a total of 40 weights coefficients and 9 bias coefficients in the neurons.

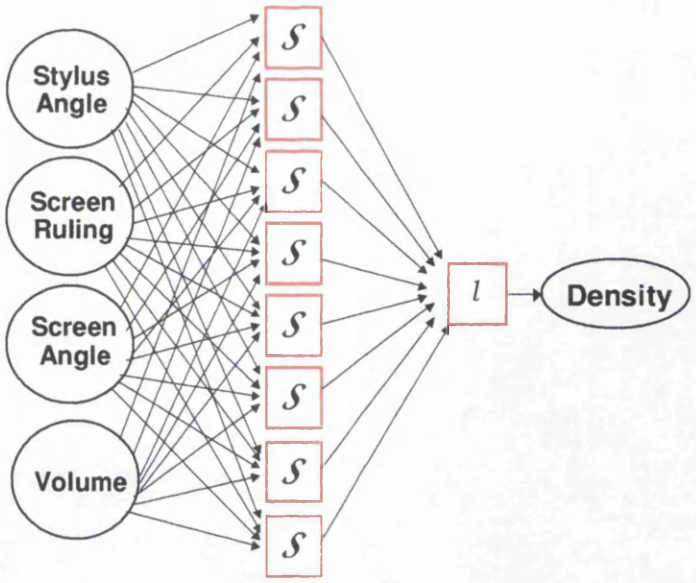

Figure 7-5: Levenberg-Marquardt MLP Perceptron layout

7.3.1.2 8 neurons Bayesian regularisation MLP design

In this design, Bayesian regularisation techniques are used in the training algorithm (in conjunction with Levenberg-Marquardt algorithm) and in the convergence performance. It is a more conservative approach than the previous one, in that it tends to enhance the regularisation, the smoothness, of the obtained model, strongly reducing any risk of over-fitting noisy data. For this model, 8 neurons were placed in the hidden layer with a hyperbolic tangent transfer function; the layout of this Artificial Neural network is identical to the one in Figure 7-5. This design is characterised by a total of 40 weights coefficients and 9 bias coefficients in the neurons.

7.3.1.3 12 neurons Bayesian regularisation MLP design

This design differs from the Bayesian regularisation MLP design previously presented in terms of the number of neurons employed in the hidden layer, which in this case is 12 neurons. Large numbers of neurons can usually be placed in the hidden layer, since the Bayesian regularisation techniques will statistically decide how many neurons are needed for an effective modelling of the problem [18]. This design is characterised by a total of 60 weights coefficients and 13 bias coefficients in the neurons.

7.3.2 Training of the Neural Networks

The three designs of Neural Networks were trained on the basis of the experimental data presented in section 5.3. Since it is known that a zero volume gives a zero density, theoretical patches have been added with values indicating the condition of zero volume, zero density, one for each combination of the three engraving parameters explored in experimental data (Section 5.3.3), giving a total of 969 datasets, at the constant viscosity of 20s Zahn2. On the basis of the selected designs and on the experimental data, the training was executed and the ANN models of the described process created. In order to guarantee good training, avoiding over-fitting, the experimental data were divided in three parts:

- Training set: used in the training of the ANN coefficients, 83% of the data
- Validation set: used to limit the risk of over-fitting, validating the ANN during the training itself, 12% of data provided
- Test set: used to test the developed ANN at the end of the training, 5% of data

The training was repeated several times randomly changing the starting values of the neuron coefficients. The quality of the obtained trained neural networks was evaluated on the basis of the balanced sum of the **mean square error** between the estimated values and the experimental datasets of the training set and tests set. For each design, one neural network with the lowest error was determined and chosen as final result; their neuron coefficients values are presented in appendix C.1

7.3.3 Analysis of the developed ANNs models for gravure

The developed neural networks estimate density on the basis of the input parameters proposed to the network. It is important to verify the obtained models and to measure their quality. In order to carry out the analysis a performance factor has to be selected; of the different ones available, the **Root Mean Square Error** (RMSE) between the actual measured values of densities and the ones predicted by the ANNs was adopted (see section 5.5.1.1).

Verification of the L-M, 8n Bayesian and 12n Bayesian models was obtained by comparing the test sets of experimental data with the values estimated by the ANN models, in Figure 7-6, Figure 7-7, Figure 7-8 respectively. The data of the test sets

were not provided to the network during training and are therefore totally "unknowns" to the models

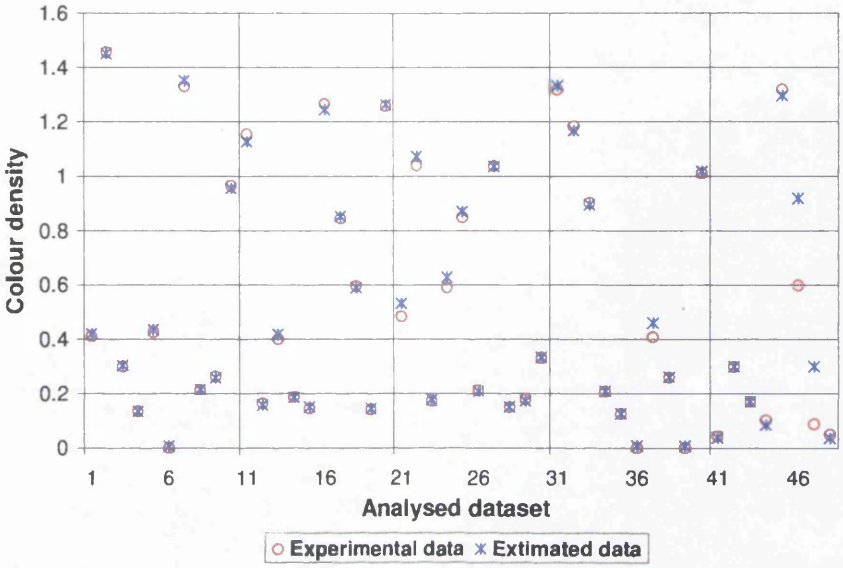

Figure 7-6: Test set comparison with L-M design

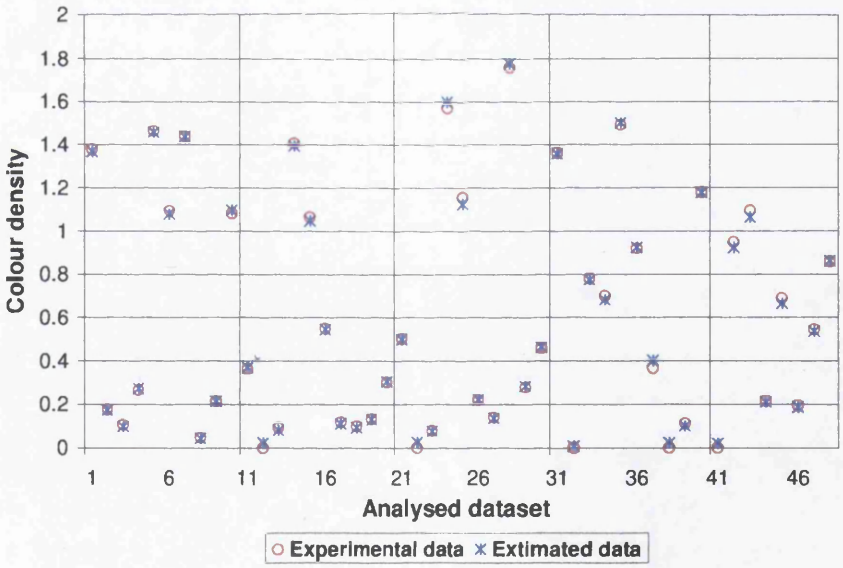

Figure 7-7: Test-set comparison with 8n Bayesian design

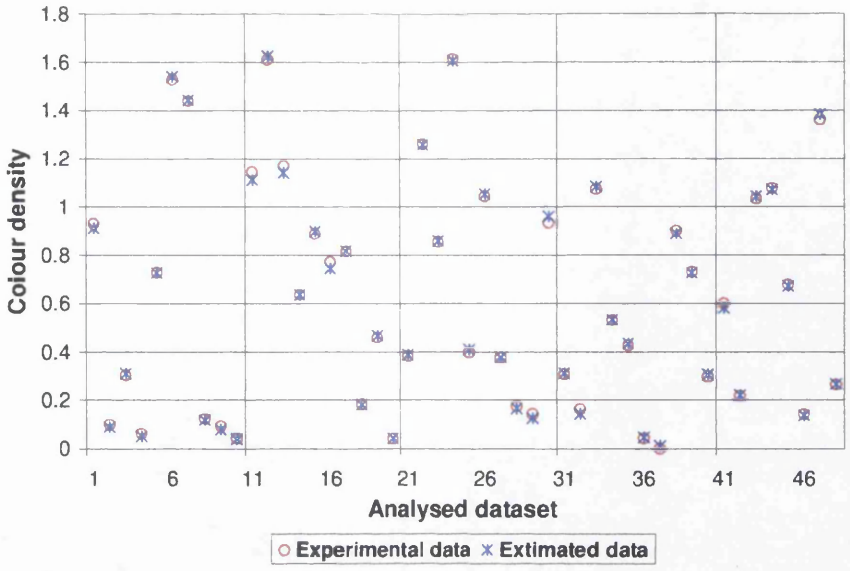

Figure 7-8:Test-set comparison with 12n Bayesian design

The figures show a good correlation between the test sets and the estimated values, from the analysis of 2×RMSE in Figure 7-9, the proposed models show good results, two within the reference selected tolerance value of 0.03. This indicates that the three models have not over-fitted the training data and are able to predict the process. The value 0.03 was designated as an indicative value for an eye tolerance to colour density.

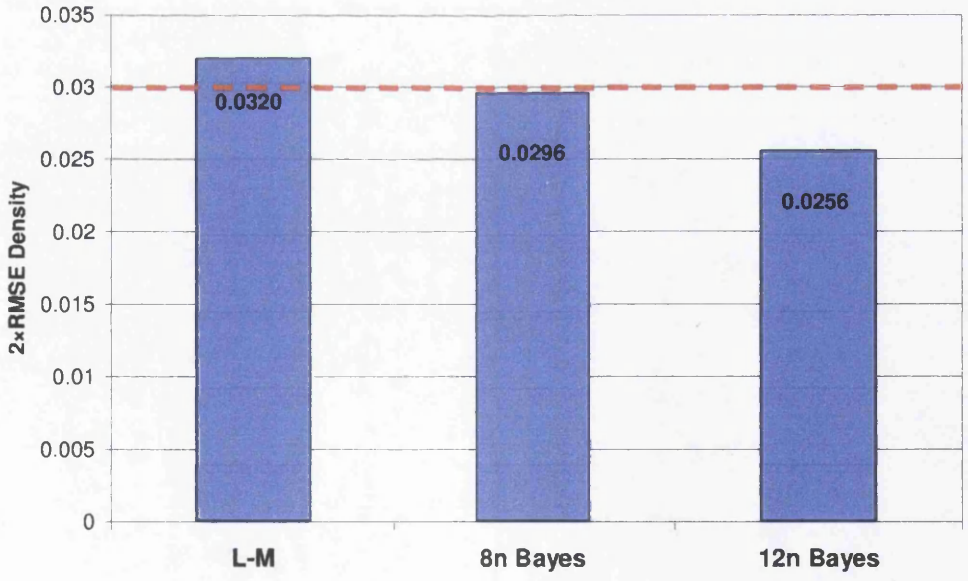

Figure 7-9: 2×RMS Error of the test set for the three models

In order to evaluate the overall accuracy of the developed models, all the experimental data were compared against the estimated ones by the ANNs. In both the models the results were optimal with a 2×RMSE in the estimation of the density of 0.02700 in the L-M design, of 0.02714 in the Bayesian design with eight hidden neurons and 0.02713 in the Bayesian design with 12 neurons. In Figure 7-10 the errors from the comparison of all the experimental data with their estimates is compared with the error achieved by the test set.

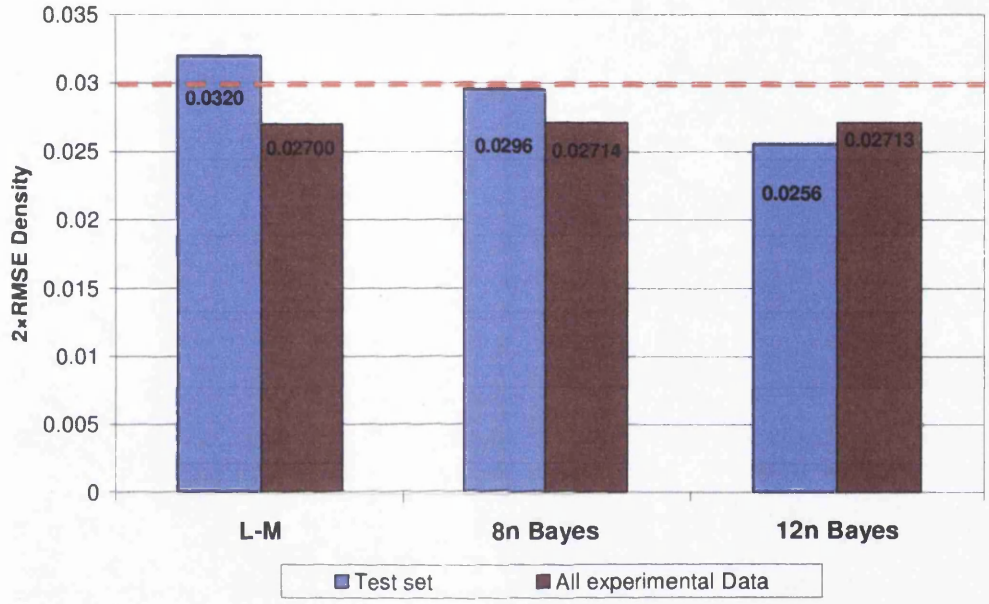

Figure 7-10: Errors from all the experimental data vs. test set

The analysis of the error proved that all the three models achieved very similar global errors on the data. The Levenberg-Marquardt showed a discrepancy between the error calculated on the test set and the average global error. This could be an indication of a non-smooth response. In the Bayesian Neural networks, the performance on the test set was comparable to the one of all the experimental data indicating a smooth response. Of the two, the Bayesian Neural network with 8 neurons gave very similar results adopting a less complex structure (with a large reduction of possible over-fittings in training).

7.4 Development of equivalent polynomial models

Polynomial modelling techniques are commonly available for process modelling. It was therefore important to compare the results achieved by the neural networks with these.

There are two main type of polynomial modelling techniques: Linear polynomial Least Squares Regression and Non-linear polynomial Least Squares Regression.

7.4.1 Linear polynomial Least Squares Regression

Linear least squares regression is by far the most widely used modelling method, [16].

The basic equation of the linear polynomial regression is:

$$y = \left(\sum_{n} \sum_{p} c_{np} * \left(x_n \right)^p \right) + c_0 \qquad (7.1)$$

Where y is the estimated output, x_n is an input, n is the number of inputs x, p represents the exponent power, selected for the polynomial, while c are the determined coefficients. For example in case of one input and power grade two the equation becomes: $y = a_0 + a_1x + a_2x^2$

The term "linear" is used even if not only a straight line is determined, because the result derives from a linear combination of the inputs x_n, therefore no correlations between the inputs can be explored. The parameters *c* can be determined by "reversing the polynomial equation": developing a linear system of equations where the unknown parameters *c* are considered variables while the explanatory variables (x_n, x_n^2...) become coefficients, deriving their values from the experimental data sets. A system (usually over-determined) of linear equations is defined that can be solved for the values of the unknown parameters, using least square means.

7.4.1.1 Application to gravure model

Polynomial linear modelling was applied to the collected experimental data, at the constant viscosity of 20s Zahn2. From the engraved roll 912 datasets were collected, see section 5.3.3. A zero density approach, as for the development of ANN, explained in 7.3.1, was adopted: theoretical patches were added with values indicating the condition of zero volume, zero density, one for each combination of the three

engraving parameters explored in experimental data. These gave 969 datasets, the same as in the ANN development.

Polynomial models were developed over increasing degrees of complexity (the polynomial power). In Figure 7-11, the 2×RMS error obtained from the comparison of all the experimental data with their linear polynomial estimates is presented at the increase of polynomial power exponent p. On the figure, the value of 0.03 is indicated as reference value.

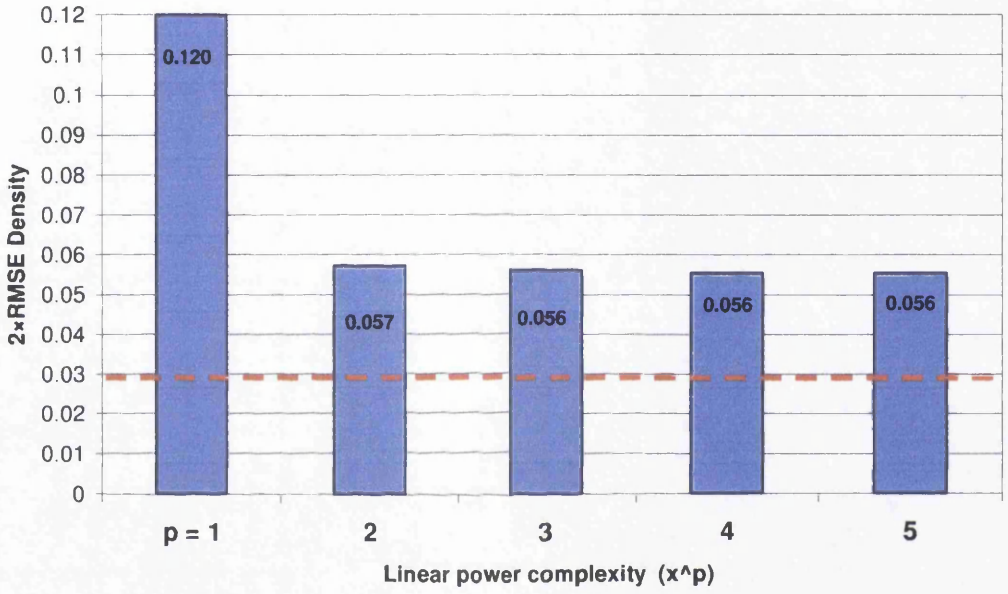

Figure 7-11: Error using linear modelling at increasing power exponent p

7.4.2 Non-Linear polynomial Least Squares Regression

Non-linear polynomial least squares regression extends linear least squares regression including the effect of interactions between the explored parameters. This model can assume the equation:

$$y = \left(\sum_{n} \sum_{p} c_{np} * \left(x_n\right)^p \right) + \sum_{k} \sum_{l=1}^{n} \sum_{m=l+1}^{n} c_{klm} * (x_l * x_m)^k + c_0 \qquad (7.2)$$

Where y is the estimated output, x is an input, n is the number of inputs x, p represents the complexity grade (the exponent) of the linear part of the equation, k the complexity of the interaction between two variables, while c are the determined coefficients. For example in the case of two input and linear power two and non-linear interaction power 1 the equation becomes:

$$y = c_0 + c_1x_1 + c_2x_1^2 + c_3x_2 + c_4x_2^2 + c_5x_1x_2$$

The same model with a non-linear interaction power 2:

$$y = c_0 + c_1x_1 + c_2x_1^2 + c_3x_2 + c_4x_2^2 + c_5x_1x_2 + c_6x_1^2x_2^2$$

The proposed model analyses the interactions between two parameters at a time, it is possible to increase the complexity, analysing the effect of three or more parameters at a time. With the increase of complexity and therefore of the number of coefficients, most datasets could be adequately fitted with large risks of over-fitting. An increase of complexity can also lead to computational inaccuracies.

Major important advantage of this modelling method is the ability to directly explore the correlation between factors, major known limitation is the susceptibility to outliers data, due to the mathematics of the least square method [13],[14]

7.4.2.1 Application to the gravure model

Several non-linear polynomial models were developed selecting different values for the exponent p of the linear part of the equation (7. 2) or the exponent of the non-linear interaction k. The experimental data were the same 969 datasets used for the development of the ANN. Polynomial models were developed over increasing degrees of complexity (the polynomial power). In Figure 7-12, the 2×RMS error obtained from the comparison of all the experimental data with their linear polynomial estimates is presented at different levels of polynomial power exponent p.

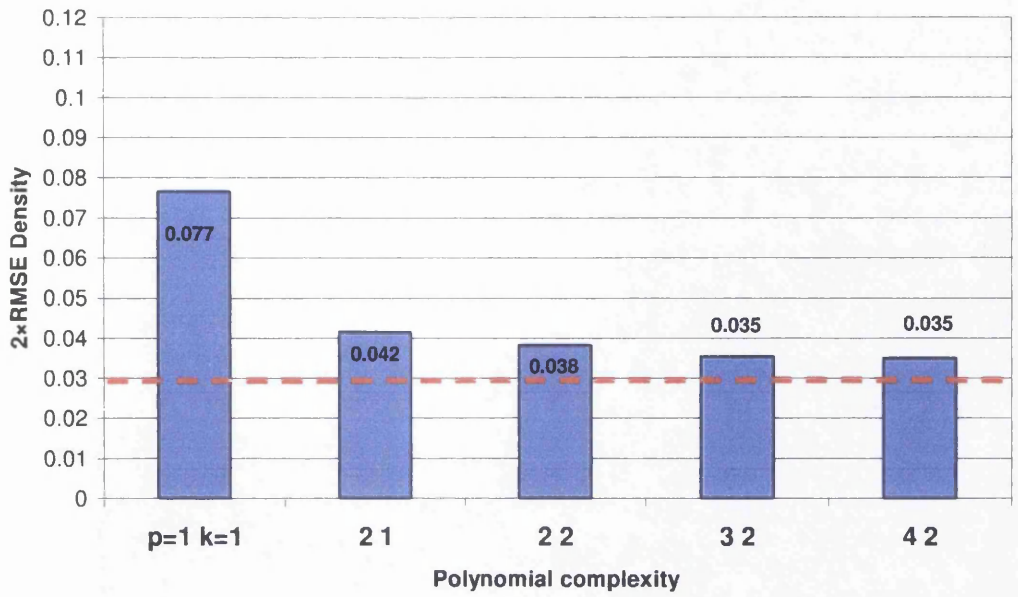

Figure 7-12: Non-linear models 2×RMSE results

The results indicated a better correlation than in the case of the linear models, with a relativly low error. The model with linear power 3 and interaction power 2 appears to be the best balance between complexity and the results achieved. This model presents an equation with the following parameters (Table 7-1):

Table 7-1: Parameters of non-linear polynomial equation

Power	SA	SR	St	Volume	Bias	
1	3.744E-02	-6.822E-03	-2.155E-01	2.423E-02	8.373E+00	
2	-2.300E-04	-7.927E-05	1.720E-03	3.583E-03		
3	4.183E-07	5.693E-07	-4.515E-06	-1.220E-04		
	SA*SR	SA*St	SA*V	SR*St	SR*SV	St*V
1	1.629E-05	-2.438E-04	-4.641E-04	1.598E-04	1.239E-03	3.763E-04
2	-6.815E-10	7.785E-09	1.255E-07	-4.798E-09	-5.973E-07	-7.255E-08

This is a relatively simple equation with 25 coefficients, where *SA* represents the value of Screen Angle, *SR* the screen ruling, *St* the stylus angle and *V* the engraved volume, D the density.

7.4.2.2 Analysis of parameters and their interaction

The determination of the non-linear coefficients allows analysing the effect of the parameters and their interaction. Normalising the resulting equation in the range [0 1] it is possible to compare the intensity of the different parameters. The normalised equation has parameters (Table 7-2):

Table 7-2: Normalised parameters of non-linear polynomial equation

Power	SA	SR	St	Volume	Bias	
1	0.049923	0.014362	-0.03729	1.492578	-0.03846	
2	-0.01482	-0.00255	0.054638	-0.19107		
3	0.000271	0.001238	-0.01554	-0.02264		
	SA*SR	SA*St	SA*V	SR*St	SR*SV	St*V
1	0.00847	-0.02373	-0.04752	0.036411	0.186449	0.027671
2	-0.00145	0.001614	0.000861	-0.01009	-0.04699	0.008016

The volume is by far the most significant factor, it has the largest parameter value, with its increase, the density increases; this happens also with the other parameters except the stylus angle. Each couple of parameters can be isolated and analysed independently, estimating the sum of effect. The coefficient multiplying the product of the volume and screen ruling has a high positive value; this indicates that volume and screen angle have a strong interaction, boosting each other in the release of ink.

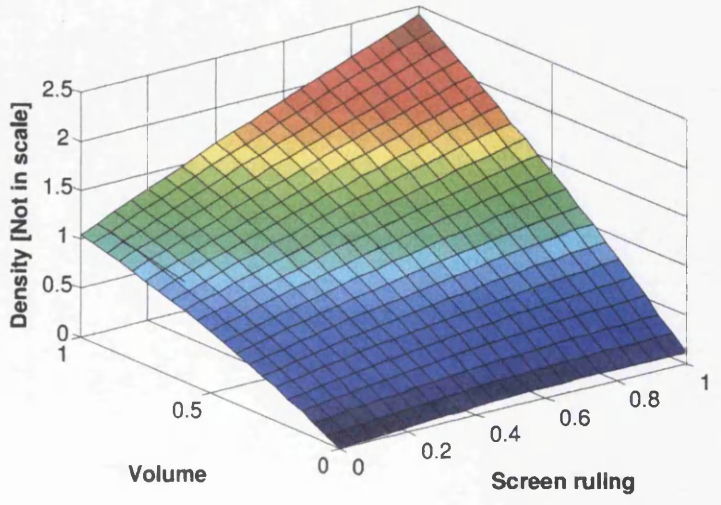

Figure 7-13: Magnified (5x) effect of Screen ruling vs. volume

The screen angle and the volume tend to counteract: at higher volumes an increase of screen angle will lead to a decrease of density

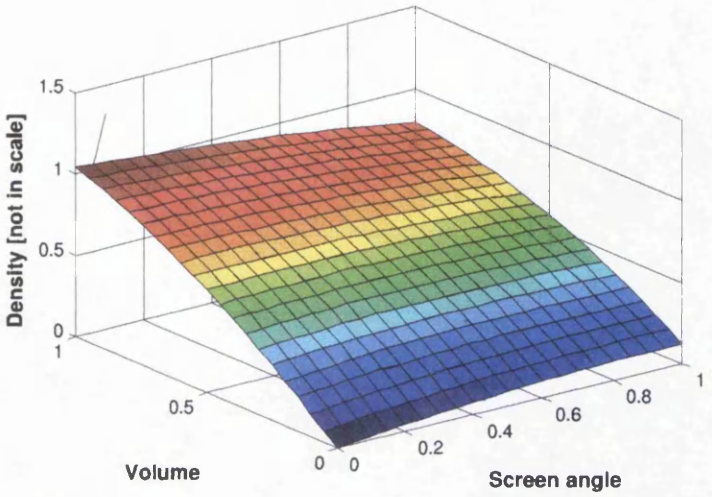

Figure 7-14: Magnified (5x) effect of Screen Angle e vs. volume

7.5 Estimation of the model reference error

The estimation of a reference error as a function of the parameters implemented is important for the evaluation of the created models. In simplifying the model, minor factors are excluded and become a source of error; another source of error is the inheritent inaccuracy of the data provided.

The proposed model, Figure 7-4, was not able to achieve a zero error; this error could be related to limits of the modelling technique or other sources of variability or noise. Variations in position and location of the engraved cells could influence the obtained densities from cells of the same size and shape due to local variations in impression pressure and the effect of surrounding cells. Another source of error could be due to inaccuracy in the data provided, such as the variability in the engraving process, which influences the reliability of the engraved parameters, and natural inaccuracy of the measurement process.

It is important to establish the total error due to these factors in order to be able to define the real capability of the developed models in relation to this "reference" error due to the variability of the data. A study was carried out to define this error, analysing the results of the experimental data taken from measurements of graduation

lines engraved on the roll with the same engraving characteristics but in different positions of the web and with different orientations.

7.5.1 Object of analysis

The analysed set of graduation lines has been previously presented in section 5.4.2. They are identified as *An, Ba, Bn, Eb* and are highlighted in Figure 7-15. These graduation lines were engraved with a nominal compression ratio of 45°, a line ruling of 70 l/cm and a stylus angle of 130°. The four strips are located across the web. The strip An is orientated in the print direction and has been studied with a descending area coverage in the direction of print. The strips *Ba, Bn* are both orientated in the print direction and they have been studied with ascending area coverage in the direction of print. The strip *Eb* is oriented across the web.

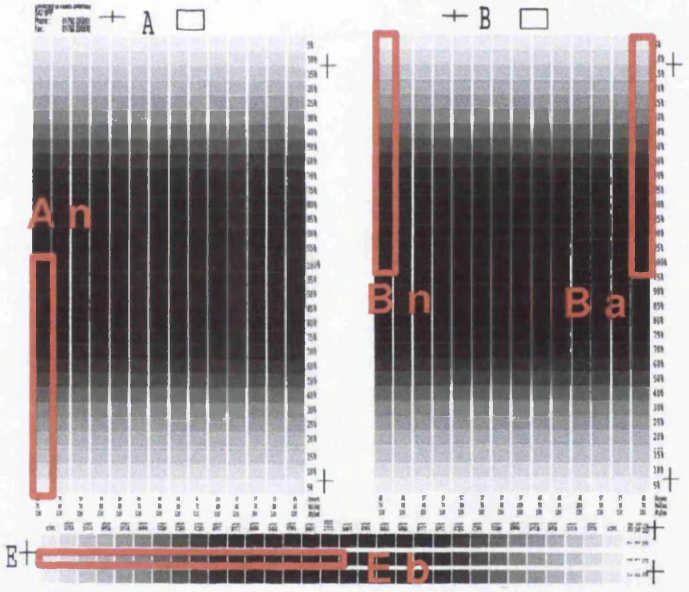

Figure 7-15: Analysed graduation lines

Each graduation line covers the same theoretical area coverage range, graduated over 16 patches. Since the patches were engraved with nominally the same screen ruling, stylus angles, the only variable for each strip should be the actual size of the cells, which, in the first developed model, is identified by the volume. In Figure 7-16, the values of colour density of these four graduation lines are plotted versus the measured values of volume. Reference densities values were the ones measured at viscosity 20s Zahn2.

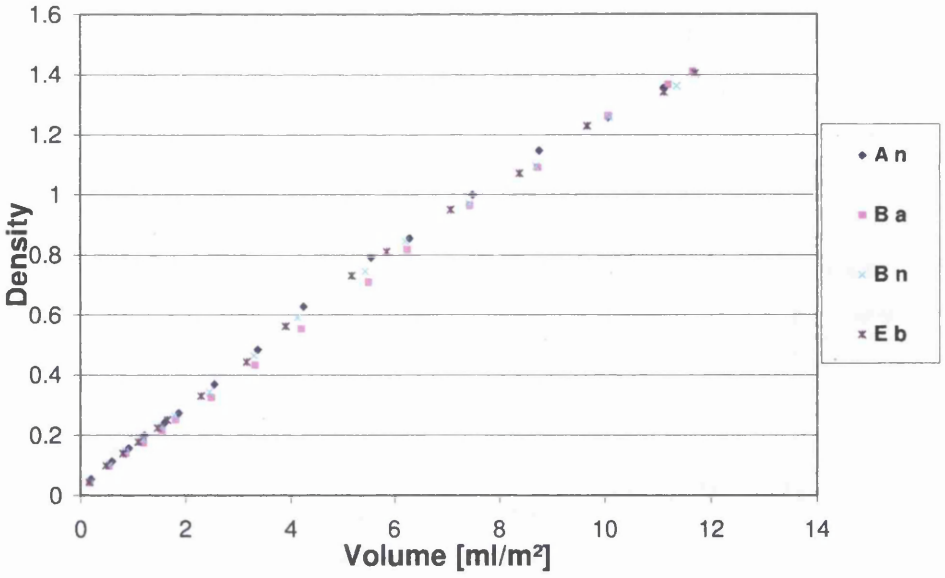

Figure 7-16: Density vs. volume for the four strips

In the mid-tones between the patches engraved in *An* and the ones engraved in *Ba* there is noticeable difference in the achieved density even for engraving that have similar volume; this could be due to an unbalanced impression pressure, since the two lines are at the two extremes of the cylinder.

7.5.2 Analysis process

The analysis was carried out by developing a reduced ANN with one input, the volume and one output, the density. The hidden layer was characterised by 2 hidden neurons, see Figure 7-17. Bayesian techniques were used during the training.

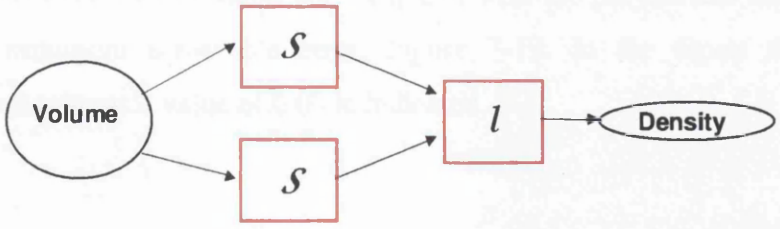

Figure 7-17: Scheme of the ANN for analysis of reference error

The experimental data were the values of volume and density of the 64 patches (16 per line) plus 4 theoretical patches added to define the 0 volume, 0 density condition. The training follows a similar format presented in section 7.3.1 with 85% of the data randomly chosen used for training, 12% for the concurrent validation and 5% for the consequent test. The fit of the model within the data is plotted in Figure 7-18.

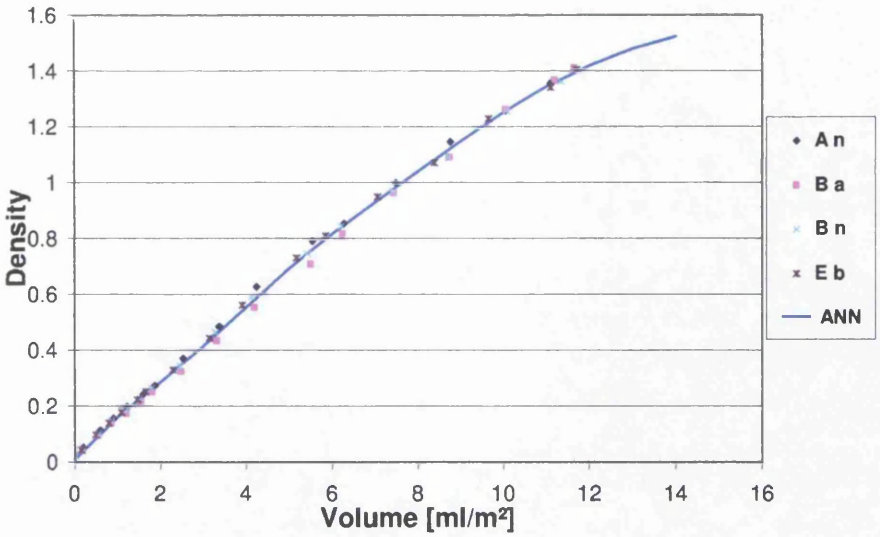

Figure 7-18: ANN analysis of the data

The 2×RMSE error between all the 69 datasets and their model estimates was 0.031 [Density]. Taking into consideration that two lines An and Bn were placed at the two extremes of the cylinder, and therefore were highly affected by any variation in impression pressure, the average error achievable by the model throughout the web should be slightly smaller. The value of 0.031 could be considered as a reference error related to the data collected and not to the modelling technique.

7.6 Evaluation and comparison of the developed ANN models

The results obtained by the ANNs are compared with the polynomial models and the determined minimum achievable error, Figure 7-19. In the figure the reference selected visual tolerance value of 0.03 is indicated.

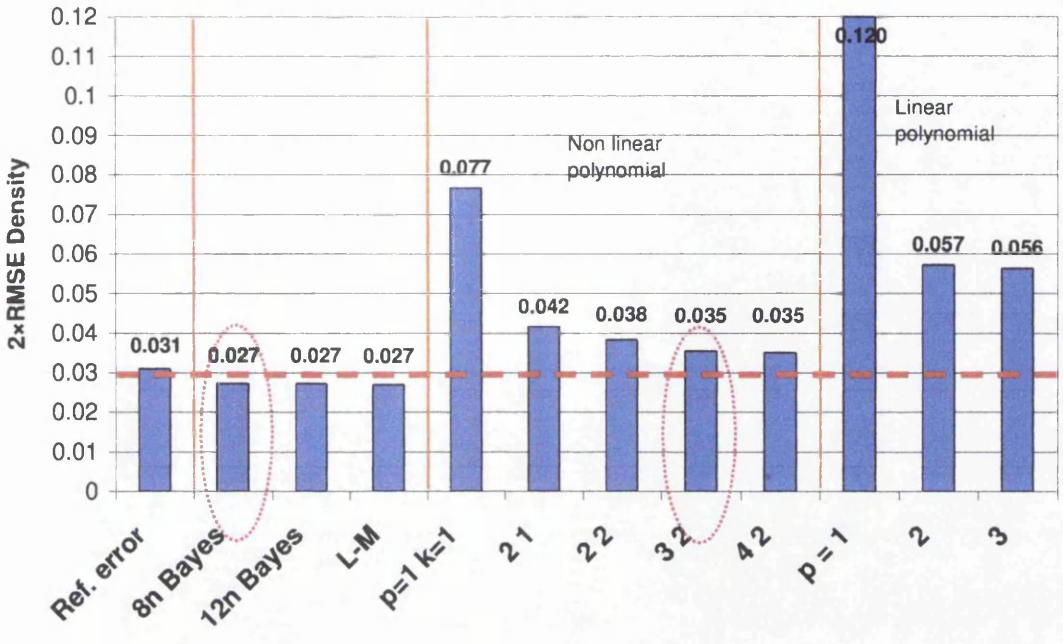

Figure 7-19: Comparison of 2×RMSE

Models developed through ANNs showed the best results, their 2×RMS Errors were the lowest reaching values close to the determined reference error and within the selected eye tolerance levels. The ANN model of particular interest is the Bayesian model with 8 neurons in the hidden layer, highlighted in Figure 7-19, it gave good results with a simpler structure (less neurons) and adopting smoothing techniques during the training, see section 7.3.

Linear polynomial models were found to be inadequate in the modelling of the gravure process. Non-linear polynomial models gave better results than the linear models but still higher errors than the selected tolerance level and 30% higher of the ANN models. Among the different non-linear polynomial models, the model with linear power 3 and interaction power 2 appeared to give the best balance between complexity and the results achieved. This model is highlighted in Figure 7-19 and presented in 7.4.2.1.

The analysis of the results and of the developments indicates that the application of ANNs in the modelling of the gravure process presents several advantages but also limitations, areas where the non-linear models are more suitable. Advantages are:

a. **Better prediction quality**: lowest RMSE error has been achieved; this is the primary and most important factor in any modelling. The achieved error

satisfies the required tolerance levels and is in line with the defined minimum achievable error.

b. **Resilience to outliers**: due to the application of smoothing Bayesian techniques it is possible to deal with local spikes in data better than with the least square method used in the non-linear polynomials. Data used during this work were collected in a laboratory environment, with time. There is therefore a probable lower variability in the data than in collection carried out in industrial practical situation. No major outliers were present in the experimental data.

Disadvantages are:

a. **Complex equation**: the defined equation appears more complex with a higher number of coefficients, it is more difficult to directly outline the interaction between the parameters, this is more easily carried out in the non-linear model, see section 7.4.2.2

b. **Complex development**: the development of an ANN model requires greater mathematical skills than non-linear models and more calculations. In practice, anyway, once the development code has been created, the actual process for the development of the ANN model is a relatively simple task.

For an end-user, the choice of either model makes no difference since both simply provide an individual function to be solved. ANN gives a superior performance at the cost of a higher complexity in the development, but not higher cost in the practical applicability and ease of use.

7.7 Alternative ANN models for the gravure printing process

The effect of cell geometry on ink release in the gravure process can be modelled in different ways to the one presented in Figure 7-4. Several parameters are available for a complete identification of the cell geometry (Figure 7-20). On the basis of different combination of these parameters, several models can be generated. From the experimental data of section 5.3, 8 parameters have been identified for the characterisation of the cell geometry: the three engraving parameters and five measured parameters, Figure 7-20.

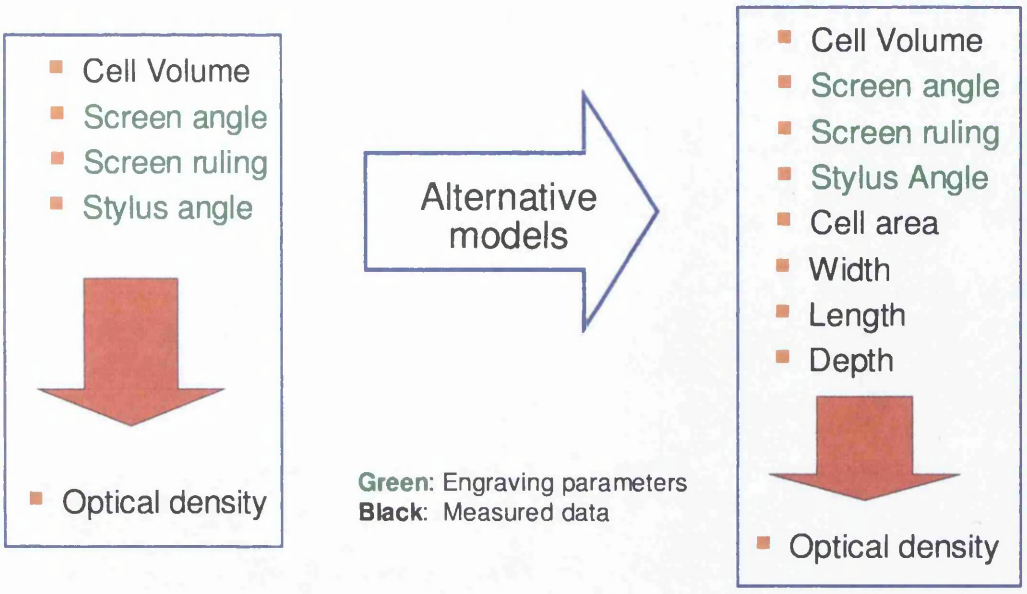

Figure 7-20: Parameters for alternative models

Not all the different combinations and number of these parameters are feasible: some models could inadequately describe the process due to a lack of an enough input variables. Another could be over-constrained, proposing infeasible inputs, i.e. for a specific set of width, length and depth, there is only one possible volume; the four cannot be used together in a prediction model. Another important element is the determination and removal of unnecessary parameters in order to simplify the model, achieving the same quality with a lower complexity. It is therefore important to analyse the quality achieved by the different combination and number of the 8 parameters.

7.7.1 Development of alternative Artificial Neural Networks models

Artificial neural network analysis was used to examine the interference among the different parameters. Artificial neural networks were created modelling the effect of cell geometry on the colour density. The cell geometry was defined as input in the models using a different combination and number of cell geometry parameters for each neural network.

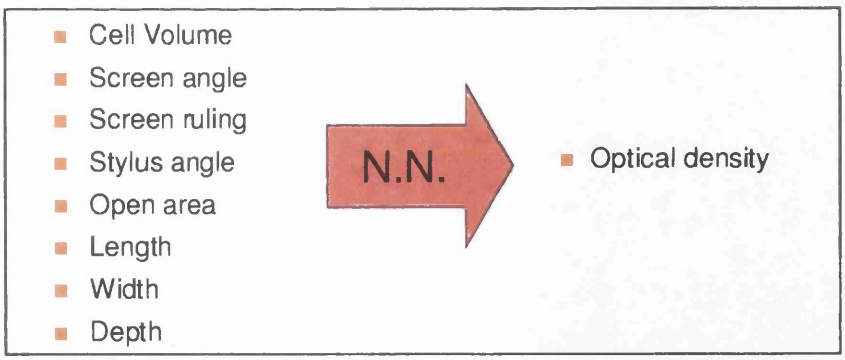

Figure 7-21: Available inputs and output for modelling

Comparing the data fitting with the variation in parameters it was possible to establish the relative importance of the parameters and the optimum combinations of factors.

7.7.1.1 Neural networks designs and training:

Since 8 parameters are available for the definition of the cell geometry, Figure 7-21, a total of (2^8-1) combinations are possible. This leads to a total of 255 networks to be developed. The networks were all designed following the same layout varying only the number of possible inputs, Figure 7-22. The networks have a MLP design with 12 neurons with a hyperbolic tangent transfer function in the hidden layer and a single linear output layer. In the training, Bayesian regularisation techniques have been adopted

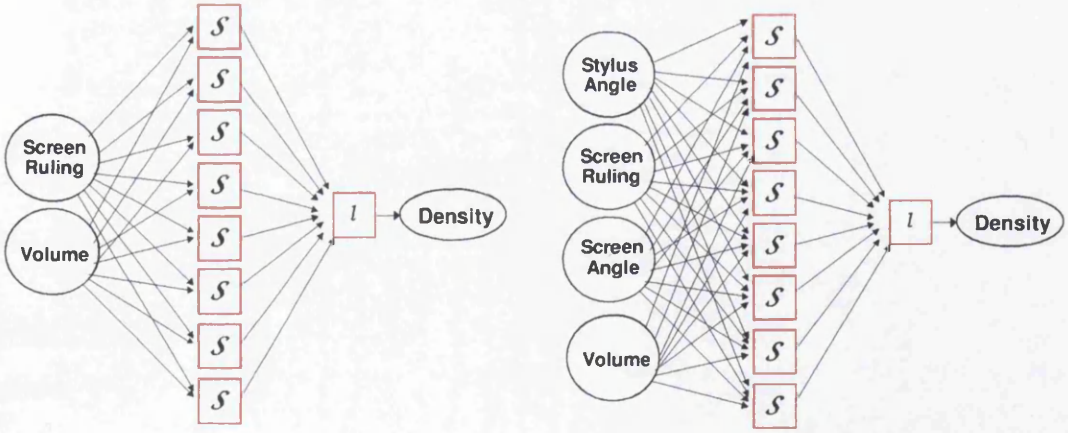

Figure 7-22: Examples of different developed model

The experimental data were the 969 datasets described in section 7.3.1. The training followed the same format presented in section 7.3.1 with 85% of the data randomly chosen used for training of the designed neural networks, 12% for the concurrent validation and 5% for the consequent test.

For each design, the training was repeated several times randomly changing the starting values of the neuron coefficients and the random composition of the datasets. The quality of the obtained trained neural networks was evaluated on the basis of the mean square error (MSE) between the estimated values and the experimental datasets for all 969 datasets.

7.7.2 Analysis of the results of developed ANNs models

The quality achieved by the developed neural networks was analysed by comparing the 2×RMS Errors calculated among the estimated values and all the 969 experimental ones. The complete results are presented in Appendix C.2. In Figure 7-23,the results are presented as a function of increasing numbers of input parameters.

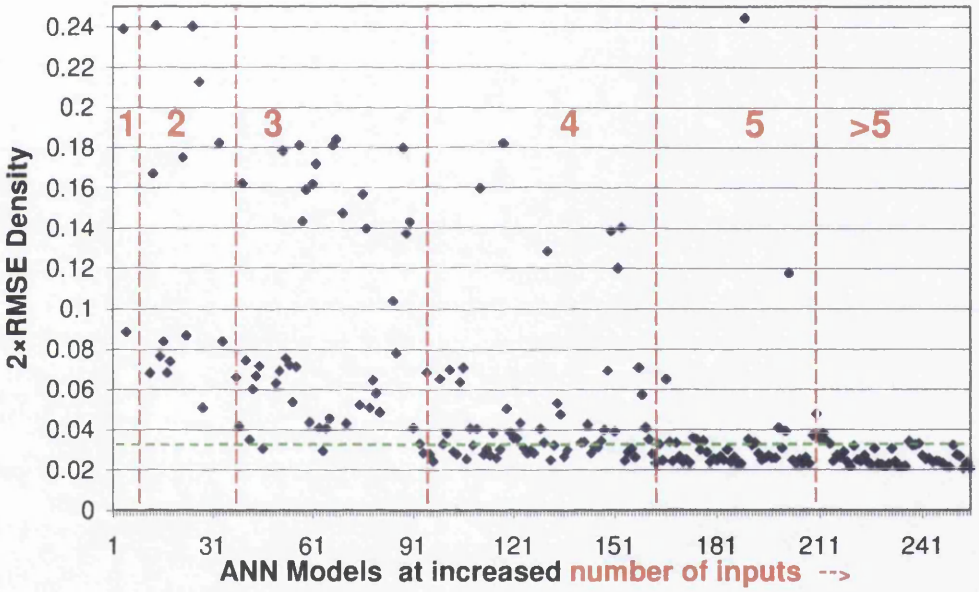

Figure 7-23: 2×RMSE of the models with increasing number of inputs

With the increase in the number of inputs into the models, the overall quality of the modelling tended to improve with lower RMS error.

7.7.2.1 Absolute best achievable quality

When all the 8 parameters were used as input in the development of the model, a 2×RMSE of **0.0194** was obtained. This is the minimum error achieved by any explored model. This model is unusable for any predicting since it is over-constrained, but act as a reference value for the highest achievable quality.

This error is lower then the previous estimates in section 7.5, since here inaccuracies related to the engraving process are compensated by the direct measurement of the dimensions. The fact that also this over-constrained error does not achieve a zero value indicates that there are some secondary factors not accounted for and not kept constant.

7.7.2.2 Analysis of a single parameter model: volume

It is interesting to compare the error achieved by the model having the volume as single input. This model generates a 2×RMS error of 0.090; which compares with the slightly larger 2×RMS error of 0.92 using a quadratic polynomial fitting, determined in section 5.5.1. This underlines the relative flexibility of the artificial neural networks.

7.7.3 Development of models for manufacturing applications

The manufacturing process requires speed and simplicity of analysis. The required model needs therefore to be simple, solid and reliable. It is important to reduce to a minimum the number of required measurements in order to reduce time in the collection of data and to rely on easy to measure parameters and known predefined factors such as the engraving parameters.

The simplest measuring equipment available is the optical microscope. It is cheap and fast but it can measure only a limited quantity of parameters during the engraving process: open area, width and length. Indications of depth, and consequent areas, are known as unreliable and require more time of analysis. The models identified in Figure 7-24 are characterised by geometric parameters measurable by the microscope.

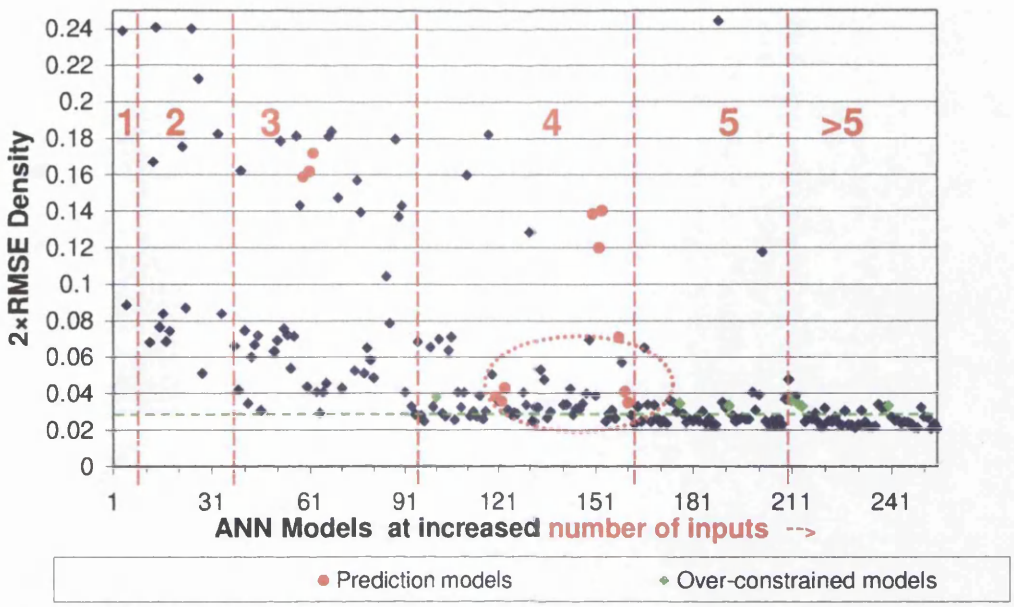

Figure 7-24: Manufacturing models

The identified models can be classified in two groups: prediction models and over-constrained models. There are a total of 7 analysed over-constrained models; these are characterised as having as inputs all the three measured parameters (while an area is in theory uniquely determined by its two diagonals) or two of these parameters in conjunction with all three engraving parameters. These models cannot be used for forecasting but are useful for verification. In these models the 2×RMS Error settles down to a consistent level of 0.029 [Density]. This is an important reference value for the definition of the maximum achievable accuracy in the estimation of the colour density as a function of the explored parameters. A major source of inaccuracy in these models is the lack to any reference to the real depth or volume.

Prediction models in Figure 7-24 are non-over constrained models that can be used in the development of forecasting gravure models applicable to existing common industrial engraving equipment. In Figure 7-24, the best models are highlighted and are shown in detail in Figure 7-25, compared to the previously evaluated model of Figure 7-4.

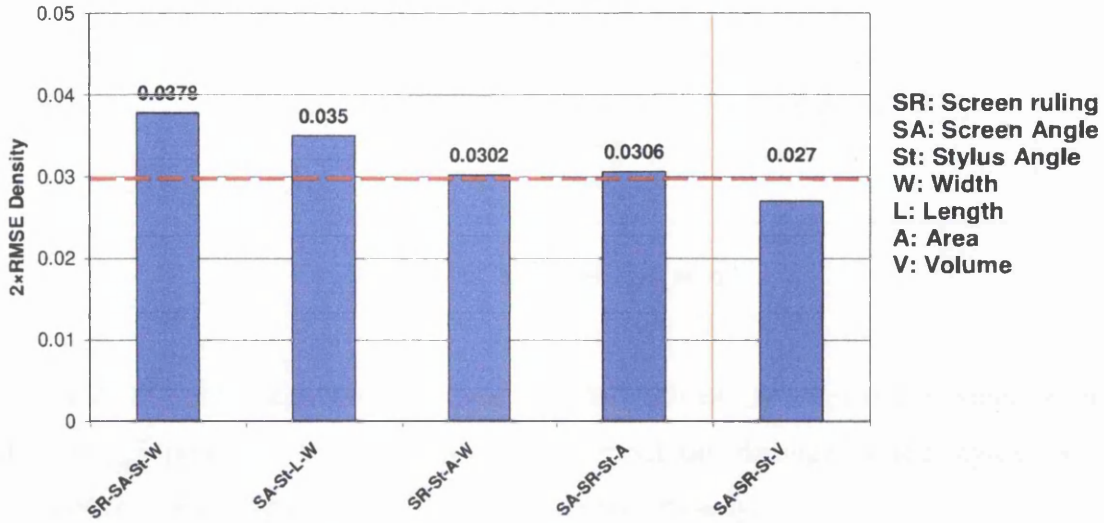

Figure 7-25: Results of manufacturing prediction models

The model based on screen ruling, stylus angle, area and width, Figure 7-25, gives the best results with a 2×RMS Error of 0.0302. This is just slightly higher than the minimum achievable error of 0.029 defined through the over-constrained models, indication of a good engraving quality. The results are practically in line with the eye tolerance limit selected of 0.03, the quality achievable by these models can satisfy a large range of jobs.

In the industry, the most common parameter adopted for the control of the process is the "width" obtained during the engraving. The model based on this parameter and the three engraving parameters gives also a performance with 2×RMSE of 0.038. This is the largest of all, but it indicates that the simple integration of the Neural Network models into the standard manufacturing line could greatly improve the quality of the results. The results clearly indicate that switching from "width" to the engraved area as a measured parameter would greatly improved the performance. It will be still easy to use since it require only one dimensional parameter. This simple model is presented in Figure 7-26, this model is based on area, screen ruling, stylus angle and screen angle; it gives a performance of 0.031.

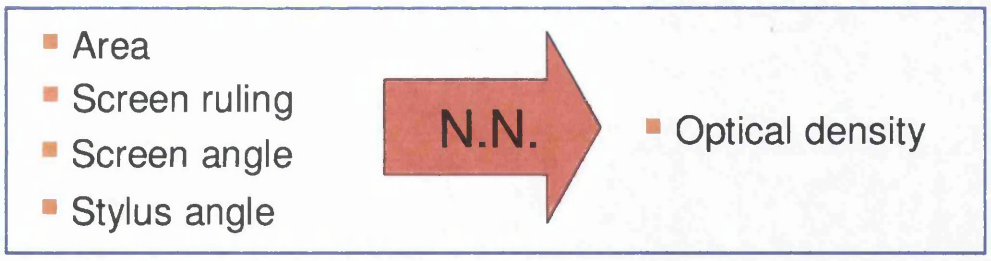

Figure 7-26: Manufacturing model

A major limit of these models is the fact that they rely on the engraved parameters; in the case of poor engraving (related to wrong set up, damage of the stylus tool, hardness of the copper) the model would not work properly.

Density correction curves developed on the basis of this model would be more reliable than the ones currently employed. Models have to be adjusted to the specific engraving machine, range of substrate, and range of ink.

7.7.4 Development of models for physical analysis

In the absence of any reference to the engraving parameters used during the engraving, the modelling has to refer directly to physical measurement of the engraved cells. In these models, the only necessary engraving parameter is the screen ruling, which can be also be measured on the roll or on the prints. Having defined a list of 5 measured parameters (volume, area, width, length, depth), a list of different models can be generated, Figure 7-27.

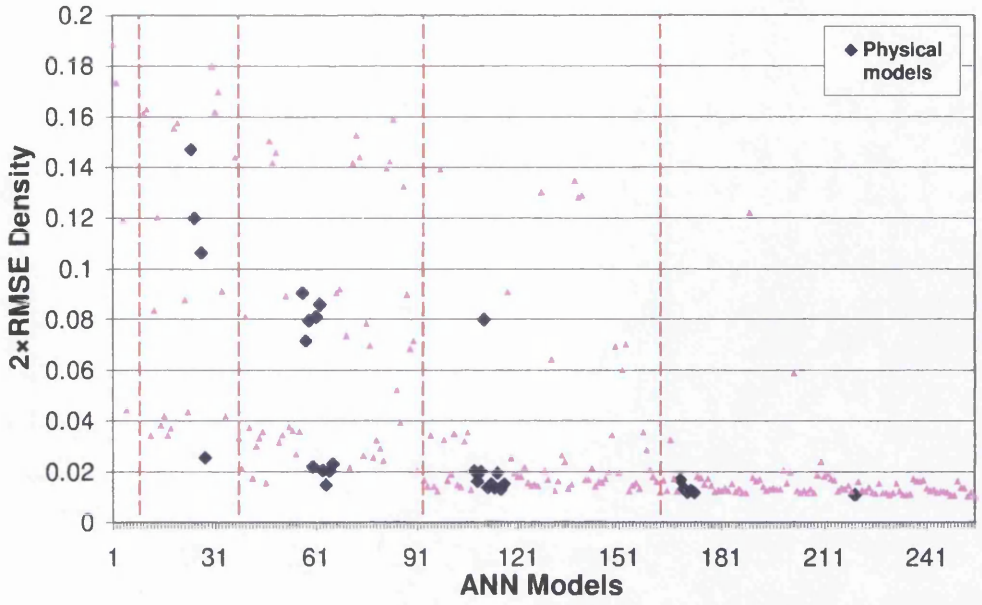

Figure 7-27: Physical models (SR and measured parameters)

Analysing the results shown in Figure 7-27, a model of interest can be based on the screen ruling and the three parameters that gave the best result: volume, open area and width (Figure 7-27). Thanks to the exclusion of depth, these parameters do not over constrain. This model achieves an extremely high quality, reaching a 2×RMSE error of only 0.023, close to the highest achievable error 0.0194.

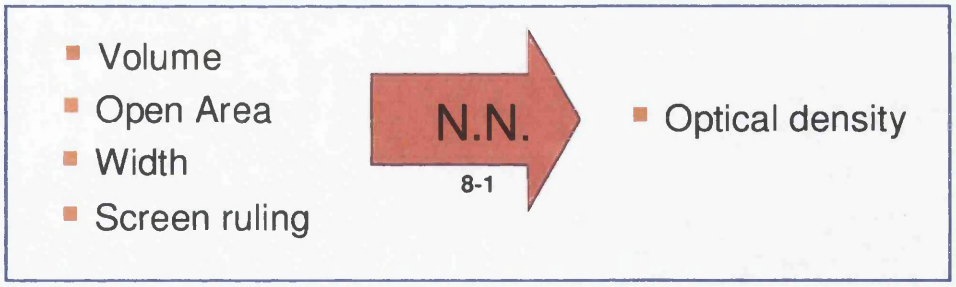

Figure 7-28: A physical model

This result demonstrates that the use of measured physical parameters gives higher quality levels than relying on pre-defined engraving parameters.

7.8 Refinement in the calculation of the error

The Root Mean Square Error is a good indication of an average error over the analysed range of data. It is not an indicator of the local error achieved by the model. Through the application of Bayesian techniques, it is possible to obtain not only a more smooth response but also a local value of the variance σ^2 as a function of training data. From the variance it is possible to calculate the local confidence interval of the results with $2\times\sigma$ equivalent to a 95% interval for a normal distribution. A comparison of the 2×RMSE with the local $2\times\sigma$ is presented in Figure 7-29, for the ANN model of the volume vs. the density developed in section 7.7.2.2.

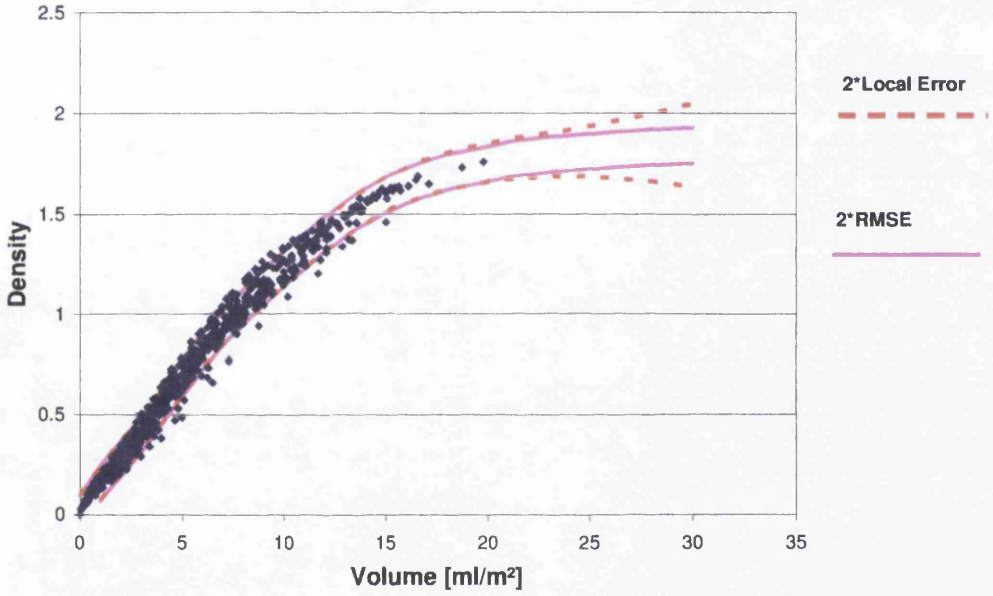

Figure 7-29: Comparison of local error with 2×RMSE

The two errors are very close throughout the range of the explored data. Externally to the range of explored data, the local $2\times\sigma$ error increases; the lack of data means a lower local confidence in the results. The analysis of the local error is therefore useful in the identification of the limits of the model and it could be helpful in warning the user when the model is extrapolating outside the experimental range.

The mathematical background for the estimation of this error is presented in appendix B.4. Since the necessary code was not present in the Matlab Neural Network toolbox, appropriate code had to be developed.

7.9 Introduction of viscosity into the modelling

The models developed until now refer to the constant viscosity of 20s Zahn2, as measured during the printing trial. During the experimental trial three different levels of viscosity were explored: 17s, 20s, 24s Zahn 2 Cup

Models can be created including a parameter defining the viscosity. Expanding the model developed in section 7.3, the model of Figure 7-30 is defined.

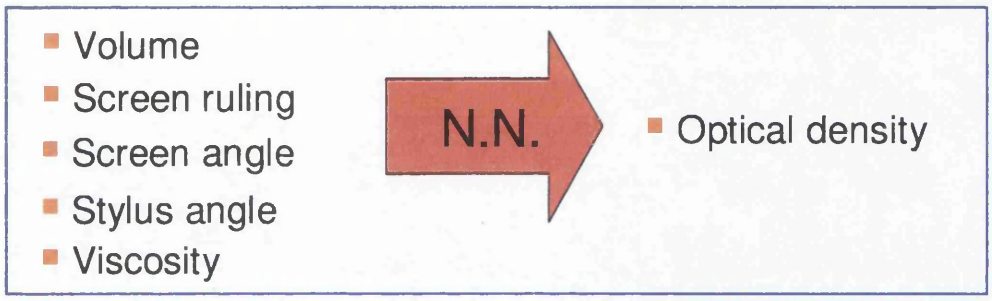

Figure 7-30: New model with viscosity

A total of 2907 datasets are available for the development of a model, 969 for each level of viscosity , see section 5.3.

An artificial neural network can be designed following the steps presented in section 7.3. The network has a MLP design with 5 inputs, there are 10 neurons with a hyperbolic tangent transfer function in the hidden layer and a single linear output layer. In the training, Bayesian regularisation techniques are adopted. The training followed the same format presented in section 7.3.1 with 85% randomly chosen of these data were used for training of the designed neural networks, 12% for the concurrent validation and 5% for the consequent test. The training was repeated several times randomly changing the starting values of the neurons coefficients and the random composition of the datasets. The quality of the obtained trained neural networks was evaluated on the basis of the **mean square error** between the estimated values and the experimental datasets for all the 2907 datasets. Following this process a ANN model was created.

The analysis of the results shows a good correlation between the estimates and the real values. The test set achieves a 2×RMSE of 0.0345, see Figure 7-31, while the 2×RMSE obtained from the comparison of the estimates and all the 2907 datasets is

0.0351. It is noticeable that the error is higher than in the model with constant viscosity, with 2×RMSE of 0.027, see section 7.6.

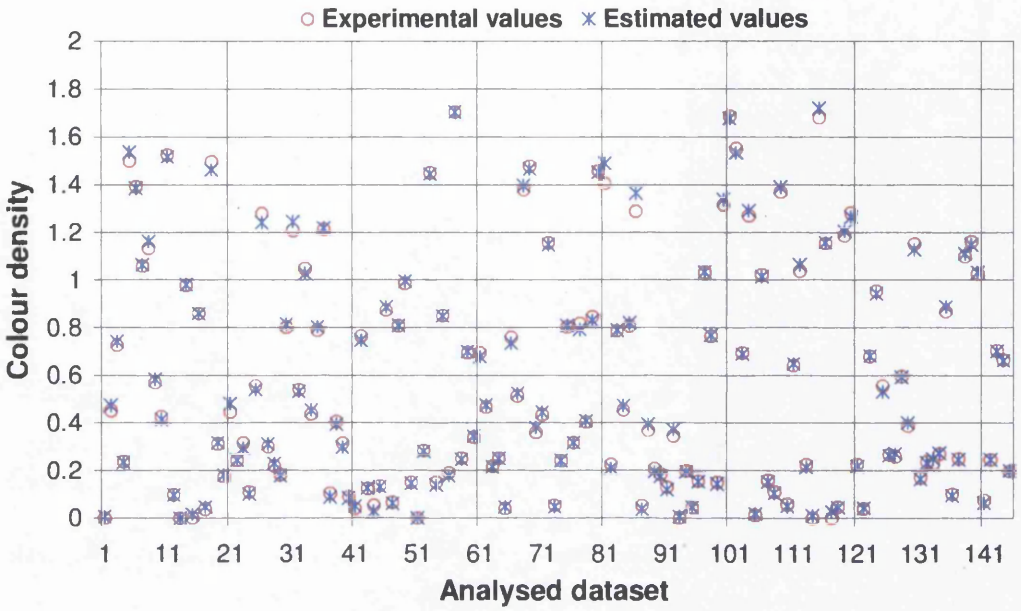

Figure 7-31: Test set results of the model

7.9.1 Limitations in current viscosity modelling

The increase in the estimated error obtained with the introduction of the viscosity suggests that the modelling of the viscosity is limited. During the trial, the viscosity was conventionally modified by adding solvent. An increase in solvent leads to a decrease in the concentration of pigment, therefore to a weaker colour. A single parameter for the characterisation of modifications, which happen in the ink, is therefore not sufficient for accurate estimates. A possible solution would be the characterisation through the application of two parameters:

a. Viscosity: the shear viscosity of the ready ink during the printing

b. Concentration of pigment/base: the percentage of pigment present in the ink during the printing stage.

The integration of these two parameters would help to better evaluate the effect of ink modifications. In presence of two parameters, three trials or data are not sufficient for the analysis of the effect: a minimum of 4 trials are necessary, each with different

combinations of viscosity and pigment concentration. An accurate analysis would require at least 9 trials with 3 levels of viscosity at 3 levels of pigment concentration.

7.10 Further development: effect of cell location

Analysis of the cell geometry effect on the ink transfer indicates that even when using the over constrained models the minimum achievable error stabilises in at a 2×RMSE value of 0.0194, see section 7.7.2.1. This indicates that there are secondary factors or noise not accounted for.

Two possible factors are the impression pressure and the effect of the surrounding patches. The impression pressure is related to the settings of the press and not to the configuration of the cylinder. The effect of the surrounding patches is instead related to the gravure cylinder and therefore it is of interest in relation to our modelling.

7.10.1 Colour density analysis of cell location

A first analysis of this effect can be carried out on the results obtained during the trials. The graduation lines engraved on the test cylinder, Figure 7-32, were characterised by theoretical area coverage progressively increasing from 0% to 100%, areas *a* in Figure 7-32, and then decreasing from 100% to 0%, areas *b* in Figure 7-32 . During printing, for the first half *a* of the graduation lines the scooping action of the doctor blade and ink transfer to substrate were moving from patches of lower volume to patches of higher volume; in the second half *b*, the opposite occurs.

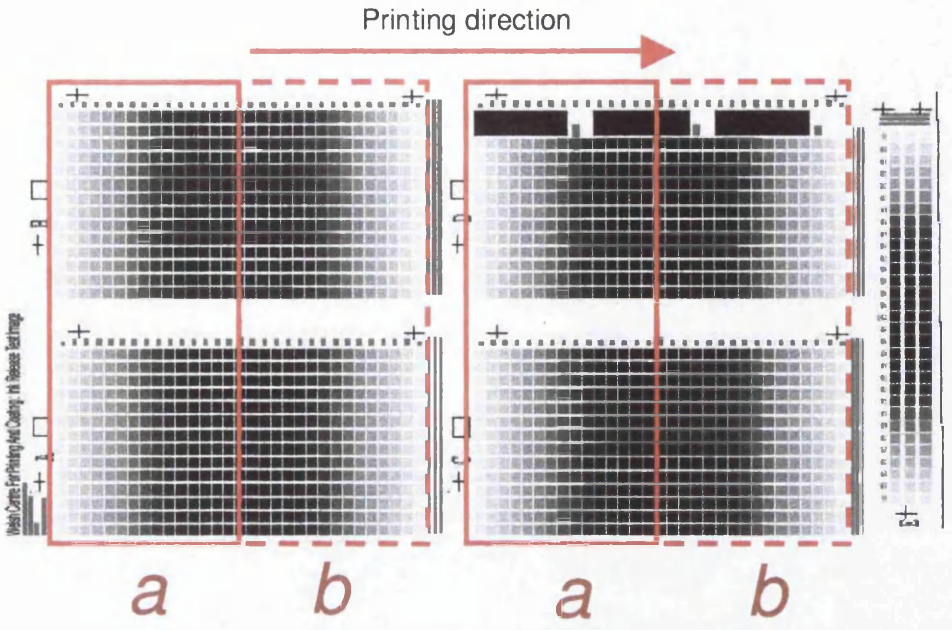

Figure 7-32: Areas for analysis of cell location

Comparing the colour densities obtained from the patches of areas a with the equivalent patches in area b, the chart of the deviation can be plotted, Figure 7-33.

The patches of areas b, printed and wiped after larger patches, give higher density compared to the one printed after smaller patches. The average difference of density is of -0.0118.

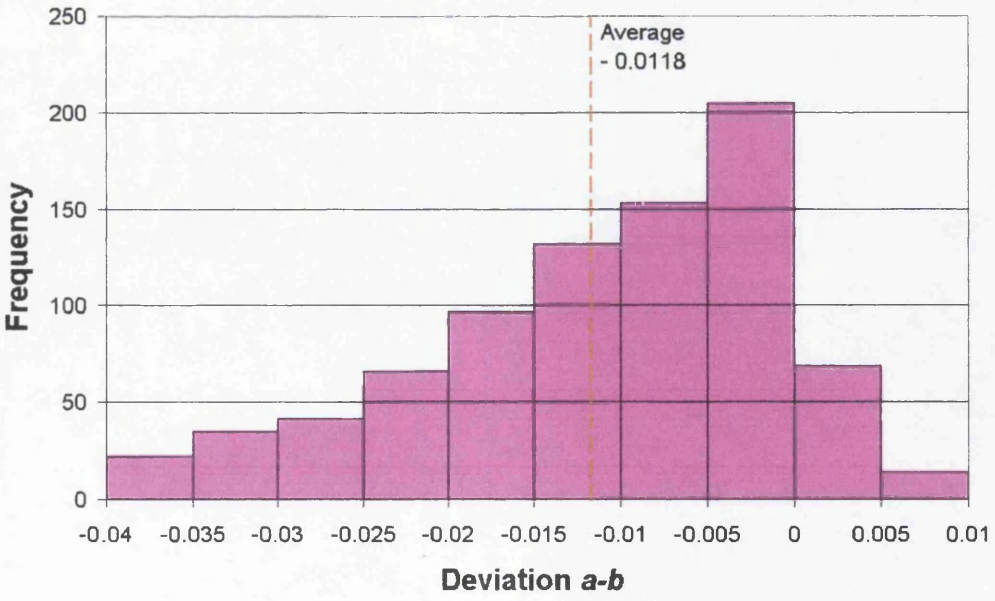

Figure 7-33: Differences between patches a and b

The margin and consistency of the difference is so large that, even considering the variability of the engraving process, the ink release from a specific patch is influenced by the surrounding cells, with larger release when the previous cells are larger. This phenomenon can depend on the variation of the scooping action of the doctor blade or at a chain effect during the actual ink release from the cells to the substrate and can be well correlated with issues found during the printing of horizontal lines vs. vertical lines, section 5.4.2.

7.10.2 Cell location modelling through artificial neural network

The previously analysed model of Figure 7-1 was developed integrating the effect of cell location, Figure 7-34. An appropriate parameter of the cell location has to be defined in relation to the experimental data available. This parameter can be indicated with the size of volume of the previous vertical patch.

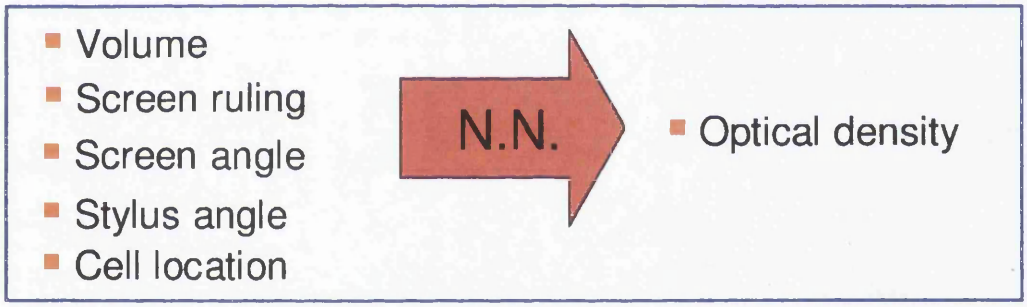

Figure 7-34: Preliminary model including cell location

A neural network was created having as input the volume of the patch of interest, the screen ruling, screen angle and stylus angle. The network has a MLP design with 5 inputs, there are 12 neurons with a hyperbolic tangent transfer function in the hidden layer and a single linear output layer. In the training, Bayesian regularisation techniques are adopted.

The experimental data was the 969 datasets described in section 7.3.1 at the constant viscosity of 20s Zahn2. The cell location parameter indicates the volume of the previous patch in the direction of print. If in the space before there is no patch this value is placed as 0. The location of the patches, from which the data were collected , is presented in Figure 7-35.

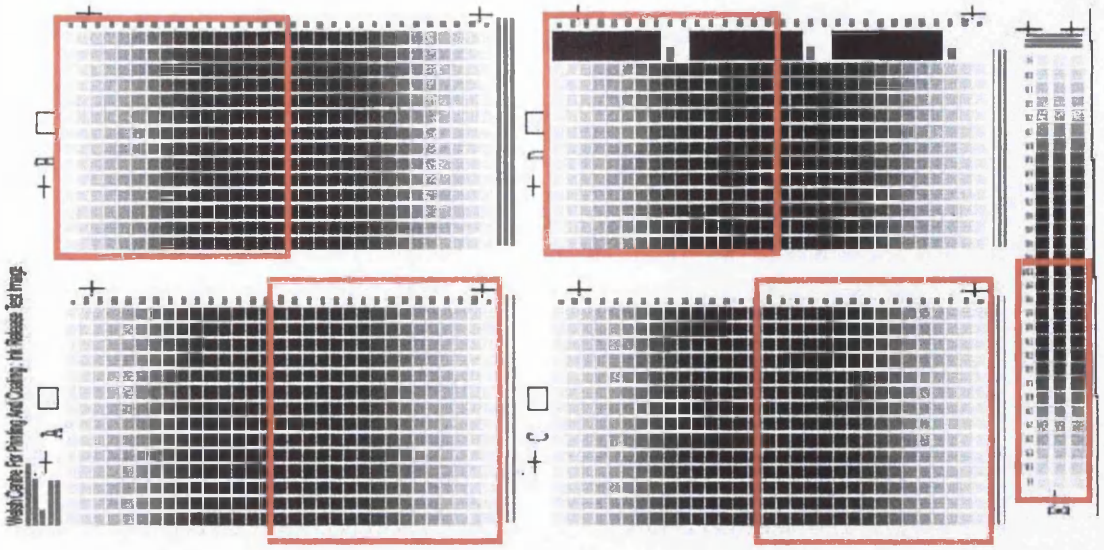

Figure 7-35: Available experimental data

The training followed the same format presented in section 7.3.1 with 85% randomly chosen of these data were used for training of the designed neural networks, 12% for the concurrent validation and 5% for the consequent test.

The results obtained by this network were unsatisfactory: the 2×RMSE reached the value of 0.028 similar to the one obtained without any cell location modelling. A possible reason for this result is that the variation between one patch and the previous one is minimal and constant (5% and 10% area coverage): the lack of range and variability negatively influences the training of the model.

A simplified alternative model has therefore been generated, where the location of the cell on the web was simply identified by three constant numbers (eg. 1,2,3). The attributed value depended on the preceding patch, if it had a larger volume, a lower volume or if it was land area (no volume). The model developed with this parameter following the same prescription previously described show a 2×RMSE of 0.023, better than in the model without cell location.

7.10.3 Limitations in cell location modelling

The proposed model clearly shows several limitations; a major limitation is the lack of range of variability in the data. A correct modelling of the effect of the cell location on the web would require specially engraved cylinders where similar patches are preceded by a range of different patches. This cylinder would allow also analysing the effect of the impression pressure on patches in different location.

7.11 Applications of developed models

The purpose of modelling is the improvement of the processes and of their understanding. In this section, a list of possible applications of the developed models will be presented in relation to common problems and issues of the gravure processes.

7.11.1 Estimation of the achievable density

When an engraved roll is presented, we want to estimate the ink release achievable from this roll. The engraved patches of interest can be optically measured obtaining their area, width and length. These values can be integrated in the model including the known values of screen ruling, screen angle stylus angle. The preliminary model of viscosity can be introduced. The model is over-constrained.

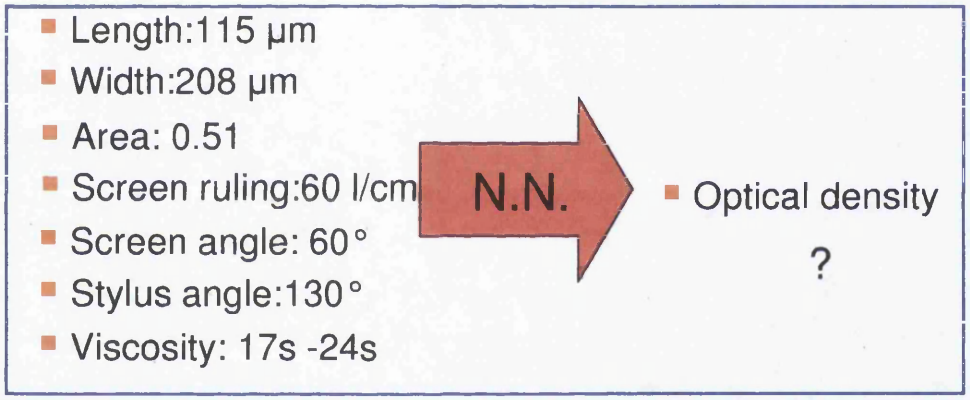

Figure 7-36 presents the resulting estimate of the optical viscosity at the variation of the viscosity. The estimate is presented as a 2xσ confidence band.

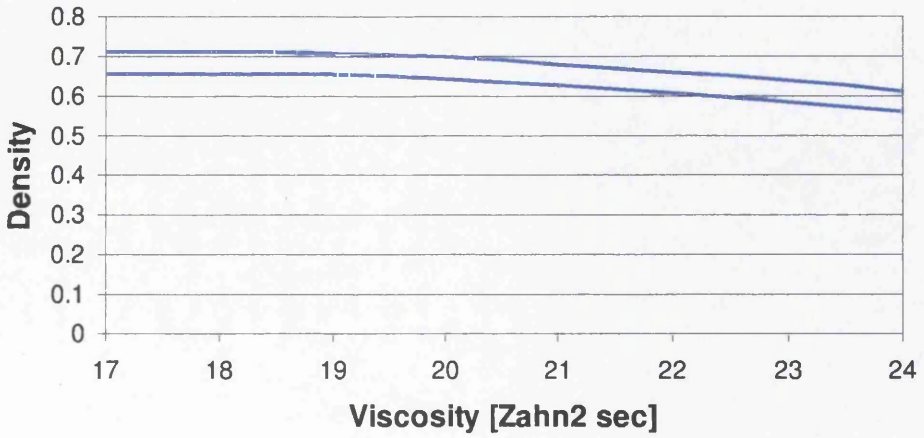

Figure 7-36: Achievable density for different viscosity: 2xσ confidence band

7.11.2 Estimation of required engraving size for required density

The screen ruling and screen angle are defined by the required job; the cell has to be engraved to reach a specific value of density. The engraving area is monitored during the engraving. The model of reference cannot be over constrained, see section 7.7

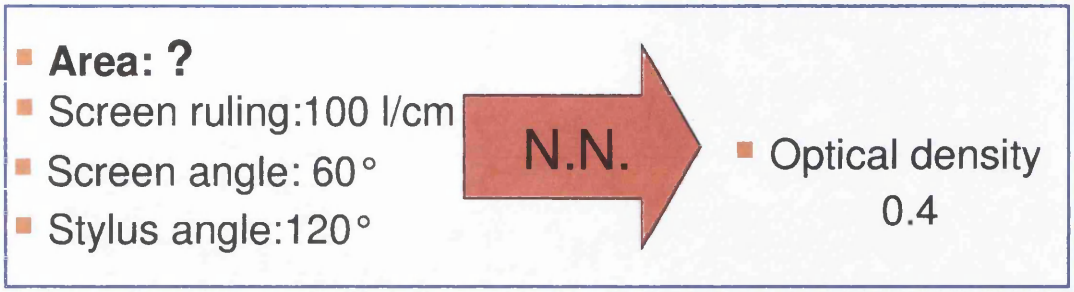

The result gives an open area of 32% equivalent to an estimated cell area of 3200 um^2

7.11.3 Training of operators: problem solving

Models can be used in the training of operators and engravers. It is important for any operator to acquire experience. An operator could use the developed neural networks as press simulators: proposing different problems, the operator can try to modify the parameters of the process until the target is reached.

7.12 Conclusions

Artificial neural networks have been shown to be a feasible modelling technique for the gravure printing process. Models have been developed and verified for an accurate prediction of the effect of cell geometry on ink release. Artificial Neural Networks have been shown to achieve better performance than alternative non-linear polynomial models at the cost of a higher complexity in the development. Once developed, Artificial Neural Networks have been shown to be as easy to use as much as simpler models. Special models have been developed that could be easily integrated in the current manufacturing process, greatly improving the colour correction process. Models that are more extensive have been explored analysing the effect of cell location or viscosity with the cell geometry in the estimation of colour density. Examples of the application of Neural Network models has been proposed, showing its easy application for accurate prediction, problem solving and training.

8 Computational Fluid Dynamics for Gravure Printing

8.1 Introduction

Direct observation of the fluid dynamics in the gravure process is difficult to achieve. The ink release happens on a microscopic scale in locations of difficult access; any measurement would easily interfere with the measurand. An alternative is the analysis of the process through analytical and computational methods. These would allow analysis in detail of the single elements of the process, without "external" interferences.

In this chapter a review is carried out of different Computational Fluid Dynamics methods, starting with an introduction to the background physics governing the fluid flow and the associated phenomenon of surface tension. Previous literature concerning the application of CFD processes in the gravure printing process is then presented. Finally, the finite volume software PHYSICA is discussed in more detail

8.2 Fluid flow dynamics

Analysis of the fluid flow and the development of numerical models is based on the constitutive equations based on the conservation of mass and momentum. This list of equations involved in the definition of flow motion is defined as Navier-Stokes equations.

The **conservation of mass** is defined as:

$$\frac{\partial \rho}{\partial t} + \nabla \cdot (\rho \mathbf{u}) = 0 \tag{8.1}$$

where ρ is the mass density (mass per unit volume), and v is the velocity of the fluid. In the case of incompressible fluid (liquids), the density remains constant in time, therefore the equation is simplified by

$$\nabla \cdot \mathbf{u} = 0 \tag{8.2}$$

The **conservation of momentum** is defined as:

$$\rho\frac{D\mathbf{u}}{Dt} = \nabla \cdot \mathbb{P} + \rho\mathbf{f} \tag{8.3}$$

The left side of the equation represents the inertia of the fluid unit, the right side has two components: the tensor **P,** or Cauchy stress tensor, representing the surface forces acting on the fluid element and **f** representing the body force vector. The Cauchy stress tensor can be separated in two parts isolating the effect of pressure.

$$\mathbb{P} = \begin{pmatrix} \sigma_{xx} & \tau_{xy} & \tau_{xz} \\ \tau_{yx} & \sigma_{yy} & \tau_{yz} \\ \tau_{zx} & \tau_{zy} & \sigma_{zz} \end{pmatrix} = -\begin{pmatrix} p & 0 & 0 \\ 0 & p & 0 \\ 0 & 0 & p \end{pmatrix} + \begin{pmatrix} \sigma_{xx}+p & \tau_{xy} & \tau_{xz} \\ \tau_{yx} & \sigma_{yy}+p & \tau_{yz} \\ \tau_{zx} & \tau_{zy} & \sigma_{zz}+p \end{pmatrix} \tag{8.4}$$

The first part represents the effect of the pressure; the second is instead related to the viscosity. The equation becomes:

$$\rho\frac{D\mathbf{u}}{Dt} = -\nabla p + \nabla \cdot \mathbb{T} + \rho\mathbf{f} \tag{8.5}$$

For Newtonian fluids, which are characterised by a pure viscous flow with constant shear viscosity, i.e. a constant ratio between the shear stress and the shear rate, the value of the tensor T is defined as

$$\mathbb{T} = 2\eta\mathbb{D} \tag{8.6}$$

In which η is the constant shear viscosity and D the rate of deformation tensor

$$\mathbb{D} = \frac{\nabla\mathbf{u} + \nabla\mathbf{u}^T}{2} \tag{8.7}$$

Ultimately the equations defining the fluid flow motion of Newtonian fluids assume the form:

$$\nabla \cdot \mathbf{u} = 0 \tag{8.8}$$

$$\frac{\partial \mathbf{u}}{\partial t} + \mathbf{u} \cdot \nabla\mathbf{u} = -\frac{1}{\rho}\nabla p + \frac{\eta}{\rho}\nabla^2\mathbf{u} + \mathbf{f}$$

Where u is velocity, ρ is density, η the dynamic viscosity (often indicated as μ), f the other surface and mass forces (gravity, surface tension). The left side of the equation

represents the inertial behaviour of the element fluid, the right side the pressure forces, the viscous forces and other forces. Water and oils are example of Newtonian fluids. Other liquids, defined as non-Newtonian, have more complex behaviours presenting viscoelastic properties. In these liquids, the stress tensor T is defined by more complex models, inducing more complications in the associated calculations. Examples of Non-Newtonian models are the Maxwell and Oldroyd-B models [24][36].

8.3 Surface tension

Surface tension is an important physical phenomenon, which is dominant in micro-scale phenomena such as the formation of droplets.

Surface tension [35][33] is caused by the attraction between the molecules of the liquid by various intermolecular forces (Van der Waals, atomic diffusion). In the bulk of the liquid each molecule is pulled equally in all directions by neighbouring liquid molecules, resulting in a net force of zero. At the surface of the liquid, the molecules are pulled by other molecules deeper inside the liquid but they are not attracted as much by the molecules in the neighbouring medium (air). The molecules at the surface are subject to an inward force of molecular attraction, balanced by the resistance of the liquid to compression. The liquid will tend to compress itself together until acquiring the local lowest surface area possible. As a result the liquid will tend to assume a flat smooth surface; in a zero gravity environment, floating liquid will assume spherical shapes.

Mathematically for any volume of fluid enclosing the interface the force due to surface tension will be:

$$\underline{F_\gamma} = \oint_l \underline{m}\gamma dl \tag{8.9}$$

where l is the line of the interface fluid, m is the unit vector tangential to the interface and normal to the volume of fluid and γ the surface tension. Across an interface with surface tension and in equilibrium there is a pressure jump that balances the force due to the surface tension. The Laplace Young Equation describes this force balance per unit area in the normal direction to the interface; over an interface in a three dimensional case the pressure jump will be:

$$\Delta P = \gamma\left(\frac{1}{R_1} + \frac{1}{R_2}\right) \tag{8.10}$$

Where R_1 and R_2 are the principal radii of curvature and γ is the surface tension.

The Laplace-Young Equation of the surface tension can be integrated into the momentum conservation equation (8.3) as an additional source term acting on the interface surface.

8.3.1 Dynamic and Static Contact angle

The contact angle is the angle at which the fluid/vapour interface intersects a solid boundary measured through the liquid, Figure 8-1

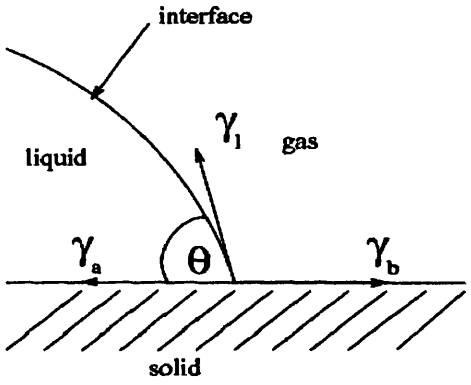

Figure 8-1: Contact angle Θ

In a static condition, the values of the equilibrium contact angle is governed by the Young equation:

$$\gamma_l \cos\theta = \gamma_b - \gamma_a \tag{8.11}$$

Where γa represents the surface tension of the fluid-solid interface, γb of the solid-gas and γl of the gas-liquid.

This angle is valid only for a static condition, like a droplet resting on a flat surface; in presence of a dynamic case, such as a wetting or de-wetting of a solid surface, the resulting dynamic contact angle, or DCA, presents a complex behaviour. No satisfactory theory has yet been found for kinetics of the DCA. Experimental trials show the dynamic contact angles during a wetting and de-wetting process depends on the speed of spreading of the fluid; the higher the wetting speed, the higher the contact angle of dynamic equilibrium, see Figure 8-2. The viscosity of the fluid has a similar

effect. In a large range of conditions, the dynamic angle of equilibrium is correlated with the capillary number describing the wetting process [49].

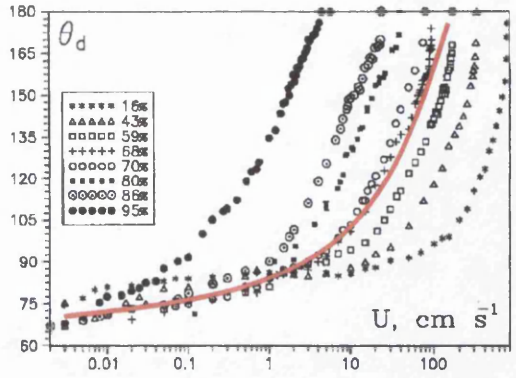

Figure 8-2: Effect of speed on DCA [39]

Experimental work [54] shows that a range of other parameters, such as the surface roughness, influences the dynamic contact angle. An example is a water droplet on a tilting plate: the droplet does not run immediately down, but maintain a steady contact area up to a certain inclination, while angles of contact change.

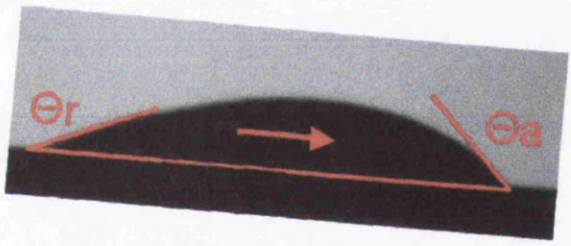

Figure 8-3: Droplet on a tilted plane

When critical angles are reached on the advancing front (Θa) and on the receding front (Θr) the droplet starts to move. This indicates that there is a range of angles around the static contact angle of equilibrium where the contact point does not change, a hysteresis, see Figure 8-4; this range has been shown to be influenced by the roughness of the substrate [40], but it is still not fully understood.

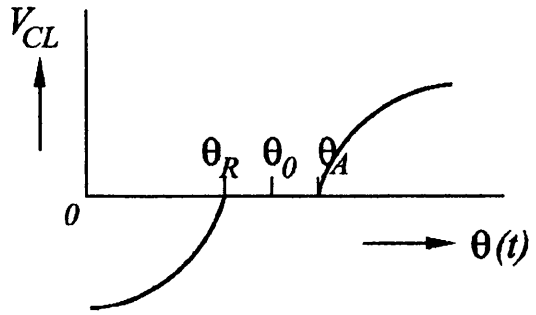

Figure 8-4: Schematic contact line velocity with hysteresis [38]

DCA models, to be integrated into fluid dynamics, are therefore still very limited. A first problem comes from the difficulty of integrating a no-slip condition, which typically describe the solid boundaries, with a dynamic point of contact; a partial diversion is the local removal of no-slip conditions. The delineation of the angle is then another problem; a basic approach is based on the direct imposition of a specific angle at the interface. At first, a unique constant angle was prescribed, this was clearly inheritantly wrong. However, the constant angle (together with constant point of contact) has been the first (and common) implemented boundary condition in the numerical modelling.

The application of empirical relationships between the speed and DCA, that allows the creation of more feasible models, where at each speed a specific angle is prescribed. Empirical models have been proposed by Jiang, Bracke and Seeberg, as discussed in [37]. Analytical studies have lead to the definition of models able to predict (partially) the angle on the basis of hydrodynamics studies, based on the analysis of local forces [37], or based on the equilibrium of forces over a molecular boundary interface [54] .

8.4 Introduction to numerical methods

In this section different numerical methods will be introduced highlighting their typical applications and common limitations [24].

Most Numerical methods are based on the respect of the conservation equations of mass and momentum. These equations are often difficult to solve being non-linear, coupled, and complex. Only for small simple geometries and simple cases, they can

be solved analytically. In more complex real situations, it is common practice to discretise the domain in simple units and to solve the equations within them. Different discretisations require different numerical methods. These can be divided in two kinds: the mesh-grid methods and the meshless methods. In the first, the domain of solutions is discretised in a grid of strictly-connected points, like the nodes in a net. In the particle-based meshless methods, the domain of interest is discretised into interactive particles able to independently move from each other.

8.4.1 Mesh-grid based numerical methods

These are the oldest and most developed numerical methods. They are the current "standard reference" in the computational simulation of solids and fluids. They include the finite difference method, the finite volume method and the finite element method.

8.4.1.1 Finite difference Method

This is the oldest method and is based on the conservation equations in differential form. The solution domain is covered by a grid. At each grid point, the differential equations are discretised as a function of the nodal values of the variables. The result is one algebraic equation per grid node, where the variable values at the nodes are unknown. After imposing values on the nodes at the boundary of the domain, i.e. boundary conditions, the set of equations is then solved. This method is commonly used in conjunction with structured simple grids. A major limit of this method is that particular care has to be taken to ensure conservation.

8.4.1.2 Finite volume methods

The FV method uses the integral form of the conservation equations as its starting point. This is the most common method used in the analysis of steady state fluid flow. Here the domain is covered by a grid of contiguous control volumes. The equations are calculated in reference to the centre of each control volume. Interpolation is used to define the values at the centre from the nodal values. The final set of equations becomes therefore a function of the nodal unknown values. To solve the set, boundary conditions have to be imposed at the boundary of the domain. This method can be

applied to any grid simple and complex (structured and un-structured) and it also enforces the conservation laws.

8.4.1.3 Finite element method

This is the most commonly used method in structural engineering. The method is similar to the Finite volume, with the domain divided into a set of discrete volumes, i.e. elements. The governing differential equations are applied to the domain of a single element. At the element level, the solution of the governing equations is replaced by continuous functions approximating the distribution of the variables over the element domain. These equations are expressed in reference to the nodal values. These are then multiplied by a weight function before they are integrated over the entire domain. Integration per part allows the elimination of differential higher orders, achieving a more stable formulation.

In the simplest FE, the differential equations are approximated by a linear function within the element, created from the values at the corners. The weight function is usually of the same order. This approximation is then substituted into the weighted integral of the conservation law and the equations to be solved are derived by requiring the derivative of the integral with respect to each nodal value to be zero. The result is a set of non-linear algebraic equations to be solved as a function of the nodal values. To solve the set, boundary conditions have to be imposed at the boundary of the domain. This method can be applied to unstructured mesh.

8.4.1.4 Limitations of mesh based methods

In the development of mesh based models two major limitations arise. The first limitation regards the definition of the boundary conditions, which have to be imposed on the boundary points of the domain. Different boundary conditions are available; two conditions are the Dirichlet condition, where the local value is defined (i.e. position) and the Neumann one, where the local derivative is defined. The necessity to impose the model behaviour at the boundary clearly limits the flexibility of the modelling process.

A further limitation is the deformability of the mesh of the domain. In a typical code, the mesh-grid follows the deformations that the domain would experience due to the applied forces. This is adequate for solids where the deformations are minimal in comparison to the original state. In the case of liquids or large plastic deformations,

the elements composing the mesh deform excessively causing instability in the calculations [24]. A solution is the execution of a re-meshing, where a new less deformed mesh is generated on the basis of the last values of previous mesh. This transposition of values presents several problems due to the required interpolation of values and it is an active field of research.

For the analysis of fluids subjected to large deformations, a possible solution is the use of "density" parameters inside the constitutive equations. In this case the grid can be kept simple and cover a large space including and surrounding the fluid of interest. The evolution of the fluid inside the grid is tracked analysing the local values of density at the grid points. Nodes (or Control volumes, or elements) with null density will indicate empty space. Nodes with full density will indicate the presence of fluid at that spot. Nodes with half densities will indicate the free-surface of the liquid.

The first integration of this method with finite difference defined the VOF (Volume of fluid) numerical method [24]. A recent evolution is the level-set method integration into the FV and FE.

8.4.2 Meshless Particle based numerical methods

Meshless Particle based methods are a recent field of research in the numerical modelling of fluids and solids. These are Lagrangian methods (where the co-ordinates move with the fluid) . These methods work by dividing the fluid into a set of discrete "fluid elements" or particles. These particles have a spatial characteristic distance over which their properties are "smoothed" by a kernel function. Several other particles are included within this characteristic distance or radius of action. Any physical quantity of any particle is obtained by the weighted sum of the relevant properties of all the particles that lie within radius of action. The particles respect the constitutive equations of the model, such as the Navier Stokes equations for the fluids.

The first meshless method, and most researched, is the Smoothed Particle Hydrodynamics derived from astrophysics research as discussed in [26]. Other particle based meshless methods have since been developed [27]. One of these modelling techniques is the "Moving particle semi-implicit" method [28].

The great advantage of these modelling techniques is their ability to deal with large deformations, tracking the free-surface of fluids and being able to cope with fragmentations of the flow. These techniques show therefore great potential in the analysis of unsteady processes and deformations with time-evolving profiles of the solid or liquid. The models are furthermore contained and do not require to state the boundary conditions, on the other hand, the interaction laws of the contact of fluids with the solid have to be modelled and appropriately defined.

Major limitations are related to the fact that these techniques are still under development and evolution. The mathematical algorithms of the models present instabilities [29], with the risk of "explosion of particles" of the models whenever the time-step presents the particles into unfeasible positions. The modelling laws of the contact between the solid and fluid are still fairly limited. Another limitation is related to the fact that the accuracy of the profile definition is related to the number of particles, while the calculation of the results is typically square proportional to their number. Large computational power is therefore necessary for accurate profiling (important for analysis of surface tensions).

8.4.3 Molecular dynamics

A completely different approach to the simulation of fluids is molecular dynamics. In this mathematical approach it is not the fluid as entity to be modelled but directly the interaction of the molecules that compose the fluid. The interactions between pairs of atoms can be generalised by attractive-repulsive laws such as Lennard-Jones type,[30]:

$$V(r) = 4\epsilon\left[\left(\frac{\sigma}{r}\right)^{12} - \left(\frac{\sigma}{r}\right)^{6}\right] \tag{8.12}$$

Where V(r) is the L-J potential, ϵ is the depth of the potential well and σ is the (finite) distance at which the interparticle potential is zero and r is the distance between the particles. This is a field of research strictly limited by the computational power available. A single drop of water contains billions of billions of H_20 molecules. The developed models present problems in the mathematical stability of the algorithms, especially on the free-surface. A modern approach is the development of macromolecules and chain of molecules [31] to reduce elements to models and improve stability. The quantity of necessary particles for the simulation of

microscopic quantity of fluid is extremely large, requiring long processing time, outside the capability of most modern computers. Articles have been presented on spreading of droplets over surfaces [31],[32]; Molecular Dynamics software (Visual Molecular Dynamics, PyMOL) has been recently developed with particular regards to biochemical studies on the evolution and interaction of proteins.

8.5 Literature Review: CFD in Gravure printing

CFD is a mature and active field of research. There is a large range of research, articles, journals dedicated to it. However, the quantity of articles dedicated to the modelling of the gravure printing is limited. This limitation can be possibly attributed to the difficulties in CFD with dealing with unsteady states, free-surfaces, contact angles and viscoelastic fluids.

Most of the articles relate to the gravure coating operation in presence of a thick continuous lubrication layer. Schwartz et al. [41] studied the withdrawal of ink from the engraved cells during the coating process. This was analysed as a periodic flow profile. This model demonstrated that smaller cells tend to empty better than larger cells. Schartz published also another paper [42] which studied the effect of cell patterning on the withdrawn of ink, showing its importance in the re-filling process.

In [43], Powell et al explored the reverse gravure coating where the web and the gravure roll turns in the same direction (clockwise or anti) opposing each other. In this study, through a bi-dimensional finite element method, they simulated the progressive evacuation of the meniscus assuming that a negligible amount of liquid is left on the land area after the transfer of fluid on the web. This model was assumed as a reference point in the study of the doctor blade action, which was experimentally scaled up in [44]. It is here noted that scaling gravure process has limited validity due the predominance of capillary forces and viscosity over the inertia in the cell evacuation.

Xiuyan Yin et al.[45], [46] analysed the flow in the nip contact during the coating operation simulating the flow near a cavity and a flexible solid boundary (the rubber roll). The pressure profiles on the cavity varied with the curvature of the rubber rolls and the thickness of the lubrication layer.

Coating processes with their continuous thick lubrication layer differ from conventional gravure printing, which is concerned of the withdrawal of ink from engraved cells for the formation of individual dots, with a negligible layer of fluid on the land area. An article about this was published by Powell el al. [48] . In this article they explored a model of the transfer of Newtonian liquid from an upturned trapezoidal trench (3-D cavity with a large transverse aspect ratio) to a horizontal substrate, which is pulled perpendicularly downwards from the cavity (Figure 8-5).

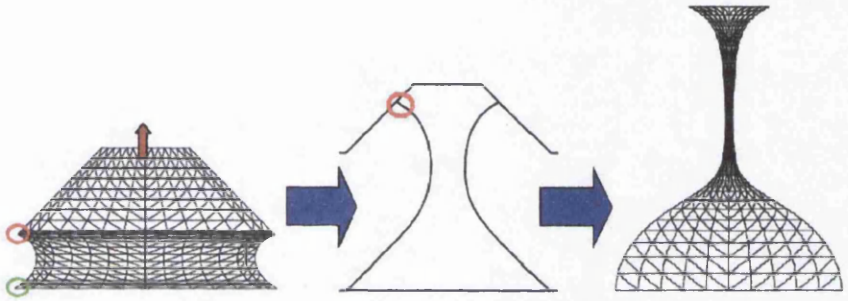

Figure 8-5: Model from Powell et al.

This model was solved computationally using a Lagrangian FEM scheme. The mesh followed the contour of the free surface of the fluid, re-meshing was executed when the mesh became too distorted. As a boundary condition a constant point of contact was imposed on the substrate (green circle in Figure 8-5), while a constant dynamic angle (red circle) was imposed on the walls of the trapezoidal cell. The treatment of boundary condition limited the feasibility of the model as it is in contrast with the known theory of the Dynamic contact angle; see section 8.3.1.

The models that have been presented are all based on the assumption of Newtonian flow. Inks tend to show often more complex viscoelatisc behaviours, mathematical models for the analysis of viscoelatisc fluids do exist but are still limited and difficult to apply. Reference work carried out on the stretching and filamentation of viscoelastic fluids has been presented by Webster et al. [47]

8.6 Preliminary requirements for Gravure modelling

From the analysis of the previous published work and from observations of the different factors of the gravure printing process (see Chapter 2); a list of preliminary

requirement can be drawn up for the effective numerical simulation of the gravure printing processes. An adequate numerical method should be able to:

- Deal with micro-scale phenomena where there is typically a low inertia component compared with the viscosity and surface tension
- Deal with unsteady flows
- Deal with large variations in free-surface shapes
- Model a range of Newtonian and visco-elastic fluids
- Implement accurate surface tension forces
- Implement viable models of dynamic contact angles for analysis of the wetting and de-wetting of surfaces.

These are the primary necessities that have to be addressed for a feasible modelling of the gravure printing process. On the basis of these it was decided to explore the applicability of the finite volume software PHYSICA.

8.7 PHYSICA

PHYSICA is a software environment programmed in Fortran 77 for the modelling of multi physics phenomena where material may behave as a solid or fluid during its processing. PHYSICA is based on the concept of finite volume solution procedures on unstructured meshes. PHYSICA has links in place with pre and post processors such as FEMGEN FEMVIEW and PATRAN.

PHYSICA can deal with a large range of physical phenomena such as solid mechanics, fluid flow, viscoelastic flow, turbulence, solidification processes, heat flows, radiosity. Physical phenomena are modeled following the equation of conservation, for scalar quantities Φ of interest, of the form:

$$\underset{Transient}{\frac{\partial(\rho\phi)}{\partial t}} + \underset{Convection}{div(\rho\underline{u}\phi)} = \underset{Diffusion}{div(\Gamma_\phi grad(\phi))} + \underset{Source}{S_\phi} \tag{8.13}$$

Suitable approximations can be made for each term in which allows them to be expressed as a linear matrix equation of the form

$$\underline{\underline{A}}\,\underline{\phi} = \underline{b} \tag{8.14}$$

where $\underline{\phi}$ is a vector of the values of Φ at a finite number of selected points, such that the solution of (8.14) gives as close an approximation as possible to the solution of (8.13).

In the Finite Volume method the domain over which the equation is to be solved is divided into a set of non-overlapping polyhedral control volumes. In each of these control volumes a single node is positioned. This set of nodes form the selected points at which the value of Φ is sought. The Finite Volume method involves integrating the conservation equation over each control volume, as well as over time, and a solution is sought which makes each of these integrals equal to zero. Assumptions are made as to the variation, between nodes, of the quantities involved in the equation. For each control volume this leads to a linear equation involving the unknown values of the scalar quantity at the node in the control volume and the nodes in the neighbouring control volumes. Considering all such linear equations together produces a matrix equation of the form of (8.14).

For the correct definition of (8.14), boundary conditions need to be imposed over a set of faces on the mesh. These boundary conditions are placed as a source term of (8.13). It should be noted that these boundaries do not need be external to the solution domain. From the iterative solution of (8.14), the evolution and spatial distribution of the quantity Φ of interest can be analysed

8.7.1 Fluids in PHYSICA

In the modelling of fluid flows, the equation (8.13) is converted in to the momentum conservation equation and in to the mass conservation equation discussed in 8.2. These two equations can be obtained by introducing in (8.13) $\Phi = u$ (velocity) for the momentum conservation equation and $\Phi=1$ for the mass conservation equation.

The derived mass conservation equation is as in section 8.2:

$$\frac{\partial \rho}{\partial t} + \nabla.(\rho \underline{u}) = 0 \tag{8.15}$$

While the momentum equation is:

$$\frac{\partial}{\partial t}(\rho \underline{u}) + \nabla.(\rho \underline{u}\underline{u}) = \nabla.(\mu \nabla \underline{u}) + S_{\underline{u}} \tag{8.16}$$

where S_u are the source terms and μ is the viscosity. Together with the Newtonian fluid flow model, visco-elastic models are included into PHYSICA such as the Upper Convected Maxwell and Oldroyd-B models.

8.7.2 Free surface tracking through level set methods in PHYSICA

In the modelling of solid mechanics, the geometry of the mesh is typically modified to follow the deformation of the materials involved. In free-surface flows (droplets, waves) the fluids are continuously changing shape; the mesh elements are subjected to large deformations causing mathematical instabilities. A possible solution is a continuous re-meshing of the domain in order to keep stable element geometries. This re-meshing process is a time consuming and complex process; the necessary re-interpolations of data tend to degrade the system. Re-meshing is still not supported by PHYSICA.

A viable alternative is keeping the mesh rigid and treating the free surface itself as a variable, following its evolution within the mesh. Different methodologies are available for the tracking of the interface between the two fluids (air-liquid, liquid-liquid) within the mesh (e.g. VOF, Volume Of Fluids). In PHYSICA the **level set method**, or LSM, is implemented into its unstructured Finite Volume CFD framework.

In the LSM a continuous scalar variable Φ is introduced. The interface between the two fluids is at the points, or at the level set, where the scalar variable assume value $\Phi=0$. The Level set method is a different approach from the conventional advecting of a discontinuous scalar field where the discontinuity represents the interface, which is the approach used with the VOF method. In LSM the scalar variable must be maintained as a distance function so that the interface stays at a constant depth, which depends on grid size.

In the LSM, the variable Φ must be continuous, smooth and monotonic in the direction normal to the interface. A common function for Φ is a distance function. The value of Φ in the domain will indicate the distance from the interface, Figure 8-6.

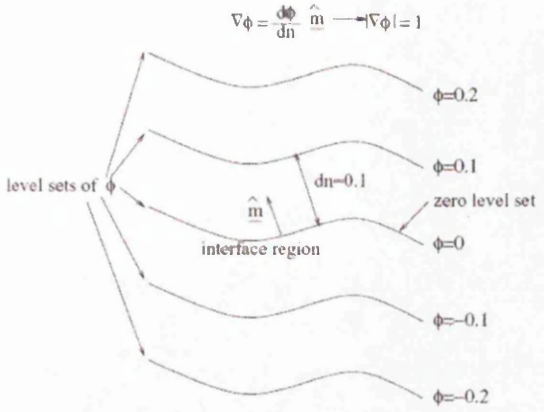

Figure 8-6: Level set diagram

Fluid properties, such as density and viscosity, are calculated with respect of the distance from the interface between the two fluids. The properties are calculated assuming a sinusoidal function, such as hyperbolic tangent, whose output will vary between the values of the two fluids, Figure 8-7. The transition between the two fluids will happen within a defined constant depth or thickness, taking into consideration the mesh size, see Figure 8-8.

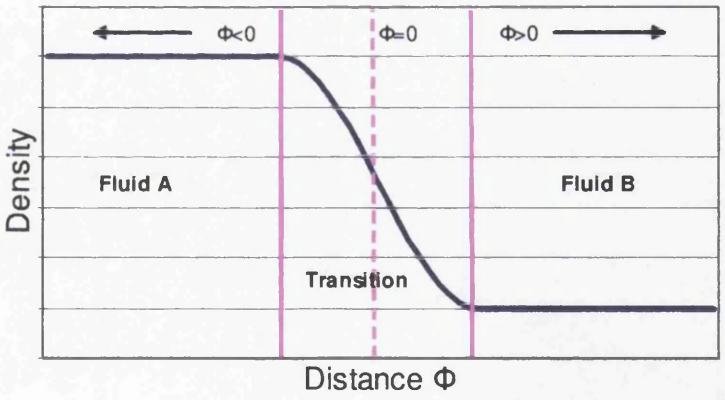

Figure 8-7: Transition between properties (e.g. density) in function of distance Φ

The LSM allows the curvature of the interface to be calculated in a straight forward manner since Φ is continuous across the interface; a drawback of LSM is that areas of high curvature can become smoothed. Another limitation is that the LSM is not

naturally conservative, thus an extra mass conservation or volume re-initialisation condition is required.

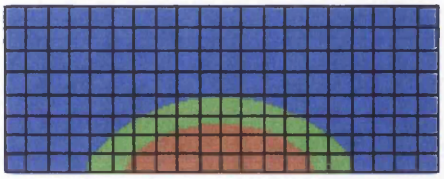

Figure 8-8: Liquid drop (red) in air (blue), transition (green)

8.7.3 Boundary conditions

Boundary conditions can be imposed in order to simulate the contact with solid boundaries, symmetry effect, outlets or inlets. Boundaries can be imposed on predefined lines or surfaces. Boundary conditions are typically imposed at the limits of the element grid. An outlet section is defined imposing on the surface of interest a pressure equal to zero; a no-slip solid boundary condition is defined imposing velocities (in all directions) equal to zero on the surface of interest, the liquid will "roll" over this surface. In absence of any indications, PHYSICA will consider the extremities of the grid acting as a symmetric boundary.

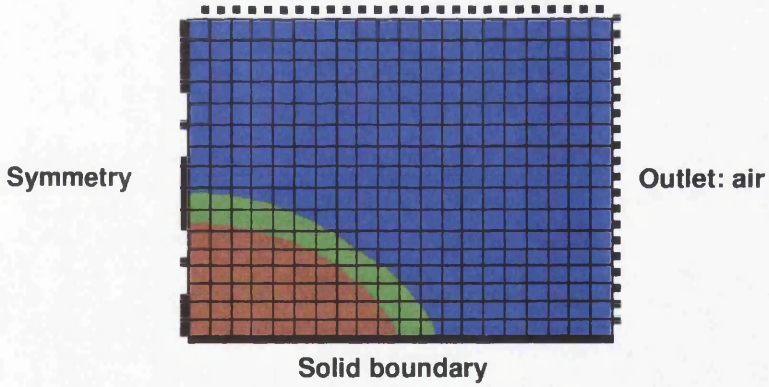

Figure 8-9: Boundary conditions for a liquid droplet

8.7.4 Surface tension and dynamic contact angle

The surface tension of a liquid is modelled as a source term in equation (8.13). A correct modelling of the surface tension is essential in the analysis of micro-scale phenomena (such as droplets). The surface tension is calculated following the Laplace Young Equation, see section 8.3. The curvature is set to zero for any element within the fluid, while on the interface the local curvature is calculated from the analysis of the Φ values across the interface.

In the released version of PHYSICA, the local curvature for each element is calculated over an extension equivalent to the transition interface thickness. In the determination of the contact angle, the PHYSICA approach is based on the imposition of an equilibrium of forces: whenever the contact angle of the fluid differs from the stated angle of equilibrium a force is imposed. This force is calculated from the Laplace Young Equation with the exception that the curvature J is corrected by the value of the cosines of the angle of equilibrium.

$$J(\phi) = \frac{1}{l}(\cos\theta - \underline{n}.\nabla\phi) \tag{8.17}$$

The validity of this method requires verification.

8.7.5 PHYSICA and requirements for Gravure

The PHYSICA Level Set Method seems to have sufficient capabilities to accomplish the list of requirements identified in section 8.6. It was created for dealing with unsteady flows in the presence of large free-surface deformations. It incorporates a surface tension and a preliminary dynamic contact angle model. Visco-elastic fluids are partially implemented. There are questions regarding the actual verification of the DCA model and the ability of the method to accurately predict micro-flow phenomena.

8.8 Closure

In this chapter, the basics of CFD have been presented. The literature review has shown the difficulties with the numerical modelling of the gravure printing process. These issues are generated not only by the complexity of the mathematical discretisation of fluid flows for visco-elatisc fluids and large deformations but also by the lack of physical understanding of phenomena such as the dynamic contact angle. Preliminary requirements have been defined for the choice of a numerical method for modelling ink release in the gravure process. Among different methodologies the Level-set Finite Volume method implemented into PHYSICA matches the requirements

9 CFD modelling of ink release in gravure printing

9.1 Introduction

The development of a CFD model of the ink release from gravure cells presents several challenges. In this chapter, the phenomena of the ink transfer from the engraved cell to the web is analysed identifying associated issues such as ink flow and ink wetting of the surfaces. The development of enhancements to the code PHYSICA, necessary for the modelling of the ink release, is then presented. The quality of the code and its modifications has been verified by analysing the contact angle model and the overall flow model and comparing simulations with experimental and literature data. Finally, a CFD model of ink release from engraved cells is presented and the analysis of the effect of press speed discussed.

9.2 Ink transfer to the web

A key moment during the gravure printing is the transfer of ink from the filled engraved cell onto the substrate. Two different mechanisms are proposed for the characterisation of this phenomenon; in the first, the ink is assumed to be withdrawn starting from the centre of the engraved cell forming a dot on the web, Figure 9-1. The second mechanism proposes that air is initially trapped between the filled cell and the web; the ink then enters into contact with the web starting from the edges of the cell, this leads to the formation of a dot with an annular ("doughnut") shape, Figure 9-2.

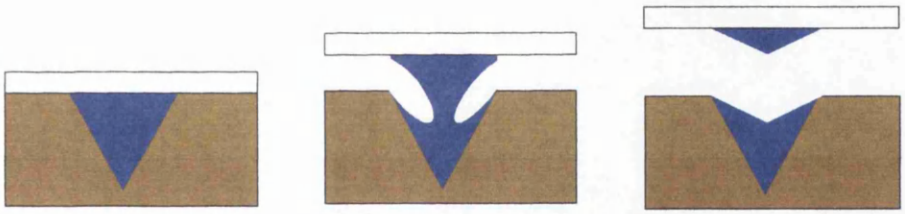

Figure 9-1: First process: ink released from the centre

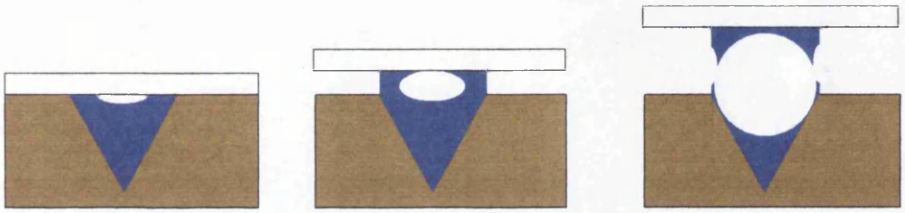

Figure 9-2: Second option, ink released from the edges

Experience shows that both these mechanisms occur. In a substrate printed at low area coverage using UV curing ink a combination of dots was obtained, some had an annular shape, some a more circular shape (Figure 9-3).

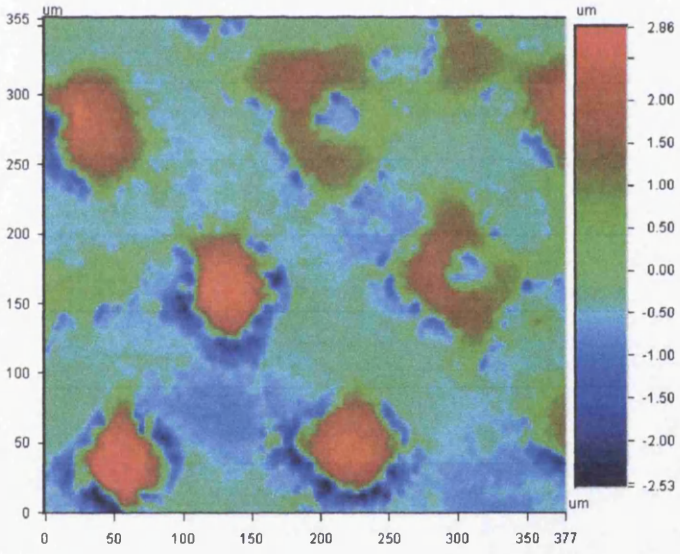

Figure 9-3: UV ink printed substrate

In the case of solvent based inks, the printed substrate tends to show a more consistent annular shape, Figure 9-4. This could be a function not of the ink transfer process but of the solvent evaporation leading to a Marangoni effect ("tea stain").

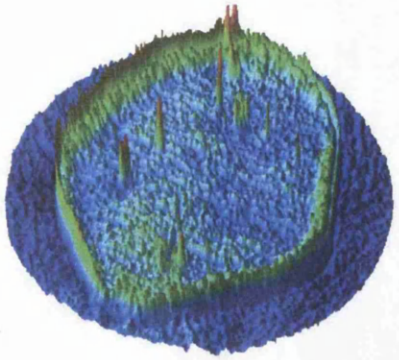

Figure 9-4: Solvent based annular dot

The development of a model for the analysis of annular dots formation requires a complex study of the effect of air bubbles with compressible fluids and gradients of pressure, currently outside our modelling capability. A feasible approach is the analysis of the first process where ink is released starting from the centre and where the air does not have a major influence. There are two major influencing factors: the dynamics of the liquid flow and the dynamic contact angle.

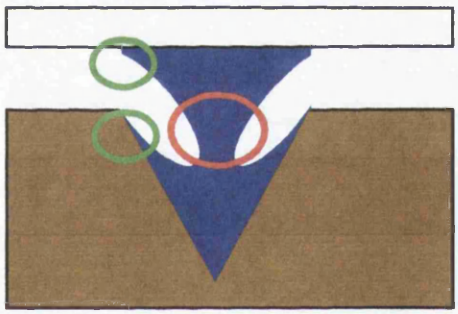

Figure 9-5: Key points of analysis: Extensional flow and DCA

In the release of ink, the flow shows an extensional behaviour as the liquid is pulled between the substrate and the cell. Flows are described by inertia, viscosity and surface tension properties; in this case, due to the limited dimensions and speeds, the flow is dominated by the surface tension and by the viscosity, while inertia has limited effect. Inks can present complex non-Newtonian behaviours, such as elastic properties. In gravure printing, inks tend towards Newtonian behaviour, thanks to the

high content of solvent, typically presenting low viscosities in order to facilitate the filling of the cells. Adopting a Newtonian model is therefore a realistic first approach to the modelling of ink release. The dynamic Contact Angle is another important element often ignored due to the complexity of its analysis as previously discussed in chapter 8.

9.3 Dimensionless numbers

Analysis of dimensionless numbers is important for a better understanding of the importance of the inertia, surface tension and viscous components on the flow of the ink. The Reynolds number is the most referred dimensionless number

$$Re = \frac{\rho v_s L}{\mu} = \frac{v_s L}{\nu} = \frac{\text{Inertial forces}}{\text{Viscous forces}}$$

It represents the ratio between the inertia forces and the viscous forces. At extremely low Reynolds numbers (Re < 1)[34], Stokes flow occurs. This flow can be approximated by the Navier-Stokes equations with the inertial and body force terms equal to zero.

The capillary number is defined as the ratio between viscous forces and the surface tension

$$Ca = \frac{\mu U}{\sigma}$$

Where μ is the dynamic viscosity, u the characteristic velocity and σ the surface tension. Low capillary numbers indicates the dominance of the surface tension over viscosity effects. In a porous media, flows with a capillary number $<10^{-4}$–10^{-5} are dominated by the capillary forces [34].

The calculation of dimensionless numbers for the gravure ink release process requires the definition of values for parameters. Assumed reference values consists of an engraved cell of 100 microns length, an ink of viscosity of 0.1 Pa·s and a surface tension of 0.025, a press running at 100-400 m/min and roll with a diameter of 0.25 m. With press speed of 100-400 m/min and a diameter of 0.25 m the ink can be estimated as withdrawn in the first hundred microns from the cell at an average characteristic speed of around 0.03- 0.50 m/s, results derived from the analysis of the

motion of a rigid cylinder over a flat surface. Given these values the resulting numbers are:

- Reynolds number= 0.015-0.25
- Capillary number = 0.24 - 2

These results indicate that the process is dominated by the viscosity with an important surface tension component, while the inertia effect is limited, even negligible (edge of stokes flow is Re < 1). The relative importance of the surface tension indicates that its modelling is crucial, a correct modelling of the wetting and de-wetting is therefore essential.

9.4 Enhancement to PHYSICA

PHYSICA has an accessible FORTRAN code; this allows the user to implement specifically developed routines. The development of the modelling of ink release created situations that the original software was not able to handle. This leaded to the specific development by the author of new sets of code routines, which expand PHYSICA capabilities to deal with moving solid boundaries and free-surfaces.

9.4.1 Mesh stretching

In the standard application of the level-set method in PHYSICA the grid of elements is rigid and fixed. Boundary conditions, such as no-slip solid interfaces, are applied to surfaces or elements of the grid; boundary conditions are therefore embedded into the grid; if the grid is static, the position of the boundaries will be also static.

In the case of ink splitting there is a progressive separation of the substrate from the engraved cell; its modelling requires the development of a code for the progressive relative movement of two solid boundaries and therefore for a progressive controlled deformation of the grid.

An experimental code routine, written by the developers of PHYSICA, allows a uniform stretching of the entire grid at a constant linear speed in a single direction, see Figure 9-6.

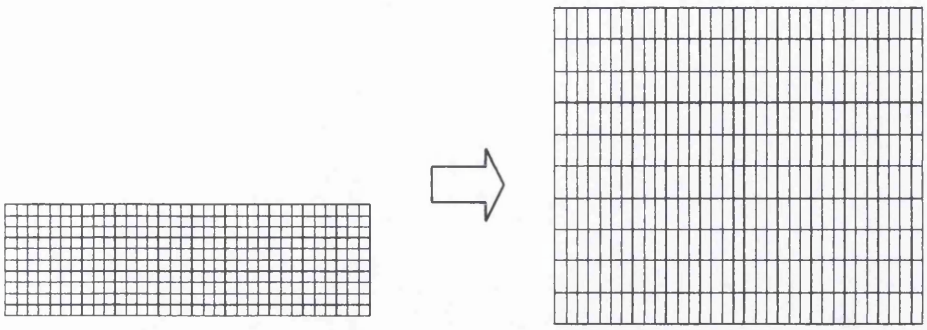

Figure 9-6: Uniform stretching of the mesh

This code presents several restrictions; first, there is a progressive loss of resolution next to the solid boundaries, which leads to large inaccuracies in the calculation of the contact angle. Most importantly, any solid boundary different from a flat surface (like an engraved cell) would lose its shape due to the stretching of the grid.

A new algorithm was therefore developed by the author. This algorithm implements two important enhancements:

1. **Local controlled grid stretching**: selected sections of the grid can be stretched, while the remaining parts remains unaltered; if the stretched part of the grid resides between two stable parts, these will move keeping their relative position within unaltered, Figure 9-8. This allows the shape of the elements within the grid to remain constant in the presence of grid stretching.

2. **Non-uniform stretching of the mesh**

   In a uniform deformation of the grid, each element deforms the same percentage in the direction of stretching, the same strain rate. The integral of all the local strains will give the final achieved global deformation.

   A new code has been implemented that allows a configurable non-uniform stretching of the grid. The new code achieves the same final global deformations while adapting the local deformations: the deformation rate can be reduced next to the boundary of the stretching grid while allowing larger deformation rates in the bulk of the fluid. Adopting this approach the mesh next to the boundaries will stretch less in time, keeping a better local

resolution in time, while allowing the larger strain rates to the bulk of the fluid. A comparison diagram is presented in Figure 9-7. The linear coefficient for the new algorithm is configurable.

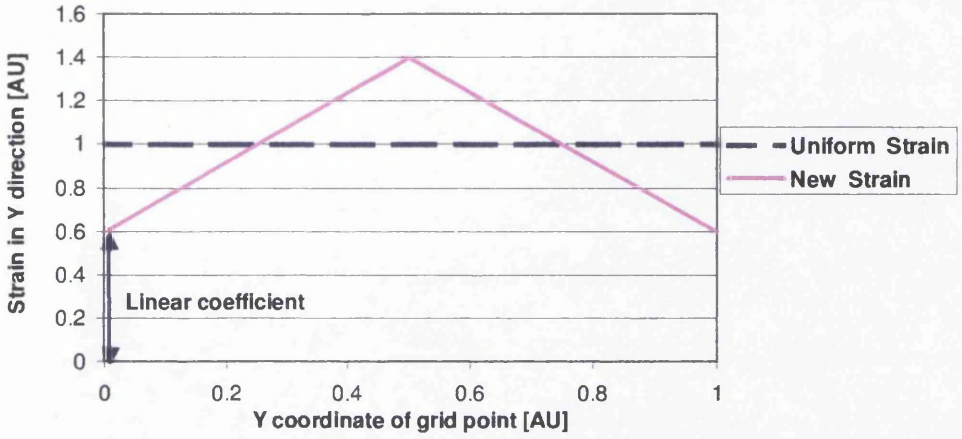

Figure 9-7: Comparison new strain algorithm with uniform strain deformation

Non-uniform grid deformation allows a smoother transition in the element size between static sections of the grid and stretched sections, Figure 9-8 . It also allows a higher resolution of the mesh next to solid boundaries giving an improved analysis of the contact angle.

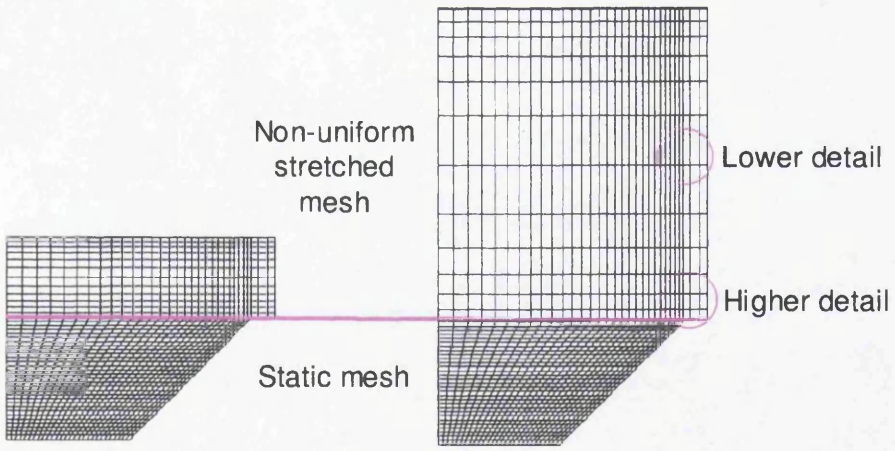

Figure 9-8: Improved mesh algorithm

9.5 Verification of Dynamic Contact Angle modelling

The dynamic Contact angle is a major issue in CFD. PHYSICA has a specific model based on the equilibrium of forces as presented in section 8.7.4. In comparison to previous models based on imposed angles or fixed points, this model allows a

variation of the angle of contact as a function of the forces involved. The feasibility of this model is strictly connected to its ability to correctly portray phenomena related to the Dynamic Contact Angles, such as wetting or de-wetting of solid surfaces. The verification of its capability is a necessary step for its inclusion in the modelling of ink release from the engraved cells.

The verification of the Dynamic Contact Angle model of PHYSICA was carried out by analysing the effect of the advancing speed of a fluid on its dynamic contact angle. This analysis was achieved by modelling the flow of a fluid through a duct at different speeds and consequently measuring the Dynamic Contact Angle.

9.5.1 Model description

A diagram of the model is displayed in Figure 9-9

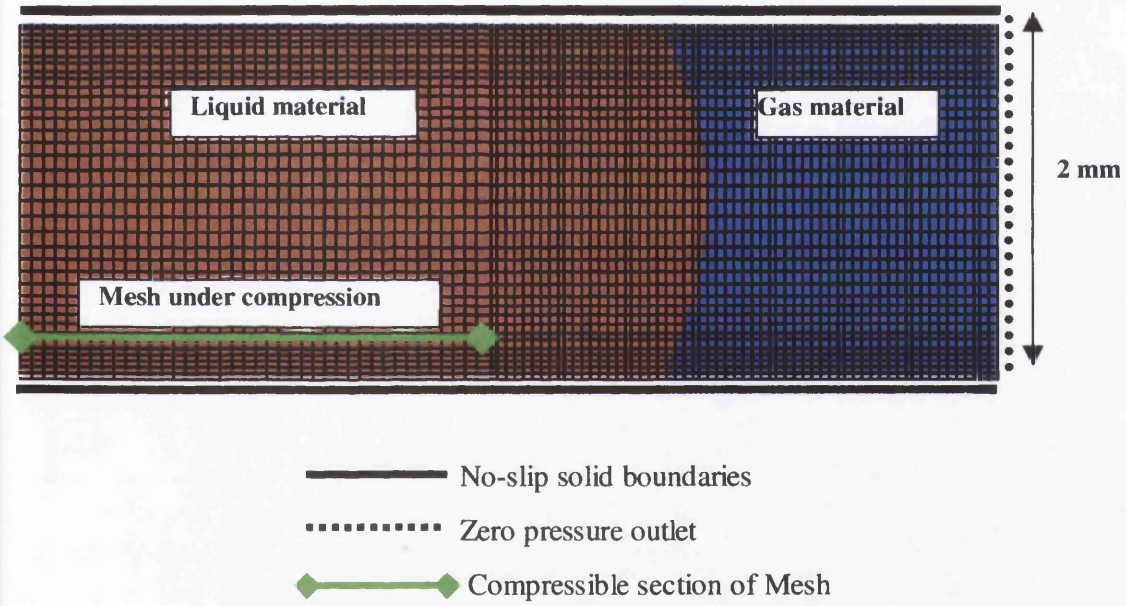

Figure 9-9: Diagram of the duct model

The model was based on a 2-D Cartesian grid of 3600 elements representing a duct of infinite thickness. The duct is only partially filled with liquid. A section of the grid compressed the fluid at a predefined speed, pushing the fluid through the "gas filled" side of the duct, similar to the action of a syringe. On the other side, there was an outlet where pressure was imposed as zero and fluid was free to flow out. The sides of the duct were defined as solid boundaries with non-slip boundary conditions and a predefined static contact angle. The syringe action mechanism allowed a defined speed while keeping the volume of the fluid constant. An alternative to this would

have been the imposition of an inlet with the disadvantage of turning the VOLUME REINITIALISATION routine off, essential to keep track of the volume.

The evolution of the flow was observed by a visual analysis of the values of the variable density, which is equivalent to the selected liquid density for the bulk liquid material and to a very low "gas density" value for the empty section. On the interface between the liquid fluid material and the "gas" fluid, the values of density vary through the interface thickness, Figure 9-10. In this model the interface thickness was set to 7 elements. A clearer visualisation of the fluid profile is achievable by the profiling of the level set Θ function; the free surface profile will be where Θ is equal to zero. In the related achieved diagram (Figure 9-10), two distinct colours distinguish the fluids, red represents the liquid fluid material and blue the "gas" fluid. The evolution of the contact angle was assessed by the visual analysis of this diagram. The deviation from the measured angle was approximated as around 5 degrees.

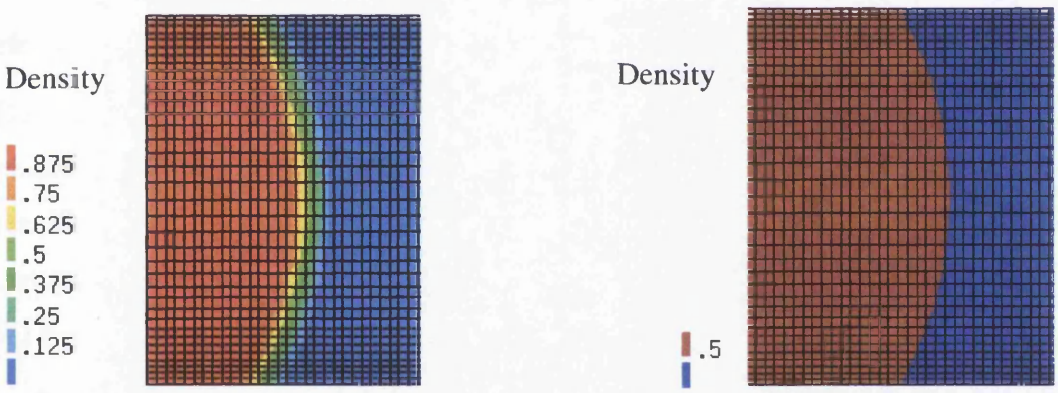

Figure 9-10: Density variation at the interface: multi levels and single threshold

9.5.2 Effect of advancing speed on DCA

The effect of speed was analysed by measuring the contact angles achieved by compressing the mesh, i.e. pushing the fluid, at different speeds. The material properties for the liquid and the "gas" are presented in
Table 9-1

Table 9-1: Material properties for first DUCT model

Material properties	Value
Liquid density	1000 kg/m^3
Liquid kinematic viscosity (dynamic)	0.0005 m^2/s (0.5 Pa·s)
Gas density	0.01 kg/m^3
Gas kinematic viscosity (dynamic)	0.0005 m^2/s (5e-6 Pa·s)
Interface liquid/gas surface tension	0.050 N/m
Contact angle at interface	60°

The "gas" fluid was incompressible and was assumed to have a very low density in order to achieve a condition close to vacuum; the two fluids were imposed with the same kinematic viscosity, the effective dynamic viscosity of the "gas" was extremely low, much lower than air, i.e.1.8e-5 Pa·s. The interface thickness was set to 7 elements.

During the initial phases of the motion of the liquid, the model presented a transient phase where the forces acting on the system were unbalanced, ultimately the model reaches a stable configuration, a dynamic equilibrium of the forces. The dynamic contact angle of equilibrium was measured when this equilibrium was reached, Figure 9-11.

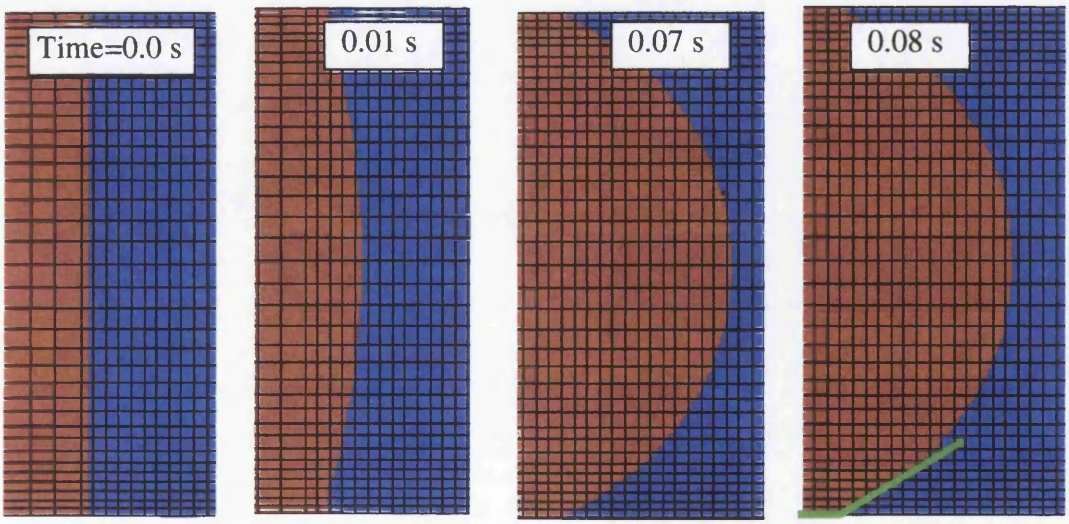

Figure 9-11: Contact angle is measured once dynamic equilibrium is achieved

Values of the measured contact angles as a function of the fluid speed through the duct are presented in Figure 9-12.

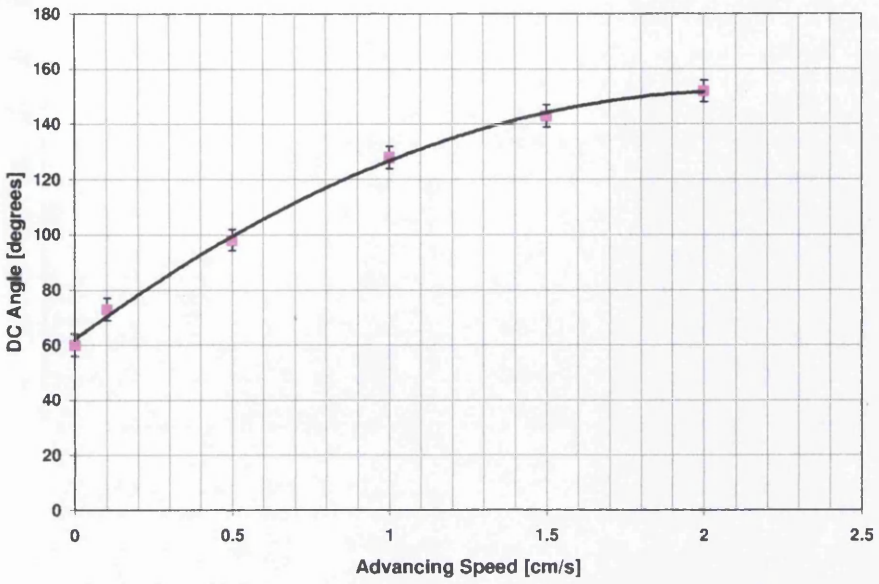

Figure 9-12: Effect of speed on Dynamic contact angle

Initially, the dynamic contact angle tends to increase with the increase of the speed of wetting. However, the angle tends to stabilise around 160 degrees.

9.5.3 Effect of viscosity and surface tension

The effect on the DCA of different viscosities and surface tensions combinations were analysed with the variation of wetting speed, Figure 9-13.

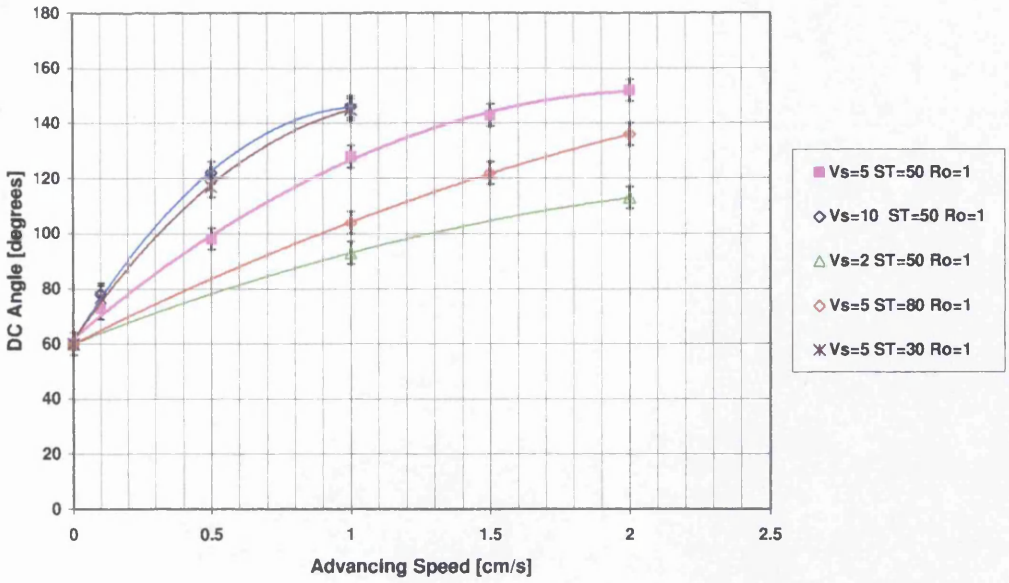

Figure 9-13: Effect of viscosity and Surface tension

An increase in viscosity or a decrease in surface tension leads to an increase of the contact angle. The results of the DCA can be observed in relation to the capillary number, in Figure 9-14.

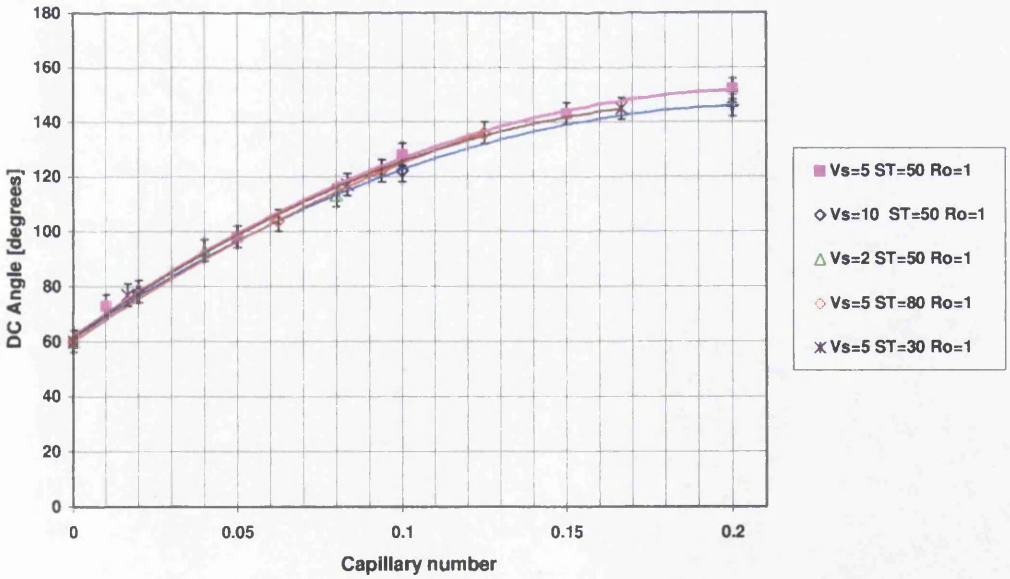

Figure 9-14: DCA vs. Capillary number

There is a strong correlation between the obtained Dynamic Contact Angle and the Capillary number of the flow. The evolution of the Dynamic Contact angle appears to

be a function of the Capillary number and of the static contact angle. This correlation agrees well with literature, starting from the observations of Hoffman [49], who experimentally analysed DCA in pipe flow and found the same correlation.

9.5.4 Model verification through experimental data

Blake et al. [50] experimentally studied the velocity-dependence of an advancing dynamic contact angle for a series of water-glycerol solutions. The experiments were carried out by accurately measuring the advancing contact angle on a PET plastic tape while the tape was perpendicularly entering into a tank filled with the different solutions, Figure 9-15.

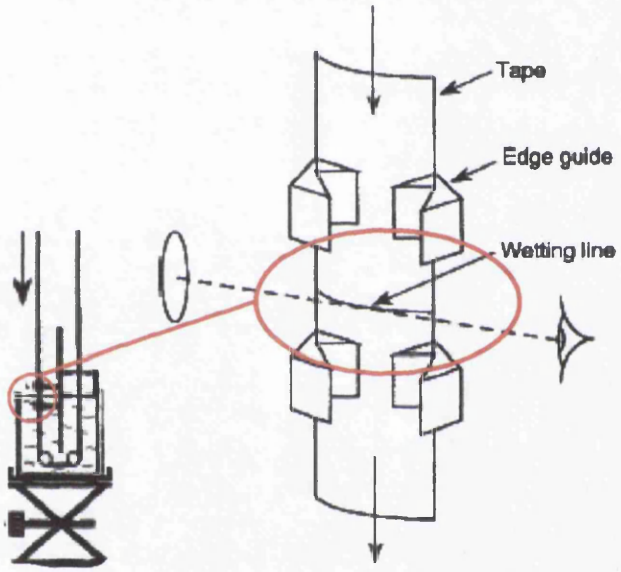

Figure 9-15: Experimental settings for [50]

This experiment was reproduced by analysing the advancing dynamic contact angle for two fluids in the duct model described in 9.5.1. The fluids were simulated imposing the experimentally determined material properties of the water-glycerol solutions, Table 9-2.

Table 9-2: Water-glycerol material properties

Percentage of glycerol	μ, mPa s	σ, dyn/cm	θs, °	ρ, g/cm3
86%	104	65.8	65.0	1.224
95%	672	64.8	62	1.248

In Figure 9-16 the results obtained at different speeds are compared with the experimental results and related theory described in [50]

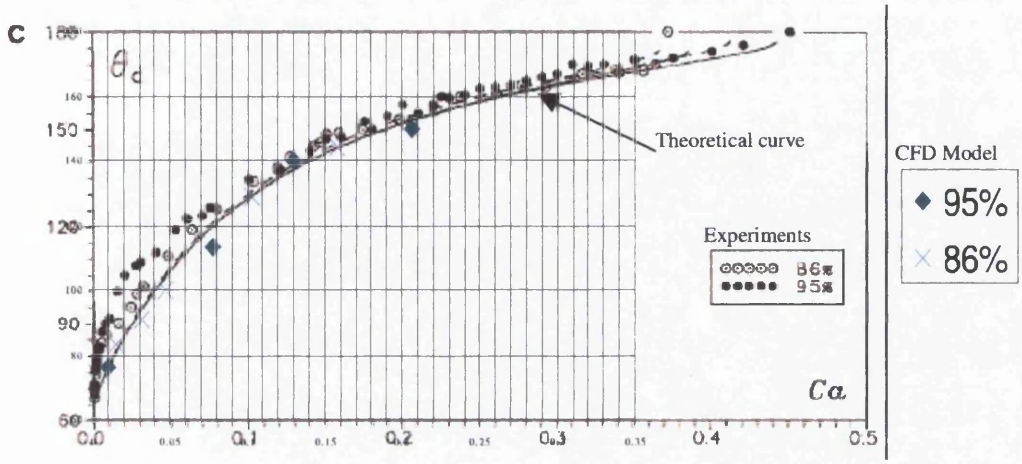

Figure 9-16: Overlapping of chart from [49] and numerical models results

The results generally show a good agreement with the experimental data and the theoretical curves. Major differences occurred at low capillary numbers, this could be mainly related to the influence of the hysteresys phenomena of the contact angle in static conditions, as discussed in [40].

These results indicate the ability of PHYSICA to model the different dynamic contact angles during wetting of surfaces. This result is important for the correct development of the modelling of ink release due to the critical importance of wetting during the process.

9.5.5 Numerical modelling effect: Interface width

In the code, the calculation of the local surface tension on an element is defined on the basis of the curvature of the free surface, which is calculated over the interface density thickness. In order to reduce the excessive smearing on the free surface, the interface thickness is typically kept very thin, typically of three elements [35], but a curvature estimated over too few elements could lead to some inaccuracies, especially next to the boundaries where the curvature has to be estimated from only half the elements. The effect of the interface width was therefore explored on the accurate determination of the DCA. The duct model was run with the same material properties, Table 9-3, at two different speeds, varying only the interface thickness.

Results are presented in Figure 9-17 in comparison with theoretical curve, defined in [50].

Table 9-3: Material properties used in analysis of interface width effect

Material properties	Value
Liquid density	1248 Kg/m^3
Liquid kinematic viscosity	0.000538 m^2/s
Gas density	1 Kg/m^3
Gas kinematic viscosity	0.000538 m^2/s
Surface tension	0.0645 N/m
Static Contact angle	62°
Explored Speeds:	0.75 cm/s, 2 cm/s

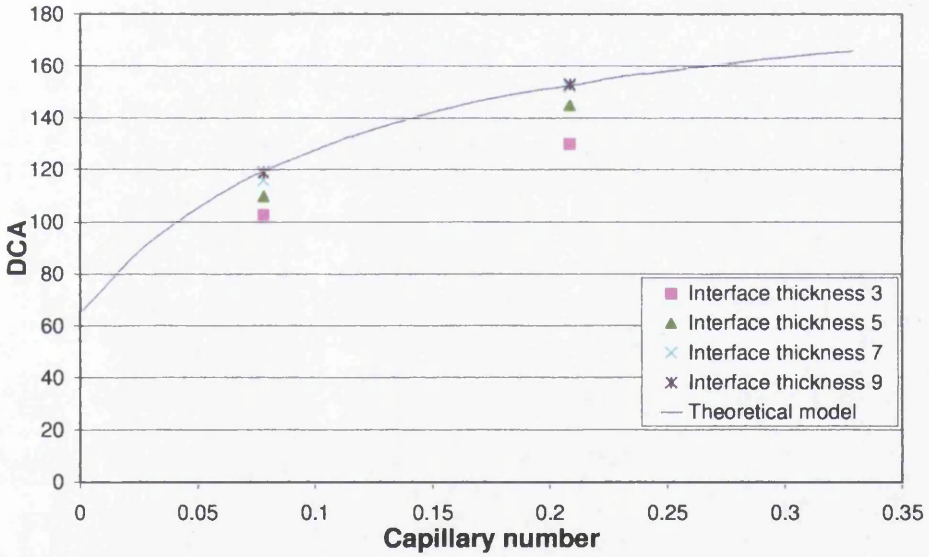

Figure 9-17: Dynamic contact angle with different interface width

Increasing the interface thickness improves the robustness and quality of the free-surface model. The interface of 7 and 9 elements reach comparable results, close to the theoretical reference. An interface of three elements differs consistently, underestimating the dynamic contact angles. These results indicate the importance of a thick interface for a correct and robust estimation of the curvature and contact angle. For this case, the adopted interface of 7 elements is a good compromise between the curvature accuracy and an excessive smearing of the free surface.

9.6 Ink splitting: Experiment vs. numerical modelling

An experiment and related numerical model were executed to verify the ability of the PHYSICA code to deal with extensional ink flows and to accurately simulate ink splitting. This comparison was carried out in order to validate the applicability of the code in the modelling of ink release from engraved cells.

The experimental trial consisted of an extensional test of a UV Curing Ink. The test was then simulated in PHYSICA adopting the experimentally measured rheological properties for the ink. The results of the experimental trial and of the CFD simulation were then compared.

9.6.1 The ink: characterisation

The ink used for the test was a cyan UV curing ink from XSYS©. This ink was primarily developed for flexographic applications. UV curing inks present several advantages that make them useful for experiments; they have a extremely low volatile content presenting therefore a stable volume in time and they retain their fluid state until exposed to high levels of UV light. Limits in their application come from the complexity of their flow behaviour due to their polymeric structure.

The rheological behaviour of the cyan UV ink was experimentally characterised in [52], using a cone and plate rheometer for the viscosity and the pendant-droplet method for the surface tension. Measures of the ink give a density value 1150 ± 10 Kg/m^3 and a surface tension of 0.0335 ± 0.004 N/m. Results of shear viscosity tests are presented in Figure 9-18

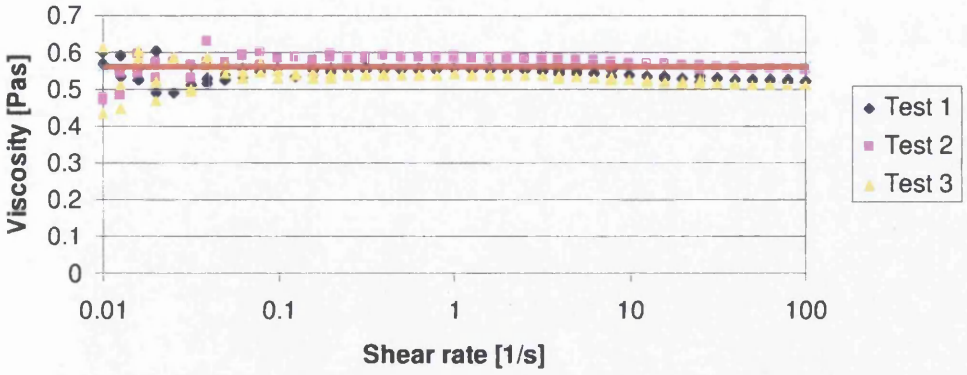

Figure 9-18: Shear viscosity tests

The ink shows a relatively low viscosity and an almost constant viscosity vs. shear rate. A weighted average of the viscosity table indicates a value of 0.56 Pa·s as a reference level. The low viscosity is similar to gravure inks and, most importantly, the almost constant viscosity indicates that this ink can be modelled following well-established Newtonian flow models.

9.6.2 Experimental trial

The experimental trial was carried out on a custom-built extensional rheometer developed at Swansea University.

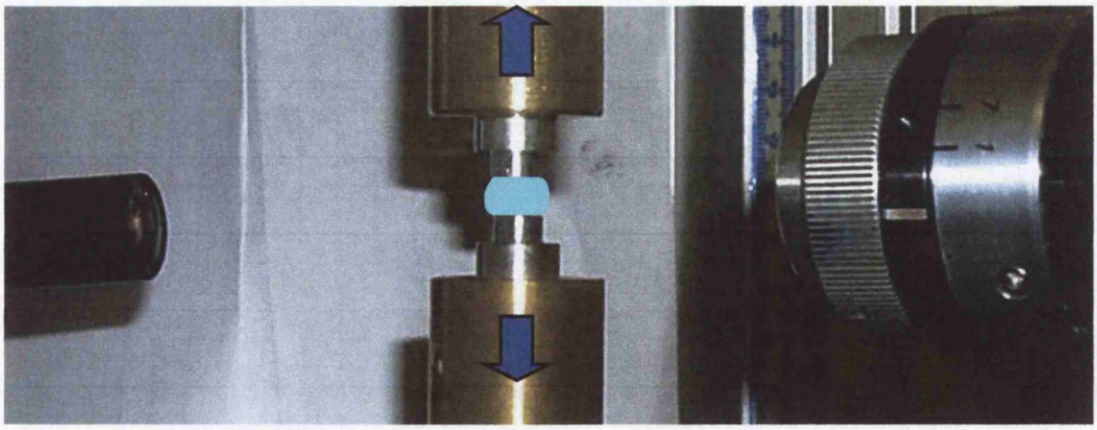

Figure 9-19: The apparatus used for experimental trial

The apparatus consists of two flat-based parallel cylindrical plates. Computer controlled motors allow the plates to be moved apart at different speeds and accelerations. A high-speed camera is placed to record the separation. The camera

was a Kodak EKTAPRO 4540mx Imager, which is able to record up to 4500 frame/s at full resolution (256x256 pixels).

During a typical test on the rheometer, fluid is placed between the two plates. The plates are then moved apart at a specific speed and distance while the camera monitors the evolution of the profile of the fluid. A range of experiments can be carried out by varying the base diameter and the speed profiles of the plates. During the experimental trial, the plates had a diameter of 7mm and a starting distance of 1.78 mm apart; the fluid was loaded between the two plates in sufficient quantity to obtain a stable cylindrical shape deposit with a diameter equal to the diameter of the of the plates, Figure 9-20.

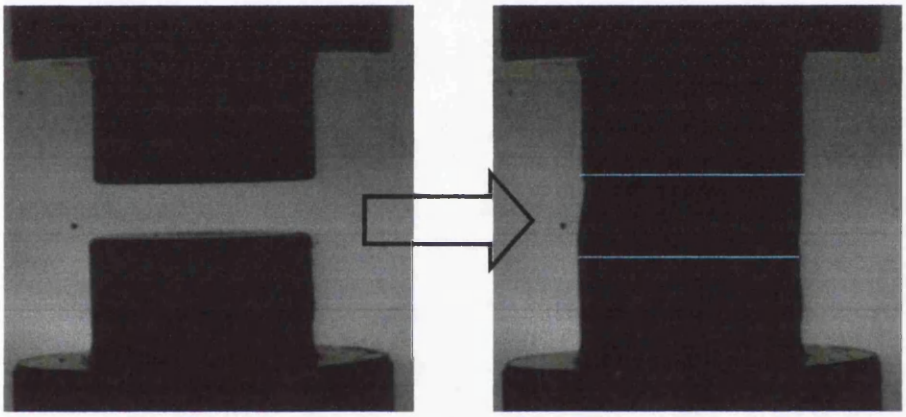

Figure 9-20: Fluid is loaded between the plate, starting profile of the fluid

The two plates were then moved apart at a constant linear speed of 2.5 mm/s while the high-speed camera recorded the progressive thinning and break-up of the fluid bridge. Analysis of the recorded images allowed an accurate confirmation of speed and of distances between the plates. In Figure 9-21 the evolution of the thinnest section of the liquid bridge is presented. Due to the action of gravity the thinnest section, that was originally at the mid-distance between the two plates, tends to move progressively upwards, since liquid tends to flow downwards.

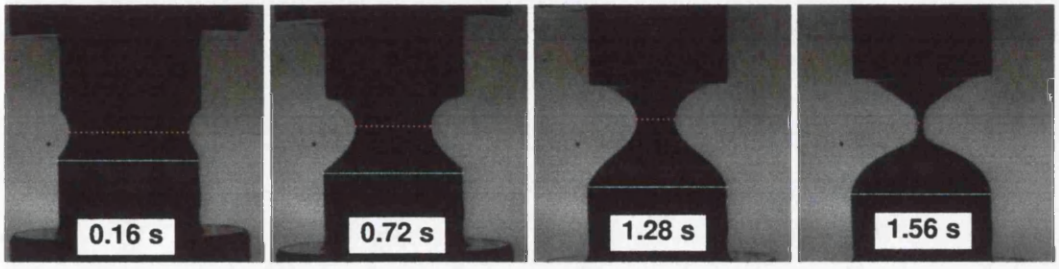

Figure 9-21: Evolution of the fluid profile; thinnest section highlighted with dotted line

Measurements of the diameter of the thinnest section of the liquid profile are plotted with respect to time up to the filament break-up in Figure 9-22. The edges of the filament can be visually measured on the images with an estimated error of ±2 pixels, equivalent to 0.1 mm.

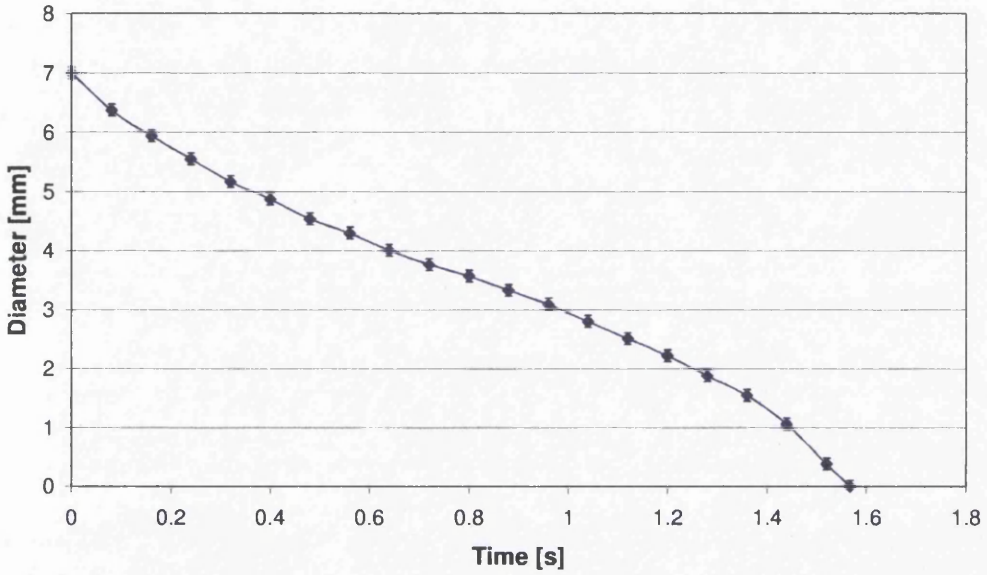

Figure 9-22: Evolution of the diameter at the thinnest section

Analysis of recorded images of small droplets of ink resting on the plates allowed an estimation of the static contact angle of the ink in contact with the plates, this was found to be approximately ~30°.

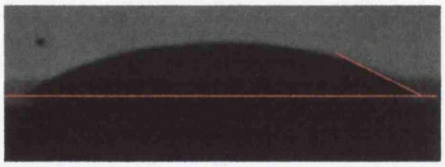

Figure 9-23: Contact angle of ink over the plate

9.6.3 CFD model of UV splitting experiment

A CFD model was developed using PHYSICA to simulate the experimental trial. The simulation was carried out on an axi-symmetric 3D geometry. PHYSICA does not include specific axi-symmetric flow algorithms, however this problem was solved by modelling the axi-symmetric geometry of interest as a 3-D mesh in a wedge shape,

obtaining a geometry from which by symmetry a cylinder is obtained. The mesh is composed of 1450 elements and a wedge angle of ± 5%

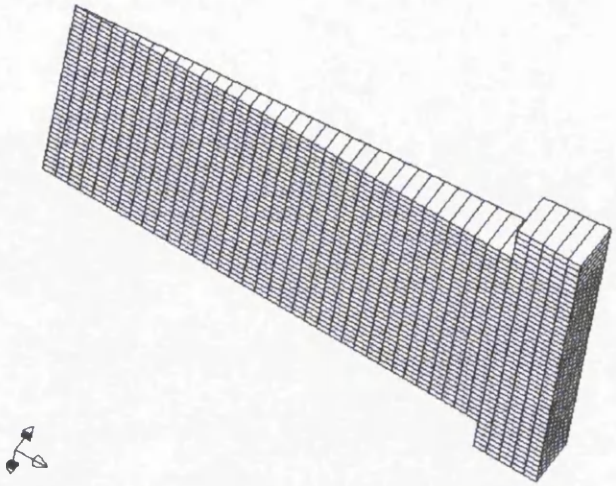

Figure 9-24: View of the 3-D axi-symmetric mesh

In Figure 9-25 a schematic of the flow domain in its starting condition is presented.

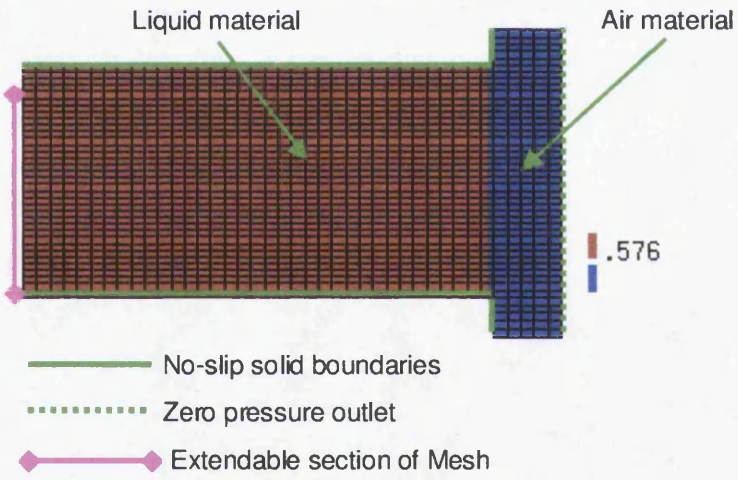

Figure 9-25: Diagram of the model

The solid boundaries in Figure 9-25 represent the plates in the experiments. The geometric dimensions employed in the design of the model were derived from the starting condition of the experimental trial: the two parallel solid boundaries are 3.5 mm long (half the diameter of the plates) and distance 1.78 mm apart. Material properties for the liquid section were assumed to be the experimentally determined properties described in section 9.6.1 and 9.6.2. The incompressible gas material

section was modelled assuming typical properties of air. Material properties for the model are summarised in Table 9-4.

Table 9-4: Material properties

Material properties	Value
Ink density	1150 Kg/m³
Ink dynamic viscosity	0.56 Pa·s
Air density	1 Kg/m³
Air dynamic viscosity	1.78E-5 Pa·s
Surface tension	0.0335 N/m
Static Contact angle	30°
Gravity	-9.81 m/s²

The interface width had a thickness of 7 elements; the density and the dynamic viscosity were set to sigmoidally vary within this interface between the ink and the air values. A section of the mesh was set to be extendable, Figure 9-25, while the section of mesh close to the top solid boundary were not modifiable in order to achieve high local resolution. The dynamic contact angle model verified in 9.5 was adopted.

The experimental trial was simulated extending the mesh at the constant linear speed of 2.5 mm/s and calculating the evolution of the free surface flow. In Figure 9-26, diagrams of the free surfaces flow evolution in time are plotted; the progression of the diameter of the thinnest section is charted in Figure 9-27. The edge of the filament was numerically defined from the analysis of the level set level variable Θ, see Section 8.7.2.

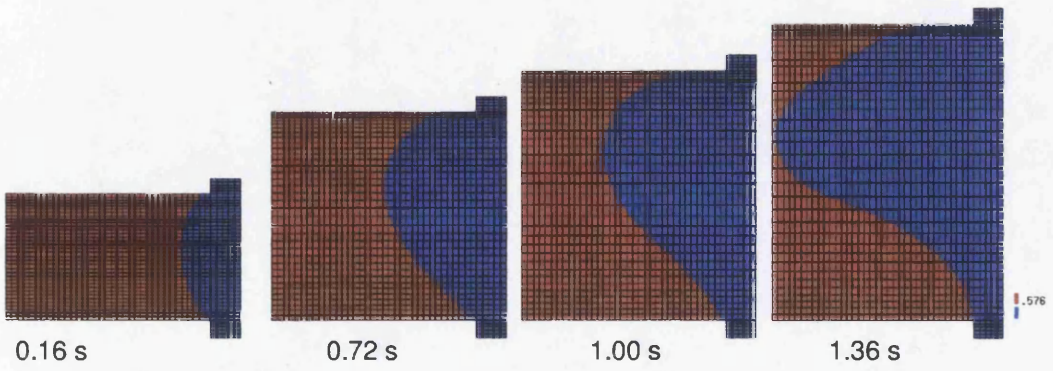

Figure 9-26: Representation of the evolution of the free-surface profile

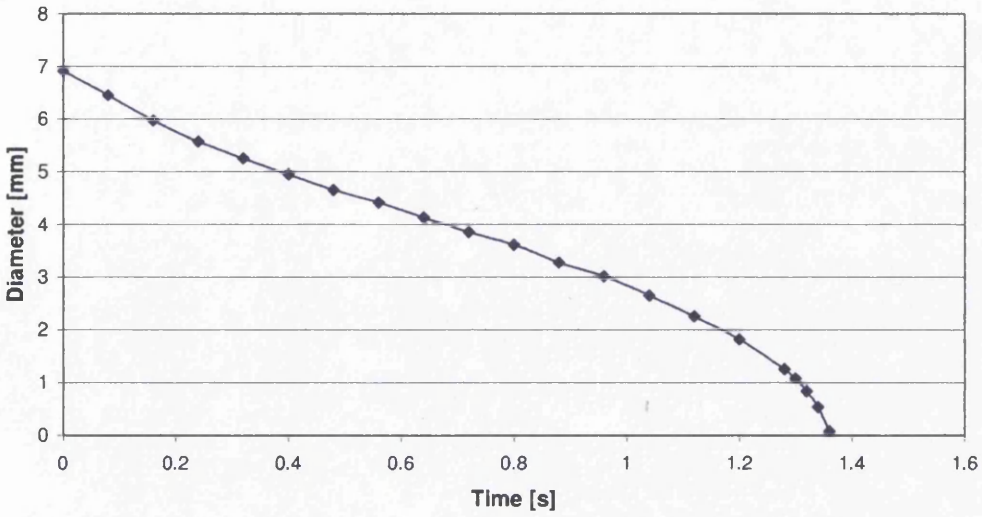

Figure 9-27: Evolution of the diameter of the thinnest section of the CFD model

The model was able to follow also the breaking up of the filament, Figure 9-28

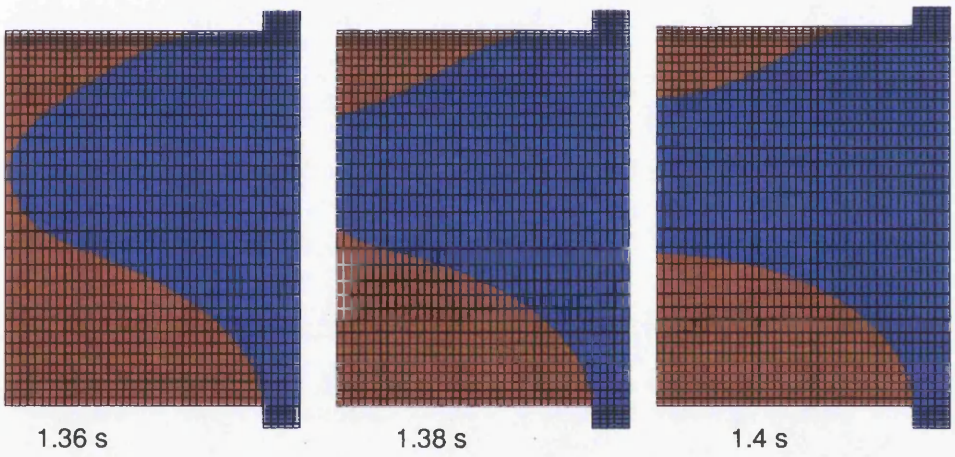

Figure 9-28: Breaking up of the filament

9.6.4 Comparison with Experimental trial

An analysis of the evolution of the thinnest section indicates a good agreement between the Newtonian model and the experimental trial (Figure 9-29).

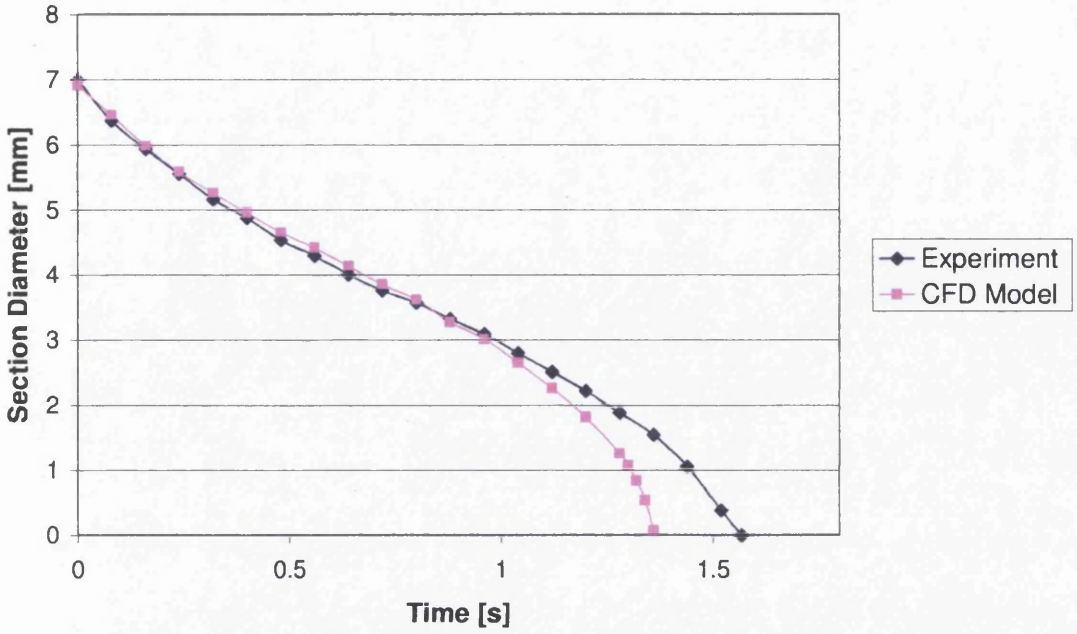

Figure 9-29: Experimental vs. CFD comparison of the area of the filament thinnest section up to break-up

In the early stage of the thinning there is an excellent match between the experimental trial and the numerical model. With the progressive thinning a divergence appears and the modelled filament reaches break-up before the experimental one. This difference could be attributed to the mesh resolution or more likely to the small differences between the real UV ink, with its complex composition, and the ideal Newtonian fluid of the model. In Figure 9-30, a picture of the experiment is overlapped with the model results.

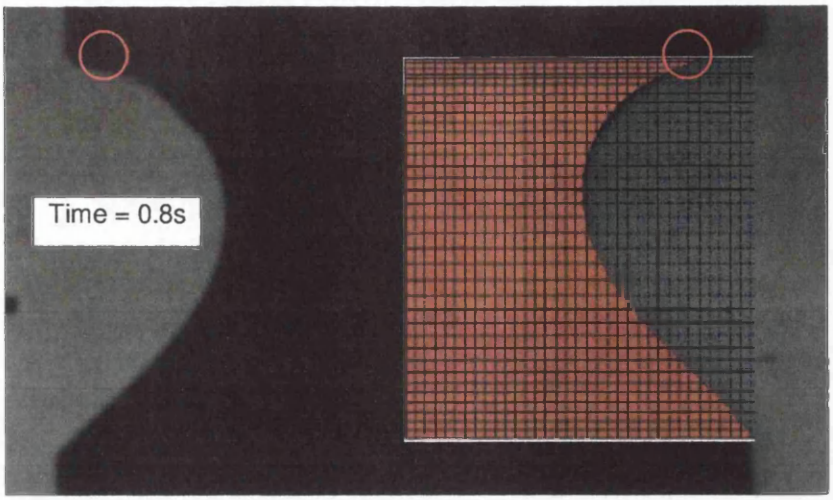

Figure 9-30: Overlapping of experimental picture with Model diagram; receded contact point highlighted

The similarity of the experimental and modelled behaviour demonstrates the accuracy achieved by the modelling. Futhermore, the point of contact of the fluid on the top plate follows the same evolution in both the experimental trial and the model, receding in both cases, further confirmation of the quality of the Dynamic Contact Angle model implemented in PHYSICA.

9.6.5 Effect of mesh resolution and interface width

The validity and robustness of the numerical model was verified by analysing different meshes and interface widths. A first comparison was made with a model created having the same characteristics but a thinner interface width of 3 elements A second comparison was made with a model characterised by a much finer mesh on the same geometry. The achieved results, Figure 9-31, gave a very close match, indicating the stability and validity of the model.

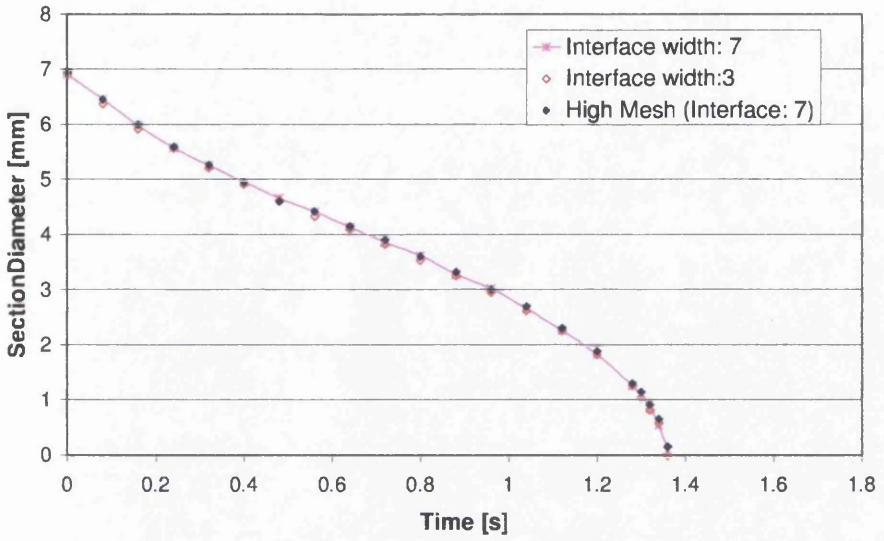

Figure 9-31: Comparison of CFD options

9.7 Modelling of liquid evacuation from a cavity

The process of ink release of an engraved cell can be described as a process of liquid evacuation from a cavity. In section 9.2, the dynamics of the liquid flow and the dynamic contact angle were identified as the two major influencing factors. In sections 9.5 and 9.6, PHYSICA has proven to correctly model these factors. It is therefore possible to develop a realistic CFD model of ink release from a cavity for a Newtonian fluid.

9.7.1 CFD Model Description

Three elements constitute the model: the engraved cell, the substrate and the fluid. The engraved cell was modelled as an axi-symmetric trapezoidal micro-cavity. The substrate surface is located over the engraved cavity and the liquid is placed between them overfilling the engraved cavity while being in contact with both (Figure 9-32). During the simulation, the substrate was pulled upwards, pulling the liquid and extracting it from the cavity. Air was free to flow at the extremities between the cavity and the substrate

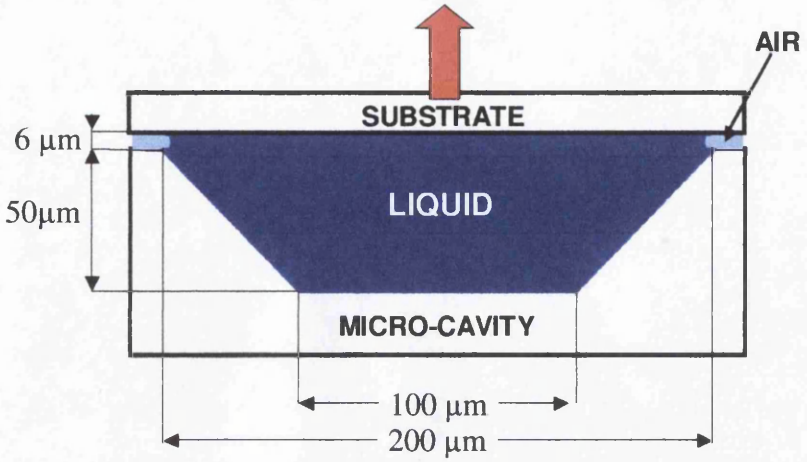

Figure 9-32: Drawing of the model with dimensions

The surfaces of the cavity and the substrate were modelled as solid boundaries with no-slip boundary conditions, each with its own specific contact angle of static equilibrium. The air was modelled as an incompressible fluid and allowed to flow freely through an outlet boundary, imposing the boundary condition of zero pressure.

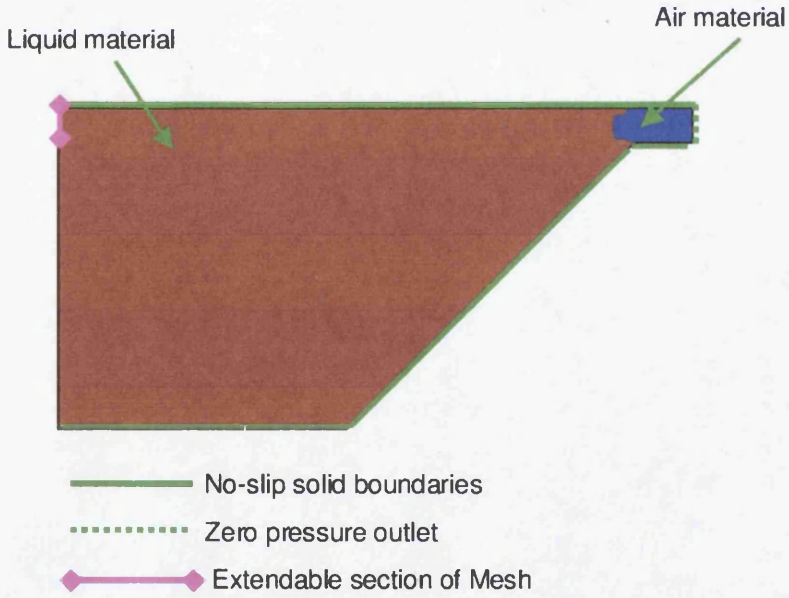

The mesh (Figure 9-33) was composed of 1677 quadrilateral elements with the section of mesh between the substrate and the top of the cavity having a high density of elements. During the modelling, this section of mesh extended simulating the separation of the substrate from the cavity.

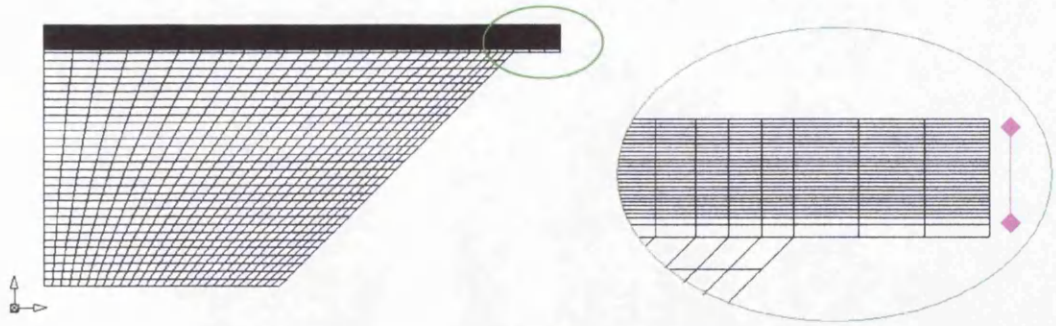

Figure 9-33: Mesh of the model with detail of the extendable section

The axi-symmetry is obtained by modelling the mesh in a 3-D wedge shape, Figure 9-34.

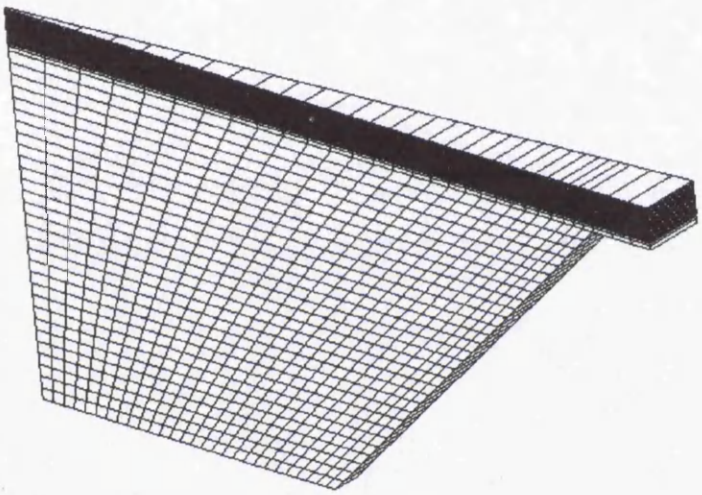

Figure 9-34: The mesh has a 3D wedge-shape for axisimmetry

9.7.2 Material properties

In order to model ink release as a liquid evacuation from a cavity, the selected liquid material has to correctly portray the ink rheology. As a first approach the UV ink presented in section 9.6 was selected as reference liquid. Material properties for the liquid section were assumed to be the experimentally determined properties described in section 9.6.1 and 9.6.2. The incompressible gas material section was modelled assuming typical properties of air. Material properties for the model are summarised in Table 9-5

Table 9-5: Material properties

Material properties	Value
Ink density	1150 Kg/m^3
Ink dynamic viscosity	0.56 Pa·s
Air density	1 Kg/m^3
Air dynamic viscosity	1.78E-5 Pa·s
Surface tension	0.0335 N/m
Static Contact angle on cavity	30°
Static Contact angle on flat substrate	20°
Gravity	0 m/s^2

The interface width had an imposed thickness of 7 elements; the density and the dynamic viscosity were set to vary sigmoidally within this interface width between the liquid material values and the air values. The static contact angle for the substrate boundary was selected to be lower than the one for the cavity solid boundary. The value of the contact angle on the cavity was derived from observation of liquid behaviour on an aluminium surface, 9.6.2.

Mass forces induced by gravity, possible centrifugal accelerations, magnetic forces were assumed to be negligible. The gravity effect was assumed as negligible due to the small scale of the phenomena investigated, which is dominated by surface tension and viscosity.

9.7.3 Evacuation speed

The evacuation speed represents the speed at which the extendable section of mesh was stretched. Assuming ideal non-deformable conditions, the outline of a perfect cylinder separation from a flat tangential substrate would assume a quadratic profile. However, PHYSICA has currently implemented only linear velocity and a set of linear speeds has to be selected that best represent the process. Assuming a cylinder of 20 cm diameter rotating at a standard production speed of 250 m/minute, the average linear separation speed in the first 200 microns is around 20 cm/s, Figure 9-35. This was assumed as reference speed for first modelling.

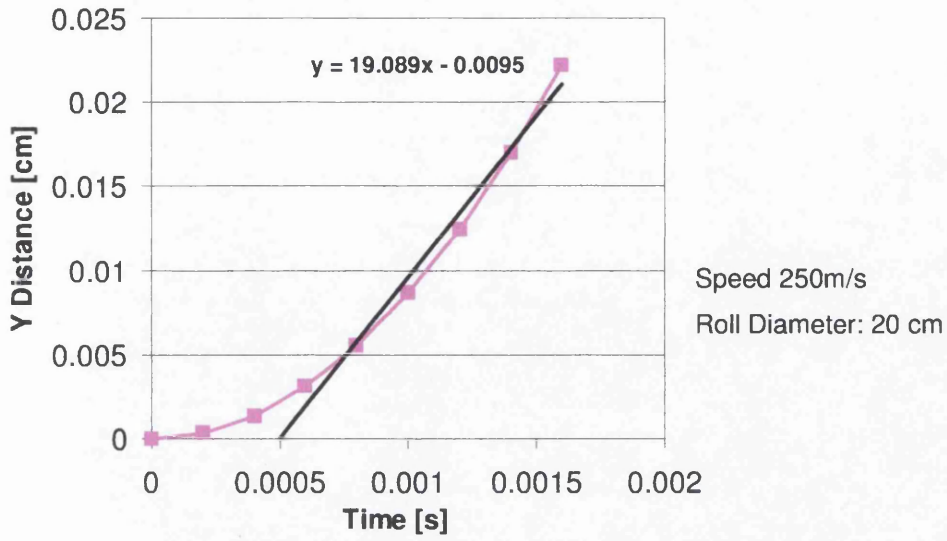

Figure 9-35: Separation speed of roll –substrate, linear approximation

9.7.4 Running of the Model

Having the material properties and the evacuation speed defined, the modelling was carried out simulating the first 0.012 seconds. On a high-end desktop computer each time step required around 10 seconds, the time step was of variable size and related to the maximum speed in the model. Total simulation time was around 2 hours.

9.7.5 Results of the modelling

The results of the modelling at different time steps is presented in Figure 9-36 and Figure 9-37.

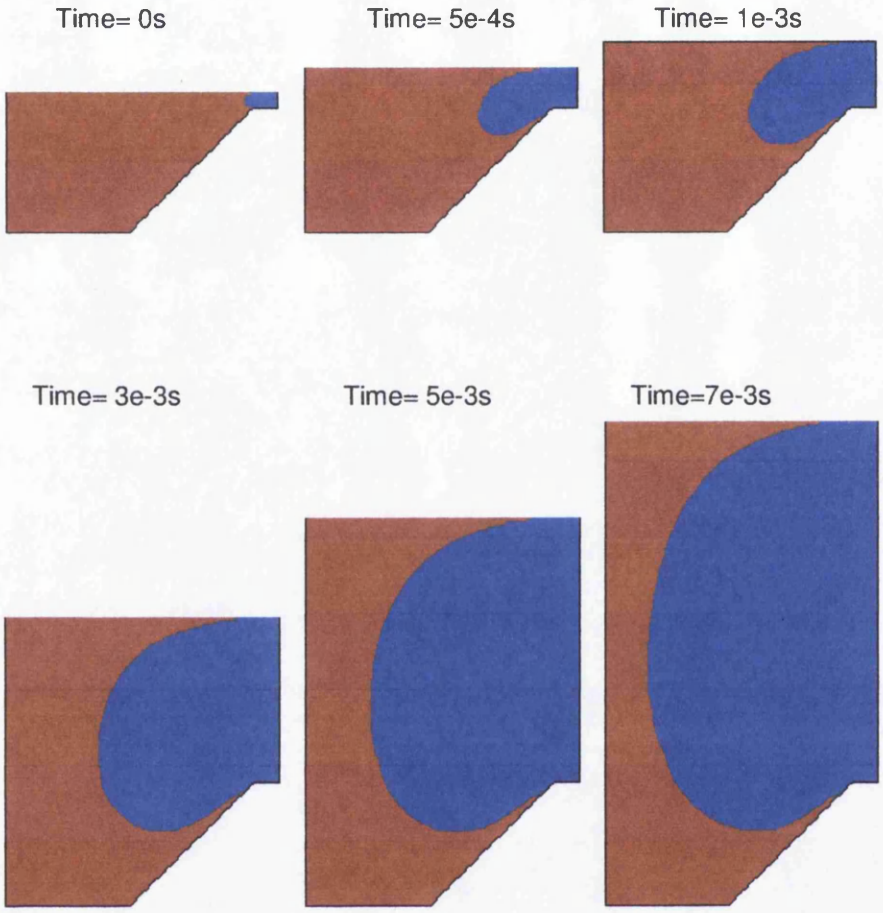

Figure 9-36: Progressive thinning of filament

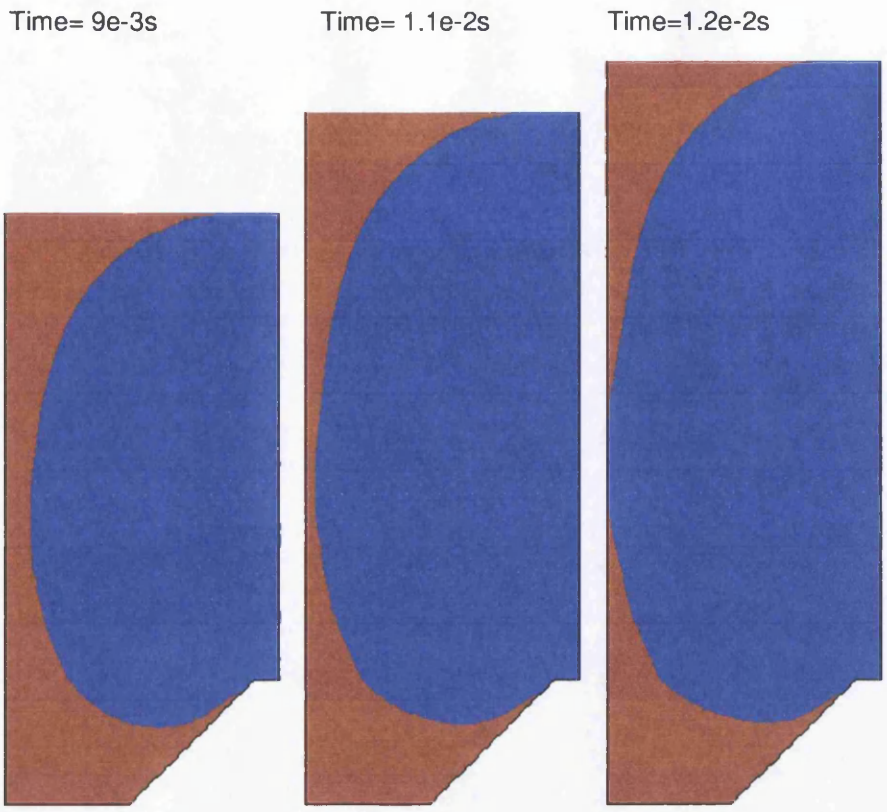

Figure 9-37: Thinning up to break-up

An evolution of the mesh is presented in Figure 9-38

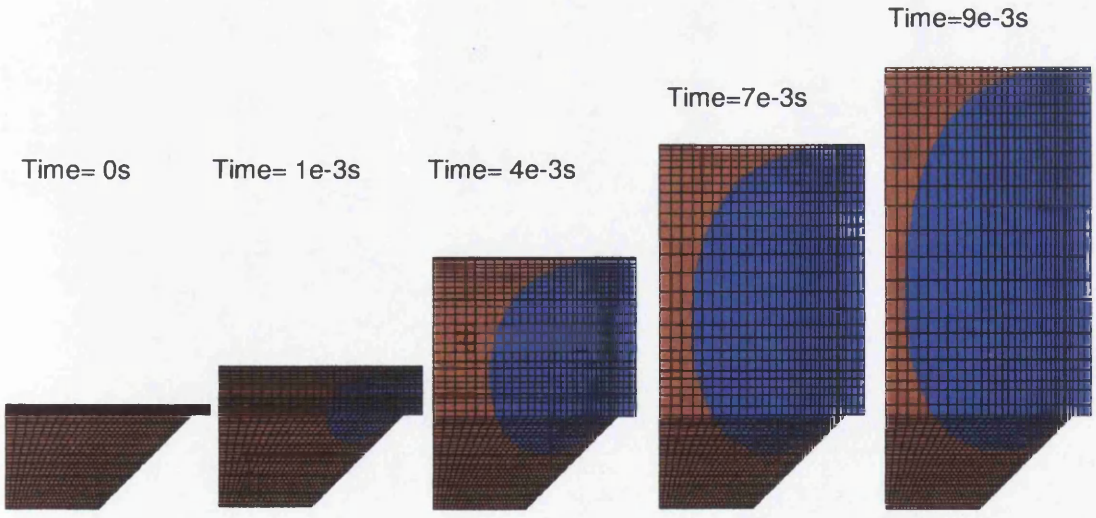

Figure 9-38: Evolution of the mesh

The filament extends significantly before break-up up to around 240 μm at 1.2e-2 seconds. In the analysis of the evolution of the diameter of the thinnest section of the filament, the first phase of the extension the diameter shows a rapid decrease, Figure 9-39. In the later stages the filament keeps thinning but at a much lower rate. The gradient of variation decreases during the extension, becoming more flat and causing the filament to stretch considerably. In the final stages (>1e-2 s) the gradient appears to slightly increase but at this point of the extension the mesh resolution around the thinnest section is limited inducing possible inaccuracies in the determined values.

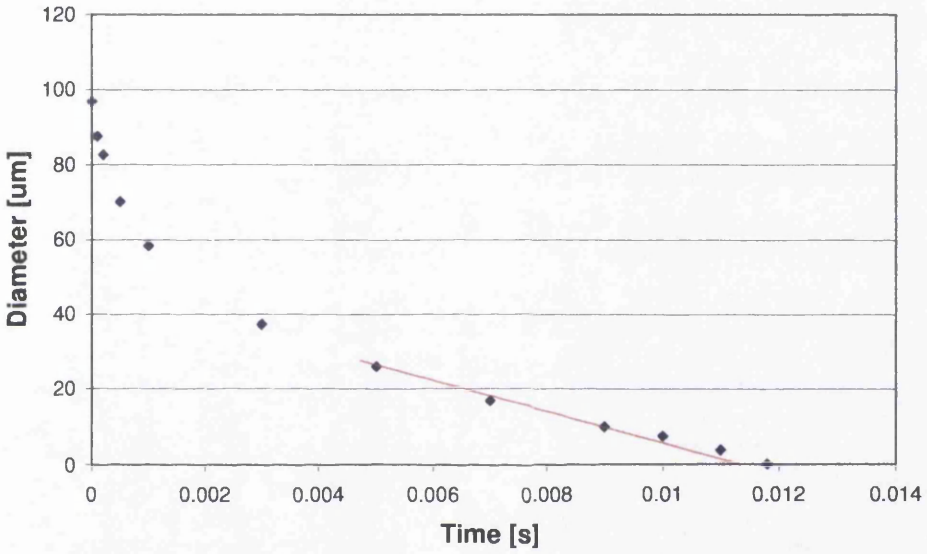

Figure 9-39: Diameter of the thinnest section

Comparing these results with the results obtained before in the two-flat-plate separation ink-splitting model, large differences in the behaviour were evident, Figure 9-40, even though the material properties were the same.

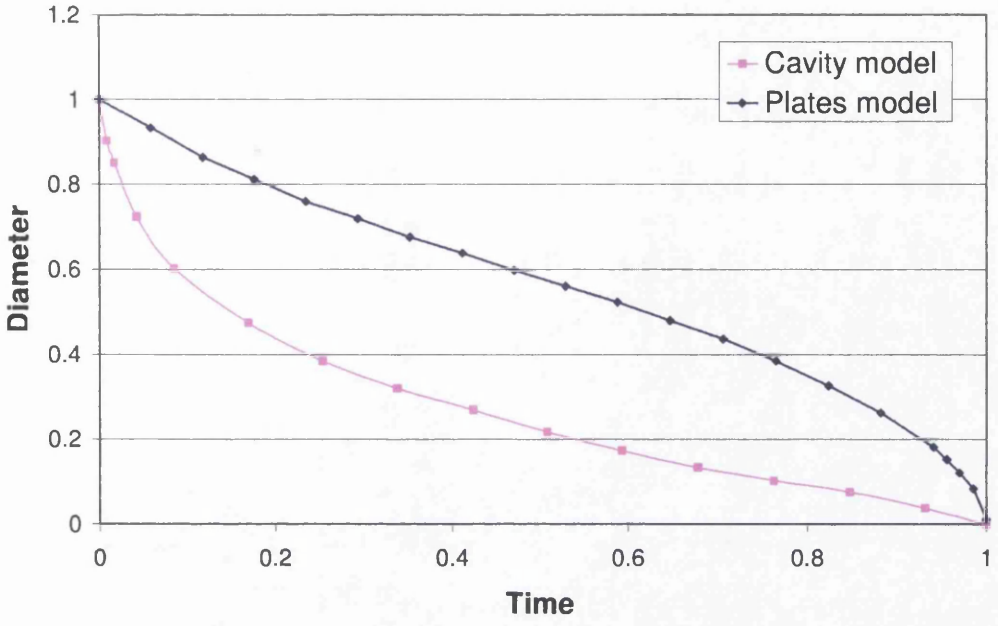

Figure 9-40: Comparison of the thinning in the two models, normalised values

In the early stages, this divergence can be attributed to the difference in shape between the two-flat-surface model and the cavity–flat surface model. In the last stages, the liquid is extensively stretching in the cavity model compared to the rapidly breaking up in the previous plate mode. This can be related to the differing effects of speed, viscosity and inertia, with the plate separation model having larger dimensions and lower speed.

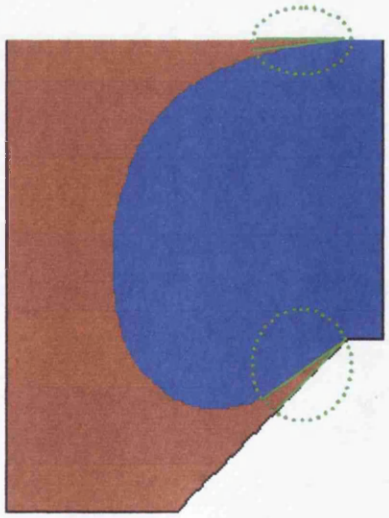

Figure 9-41: Dynamic Contact angles (time=4e-3)

In the cavity model, the contact point of the liquid with the solid substrate does not move, Figure 9-41; the liquid on the shoulders of the cavity and on the substrate acquires a layout in the early stage that then tends to remain constant. The angles are very small. On the shoulders of the cavity, it was estimated by digital analysis of the images to be of the order <10°, while on the flat surface <5°. The coarseness of the mesh limits the ability to accurately define the values of the angles, especially in the definition of low angles; the angles tend to a very low value. This agrees with the theory: due to the high speed of the process, the receding dynamic angle of equilibrium would tend to a very low value.

9.7.6 Effect of evacuation speed

The primary model was developed analysing an evacuation speed of 20 cm/s, a speed estimated to simulate conditions similar to a gravure press in production. Different speeds of evacuation could affect the evacuation flow of the cell; two models were therefore developed to analyse the effect of speed. A first model was characterised by a high speed of evacuation of 50 cm/s, approximating a high press speed (around 500 m/min with 20cm diameter roll); a second model was developed with an evacuation speed of 1 cm/s, equivalent to some extent to a proof-press (around 10 m/ with a 20 cm diameter roll).

The evolution of the cavity evacuation at 50 cm/s is presented in Figure 9-42

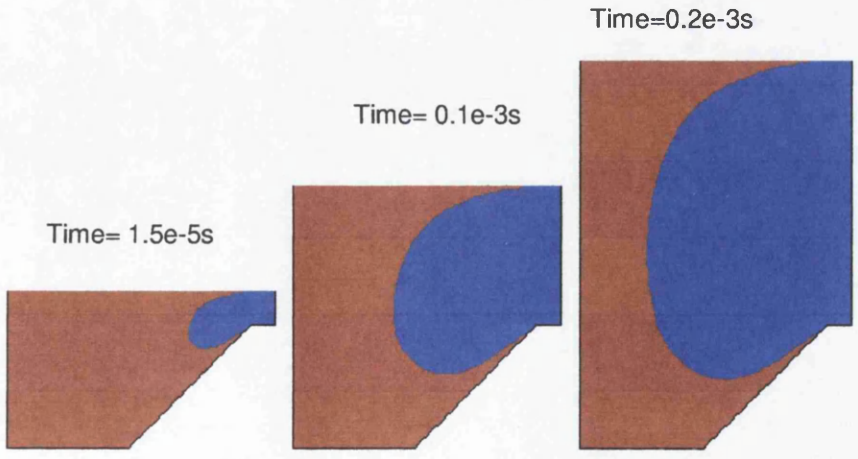

Figure 9-42: Progressive filament thinning at 50 cm/s

The break up of the filament happens at 0.62e-3 seconds, the bridge filament extends considerably before break-up, Figure 9-43.

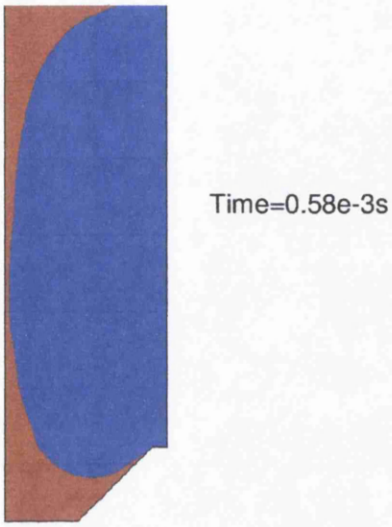

Figure 9-43: The filament extends considerably before break-up with 50 cm/s evacuation speed

The evolution of the cavity evacuation at 1 cm/s is presented in Figure 9-44. In this case the break up happened at 0.0112s, while the plates were still close together.

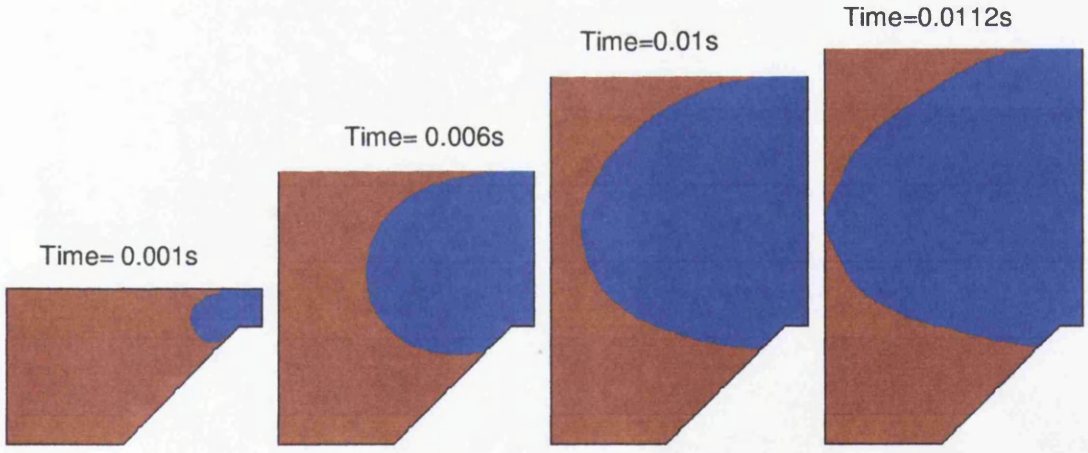

Figure 9-44: Filament thinning and break up at 1 cm/s

9.7.6.1 Thinning of filament

The evolution of the thinnest section of the filament is shown in figure Figure 9-45 and in Figure 9-46 as function of time and distance respectively.

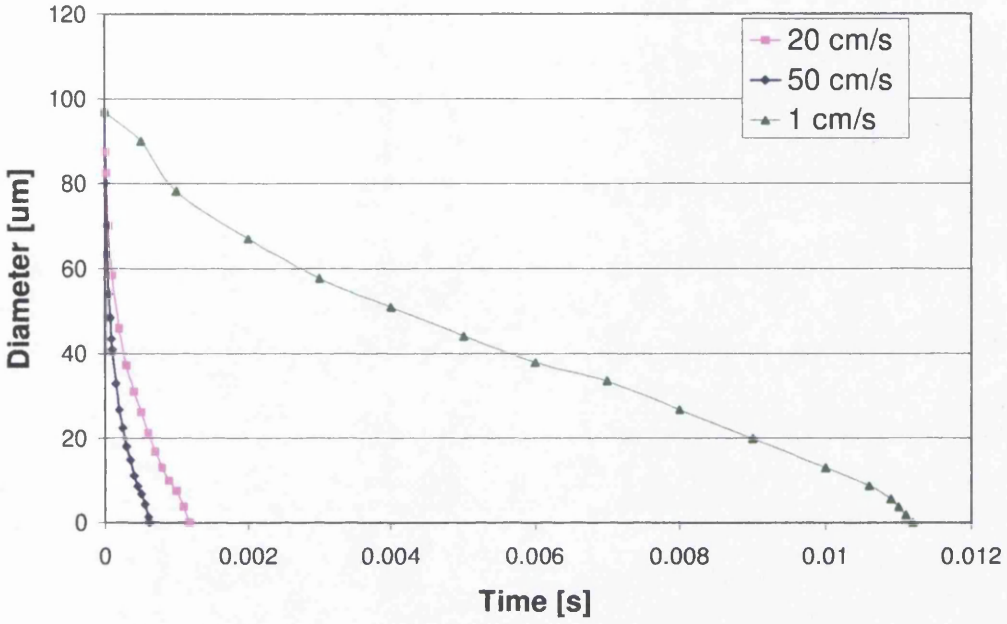

Figure 9-45: Evolution of the filament diameter at its thinnest section in time

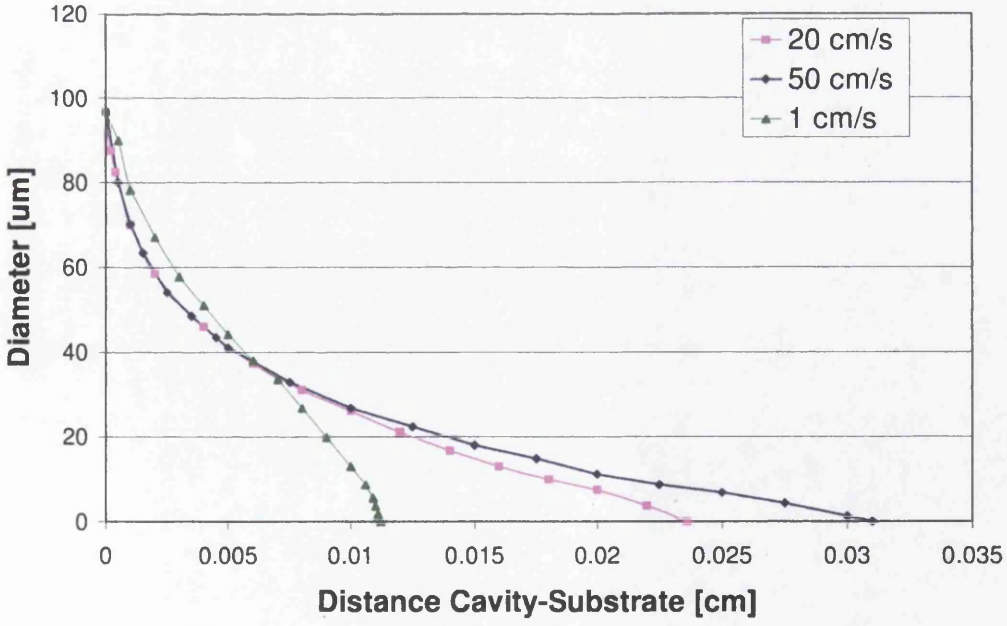

Figure 9-46: Evolution of the filament diameter at its thinnest section in distance

Different speeds induce a completely different behaviour in the evolution of the filament section. At 20cm/s and 50 cm/s, the filaments progress in a similar way in

the first stages of separation, the profiles of the filament diameter overlap well at corresponding distances between the plate and the cavity. In the later stages the filament at 50 cm/s keeps thinning at a lower rate than at 20 cm/s. This can be attributed to the surface tension component since it has less time to act. The 50 cm/s filament induces therefore the formation of the longest bridge between the cavity and the substrate. This phenomenon could help explain misting at higher speeds, generated at the nip of the rolls. A very long thin bridge of liquid would be likely to break up at different points, forming several micro-peripheral droplets that spread in the air forming a mist.

The low speed evacuation filamentation behaves in a completely different manner; this could be explained by the different order of magnitude of the speed of the phenomena. The filamentation at lower speed behaves similarly to the two-flat-plate separation ink-splitting model, which was also carried at low speed. This clearly indicates the influence of speed on the filamentation process.

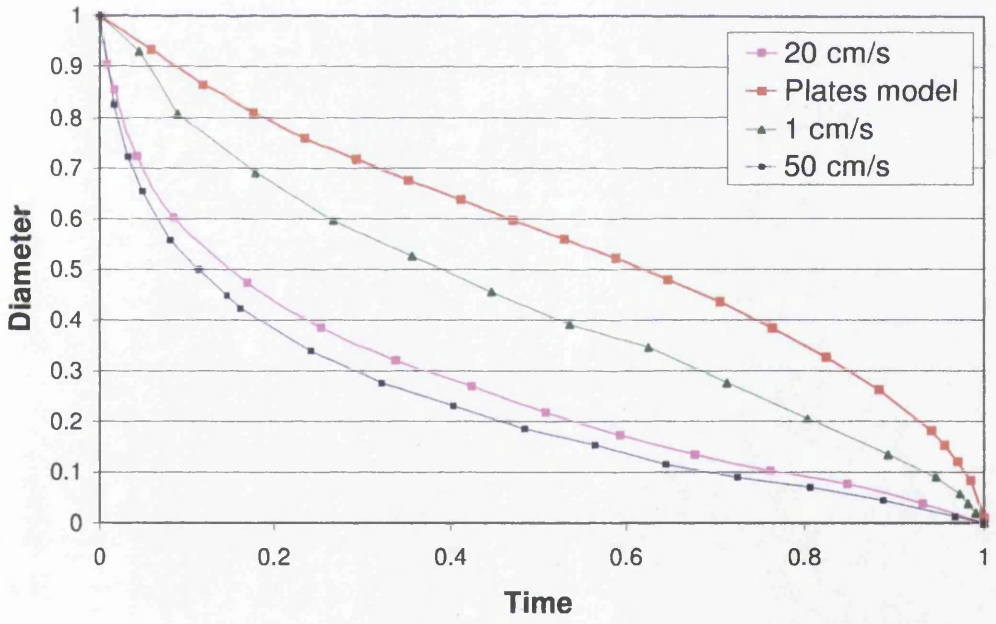

Figure 9-47: A-dimensional comparison of diameter profiles (normalised values)

9.7.6.2 Dynamic Contact Angle

The speed affects the Dynamic Contact Angle behaviour, Figure 9-49 and Figure 9-49. The contact angles on the cavity and on the substrate at 20 cm/s and at 50 cm/s are identical: the contact point does not move and the angle tends towards zero. At

low speed the contact angle behaves completely differently: the contact point with the cavity is not fixed in time: in the early stages it recedes markedly and then it partially advances back; the contact angle varies with the position of the contact point varying from 10 to 60 degrees. The contact point with the substrate is instead stable and the angle tends towards a low value.

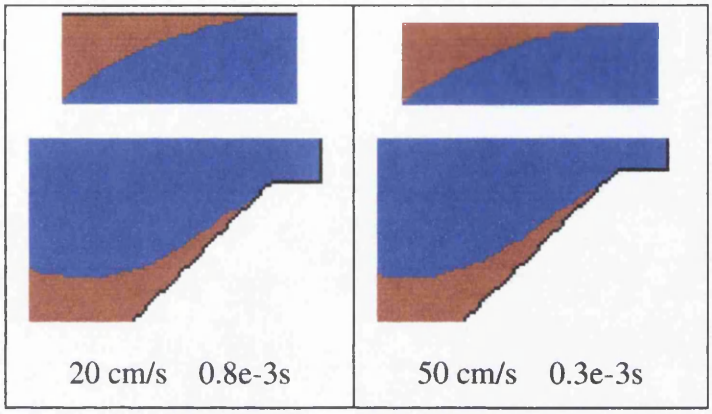

Figure 9-48: Stable contact angles at the cavity and substrate at medium-high speeds

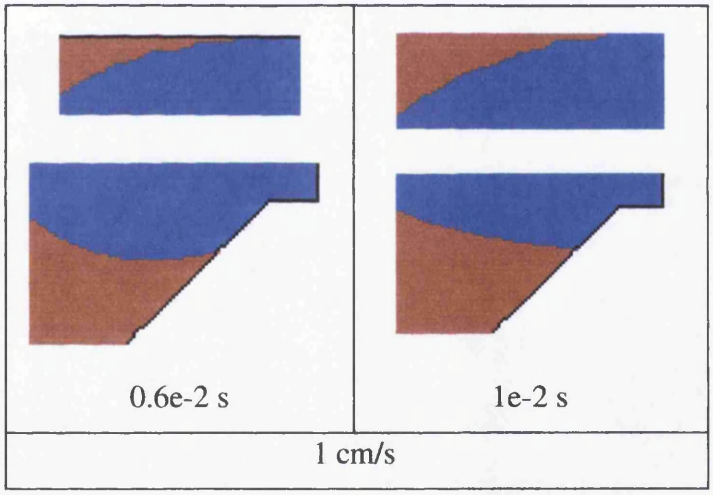

Figure 9-49: Variable contact angles at the cavity and substrate at low speed

These differences in the phenomena can be explained by the capillary numbers. The capillary numbers can be estimated as a function of the evacuation speed, Table 9-6

Table 9-6: Capillary numbers

Speed	Capillary Number
50 cm/s	8.5
20 cm/s	3.4
1 cm/s	0.17

As shown by theory and previously discussed in section 9.5, the dynamic contact angle of equilibrium is related to the capillary number. In the first two cases the capillary numbers are in the high range values leading to very low receding angles, tending to zero. At low speed, the capillary number enters in the mid-range values and the contact angle varies in accordance to the local velocity. The local velocity next to the substrate can be related to the evacuation speed, this can explain the relatively constant point of contact and angle. The more complex shape of the cavity determines a greater range of possible directions of the forces around the cavity contact point and the variation of the free surface profile. This determines a greater local range of possible velocities (positive and negative) of the contact point.

This great difference in the filament thinning and the variability of the contact angle could determine a higher variability in the flow at low speeds, especially when other elements such as roughness are taken into account; this could explain the differences and sometimes the inconsistencies that are obtained on the proof-press and when presses are run at low speeds.

The dynamic contact angle has a clear effect on the actual modelling of the evacuation. The small contact angles at higher speeds determine profiles that differ from previous modelling attempts presented in [48], where the contact angle was kept constant. In order to ignore the contact angle dynamic, in [48] the liquid evacuation was kept with an extremely low capillary number of 0.1, lower than the minor capillary value identified in Table 9-6 for gravure printing.

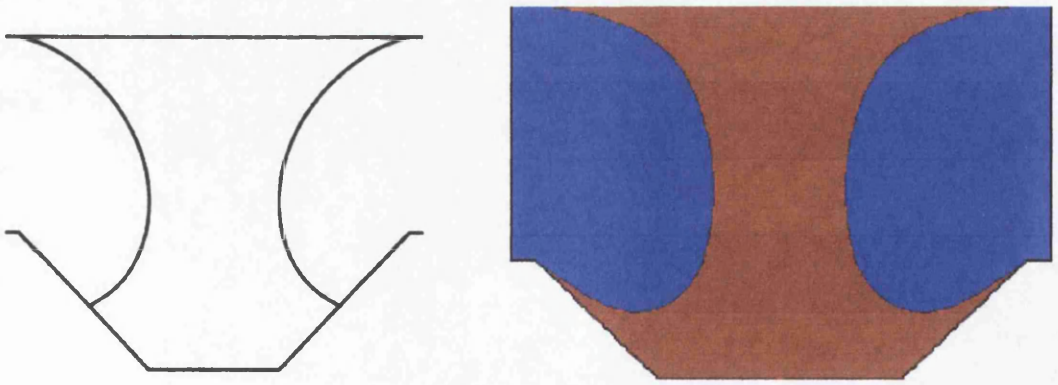

Figure 9-50: Schematic of Powell Savage model [48] vs. developed model

9.7.7 Conclusions

A model has been developed for the analysis of the liquid evacuation of a cavity. This model reproduces the action of ink release from an overfilled engraved cell onto the substrate. This is the first model that takes into account the dynamic contact angle in conjunction with flow properties such as inertia, viscosity and surface tension in the modelling of ink release. The model demonstrates the relevance of the evacuation speed on to the evolution of the profile. Speed affects the time of action for forces such as the surface tension, inducing longer filaments at higher speeds, which could lead to the formation of misting. Speed also influences the dynamic contact angle; at high speeds, the contact point remains fixed in the original position while the contact angle decreases tending to zero, lower speeds induce a receding oscillating contact point and angle between the liquid and the cavity. This could help explaining the inconsistencies in press quality sometimes observed at lower press speeds.

9.8 Closure

The aim of the chapter was the development of a model of ink release from an engraved cell. Critical points have been identified in the flow dynamics and in the dynamic of the contact angle. The code PHYSICA was selected as a CFD modelling tool, this code integrated with specially developed routines has proved to accurate model the flow and the dynamic contact angle. Comparison with experimental trials and literature data proves the capability and reliability of the developed code. The ability to correctly model the dynamic contact angle, a major issue in CFD, makes PHYSICA a useful CFD software.

On the base of these results, a CFD model of liquid evacuation from a cavity was successfully developed; this model represented the ink release from an engraved cell on to a non-absorbent substrate. This is the first model in literature taking into consideration the dynamic contact angle in the analysis of ink release from cavity, a factor that has been shown to greatly influence the free-surface profile. The developed model has proven the importance of evacuation speed not only on the extensional flow (with higher speeds increasing the filament length and the risk of misting) but also on the dynamics of the contact angles (with lower speeds decreasing the stability of the contact angles and therefore increasing inconsistency in ink release).

10 Conclusions & further work

10.1 Introduction

A comprehensive investigation into the rotogravure printing process has been undertaken. Experimental trials were analysed, leading to the development of models able to predict the ink release in the gravure printing process. Two different, but complementary, modelling approaches have been investigated: Artificial Neural Networks and Computational Fluid Dynamics.

In addition to the analysis of the different modelling approaches, to facilitate the extensive collection of data required for the development of neural networks, new software has been developed for automatic and accurate geometric characterisation of the engraved cells from their interferometric profiles. The main conclusions are detailed below.

10.2 Artificial Neural Networks

- Artificial neural networks have shown to be a feasible modelling technique for the gravure printing process. This work was the first investigation of Neural Networks for the modelling of the gravure process. Adopting a Multi-layer Perceptron layout, neural networks were able to accurately correlate experimental data developing models that accurately predict the effect of cell geometry on ink release.

  A model was developed to predict the values of colour density as a function of the geometry of the engraved cell, identified by its stylus angle, screen ruling, screen angle and engraved volume, Figure 10-1. The model was able to predict colour density within the defined eye tolerance level (<0.03).

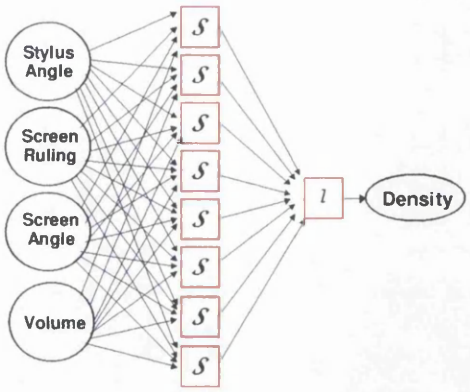

Figure 10-1: ANN model of ink release

- An alternative model, correlating the open area, screen ruling, screen angle and stylus angle to colour density, was developed that could be easily integrated with the current manufacturing process, greatly improving the colour correction process. Its practicality is based on the use of easily measurable geometric parameters, which could be measured with common optical devises.

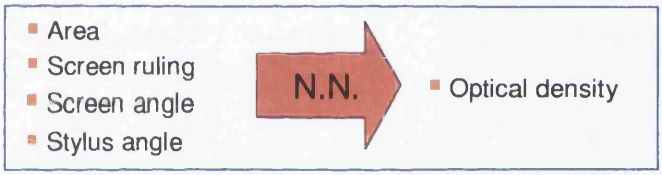

Figure 10-2: Alternative model of ink release for manufacturing applications

More extensive models were also explored to predict the effect of cell geometry in combination with the cell location or ink viscosity. Engraved cells were found to release more, when preceded by larger cells.

- Comparisons with non-linear and linear polynomial models showed that Neural Networks achieve better performances using the same data. Neural Network models do not present any difficulty in their application, once the models have been developed: they work as a straightforward equation estimating the output as a function of the inputs, being as easy to use as simpler models.

- The development of N.N. presents a higher degree of complexity than standard polynomial models in terms of employed algorithms and the range of options for the developer. Among different configurations, Neural Networks based on statistical Bayesian techniques are particularly interesting since they

tend to enhance the regularisation, the smoothness, of the obtained model, strongly reducing any risk of over-fitting noisy data. Their smoothness tends to decrease the number of experimental data required for the modelling and they allow an estimation of the local error of the estimate.

10.3 Software for the cell geometric characterisation

A unique software has been developed for the automatic geometric characterisation of engraved cells from interferometric profiles. This enables a rapid gathering of experimental input data for the development of the neural network. The software is accurate, achieving better than 1% accuracy in terms of cell volume. It is also objective, independent of the operator, and able to deal with a large range of cells, independently from the engraving technique and quality of engraving. It calculates a large number of geometric parameters, which completely identify the cell, such as volume, width, length, depth, top area, stylus angles, offset and the cell edge angles.

In addition to its application in data gathering for modelling, the software can be used in industry on gravure cylinders and anilox rolls for characterising engraving for quality control purposes.

10.4 Computational fluid dynamic modelling

- A Computational Fluid Dynamic model of the evacuation of a Newtonian liquid from an axi-symmetric cavity was successfully developed; this model simulates the process of ink release from an engraved cell on to a non-absorbent substrate, Figure 10-4. It shows the progressive splitting of the ink and retention of ink in the cell. This is a unique model, being the first that takes into consideration the dynamic contact angle in the analysis of ink release from a cavity.

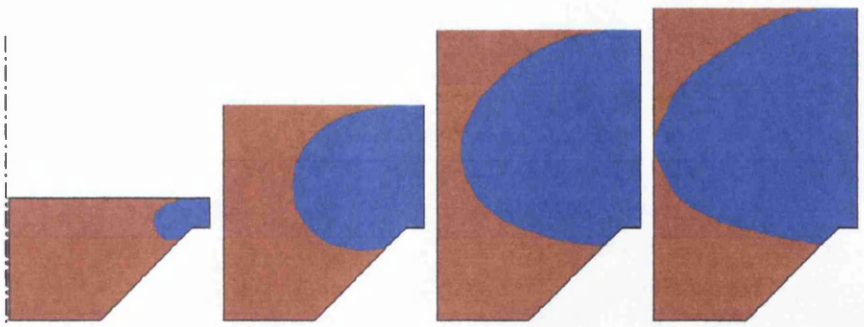

Figure 10-3:Axi-symmetric model of ink (in red, air in blue) release from engraved cell

- The model was developed using the Level-Set Finite volume method, encoded within PHYSICA, a Swansea University based computational software. Specific requirements for the modelling of ink release lead to the personal development and integration into the code of new sets of routines, for a controlled stretching of the mesh. These new additions to the code were not only useful for the investigated modelling but greatly expanded PHYSICA capabilities to deal with any fluid flow in the presence of moving solid boundaries.

- The reliability of the modelling method was verified by comparing models with experimental and literature data. The method has shown to be able to accurately model the dynamic contact angle in comparison with literature data and to correctly simulate a specifically designed experiment of the UV ink splitting between two parallel plates. The ability to correctly model the dynamic contact angle is of particularly interest, being that the modelling of the dynamic angle is a current argument of significant scientific discussions.

- The model has demonstrated the importance of the dynamics of the contact angle together with the flow extensional dynamic during the process of ink release from the engraved cells. Analysis of the effect of evacuation speed (i.e. speed of the press) indicates that the extensional flow of the ink is strongly influenced by the speed: higher speeds induce longer filaments between the cell and the substrate, increasing the risk of formation of peripheral droplets and therefore misting. Importantly, the dynamics of the contact angle are also affected by speed: lower evacuation speeds decrease the stability of the contact angles and can therefore increase inconsistency in ink release.

10.5 Further work & suggestions

10.5.1 Neural networks

The developed models have been shown to be capable of accurately predicting the effect of cell geometry on the release of ink. New models could be developed expanding the range of analysed factors for a better evaluation of the ink release; this would require new experimental trials in order to expand the bank of reference data.

Expanding the model would require more accurate characterisation of the new factors. For example, in the case of a more accurate analysis of the effect of viscosity variation by solvent addition, a model could be developed by integrating the ink viscosity value with its pigment content. Additionally, it would be interesting to integrate the optical densities with the actual physical measurements of the quantity of transferred ink.

For future tests, it is suggested that a standard test image is developed integrating different graduated patches scattered throughout the web in order to analyse also the effect of cell location and impression pressure.

10.5.2 Computational Fluid Dynamics modelling

The development of the presented CFD model opens a new range of possible investigations. The effect of viscosity and surface tension could be explored and the integration of more complex fluid models would allow the study of non-Newtonian inks. The effect of cell shape could be also investigated. The range of geometric shapes is currently limited by the distortion of the quadrilateral elements; in the current coding of PHYSICA excessively deformed elements induce instability in the calculations. A possible solution would be the adoption of more stable solution techniques; this would also allow the analysis of more complex models, such as under-filled cavity meshes. Another solution would be switching to triangular elements. Triangular elements have shown difficulties in the correct identification of the contact angle, Figure 10-4. An accurate study needs therefore to be carried out identifying the necessary interface thickness.

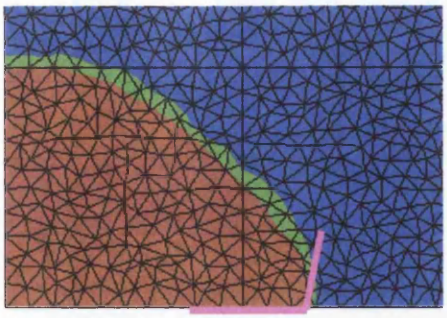

Figure 10-4: Error with triangular elements: the contact angle should be 60°

Ultimately controlled re-meshing techniques should be developed; these would allow the analysis of other phases of the gravure process such as the doctor blade action, the filling action at the ink bath or the squeezing of ink between two rolls. All these phenomena are characterised by the parallel sliding of surfaces, Figure 10-5; elements between the surfaces would be subject to great deformations hence the need to re-mesh.

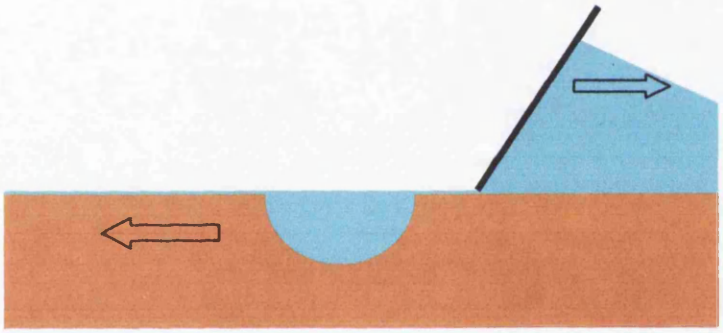

Figure 10-5: Schematic for a Doctor blade model

References

[1] *Gravure: process and technology*, Gravure Association of America, 1992

[2] H. Kipphan, *Handbook of print media*, Heidelberg, 2001

[3] *Global market share of printing processes 2005*, PrintWeek, 19 Jan 2006

[4] *ERA* European Rotogravure Association, http://www.era.eu.org/ , 2005

[5] M.F.J. Bohan, A.M.Clist, T.C. Claypole, D.T. Gethin, *Characterisation of gravure Cylinders* TAGA, 1-12, 2001

[6] J.B.T.M. Roerdink and A. Meijster, *"The Watershed Trasform: Definitions, Algorithms and Parallelization Strategies"*, Fundamenta Informaticae, 41, 187-228,2001

[7] A. Clist -*"Ink transfer in image and non image areas in the rotogravure process"*, Phd thesis, Swansea University, 2003

[8] J. Cherry, S. Hamblyn, M. F. Bohan, T. C. Claypole, and D. T. Gethin, *Measurement of the Cell Volume of Anilox Rolls* - TAGA 2005

[9] J. Cherry, D. Deganello, D. Beynon, *"Measurement of IGT Anilox Rolls"*, WCPC report, 2006

[10] D. James, *Evaluation of process parameters in rotogravure printing*, M.Sc., Swansea University 2003

[11] M.F.J. Bohan, T.C. Claypole, D.T Gethin , *The effects of process parameters on production quality of rotogravure printing* , Proc. Istn Mech Engrs, 214:B, 2000

[12] M.F.J. Bohan, T.C.Claypole, D.T Gethin ,*An investigation into ink transfer in Rotogravure Printing* , TAGA Proc., 1998

[13] *NIST/SEMATECH e-Handbook of Statistical Methods*, National Institute of Standards and Technology, 2006, http://www.itl.nist.gov/div898/handbook/

[14] L.L. Lapin, *Probability and statistics for modern engineering*, Waveland Press, 1998

[15] C.M. Bishop, *Neural Networks for Pattern Recognition*, Oxford University Press, 1995

[16] StatSoft Inc., *Electronic Statistics Textbook*, Tulsa, 2004

[17] L. Tarassenko., *A Guide to Neural Computing Applications*, NCAF, 1998

[18] H. Demuth, M. Beale, *Neural Network Toolbox User's guide*, Mathworks, 2005

[19] I.T. Nabney, *NETLAB Algorithms for Pattern recognition*, Springer, 2003

[20] R. Holub, *The future of parallel, analog and neural computing architectures in the graphic art*, TAGA Proceedings, 1988

[21] S. Al-Mutawa, Y.B. Moon, *A connectionist Expert system approach for representing a press operator's machine-specific knowledge*, TAGA proceedings, 1994

[22] A. Verikas, K. Malmqvist, L. Malmqvist, L. Bergman, *A new method for colour measurements in graphic arts*, Color Research & Application, 24, 1999

[23] L.Ding, L., P.E.Bamforth, M.R. Jackson and R. Parkin, *Fuzzy Neural Network Control for Gravure Printing*, Proceedings Control 2004, University of Bath, 6-9th September 2004

[24] J.H.Ferziger M. Peric, *Computational methods for fluid dynamics*, 3rd edition, Editor Springer, 2002

[25] C.W. Hirt, B.D. Nichols, *Volume of fluid /VOF/ method for the dynamics of free boundaries*, Journal of Computational Physics, vol. 39, p. 201-225, 1981

[26] J.J Monaghan, *Simulating free surface flow with SPH*, Journal of computational physics, 110, 309-406, 1994

[27] T. Belytschko & Others *Meshless methods: An overview and recent developments*, Comput. Methods Appl. Mech. Engrg., 139 ,3-47, 1996

[28] S. Koshizuka, Y. Oka, *Moving particle semi-implicit Method for fragmentation of Incompressible fluid*, Nuclear Science of engineering, 123 , 421-434, 1996

[29] B. Ataie-Ashtiani , Leila Farhad, *A stable moving-particle semi-implicit method for free surface flows*, Fluid Dynamics Research , 38 , 241–256, 2006

[30] M. P. Allen, D. J. Tildesley, *Computer simulation of liquids* , Oxford University Press, 1989

[31] J. De Conick, *Terraced Spreading of Chain Molecules via Molecular Dynamics*, Physical Review Letters, 74, 928-931, 1995

[32] M.H. Adã & others, *Droplet spreading on heterogeneous substrates using molecular dynamics*, Physical Review E, 59, 746-750, 1999

[33] J.W.M. Bush , *Surface Tension: Lecture notes*, MIT, 2007

[34] N. Cheremisinoff, R. Gupta, *Handbook of Fluids in motion* , ANN Arbor Science

[35] D. Wheeler, *Computational Modelling of Surface Tension Phenomena In Metals Processing*, PhD thesis, University of Greenwich, 2000

[36] *Theory Guide for PHYSICA: a framework for multi-physics Computational Fluid Dynamics and Computational Solid Mechanics* , Multi-Physics Software Ltd., 2005

[37] S. van Mourik, *Numerical modelling of the dynamic contact angle*, Master Thesis, University of Groningen, 2002

[38] S. van Mourik, A.E.P. Veldman and M.E. Dreyer, *Simulation of Capillary Flow with a Dynamic Contact Angle*, Microgravity sci. technol. XVII-3 , 2005

[39] T.D. Blake and S.D.Shikhmurzaev, *Dynamic Wetting by Liquids of Different Viscosity* Journal of Colloid and Interface Science, 253, 196–202 , 2002

[40] P.G. De Genes, *Wetting: static and dynamics*, Review of Modern Physics, 57, 1985

[41] L.W. Schwartz, P. Moussalli, P. Campbell and R. R. Eley, *Numerical modeling of liquid withdrawal from gravure cavities in coating operations*. Chem. Eng. Res.& Design Trans. Inst. Chem. Engrs. 76, 1998

[42] L.W. Schwartz, *Numerical modeling of liquid withdrawal from gravure cavities in coating operations; the effect of cell pattern*, Journal of engineering mathematics, 42, 2002

[43] C.A. Powell MD Savage, P.H Gaskell, *Modelling the meniscus evacuation problem in direct gravure coating, Trans IchemE, 78-A* , 2000

[44] Xiuyan Yin, Satish Kumar, *Flow Visualization Studies in Scaled-Up Gravure Grooves and Cells, TAGA*, 2003

[45] Xiuyan Yin, Satish Kumar, *Lubrication flow between a cavity and a flexible wall*, Physics of fluids, 17, 2005

[46] Xiuyan Yin, Satish Kumar, *Two-dimensional simulations of flow near a cavity and a flexible solid boundary*, Physics of fluids, 17, 2005

[47] P. Wapperom, M.F. Webster, *Simulation for viscoelastic flow by a finite volume/ element method*, Comput. Methods Appl. Mech. Engrg. 180,1999

[48] C.A.Powell, MD Savage, *Computational simulation of the printing of Newtonian liquid from a trapezoidal cavity,* International Journal of Numerical Methods for Heat & Fluid Flow, 12:4, 338-355, 2004.

[49] R.L. Hoffman, *Study of the advancing interface. Pt. 1. Interface shape in liquid-gas systems*, J. Colloid Interface Sci , 50:2, 1975

[50] T. D. Blake and Y. D. Shikhmurzaev, *Dynamic Wetting by Liquids of Different Viscosity*, Journal of Colloid and Interface Science, 253, 196–202, 2002

[51] G.R. Davies, *An investigation of the contact angle between Rotogravure substrates and process inks*, Swansea University, 2000

[52] H. Chatoux, *Relation ink/anilox/substrate flexography report*, WCPC Swansea University, EFPG Grenoble, 2007

[53] K.Nomura, S.Koshizuka, et al., *Numerical analysis of droplet break up behaviour using Particle method*, Journal of Nuclear Science and Technology, 38:12, 1057-1064, 2001

[54] T. D. Blake, *The physics of moving wetting lines*, Journal of Colloid and Interface Science 299, 1-13, 2006

Appendix A: Data collection

The list of experimentally collected data from press trial described in chapter 5 is here presented:

Location		Engraving parameters			Geometric Characterisation					Colour Density		
Sector	Line	Screen angle	Stylus angle	Ruling	Open area [%]	Volume [ml/cm^2]	Width [um]	Depth [um]	Length [um]	Viscosity [Zahn2] 24s	20s	17s
A	a	45	130	60	7.49	0.33	45.64	-9.44	72.17	0.07	0.07	0.07
...	...	...	...	...	...	...	...	...	...	...	...	...

A	a	45	130	60	7.49	0.33	45.64	-9.44	72.17	0.07	0.07	0.07
A	a	45	130	60	13.47	0.84	65.80	-14.04	90.38	0.12	0.13	0.13
A	a	45	130	60	17.19	1.23	75.77	-16.32	100.13	0.17	0.17	0.18
A	a	45	130	60	20.41	1.64	83.58	-18.33	107.10	0.21	0.22	0.23
A	a	45	130	60	23.74	2.06	89.86	-20.07	115.09	0.25	0.27	0.28
A	a	45	130	60	25.88	2.38	97.45	-21.31	118.24	0.28	0.30	0.33
A	a	45	130	60	30.84	3.14	108.07	-23.84	126.79	0.37	0.41	0.44
A	a	45	130	60	36.86	4.13	121.95	-26.87	138.31	0.46	0.55	0.57
A	a	45	130	60	42.38	5.10	131.27	-29.09	146.58	0.59	0.69	0.70
A	a	45	130	60	50.07	6.56	144.93	-32.08	158.47	0.79	0.87	0.85
A	a	45	130	60	54.87	7.35	152.73	-33.28	167.10	0.85	0.94	0.91
A	a	45	130	60	60.01	8.67	162.49	-35.73	175.56	1.01	1.08	1.03
A	a	45	130	60	65.87	10.00	170.08	-37.69	186.80	1.11	1.21	1.16
A	a	45	130	60	73.97	11.68	181.79	-40.12	202.22	1.40	1.33	1.26
A	a	45	130	60	78.11	12.73	186.77	-41.35	220.15	1.55	1.43	1.33
A	a	45	130	60	77.46	13.18	187.21	-42.13	228.51	1.58	1.45	1.36
A	b	37	130	80	5.21	0.16	30.89	-5.98	40.87	0.05	0.05	0.04
A	b	37	130	80	10.28	0.47	47.15	-9.79	55.64	0.10	0.10	0.10
A	b	37	130	80	13.85	0.73	56.04	-11.82	62.42	0.14	0.14	0.14
A	b	37	130	80	16.70	0.97	62.33	-13.09	68.08	0.18	0.18	0.18
A	b	37	130	80	20.57	1.31	71.22	-14.83	72.18	0.22	0.22	0.22
A	b	37	130	80	21.98	1.52	74.25	-15.83	74.77	0.24	0.24	0.24
A	b	37	130	80	26.33	2.02	81.63	-17.70	80.35	0.33	0.33	0.33
A	b	37	130	80	32.23	2.73	92.25	-20.29	88.71	0.41	0.42	0.42
A	b	37	130	80	38.28	3.46	102.22	-22.12	96.88	0.51	0.53	0.52
A	b	37	130	80	44.72	4.50	112.41	-24.52	104.50	0.66	0.69	0.66
A	b	37	130	80	50.11	5.12	119.56	-25.70	110.44	0.69	0.75	0.72
A	b	37	130	80	54.85	6.08	124.77	-27.66	115.09	0.87	0.88	0.85
A	b	37	130	80	61.74	7.22	134.52	-29.45	123.73	1.05	1.04	0.96
A	b	37	130	80	69.64	8.45	143.20	-31.73	132.27	1.28	1.16	1.08
A	b	37	130	80	74.31	9.58	148.83	-32.74	140.07	1.41	1.28	1.19
A	b	37	130	80	75.40	10.22	150.13	-33.80	152.43	1.47	1.34	1.25
A	c	37	130	70	6.41	0.25	39.57	-8.12	52.85	0.06	0.06	0.06
A	c	37	130	70	11.88	0.66	57.34	-12.18	67.34	0.12	0.12	0.12
A	c	37	130	70	15.79	0.99	68.18	-14.28	76.17	0.16	0.17	0.17
A	c	37	130	70	18.48	1.32	74.04	-16.18	81.09	0.21	0.21	0.21
A	c	37	130	70	21.60	1.66	82.06	-17.71	86.29	0.24	0.25	0.25
A	c	37	130	70	23.66	1.93	85.96	-18.81	89.64	0.27	0.28	0.29
A	c	37	130	70	28.60	2.59	97.45	-21.26	97.07	0.36	0.38	0.39
A	c	37	130	70	34.03	3.37	107.86	-23.79	104.31	0.44	0.49	0.49
A	c	37	130	70	39.91	4.22	117.83	-26.13	114.35	0.55	0.61	0.61
A	c	37	130	70	47.25	5.41	129.54	-28.74	123.08	0.72	0.78	0.75
A	c	37	130	70	51.34	6.10	138.43	-29.77	128.65	0.75	0.84	0.81
A	c	37	130	70	56.42	7.20	144.28	-31.87	136.45	0.94	0.97	0.93
A	c	37	130	70	63.51	8.36	152.52	-33.80	146.85	1.12	1.15	1.06
A	c	37	130	70	70.46	9.76	164.01	-36.00	155.49	1.39	1.26	1.18
A	c	37	130	70	75.94	10.97	169.22	-37.45	176.21	1.51	1.38	1.29
A	c	37	130	70	78.18	11.81	171.38	-39.04	173.42	1.56	1.44	1.35
A	d	37	130	60	5.97	0.27	43.47	-10.35	61.40	0.06	0.06	0.06
A	d	37	130	60	11.77	0.77	66.67	-15.44	78.86	0.12	0.12	0.12
A	d	37	130	60	15.24	1.15	78.59	-18.14	87.22	0.16	0.17	0.17
A	d	37	130	60	18.32	1.56	87.91	-20.36	94.56	0.21	0.22	0.22
A	d	37	130	60	21.52	1.97	96.15	-22.27	101.34	0.25	0.27	0.27
A	d	37	130	60	23.99	2.33	102.44	-23.91	105.24	0.28	0.30	0.32
A	d	37	130	60	28.83	3.15	115.01	-27.01	113.98	0.37	0.42	0.44
A	d	37	130	60	34.87	4.17	128.02	-29.88	124.38	0.46	0.55	0.58
A	d	37	130	60	41.23	5.17	141.46	-32.57	134.97	0.59	0.71	0.71
A	d	37	130	60	47.32	6.57	153.39	-35.38	145.37	0.79	0.90	0.86
A	d	37	130	60	52.47	7.49	161.84	-37.51	152.61	0.85	0.97	0.93
A	d	37	130	60	57.21	8.81	170.08	-39.67	160.42	1.05	1.11	1.05
A	d	37	130	60	64.92	10.22	183.09	-41.83	174.82	1.22	1.26	1.21
A	d	37	130	60	70.85	11.90	191.11	-44.55	194.14	1.54	1.41	1.33
A	d	37	130	60	77.68	13.34	201.30	-46.26	204.81	1.64	1.53	1.45
A	d	37	130	60	79.26	14.40	205.20	-47.70	204.07	1.69	1.59	1.50
A	e	60	130	80	4.24	0.09	20.05	-3.85	48.30	0.04	0.03	0.03
A	e	60	130	80	9.99	0.31	33.71	-6.58	71.61	0.08	0.08	0.08
A	e	60	130	80	12.96	0.50	37.61	-7.88	80.81	0.11	0.11	0.11
A	e	60	130	80	16.05	0.70	44.33	-9.04	88.89	0.15	0.14	0.14
A	e	60	130	80	19.53	0.95	49.76	-10.31	98.46	0.18	0.18	0.17
A	e	60	130	80	22.91	1.15	54.09	-11.12	103.76	0.20	0.20	0.20
A	e	60	130	80	27.19	1.59	58.21	-12.71	112.77	0.26	0.27	0.27
A	e	60	130	80	33.38	2.21	66.77	-14.65	123.91	0.33	0.34	0.34
A	e	60	130	80	39.26	2.81	74.69	-16.00	132.28	0.42	0.42	0.43
A	e	60	130	80	48.92	3.72	84.44	-17.93	146.11	0.54	0.56	0.53
A	e	60	130	80	51.51	4.22	86.18	-18.89	151.29	0.60	0.62	0.59
A	e	60	130	80	58.27	5.04	91.17	-20.43	161.63	0.74	0.74	0.68
A	e	60	130	80	65.58	6.01	100.70	-21.75	172.77	0.87	0.83	0.78
A	e	60	130	80	72.19	7.03	105.47	-23.42	183.73	1.00	0.93	0.88
A	e	60	130	80	76.07	7.58	109.38	-23.85	191.25	1.08	1.00	0.95
A	e	60	130	80	76.72	7.75	110.68	-24.04	192.09	1.09	1.01	0.96
A	f	60	130	70	5.45	0.15	25.47	-5.10	64.71	0.05	0.04	0.04
A	f	60	130	70	11.35	0.44	39.35	-8.16	89.45	0.09	0.09	0.09
A	f	60	130	70	14.68	0.69	46.07	-9.71	101.15	0.12	0.12	0.12
A	f	60	130	70	18.46	0.93	53.66	-11.06	110.91	0.16	0.15	0.15
A	f	60	130	70	21.25	1.19	57.13	-12.37	118.25	0.19	0.19	0.19
A	f	60	130	70	23.37	1.40	60.38	-13.03	121.87	0.21	0.21	0.21
A	f	60	130	70	28.90	1.91	68.62	-14.88	134.31	0.27	0.28	0.28
A	f	60	130	70	35.16	2.60	77.51	-16.96	146.02	0.34	0.35	0.36
A	f	60	130	70	40.30	3.26	84.23	-18.52	154.75	0.42	0.44	0.46
A	f	60	130	70	48.75	4.27	95.50	-20.68	169.15	0.54	0.59	0.57
A	f	60	130	70	51.63	4.76	97.67	-21.44	178.07	0.61	0.65	0.64
A	f	60	130	70	58.64	5.73	105.26	-23.16	188.28	0.75	0.78	0.73
A	f	60	130	70	66.99	6.80	114.36	-24.83	202.59	0.89	0.88	0.83
A	f	60	130	70	73.15	7.96	120.43	-26.32	218.01	1.06	0.97	0.93

A f	60	130	70	77.83	8.56	124.77	-27.15	226.74	1.14	1.06	1.01
A f	60	130	70	78.44	8.83	124.99	-27.58	230.73	1.16	1.08	1.02
A g	60	130	60	5.92	0.16	31.33	-5.90	77.28	0.05	0.04	0.04
A g	60	130	60	11.27	0.50	45.85	-9.50	106.73	0.09	0.09	0.09
A g	60	130	60	14.89	0.76	54.31	-11.18	118.43	0.12	0.12	0.12
A g	60	130	60	17.99	1.05	60.60	-12.89	129.49	0.15	0.15	0.15
A g	60	130	60	21.42	1.38	66.88	-14.34	139.33	0.18	0.18	0.19
A g	60	130	60	23.53	1.59	71.65	-15.25	145.65	0.20	0.21	0.21
A g	60	130	60	28.78	2.17	79.67	-17.27	158.93	0.26	0.27	0.28
A g	60	130	60	34.25	2.92	86.83	-19.51	170.63	0.33	0.35	0.37
A g	60	130	60	39.96	3.68	97.34	-21.42	183.64	0.41	0.45	0.47
A g	60	130	60	47.84	4.83	108.94	-24.03	200.18	0.53	0.60	0.61
A g	60	130	60	52.33	5.51	114.58	-24.89	209.83	0.62	0.69	0.68
A g	60	130	60	58.83	6.63	122.60	-26.93	223.49	0.75	0.82	0.79
A g	60	130	60	66.36	7.76	130.62	-28.50	239.19	0.90	0.94	0.88
A g	60	130	60	72.17	9.00	137.78	-30.44	255.25	1.10	1.04	0.99
A g	60	130	60	78.35	10.01	144.49	-31.55	276.25	1.25	1.15	1.09
A g	60	130	60	79.55	10.48	145.36	-32.41	287.11	1.28	1.18	1.12
A h	40	130	80	5.42	0.15	31.33	-5.83	42.26	0.05	0.04	0.04
A h	40	130	80	10.68	0.47	46.29	-9.58	56.76	0.10	0.10	0.10
A h	40	130	80	14.30	0.74	56.04	-11.49	63.82	0.14	0.14	0.14
A h	40	130	80	17.01	1.01	60.81	-13.23	69.57	0.19	0.19	0.18
A h	40	130	80	20.59	1.33	69.48	-14.72	75.14	0.22	0.23	0.23
A h	40	130	80	22.74	1.60	73.82	-15.78	78.30	0.26	0.26	0.26
A h	40	130	80	27.95	2.16	81.84	-17.96	84.34	0.35	0.36	0.36
A h	40	130	80	34.25	2.94	93.66	-20.30	92.42	0.45	0.46	0.46
A h	40	130	80	39.94	3.70	101.57	-22.36	99.11	0.57	0.59	0.56
A h	40	130	80	48.51	4.82	116.10	-24.98	108.59	0.75	0.75	0.70
A h	40	130	80	50.79	5.45	117.40	-25.96	113.05	0.78	0.81	0.77
A h	40	130	80	57.13	6.54	125.85	-27.94	119.17	0.96	0.97	0.89
A h	40	130	80	65.11	7.64	135.17	-29.51	128.65	1.19	1.10	1.01
A h	40	130	80	72.08	8.93	143.20	-31.93	134.78	1.33	1.22	1.14
A h	40	130	80	76.34	9.93	148.83	-33.40	145.37	1.45	1.33	1.24
A h	40	130	80	76.27	10.44	148.62	-33.95	154.56	1.49	1.37	1.28
A i	40	130	70	5.72	0.18	35.66	-6.94	50.81	0.05	0.05	0.04
A i	40	130	70	10.90	0.54	53.01	-11.03	66.60	0.11	0.11	0.10
A i	40	130	70	14.71	0.85	62.98	-13.24	75.33	0.14	0.15	0.15
A i	40	130	70	17.43	1.16	69.70	-15.14	79.98	0.19	0.19	0.19
A i	40	130	70	20.84	1.53	77.51	-16.84	89.08	0.22	0.23	0.23
A i	40	130	70	23.22	1.79	82.71	-17.91	90.01	0.25	0.27	0.27
A i	40	130	70	27.76	2.43	91.60	-20.39	97.63	0.34	0.37	0.38
A i	40	130	70	34.34	3.25	105.69	-22.88	107.66	0.43	0.48	0.49
A i	40	130	70	39.25	4.08	114.15	-25.13	114.44	0.55	0.61	0.60
A i	40	130	70	47.45	5.33	126.50	-28.04	126.23	0.74	0.78	0.74
A i	40	130	70	51.37	6.03	132.57	-29.04	130.69	0.79	0.84	0.80
A i	40	130	70	55.84	7.14	141.46	-31.18	136.45	0.97	0.97	0.94
A i	40	130	70	64.02	8.36	151.22	-33.07	148.34	1.11	1.15	1.06
A i	40	130	70	70.80	9.84	161.19	-35.77	157.63	1.39	1.28	1.19
A i	40	130	70	75.95	11.07	166.61	-36.98	173.98	1.51	1.40	1.31
A i	40	130	70	77.88	11.80	167.70	-38.27	184.75	1.56	1.45	1.37
A j	40	130	60	6.85	0.32	46.39	-9.77	64.84	0.07	0.06	0.06
A j	40	130	60	13.14	0.85	70.35	-14.72	83.50	0.13	0.13	0.13
A j	40	130	60	16.97	1.27	80.98	-17.36	93.16	0.18	0.18	0.19
A j	40	130	60	19.83	1.69	86.39	-19.52	98.56	0.22	0.23	0.24
A j	40	130	60	23.43	2.15	98.10	-21.51	106.36	0.27	0.29	0.30
A j	40	130	60	26.20	2.51	105.47	-23.08	110.63	0.30	0.33	0.35
A j	40	130	60	30.78	3.33	116.53	-25.83	118.43	0.40	0.46	0.48
A j	40	130	60	37.16	4.46	129.97	-28.95	130.51	0.51	0.62	0.62
A j	40	130	60	43.33	5.50	142.11	-31.67	138.96	0.66	0.77	0.74
A j	40	130	60	51.87	7.11	158.59	-34.75	152.15	0.89	0.95	0.89
A j	40	130	60	55.93	8.06	164.23	-36.09	159.12	0.93	1.01	0.96
A j	40	130	60	62.14	9.40	174.85	-38.62	167.29	1.12	1.15	1.12
A j	40	130	60	68.72	10.81	185.04	-40.69	179.18	1.27	1.33	1.25
A j	40	130	60	74.23	12.60	193.71	-43.44	192.65	1.56	1.45	1.37
A j	40	130	60	78.90	13.78	202.38	-44.80	213.09	1.65	1.53	1.46
A j	40	130	60	80.77	14.52	205.42	-46.13	214.48	1.68	1.58	1.50
A k	30	130	80	4.25	0.11	29.81	-5.65	34.18	0.04	0.03	0.03
A k	30	130	80	9.27	0.40	48.24	-9.76	48.77	0.09	0.09	0.09
A k	30	130	80	12.34	0.64	56.69	-11.86	55.64	0.13	0.12	0.12
A k	30	130	80	15.47	0.89	63.41	-13.57	60.47	0.16	0.17	0.16
A k	30	130	80	18.50	1.20	72.30	-15.28	65.67	0.20	0.20	0.20
A k	30	130	80	20.71	1.44	76.21	-16.48	68.08	0.23	0.23	0.23
A k	30	130	80	25.27	1.97	85.53	-18.67	75.51	0.31	0.31	0.31
A k	30	130	80	31.26	2.71	97.67	-21.12	82.95	0.39	0.40	0.41
A k	30	130	80	36.57	3.47	107.21	-23.41	89.08	0.50	0.53	0.53
A k	30	130	80	44.60	4.55	119.35	-26.05	98.93	0.68	0.72	0.66
A k	30	130	80	48.47	5.19	124.99	-27.12	101.71	0.75	0.79	0.74
A k	30	130	80	54.57	6.32	133.22	-29.46	108.40	0.95	0.94	0.87
A k	30	130	80	61.85	7.46	141.03	-31.24	117.69	1.20	1.09	1.00
A k	30	130	80	66.84	8.72	147.32	-33.24	125.95	1.33	1.21	1.11
A k	30	130	80	74.05	9.96	155.55	-34.73	135.52	1.45	1.32	1.21
A k	30	130	80	76.65	10.75	157.07	-36.37	134.59	1.52	1.38	1.27
A L	30	130	70	5.41	0.21	38.26	-7.95	45.42	0.05	0.05	0.05
A L	30	130	70	10.88	0.59	59.29	-12.41	59.91	0.11	0.11	0.10
A L	30	130	70	14.00	0.89	69.05	-14.52	66.23	0.15	0.15	0.15
A L	30	130	70	16.90	1.18	77.07	-16.58	72.73	0.19	0.19	0.19
A L	30	130	70	20.04	1.54	83.58	-18.24	77.84	0.22	0.23	0.22
A L	30	130	70	21.93	1.79	88.13	-19.45	81.65	0.25	0.26	0.26
A L	30	130	70	26.41	2.44	100.05	-22.01	88.15	0.34	0.35	0.36
A L	30	130	70	32.76	3.22	113.71	-24.37	97.81	0.41	0.45	0.48
A L	30	130	70	37.55	4.01	122.82	-26.66	103.76	0.52	0.59	0.59
A L	30	130	70	44.63	5.22	134.52	-29.64	113.60	0.68	0.77	0.73
A L	30	130	70	48.74	5.96	141.90	-30.90	118.06	0.75	0.84	0.80
A L	30	130	70	54.36	7.06	149.92	-33.27	125.49	0.96	0.98	0.93
A L	30	130	70	60.97	8.30	160.54	-35.31	135.24	1.10	1.16	1.06
A L	30	130	70	66.05	9.58	166.39	-37.42	146.95	1.40	1.28	1.18
A L	30	130	70	72.58	10.92	174.20	-39.06	153.36	1.52	1.39	1.29
A L	30	130	70	75.38	11.82	177.88	-40.74	150.94	1.58	1.46	1.35
A m	30	130	60	4.93	0.21	44.33	-8.92	49.60	0.05	0.05	0.04
A m	30	130	60	10.49	0.66	68.40	-14.61	68.64	0.10	0.11	0.10
A m	30	130	60	13.78	1.04	81.41	-17.47	75.89	0.15	0.15	0.15
A m	30	130	60	17.08	1.43	90.95	-20.10	83.32	0.19	0.20	0.20
A m	30	130	60	20.55	1.88	102.22	-22.41	90.94	0.23	0.25	0.25
A m	30	130	60	22.26	2.18	107.21	-23.80	94.84	0.26	0.28	0.29
A m	30	130	60	27.69	3.02	121.30	-26.71	104.50	0.35	0.38	0.40
A m	30	130	60	33.89	4.09	137.34	-29.95	116.39	0.43	0.51	0.56
A m	30	130	60	39.17	5.12	148.83	-33.01	123.36	0.57	0.69	0.70
A m	30	130	60	48.06	6.72	166.39	-36.56	138.50	0.76	0.89	0.85
A m	30	130	60	51.59	7.60	172.46	-37.92	142.02	0.83	0.98	0.94
A m	30	130	60	57.87	9.21	183.30	-41.00	149.83	1.09	1.11	1.10
A m	30	130	60	64.46	10.67	194.79	-43.33	160.88	1.26	1.34	1.25
A m	30	130	60	70.28	12.35	204.77	-46.19	171.94	1.58	1.47	1.37
A m	30	130	60	75.96	13.74	211.49	-47.94	179.09	1.67	1.57	1.46
A m	30	130	60	78.15	14.82	214.74	-49.83	179.55	1.72	1.62	1.51
A n	45	130	70	5.93	0.20	35.01	-7.89	56.10	0.05	0.06	0.05
A n	45	130	70	12.02	0.59	51.49	-11.89	74.96	0.11	0.11	0.11
A n	45	130	70	15.55	0.91	62.76	-13.99	84.06	0.15	0.16	0.15
A n	45	130	70	18.75	1.22	67.97	-15.84	89.83	0.20	0.20	0.19
A n	45	130	70	22.26	1.59	75.77	-17.42	97.44	0.23	0.24	0.23
A n	45	130	70	24.13	1.87	80.54	-18.51	99.67	0.26	0.28	0.27
A n	45	130	70	28.80	2.53	89.21	-21.00	107.29	0.34	0.37	0.37
A n	45	130	70	35.65	3.37	101.36	-23.39	117.60	0.43	0.49	0.49
A n	45	130	70	41.09	4.23	109.81	-25.60	125.03	0.56	0.63	0.61
A n	45	130	70	49.80	5.53	122.82	-28.24	137.66	0.74	0.79	0.75
A n	45	130	70	52.99	6.27	128.24	-29.86	141.47	0.82	0.86	0.81
A n	45	130	70	60.16	7.47	138.43	-31.95	153.36	1.00	1.00	0.95
A n	45	130	70	66.38	8.74	145.36	-33.78	162.09	1.13	1.15	1.06
A n	45	130	70	71.99	10.05	152.08	-35.78	176.67	1.37	1.26	1.16
A n	45	130	70	78.08	11.08	157.94	-37.08	200.54	1.47	1.36	1.22
A n	45	130	70	80.26	11.81	161.62	-37.98	203.52	1.52	1.40	1.27
B a	45	130	70	5.35	0.18	32.19	-7.32	55.36	0.04	0.04	0.04
B a	45	130	70	11.24	0.54	49.32	-11.37	74.03	0.10	0.10	0.10
B a	45	130	70	14.90	0.85	58.86	-13.86	82.58	0.14	0.14	0.14
B a	45	130	70	18.59	1.19	67.75	-15.74	90.20	0.17	0.18	0.18

B a	45	130	70	21.61	1.54	74.25	-17.35	94.84	0.21	0.22	0.22
B a	45	130	70	24.26	1.81	79.46	-18.89	99.85	0.24	0.25	0.26
B a	45	130	70	29.72	2.48	90.08	-21.09	108.03	0.30	0.33	0.34
B a	45	130	70	35.01	3.31	100.05	-23.34	116.76	0.39	0.44	0.46
B a	45	130	70	40.67	4.18	108.73	-25.58	125.49	0.49	0.56	0.57
B a	45	130	70	49.08	5.48	121.73	-28.44	136.64	0.63	0.71	0.72
B a	45	130	70	53.16	6.22	128.24	-29.76	142.95	0.73	0.82	0.81
B a	45	130	70	60.08	7.41	136.69	-31.85	153.54	0.90	0.96	0.91
B a	45	130	70	66.65	8.72	147.53	-33.63	164.23	1.06	1.09	1.06
B a	45	130	70	73.01	10.05	152.74	-35.65	179.74	1.30	1.26	1.18
B a	45	130	70	77.84	11.18	159.24	-37.15	199.43	1.49	1.37	1.27
B a	45	130	70	78.82	11.65	160.76	-37.79	199.43	1.53	1.41	1.31
B b	57	130	90	4.92	0.10	19.84	-4.50	49.32	0.04	0.04	0.03
B b	57	130	90	10.72	0.32	31.33	-7.00	69.66	0.08	0.08	0.08
B b	57	130	90	14.20	0.51	36.75	-8.55	77.47	0.12	0.11	0.11
B b	57	130	90	17.78	0.70	41.73	-9.56	85.18	0.14	0.14	0.14
B b	57	130	90	20.31	0.90	45.42	-10.52	90.19	0.17	0.17	0.17
B b	57	130	90	22.78	1.05	48.24	-11.22	95.02	0.19	0.19	0.19
B b	57	130	90	27.42	1.46	54.09	-12.66	102.83	0.24	0.24	0.23
B b	57	130	90	34.34	1.96	61.03	-14.07	111.84	0.30	0.30	0.30
B b	57	130	90	38.59	2.50	67.10	-15.50	120.48	0.37	0.37	0.37
B b	57	130	90	45.99	3.21	73.39	-17.09	128.93	0.46	0.46	0.47
B b	57	130	90	50.82	3.75	76.64	-17.97	135.99	0.53	0.55	0.53
B b	57	130	90	57.82	4.49	82.71	-19.16	146.76	0.63	0.64	0.62
B b	57	130	90	65.22	5.33	89.00	-20.65	158.47	0.74	0.75	0.70
B b	57	130	90	71.02	6.11	93.98	-21.70	176.30	0.91	0.85	0.80
B b	57	130	90	71.61	6.46	94.63	-22.25	178.25	0.99	0.90	0.85
B b	57	130	90	72.32	6.62	95.28	-22.60	172.96	1.02	0.92	0.86
B c	57	130	50	6.80	0.27	41.08	-8.41	99.20	0.05	0.05	0.05
B c	57	130	50	12.87	0.75	60.38	-12.90	129.67	0.09	0.10	0.09
B c	57	130	50	16.58	1.13	72.09	-15.23	143.79	0.13	0.13	0.13
B c	57	130	50	19.85	1.53	80.98	-17.41	153.54	0.16	0.17	0.17
B c	57	130	50	23.31	1.93	86.83	-19.12	166.27	0.19	0.20	0.21
B c	57	130	50	25.62	2.25	93.55	-20.45	171.84	0.21	0.23	0.24
B c	57	130	50	30.32	2.98	103.31	-22.80	186.05	0.27	0.29	0.31
B c	57	130	50	36.69	3.97	115.88	-25.59	203.24	0.34	0.38	0.43
B c	57	130	50	42.09	4.98	126.07	-28.14	215.13	0.42	0.49	0.56
B c	57	130	50	50.78	6.48	141.25	-31.25	235.47	0.54	0.66	0.74
B c	57	130	50	54.43	7.28	146.23	-32.82	245.88	0.62	0.77	0.83
B c	57	130	50	61.73	8.74	159.46	-35.07	263.71	0.77	0.94	0.94
B c	57	130	50	68.57	10.19	167.69	-37.32	281.73	0.93	1.08	1.02
B c	57	130	50	75.27	11.69	178.10	-39.26	303.93	1.16	1.20	1.18
B c	57	130	50	79.75	12.86	183.95	-40.66	324.46	1.39	1.34	1.27
B c	57	130	50	80.05	13.36	183.95	-41.28	330.40	1.45	1.37	1.30
B d	45	130	100	5.78	0.15	22.66	-5.50	39.29	0.05	0.05	0.04
B d	45	130	100	11.92	0.43	35.45	-8.19	53.04	0.10	0.10	0.09
B d	45	130	100	15.30	0.62	42.60	-9.64	59.63	0.14	0.14	0.13
B d	45	130	100	17.73	0.82	46.72	-10.58	63.07	0.17	0.17	0.17
B d	45	130	100	21.87	1.10	51.92	-11.91	68.46	0.21	0.21	0.20
B d	45	130	100	23.52	1.26	54.09	-12.65	71.62	0.23	0.23	0.23
B d	45	130	100	27.87	1.67	59.73	-14.09	76.44	0.30	0.30	0.29
B d	45	130	100	33.86	2.23	67.53	-15.75	83.32	0.38	0.38	0.37
B d	45	130	100	39.78	2.78	74.47	-17.16	88.89	0.47	0.46	0.45
B d	45	130	100	48.76	3.70	83.14	-19.06	96.51	0.59	0.58	0.55
B d	45	130	100	51.35	4.16	86.39	-20.00	101.34	0.69	0.67	0.62
B d	45	130	100	58.82	5.02	93.33	-21.46	108.86	0.80	0.78	0.73
B d	45	130	100	65.39	5.88	99.19	-22.99	117.22	0.93	0.90	0.83
B d	45	130	100	71.11	6.70	103.96	-24.14	125.77	1.12	1.01	0.93
B d	45	130	100	74.32	7.25	106.56	-24.81	137.75	1.19	1.07	1.00
B d	45	130	100	75.34	7.54	108.94	-25.36	143.32	1.22	1.10	1.01
B e	45	130	90	5.23	0.12	24.82	-4.58	37.99	0.04	0.04	0.03
B e	45	130	90	11.60	0.42	38.92	-7.68	56.29	0.09	0.09	0.09
B e	45	130	90	14.89	0.62	45.20	-9.25	62.89	0.13	0.14	0.13
B e	45	130	90	18.02	0.86	50.84	-10.53	68.08	0.17	0.17	0.17
B e	45	130	90	21.20	1.13	56.91	-11.71	72.73	0.21	0.21	0.21
B e	45	130	90	22.74	1.33	58.65	-12.81	75.98	0.24	0.24	0.24
B e	45	130	90	28.31	1.81	68.40	-14.47	82.58	0.30	0.31	0.31
B e	45	130	90	34.79	2.48	75.99	-16.34	90.94	0.39	0.40	0.39
B e	45	130	90	40.46	3.08	83.36	-18.02	98.09	0.49	0.49	0.48
B e	45	130	90	48.99	4.09	93.98	-20.05	106.36	0.62	0.62	0.60
B e	45	130	90	51.54	4.50	96.37	-20.80	109.70	0.72	0.71	0.67
B e	45	130	90	58.65	5.51	103.31	-22.73	118.06	0.84	0.83	0.79
B e	45	130	90	65.90	6.36	110.89	-24.02	125.68	0.98	0.96	0.89
B e	45	130	90	72.17	7.41	117.18	-25.64	134.78	1.20	1.08	1.00
B e	45	130	90	74.83	8.07	119.35	-26.44	141.65	1.28	1.16	1.08
B e	45	130	90	74.39	8.29	118.92	-26.78	146.76	1.31	1.18	1.10
B f	45	130	50	7.16	0.36	52.14	-10.72	85.36	0.06	0.06	0.06
B f	45	130	50	13.39	0.95	76.42	-16.14	108.40	0.12	0.13	0.13
B f	45	130	50	16.95	1.38	86.83	-18.98	120.85	0.16	0.17	0.18
B f	45	130	50	20.23	1.85	98.54	-21.39	130.32	0.19	0.21	0.23
B f	45	130	50	23.30	2.33	107.21	-23.55	137.10	0.23	0.26	0.28
B f	45	130	50	25.54	2.73	114.58	-25.13	142.39	0.26	0.30	0.33
B f	45	130	50	30.90	3.62	127.80	-28.51	154.85	0.33	0.39	0.45
B f	45	130	50	36.89	4.80	143.20	-31.62	167.85	0.42	0.53	0.61
B f	45	130	50	42.49	5.95	155.12	-34.32	179.55	0.53	0.69	0.76
B f	45	130	50	50.02	7.60	171.17	-37.85	194.79	0.70	0.90	0.92
B f	45	130	50	53.72	8.59	178.54	-39.57	203.15	0.81	1.03	1.01
B f	45	130	50	60.66	10.17	190.68	-42.20	217.45	0.99	1.17	1.10
B f	45	130	50	67.03	11.79	204.55	-44.75	232.87	1.15	1.27	1.26
B f	45	130	50	74.19	13.56	214.52	-47.40	253.21	1.42	1.45	1.41
B f	45	130	50	79.30	15.05	220.60	-49.10	283.40	1.60	1.57	1.51
B f	45	130	50	80.12	15.69	223.19	-49.94	281.91	1.71	1.62	1.55
B g	37	130	100	5.59	0.14	25.69	-5.90	34.93	0.04	0.04	0.03
B g	37	130	100	11.53	0.42	40.11	-9.04	45.98	0.10	0.10	0.09
B g	37	130	100	14.74	0.66	46.28	-10.55	50.81	0.14	0.14	0.13
B g	37	130	100	18.39	0.88	52.57	-11.83	55.64	0.17	0.17	0.17
B g	37	130	100	21.02	1.13	57.78	-13.23	58.79	0.21	0.21	0.20
B g	37	130	100	22.97	1.31	61.46	-13.94	61.21	0.25	0.24	0.23
B g	37	130	100	27.54	1.79	68.18	-15.66	66.41	0.32	0.31	0.30
B g	37	130	100	33.44	2.42	76.64	-18.00	71.34	0.41	0.40	0.39
B g	37	130	100	38.65	3.01	83.14	-19.20	78.58	0.51	0.50	0.48
B g	37	130	100	46.80	3.96	92.68	-21.51	85.46	0.64	0.64	0.59
B g	37	130	100	49.94	4.46	95.93	-22.61	88.71	0.76	0.73	0.67
B g	37	130	100	58.00	5.40	104.61	-24.23	94.65	0.90	0.86	0.79
B g	37	130	100	64.90	6.37	110.03	-25.76	101.34	1.09	0.98	0.90
B g	37	130	100	71.60	7.45	118.26	-27.31	108.77	1.23	1.11	1.01
B g	37	130	100	75.07	8.25	120.43	-28.39	118.99	1.31	1.19	1.09
B g	37	130	100	73.49	8.58	120.65	-28.97	119.92	1.35	1.22	1.12
B h	37	130	90	5.33	0.14	27.42	-5.18	35.48	0.04	0.04	0.03
B h	37	130	90	11.33	0.45	43.90	-8.74	49.51	0.10	0.10	0.09
B h	37	130	90	14.82	0.70	52.14	-10.47	55.18	0.14	0.14	0.13
B h	37	130	90	18.12	0.95	57.99	-11.97	60.28	0.18	0.18	0.17
B h	37	130	90	21.56	1.24	64.93	-13.43	64.37	0.22	0.22	0.21
B h	37	130	90	23.66	1.46	67.97	-14.39	67.71	0.25	0.25	0.24
B h	37	130	90	28.54	1.97	75.34	-16.25	73.48	0.32	0.32	0.32
B h	37	130	90	34.50	2.64	84.66	-18.36	79.61	0.43	0.42	0.41
B h	37	130	90	39.99	3.32	93.33	-20.13	85.36	0.53	0.54	0.51
B h	37	130	90	47.23	4.36	102.87	-22.47	92.98	0.67	0.68	0.64
B h	37	130	90	51.08	4.92	108.07	-23.72	97.07	0.80	0.78	0.73
B h	37	130	90	58.19	5.91	115.45	-25.38	104.13	0.94	0.91	0.84
B h	37	130	90	64.87	6.93	122.60	-26.98	111.00	1.16	1.04	0.95
B h	37	130	90	71.57	8.07	131.27	-28.78	119.17	1.30	1.17	1.08
B h	37	130	90	74.93	8.92	133.44	-29.79	125.95	1.39	1.26	1.17
B h	37	130	90	75.45	9.37	132.79	-30.72	132.93	1.43	1.30	1.20
B i	57	130	50	7.10	0.37	55.83	-11.68	77.28	0.06	0.07	0.06
B i	37	130	50	12.87	1.00	82.06	-17.78	97.91	0.13	0.14	0.13
B i	37	130	50	16.75	1.49	96.59	-21.08	110.26	0.17	0.19	0.19
B i	37	130	50	20.04	1.98	107.42	-23.51	117.50	0.21	0.23	0.24
B i	37	130	50	22.91	2.50	117.83	-25.82	125.31	0.25	0.29	0.30
B i	37	130	50	25.54	2.89	124.55	-27.48	130.51	0.29	0.33	0.35
B i	37	130	50	30.42	3.85	138.43	-30.69	141.84	0.36	0.42	0.47
B i	37	130	50	36.87	5.08	155.99	-34.33	154.29	0.47	0.57	0.64
B i	37	130	50	42.08	6.27	168.56	-37.62	164.32	0.58	0.74	0.79
B i	37	130	50	49.32	7.96	184.82	-41.04	179.55	0.75	0.95	0.95

B i	37	130	50	53.35	8.89	193.06	-42.73	186.98	0.85	1.06	1.04
B i	37	130	50	59.34	10.46	206.50	-45.53	198.50	1.01	1.21	1.12
B i	37	130	50	65.49	12.09	218.64	-48.19	212.99	1.19	1.32	1.32
B i	37	130	50	71.39	13.85	228.18	-50.83	231.38	1.39	1.53	1.45
B i	37	130	50	77.24	15.46	239.89	-53.01	244.76	1.70	1.63	1.56
B i	37	130	50	79.29	16.57	243.57	-54.40	247.92	1.76	1.69	1.61
B j	57	130	80	4.86	0.11	22.87	-4.41	50.53	0.04	0.04	0.03
B j	57	130	80	11.07	0.40	36.31	-7.22	72.36	0.09	0.09	0.08
B j	57	130	80	14.72	0.62	43.69	-8.76	81.84	0.13	0.13	0.13
B j	57	130	80	18.53	0.86	49.97	-10.17	89.63	0.16	0.16	0.16
B j	57	130	80	20.99	1.11	54.09	-11.28	95.58	0.20	0.20	0.20
B j	57	130	80	23.82	1.32	58.43	-12.19	99.95	0.23	0.23	0.23
B j	57	130	80	29.21	1.82	66.02	-13.94	108.96	0.28	0.29	0.29
B j	57	130	80	35.22	2.46	73.60	-15.67	119.64	0.37	0.38	0.38
B j	57	130	80	40.98	3.07	80.76	-17.31	127.91	0.45	0.47	0.47
B j	57	130	80	48.24	4.06	85.74	-19.42	139.98	0.57	0.60	0.58
B j	57	130	80	54.64	4.62	95.50	-20.16	146.86	0.67	0.70	0.65
B j	57	130	80	60.60	5.56	101.14	-21.96	155.96	0.78	0.80	0.75
B j	57	130	80	68.50	6.52	107.42	-23.31	167.85	0.92	0.90	0.85
B j	57	130	80	74.34	7.63	112.74	-24.89	178.00	1.11	1.02	0.96
B j	57	130	80	76.59	8.07	115.23	-25.42	181.41	1.17	1.08	1.02
B j	57	130	80	75.24	8.16	114.36	-25.52	181.59	1.19	1.10	1.02
B k	57	130	70	4.66	0.11	24.39	-4.64	57.77	0.04	0.04	0.03
B k	57	130	70	10.21	0.40	38.27	-7.97	81.46	0.08	0.09	0.08
B k	57	130	70	14.15	0.63	48.02	-9.61	93.45	0.12	0.12	0.12
B k	57	130	70	17.29	0.89	53.66	-11.14	102.45	0.15	0.15	0.15
B k	57	130	70	20.00	1.15	58.21	-12.37	109.61	0.18	0.19	0.18
B k	57	130	70	23.10	1.42	64.28	-13.50	115.37	0.21	0.22	0.21
B k	57	130	70	28.22	1.95	71.43	-15.44	125.86	0.26	0.28	0.28
B k	57	130	70	34.56	2.65	81.84	-17.55	137.85	0.34	0.36	0.37
B k	57	130	70	39.52	3.32	85.96	-19.47	147.04	0.42	0.46	0.47
B k	57	130	70	46.54	4.31	97.45	-21.38	159.77	0.54	0.60	0.60
B k	57	130	70	52.07	4.99	104.39	-22.64	168.22	0.63	0.70	0.67
B k	57	130	70	58.98	5.96	112.41	-24.42	179.92	0.75	0.81	0.77
B k	57	130	70	66.68	7.07	118.91	-26.11	192.56	0.89	0.92	0.86
B k	57	130	70	72.65	8.17	124.99	-27.69	204.45	1.09	1.05	0.99
B k	57	130	70	76.77	9.07	131.05	-28.75	216.06	1.21	1.13	1.06
B k	57	130	70	75.52	9.24	130.19	-29.01	216.99	1.27	1.17	1.09
B L	57	130	60	4.73	0.13	29.16	-5.48	68.74	0.04	0.04	0.03
B L	57	130	60	10.30	0.46	46.07	-9.39	95.30	0.08	0.09	0.08
B L	57	130	60	13.93	0.73	55.61	-11.45	109.70	0.12	0.12	0.11
B L	57	130	60	17.02	1.03	61.68	-13.11	119.64	0.15	0.15	0.15
B L	57	130	60	20.31	1.34	69.48	-14.60	128.28	0.18	0.19	0.18
B L	57	130	60	22.84	1.59	72.95	-15.74	134.59	0.20	0.22	0.21
B L	57	130	60	27.66	2.19	83.14	-17.97	146.58	0.26	0.27	0.28
B L	57	130	60	33.92	2.96	94.09	-20.37	159.86	0.33	0.36	0.38
B L	57	130	60	39.33	3.75	103.52	-22.51	170.64	0.40	0.46	0.49
B L	57	130	60	47.03	4.96	114.15	-25.10	187.17	0.53	0.62	0.64
B L	57	130	60	51.82	5.66	121.52	-26.48	196.00	0.61	0.73	0.72
B L	57	130	60	57.45	6.81	129.10	-28.51	207.79	0.74	0.85	0.83
B L	57	130	60	64.48	8.01	138.21	-30.29	220.79	0.90	0.98	0.91
B L	57	130	60	72.64	9.42	146.23	-32.26	239.00	1.11	1.10	1.05
B L	57	130	60	76.94	10.58	152.52	-33.81	255.44	1.26	1.21	1.16
B L	57	130	60	76.95	10.98	152.95	-34.22	261.76	1.36	1.26	1.19
B m	45	130	80	4.63	0.11	25.91	-4.69	43.01	0.04	0.04	0.03
B m	45	130	80	10.29	0.41	42.38	-8.37	59.91	0.09	0.09	0.09
B m	45	130	80	14.24	0.66	50.84	-10.35	68.83	0.13	0.13	0.13
B m	45	130	80	17.68	0.93	57.78	-11.79	75.33	0.17	0.17	0.17
B m	45	130	80	20.18	1.22	62.76	-13.19	79.61	0.21	0.21	0.21
B m	45	130	80	23.22	1.46	67.53	-14.31	84.62	0.24	0.25	0.24
B m	45	130	80	27.94	1.98	75.34	-16.23	91.12	0.30	0.32	0.32
B m	45	130	80	34.84	2.74	86.18	-18.63	100.41	0.40	0.42	0.42
B m	45	130	80	39.57	3.44	93.12	-20.40	107.29	0.50	0.53	0.51
B m	45	130	80	47.35	4.56	104.82	-23.06	116.67	0.64	0.67	0.64
B m	45	130	80	52.56	5.19	111.76	-24.07	122.33	0.75	0.77	0.72
B m	45	130	80	58.87	6.23	119.13	-26.04	129.95	0.87	0.88	0.83
B m	45	130	80	65.17	7.33	125.20	-27.75	137.75	1.02	1.03	0.95
B m	45	130	80	71.74	8.55	134.31	-29.62	147.51	1.26	1.14	1.06
B m	45	130	80	75.91	9.46	139.29	-30.65	156.70	1.35	1.23	1.14
B m	45	130	80	75.37	9.85	137.56	-31.27	159.58	1.40	1.27	1.17
B n	45	130	70	5.42	0.18	31.54	-7.50	55.55	0.05	0.05	0.04
B n	45	130	70	11.05	0.55	48.45	-11.58	73.29	0.10	0.11	0.10
B n	45	130	70	14.85	0.86	59.73	-13.53	81.83	0.15	0.15	0.14
B n	45	130	70	18.01	1.19	66.67	-15.55	87.78	0.18	0.19	0.18
B n	45	130	70	21.31	1.54	72.95	-17.11	95.58	0.22	0.23	0.23
B n	45	130	70	23.57	1.79	78.59	-18.32	99.11	0.25	0.27	0.26
B n	45	130	70	29.05	2.45	89.21	-20.69	107.29	0.32	0.34	0.35
B n	45	130	70	35.21	3.28	100.92	-23.08	116.57	0.42	0.47	0.47
B n	45	130	70	40.94	4.12	109.16	-25.36	125.31	0.53	0.59	0.58
B n	45	130	70	47.91	5.43	119.35	-28.18	135.89	0.68	0.75	0.73
B n	45	130	70	53.09	6.20	126.72	-29.67	142.67	0.80	0.84	0.80
B n	45	130	70	59.87	7.41	136.48	-31.50	152.61	0.93	0.97	0.90
B n	45	130	70	66.64	8.69	145.58	-33.64	162.46	1.09	1.09	1.05
B n	45	130	70	73.09	10.07	153.61	-35.60	178.72	1.33	1.26	1.17
B n	45	130	70	79.03	11.34	160.32	-37.20	200.91	1.49	1.36	1.25
B n	45	130	70	81.53	12.10	162.27	-38.15	199.24	1.55	1.43	1.30
C a	37	110	70	4.50	0.20	32.63	-10.15	45.42	0.05	0.05	0.05
C a	37	110	70	9.80	0.66	50.84	-16.23	62.70	0.10	0.11	0.11
C a	37	110	70	13.25	1.05	60.81	-18.90	70.69	0.16	0.16	0.16
C a	37	110	70	16.42	1.44	69.05	-21.50	77.56	0.20	0.21	0.21
C a	37	110	70	19.04	1.88	74.90	-24.18	82.21	0.24	0.25	0.26
C a	37	110	70	21.20	2.23	81.19	-25.82	86.48	0.27	0.29	0.31
C a	37	110	70	27.50	3.13	91.82	-29.25	98.00	0.36	0.40	0.42
C a	37	110	70	32.51	4.20	103.52	-32.82	104.87	0.47	0.54	0.58
C a	37	110	70	37.59	5.30	111.98	-36.08	114.16	0.59	0.70	0.70
C a	37	110	70	45.55	6.93	124.33	-40.09	124.56	0.78	0.89	0.86
C a	37	110	70	48.19	7.80	129.54	-41.97	129.76	0.88	0.98	0.94
C a	37	110	70	56.04	9.38	140.16	-45.25	140.72	1.06	1.12	1.07
C a	37	110	70	62.61	10.96	148.78	-46.94	145.60	1.28	1.29	1.23
C a	37	110	70	69.27	12.66	155.12	-49.88	157.82	1.50	1.44	1.37
C a	37	110	70	73.50	14.10	162.49	-52.31	175.65	1.66	1.56	1.48
C a	37	110	70	76.58	15.30	165.74	-54.09	174.72	1.71	1.62	1.53
C b	45	110	80	4.21	0.14	24.82	-7.66	41.52	0.05	0.05	0.04
C b	45	110	80	9.85	0.50	38.91	-12.45	63.07	0.10	0.10	0.10
C b	45	110	80	12.80	0.79	45.20	-14.58	69.57	0.14	0.14	0.15
C b	45	110	80	15.79	1.10	51.92	-16.84	75.33	0.18	0.19	0.19
C b	45	110	80	18.47	1.47	56.91	-18.44	80.54	0.22	0.23	0.23
C b	45	110	80	21.06	1.72	61.68	-19.89	84.62	0.25	0.26	0.27
C b	45	110	80	25.63	2.39	69.70	-22.32	91.49	0.33	0.36	0.37
C b	45	110	80	32.09	3.28	79.46	-25.39	100.23	0.45	0.49	0.49
C b	45	110	80	36.75	4.14	85.09	-27.66	106.91	0.57	0.61	0.60
C b	45	110	80	44.13	5.52	96.15	-31.39	116.94	0.75	0.78	0.74
C b	45	110	80	47.82	6.26	101.35	-32.65	121.96	0.83	0.86	0.82
C b	45	110	80	54.92	7.57	108.51	-35.26	132.37	0.98	0.99	0.95
C b	45	110	80	60.81	8.86	115.23	-37.27	141.28	1.18	1.16	1.09
C b	45	110	80	67.93	10.39	122.16	-39.69	155.59	1.39	1.29	1.22
C b	45	110	80	74.65	11.64	130.19	-41.46	174.53	1.52	1.41	1.31
C b	45	110	80	74.45	12.33	130.41	-42.72	174.16	1.57	1.47	1.38
C c	45	110	60	5.33	0.25	36.31	-10.73	62.79	0.06	0.06	0.06
C c	45	110	60	10.64	0.80	55.61	-17.48	87.22	0.11	0.11	0.12
C c	45	110	60	14.30	1.24	65.58	-20.76	97.26	0.16	0.17	0.18
C c	45	110	60	17.49	1.71	73.82	-23.43	105.62	0.20	0.22	0.23
C c	45	110	60	20.51	2.21	81.41	-26.22	112.12	0.24	0.27	0.29
C c	45	110	60	22.61	2.59	84.87	-27.80	116.76	0.27	0.31	0.34
C c	45	110	60	28.28	3.59	98.97	-31.31	127.72	0.35	0.43	0.48
C c	45	110	60	34.24	4.81	110.03	-35.22	138.13	0.46	0.61	0.65
C c	45	110	60	38.93	5.98	117.61	-38.24	146.30	0.61	0.78	0.78
C c	45	110	60	46.55	7.80	132.36	-42.53	161.16	0.85	0.97	0.94
C c	45	110	60	49.71	8.74	138.21	-44.53	166.92	0.98	1.07	1.02
C c	45	110	60	57.04	10.45	148.62	-47.74	180.94	1.11	1.21	1.14
C c	45	110	60	62.49	12.07	155.99	-49.80	193.11	1.28	1.30	1.32
C c	45	110	60	68.60	13.79	165.74	-52.55	210.11	1.51	1.51	1.45
C c	45	110	60	74.75	15.32	171.60	-54.59	234.54	1.69	1.61	1.53
C c	45	110	60	75.92	16.47	173.77	-56.52	234.36	1.74	1.67	1.58

C d	45	110	50	6.28	0.40	48.24	-14.38	83.79	0.07	0.07	0.07
C d	45	110	50	12.11	1.13	70.35	-22.39	111.37	0.13	0.13	0.14
C d	45	110	50	15.65	1.69	82.28	-26.04	121.03	0.17	0.19	0.20
C d	45	110	50	18.86	2.27	91.16	-29.66	131.53	0.21	0.24	0.26
C d	45	110	50	22.22	2.92	101.79	-31.99	140.35	0.25	0.30	0.33
C d	45	110	50	24.32	3.41	106.56	-34.40	144.44	0.28	0.34	0.40
C d	45	110	50	29.73	4.63	120.87	-38.67	156.33	0.37	0.47	0.57
C d	45	110	50	35.35	6.22	134.74	-43.30	170.26	0.48	0.69	0.77
C d	45	110	50	40.82	7.67	146.88	-47.22	181.41	0.62	0.90	0.92
C d	45	110	50	48.73	9.99	162.28	-52.73	199.43	0.90	1.14	1.10
C d	45	110	50	51.88	11.07	169.21	-54.42	205.75	1.05	1.24	1.18
C d	45	110	50	58.77	13.17	180.92	-58.24	223.03	1.21	1.37	1.31
C d	45	110	50	63.88	14.99	189.37	-60.54	239.74	1.37	1.46	1.49
C d	45	110	50	69.91	17.11	200.43	-64.26	266.96	1.62	1.65	1.59
C d	45	110	50	75.21	18.72	206.72	-66.21	282.28	1.78	1.73	1.66
C d	45	110	50	77.07	19.77	209.10	-67.79	280.98	1.80	1.76	1.67
C e	60	110	70	5.74	0.22	26.56	-8.38	69.48	0.06	0.06	0.06
C e	60	110	70	11.76	0.66	41.09	-13.20	97.63	0.12	0.11	0.11
C e	60	110	70	15.93	1.06	49.11	-15.63	106.08	0.16	0.16	0.17
C e	60	110	70	19.88	1.49	55.39	-17.92	118.43	0.20	0.21	0.21
C e	60	110	70	22.97	1.84	60.16	-19.34	126.42	0.24	0.25	0.26
C e	60	110	70	25.31	2.23	64.06	-20.91	131.81	0.27	0.29	0.30
C e	60	110	70	30.40	2.89	71.44	-22.88	142.39	0.34	0.37	0.39
C e	60	110	70	34.32	3.62	76.86	-25.05	150.94	0.42	0.47	0.50
C e	60	110	70	39.37	4.42	83.79	-27.05	160.23	0.51	0.60	0.61
C e	60	110	70	45.21	5.47	90.30	-29.61	170.36	0.63	0.74	0.72
C e	60	110	70	48.05	5.94	92.90	-30.40	177.42	0.69	0.79	0.77
C e	60	110	70	52.32	6.66	100.05	-31.80	182.62	0.78	0.86	0.83
C e	60	110	70	55.91	7.32	102.44	-33.14	190.51	0.87	0.93	0.87
C e	60	110	70	61.75	8.66	108.94	-35.31	201.01	1.03	1.03	0.97
C e	60	110	70	72.80	10.84	118.26	-38.12	225.81	1.35	1.25	1.20
C e	60	110	70	76.46	12.29	120.87	-40.40	240.77	1.48	1.39	1.33
C f	40	110	70	5.48	0.25	34.58	-10.79	51.74	0.06	0.06	0.06
C f	40	110	70	11.44	0.77	53.93	-16.70	69.67	0.12	0.12	0.13
C f	40	110	70	14.89	1.18	61.89	-19.26	77.37	0.17	0.18	0.19
C f	40	110	70	17.50	1.59	68.62	-21.94	83.04	0.22	0.23	0.24
C f	40	110	70	19.66	2.06	81.84	-26.18	80.72	0.27	0.29	0.30
C f	40	110	70	23.38	2.46	82.49	-26.15	92.61	0.30	0.34	0.35
C f	40	110	70	28.51	3.35	91.38	-29.38	102.64	0.40	0.46	0.49
C f	40	110	70	35.26	4.49	103.31	-32.94	110.81	0.54	0.64	0.63
C f	40	110	70	39.07	5.56	111.54	-36.05	118.06	0.70	0.78	0.76
C f	40	110	70	48.18	7.35	124.12	-40.02	128.65	0.92	0.96	0.90
C f	40	110	70	50.47	8.24	128.02	-41.78	132.92	1.02	1.05	0.97
C f	40	110	70	59.48	9.86	141.25	-44.74	143.70	1.20	1.16	1.15
C f	40	110	70	65.85	11.60	149.27	-47.06	155.03	1.39	1.37	1.30
C f	40	110	70	71.42	13.29	154.91	-49.58	180.02	1.60	1.51	1.43
C f	40	110	70	76.44	14.68	160.97	-51.96	182.34	1.69	1.61	1.53
C f	40	110	70	77.42	15.63	163.79	-53.54	185.31	1.73	1.64	1.56
C g	30	110	70	4.42	0.20	33.93	-10.72	41.33	0.05	0.05	0.05
C g	30	110	70	10.06	0.69	55.18	-17.15	59.35	0.11	0.11	0.11
C g	30	110	70	13.18	1.12	64.93	-20.68	66.60	0.16	0.17	0.17
C g	30	110	70	16.49	1.54	74.25	-23.29	74.59	0.20	0.21	0.21
C g	30	110	70	19.24	2.03	81.63	-25.88	79.42	0.26	0.27	0.28
C g	30	110	70	22.01	2.40	87.04	-27.76	86.48	0.29	0.31	0.32
C g	30	110	70	27.80	3.39	100.05	-31.91	99.95	0.38	0.41	0.45
C g	30	110	70	34.70	4.63	113.49	-35.67	108.31	0.48	0.59	0.62
C g	30	110	70	39.24	5.75	120.65	-38.92	118.34	0.62	0.77	0.75
C g	30	110	70	47.19	7.51	133.87	-43.32	124.56	0.89	0.96	0.90
C g	30	110	70	51.43	8.63	140.81	-45.35	130.51	1.03	1.04	1.01
C g	30	110	70	59.18	10.16	150.78	-48.25	137.38	1.18	1.25	1.17
C g	30	110	70	64.15	11.77	158.15	-50.68	147.60	1.52	1.40	1.37
C g	30	110	70	70.05	13.54	164.01	-53.52	151.87	1.63	1.54	1.44
C g	30	110	70	74.38	14.99	170.29	-55.54	154.57	1.70	1.60	1.50
C g	30	110	70	76.42	16.11	172.46	-57.59	155.03	1.73	1.64	1.54
C h	57	110	70	4.85	0.17	25.47	-8.41	61.21	0.05	0.05	0.05
C h	57	110	70	10.04	0.52	38.26	-12.24	88.24	0.10	0.10	0.10
C h	57	110	70	13.38	0.83	44.55	-14.48	98.93	0.14	0.14	0.14
C h	57	110	70	16.43	1.15	51.49	-16.44	106.73	0.17	0.17	0.18
C h	57	110	70	19.44	1.46	57.13	-18.31	114.53	0.20	0.21	0.22
C h	57	110	70	21.69	1.73	60.81	-19.20	119.92	0.23	0.24	0.25
C h	57	110	70	26.15	2.38	67.53	-21.58	130.32	0.29	0.32	0.34
C h	57	110	70	32.69	3.25	76.64	-24.41	141.00	0.38	0.43	0.46
C h	57	110	70	37.36	4.07	82.71	-26.74	152.06	0.48	0.56	0.57
C h	57	110	70	43.85	5.40	91.38	-29.93	164.04	0.63	0.74	0.71
C h	57	110	70	47.92	6.05	96.15	-31.12	172.22	0.73	0.82	0.79
C h	57	110	70	54.53	7.38	105.04	-33.77	183.36	0.87	0.93	0.88
C h	57	110	70	61.61	8.68	112.19	-35.99	198.78	1.05	1.05	0.98
C h	57	110	70	66.55	10.10	116.31	-38.21	207.61	1.25	1.18	1.12
C h	57	110	70	74.40	11.42	124.55	-39.91	235.84	1.42	1.31	1.25
C h	57	110	70	76.14	12.27	126.50	-41.35	246.06	1.48	1.38	1.32
C i	45	110	70	5.99	0.29	35.01	-10.87	55.73	0.07	0.07	0.07
C i	45	110	70	12.57	0.82	52.14	-16.44	77.47	0.13	0.13	0.14
C i	45	110	70	15.78	1.26	59.73	-18.99	85.36	0.18	0.19	0.20
C i	45	110	70	18.85	1.68	66.67	-21.56	92.05	0.22	0.24	0.25
C i	45	110	70	22.13	2.16	73.17	-23.55	98.18	0.27	0.30	0.32
C i	45	110	70	24.40	2.54	78.59	-25.16	101.52	0.31	0.35	0.38
C i	45	110	70	29.64	3.41	87.48	-28.12	109.70	0.40	0.49	0.50
C i	45	110	70	36.42	4.58	100.49	-31.66	119.17	0.54	0.66	0.64
C i	45	110	70	40.93	5.67	107.42	-34.39	127.16	0.71	0.79	0.75
C i	45	110	70	50.03	7.36	118.05	-38.19	139.61	0.94	0.95	0.90
C i	45	110	70	52.67	8.26	123.25	-39.71	145.18	1.04	1.05	0.98
C i	45	110	70	59.26	9.83	131.92	-42.57	154.47	1.19	1.17	1.15
C i	45	110	70	66.79	11.44	141.68	-44.75	168.96	1.38	1.35	1.29
C i	45	110	70	70.80	12.98	145.80	-47.63	185.78	1.58	1.48	1.38
C i	45	110	70	76.89	14.24	154.04	-49.08	199.43	1.67	1.57	1.46
C i	45	110	70	77.23	15.09	154.90	-50.31	199.80	1.70	1.61	1.50
C j	37	110	70	4.47	0.19	33.06	-10.28	45.24	0.05	0.05	0.05
C j	37	110	70	10.06	0.65	52.36	-15.99	63.44	0.10	0.11	0.11
C j	37	110	70	12.87	0.98	60.16	-17.90	66.97	0.15	0.16	0.16
C j	37	110	70	16.00	1.44	68.40	-21.41	75.70	0.19	0.20	0.21
C j	37	110	70	19.10	1.88	75.12	-24.16	82.95	0.24	0.26	0.27
C j	37	110	70	21.25	2.21	80.76	-25.63	87.41	0.27	0.30	0.31
C j	37	110	70	26.13	3.09	90.30	-29.04	97.44	0.36	0.41	0.44
C j	37	110	70	32.98	4.23	103.74	-32.81	104.87	0.48	0.57	0.58
C j	37	110	70	37.84	5.27	111.98	-36.05	113.23	0.61	0.73	0.70
C j	37	110	70	45.06	6.90	123.90	-40.14	124.38	0.83	0.91	0.86
C j	37	110	70	49.14	7.86	130.84	-41.90	129.39	0.93	0.99	0.93
C j	37	110	70	56.70	9.38	141.03	-44.99	139.05	1.12	1.12	1.09
C j	37	110	70	62.22	10.90	148.84	-47.33	145.93	1.32	1.32	1.25
C j	37	110	70	68.25	12.58	155.77	-49.87	155.03	1.54	1.45	1.38
C j	37	110	70	73.85	14.06	162.27	-52.42	176.77	1.66	1.57	1.48
C j	37	110	70	76.81	15.24	165.96	-54.33	174.53	1.71	1.63	1.54
C k	51	130	80	3.94	0.09	22.01	-4.23	41.15	0.03	0.03	0.03
C k	51	130	80	9.13	0.34	36.53	-7.46	62.33	0.09	0.08	0.08
C k	51	130	80	12.56	0.54	42.82	-9.04	72.08	0.12	0.12	0.12
C k	51	130	80	15.72	0.77	50.19	-10.49	78.49	0.15	0.15	0.15
C k	51	130	80	19.05	1.03	55.39	-11.67	85.55	0.19	0.19	0.19
C k	51	130	80	21.16	1.23	59.08	-12.73	88.62	0.21	0.22	0.22
C k	51	130	80	26.64	1.75	67.10	-14.48	98.74	0.27	0.28	0.29
C k	51	130	80	33.23	2.41	78.16	-16.73	107.84	0.36	0.38	0.38
C k	51	130	80	38.05	3.06	83.79	-18.30	115.28	0.45	0.48	0.47
C k	51	130	80	45.06	4.02	92.68	-20.55	125.68	0.59	0.62	0.59
C k	51	130	80	50.45	4.64	99.19	-21.60	132.18	0.68	0.70	0.66
C k	51	130	80	56.95	5.62	105.69	-23.44	140.72	0.80	0.82	0.76
C k	51	130	80	63.38	6.56	114.14	-24.84	149.08	0.95	0.93	0.87
C k	51	130	80	69.36	7.68	118.91	-26.53	158.37	1.12	1.04	0.97
C k	51	130	80	73.61	8.33	123.04	-27.33	165.53	1.22	1.12	1.04
C k	51	130	80	75.42	8.69	124.12	-27.92	171.01	1.25	1.15	1.07
C L	51	130	70	5.32	0.14	30.24	-5.45	54.71	0.04	0.04	0.04
C L	51	130	70	9.78	0.42	40.22	-8.88	75.61	0.10	0.09	0.10
C L	51	130	70	13.50	0.67	50.62	-10.58	84.06	0.13	0.13	0.13
C L	51	130	70	16.17	0.92	56.69	-12.19	92.79	0.16	0.16	0.16
C L	51	130	70	19.38	1.21	61.68	-13.62	100.41	0.19	0.20	0.20
C L	51	130	70	21.85	1.44	66.88	-14.81	104.50	0.21	0.22	0.22

C L	51	130	70	26.12	1.95	74.04	-16.57	114.35	0.27	0.29	0.29
C L	51	130	70	32.44	2.68	85.74	-18.88	123.45	0.35	0.38	0.39
C L	51	130	70	38.14	3.37	93.98	-20.59	132.92	0.43	0.48	0.48
C L	51	130	70	44.77	4.39	104.39	-23.06	145.00	0.56	0.63	0.61
C L	51	130	70	48.44	4.98	109.81	-24.11	149.64	0.64	0.71	0.68
C L	51	130	70	55.54	6.04	118.92	-26.00	160.97	0.77	0.82	0.78
C L	51	130	70	61.47	7.06	125.20	-27.64	170.82	0.91	0.94	0.88
C L	51	130	70	68.10	8.20	132.79	-29.40	182.80	1.07	1.06	0.99
C L	51	130	70	73.66	9.15	140.59	-30.48	195.81	1.26	1.16	1.08
C L	51	130	70	76.89	10.00	142.98	-31.70	209.27	1.31	1.21	1.11
C m	51	130	60	5.22	0.18	33.93	-6.67	66.14	0.05	0.05	0.05
C m	51	130	60	11.08	0.57	53.66	-11.15	90.75	0.10	0.10	0.10
C m	51	130	60	14.82	0.88	62.54	-13.34	101.71	0.14	0.14	0.14
C m	51	130	60	17.81	1.22	70.79	-15.30	111.56	0.17	0.18	0.18
C m	51	130	60	21.06	1.58	79.24	-16.98	119.17	0.20	0.22	0.22
C m	51	130	60	23.20	1.86	81.84	-18.20	123.45	0.23	0.25	0.25
C m	51	130	60	28.00	2.56	91.38	-20.63	134.13	0.29	0.33	0.34
C m	51	130	60	35.31	3.47	106.77	-23.42	146.76	0.38	0.45	0.47
C m	51	130	60	39.90	4.34	115.23	-25.56	156.33	0.47	0.58	0.59
C m	51	130	60	47.81	5.68	128.67	-28.40	170.26	0.63	0.76	0.74
C m	51	130	60	52.33	6.51	135.61	-29.84	178.25	0.73	0.84	0.82
C m	51	130	60	58.54	7.70	145.58	-32.13	190.79	0.87	0.97	0.90
C m	51	130	60	64.91	8.96	153.39	-33.87	201.84	1.03	1.08	1.02
C m	51	130	60	71.68	10.35	162.06	-35.91	216.15	1.24	1.22	1.15
C m	51	130	60	76.65	11.39	167.04	-36.86	229.34	1.44	1.32	1.24
C m	51	130	60	79.49	12.07	171.60	-37.95	239.00	1.49	1.37	1.27
C n	57	130	100	3.66	0.05	15.28	-3.52	41.15	0.03	0.03	0.02
C n	57	130	100	8.53	0.21	25.04	-5.76	57.03	0.07	0.07	0.07
C n	57	130	100	10.82	0.34	28.51	-6.85	61.49	0.11	0.10	0.09
C n	57	130	100	14.37	0.50	34.15	-8.05	70.13	0.13	0.13	0.12
C n	57	130	100	16.76	0.66	37.61	-8.88	75.15	0.16	0.16	0.15
C n	57	130	100	19.57	0.82	39.78	-9.44	80.91	0.18	0.18	0.17
C n	57	130	100	23.51	1.12	44.77	-10.89	88.15	0.23	0.23	0.22
C n	57	130	100	30.35	1.59	52.57	-12.25	97.44	0.29	0.29	0.28
C n	57	130	100	35.12	2.02	56.05	-13.34	103.76	0.35	0.34	0.34
C n	57	130	100	41.94	2.68	63.63	-14.90	113.05	0.45	0.43	0.42
C n	57	130	100	45.99	3.07	66.67	-15.75	119.18	0.51	0.49	0.47
C n	57	130	100	53.92	3.77	72.30	-17.15	127.91	0.60	0.58	0.54
C n	57	130	100	59.96	4.41	77.07	-18.04	134.69	0.73	0.68	0.62
C n	57	130	100	64.81	5.05	80.32	-18.95	143.88	0.84	0.76	0.70
C n	57	130	100	67.51	5.42	82.49	-19.91	150.94	0.90	0.83	0.76
C n	57	130	100	70.58	5.85	84.01	-20.30	155.87	0.93	0.86	0.79
D a	51	140	70	5.79	0.15	30.24	-5.82	61.58	0.04	0.04	0.04
D a	51	140	70	11.02	0.41	44.55	-8.43	79.97	0.09	0.09	0.08
D a	51	140	70	14.75	0.63	53.44	-9.97	90.94	0.12	0.12	0.12
D a	51	140	70	17.14	0.83	58.64	-11.18	96.23	0.14	0.14	0.14
D a	51	140	70	20.49	1.08	64.28	-12.29	103.66	0.17	0.17	0.17
D a	51	140	70	22.56	1.23	69.48	-13.09	108.59	0.19	0.19	0.20
D a	51	140	70	27.60	1.67	78.59	-14.61	116.76	0.24	0.25	0.25
D a	51	140	70	33.28	2.24	88.35	-16.32	125.77	0.31	0.32	0.32
D a	51	140	70	38.12	2.77	95.50	-17.73	134.50	0.37	0.38	0.39
D a	51	140	70	45.31	3.59	106.12	-19.49	146.58	0.46	0.48	0.49
D a	51	140	70	49.55	4.12	111.98	-20.53	153.27	0.52	0.54	0.55
D a	51	140	70	55.03	4.89	119.56	-21.77	161.35	0.60	0.65	0.66
D a	51	140	70	62.17	5.76	127.59	-23.21	175.00	0.73	0.77	0.76
D a	51	140	70	68.00	6.62	133.22	-24.69	185.68	0.86	0.90	0.85
D a	51	140	70	72.48	7.43	139.51	-25.61	203.42	1.00	0.99	0.92
D a	51	140	70	71.63	7.70	139.08	-26.09	202.77	1.05	1.02	0.94
D b	45	140	80	5.72	0.14	28.94	-5.58	48.30	0.05	0.04	0.04
D b	45	140	80	11.52	0.40	44.12	-8.11	65.11	0.09	0.09	0.09
D b	45	140	80	14.38	0.59	49.76	-9.47	71.62	0.13	0.13	0.12
D b	45	140	80	16.85	0.78	56.04	-10.55	76.45	0.16	0.16	0.15
D b	45	140	80	20.11	1.02	61.90	-11.73	81.74	0.19	0.19	0.19
D b	45	140	80	22.99	1.18	67.32	-12.37	86.48	0.21	0.21	0.21
D b	45	140	80	28.14	1.59	75.12	-13.88	92.89	0.27	0.27	0.27
D b	45	140	80	33.43	2.13	84.01	-15.49	103.01	0.34	0.34	0.34
D b	45	140	80	38.35	2.68	90.73	-16.88	109.89	0.41	0.40	0.41
D b	45	140	80	44.83	3.40	100.27	-18.56	118.34	0.51	0.51	0.51
D b	45	140	80	49.26	3.89	106.77	-19.60	122.61	0.56	0.58	0.58
D b	45	140	80	56.05	4.67	114.15	-20.85	131.07	0.66	0.69	0.67
D b	45	140	80	61.06	5.43	120.65	-22.14	139.15	0.79	0.81	0.78
D b	45	140	80	67.18	6.22	125.85	-23.43	148.16	0.92	0.93	0.87
D b	45	140	80	70.67	6.88	130.73	-24.27	165.90	1.08	1.02	0.95
D b	45	140	80	72.64	7.29	132.79	-24.87	175.28	1.15	1.05	0.98
D c	45	140	60	6.80	0.24	42.82	-8.04	71.34	0.06	0.06	0.05
D c	45	140	60	12.50	0.63	61.68	-11.60	90.20	0.11	0.11	0.11
D c	45	140	60	15.94	0.93	72.09	-13.40	100.04	0.15	0.15	0.15
D c	45	140	60	19.30	1.24	80.97	-14.98	108.03	0.18	0.18	0.19
D c	45	140	60	22.53	1.57	88.35	-16.47	115.18	0.21	0.22	0.23
D c	45	140	60	25.41	1.81	94.42	-17.54	122.24	0.24	0.25	0.26
D c	45	140	60	30.84	2.44	107.86	-19.56	130.88	0.30	0.33	0.34
D c	45	140	60	36.55	3.20	118.48	-21.73	142.58	0.39	0.43	0.44
D c	45	140	60	42.51	3.96	129.97	-23.50	151.87	0.48	0.52	0.54
D c	45	140	60	50.07	5.15	142.54	-25.90	163.95	0.60	0.65	0.68
D c	45	140	60	53.78	5.75	149.27	-27.15	170.73	0.67	0.72	0.75
D c	45	140	60	60.91	6.80	161.84	-28.88	181.78	0.78	0.85	0.86
D c	45	140	60	67.98	7.89	171.38	-30.47	197.76	0.96	1.02	0.98
D c	45	140	60	72.75	9.01	177.67	-31.98	219.03	1.18	1.17	1.09
D c	45	140	60	76.00	9.76	185.26	-32.94	234.54	1.32	1.24	1.17
D c	45	140	60	75.29	9.97	183.52	-33.32	235.10	1.37	1.27	1.19
D d	57	140	70	5.44	0.12	26.56	-5.19	66.51	0.04	0.04	0.04
D d	57	140	70	10.96	0.36	40.87	-7.62	88.52	0.09	0.08	0.08
D d	57	140	70	14.89	0.56	48.45	-9.02	100.13	0.12	0.11	0.11
D d	57	140	70	17.37	0.76	53.87	-10.07	107.28	0.14	0.14	0.14
D d	57	140	70	20.14	0.98	58.86	-11.24	114.25	0.17	0.17	0.17
D d	57	140	70	22.74	1.15	63.20	-11.94	120.38	0.19	0.19	0.19
D d	57	140	70	29.07	1.60	73.82	-13.37	132.64	0.24	0.24	0.24
D d	57	140	70	33.55	2.13	78.81	-15.03	141.28	0.30	0.30	0.31
D d	57	140	70	39.07	2.67	87.04	-16.25	150.66	0.37	0.37	0.37
D d	57	140	70	46.81	3.44	96.37	-17.94	164.04	0.46	0.46	0.47
D d	57	140	70	50.59	3.94	101.57	-18.80	171.01	0.51	0.52	0.52
D d	57	140	70	57.65	4.69	109.16	-20.05	183.82	0.60	0.62	0.62
D d	57	140	70	64.30	5.44	116.53	-21.22	196.65	0.72	0.74	0.71
D d	57	140	70	69.54	6.27	121.30	-22.57	211.41	0.83	0.84	0.79
D d	57	140	70	73.58	6.82	127.15	-23.25	224.79	0.92	0.90	0.85
D d	57	140	70	72.53	6.99	126.50	-23.47	223.40	0.96	0.92	0.87
D e	45	140	70	5.37	0.15	30.89	-6.23	54.99	0.05	0.04	0.04
D e	45	140	70	10.88	0.45	49.32	-9.39	71.99	0.10	0.10	0.09
D e	45	140	70	14.54	0.70	58.21	-11.23	81.09	0.13	0.13	0.13
D e	45	140	70	17.76	0.95	66.67	-12.43	88.43	0.17	0.17	0.17
D e	45	140	70	20.82	1.22	73.39	-13.68	93.82	0.21	0.21	0.21
D e	45	140	70	23.35	1.42	78.59	-14.73	99.76	0.23	0.24	0.24
D e	45	140	70	28.99	1.94	89.00	-16.31	107.38	0.30	0.31	0.31
D e	45	140	70	35.13	2.61	100.05	-18.46	118.53	0.38	0.40	0.40
D e	45	140	70	40.46	3.25	108.94	-20.06	125.75	0.47	0.48	0.48
D e	45	140	70	47.54	4.25	120.43	-22.01	134.96	0.59	0.61	0.62
D e	45	140	70	52.71	4.81	127.80	-23.17	142.58	0.65	0.69	0.69
D e	45	140	70	59.10	5.67	136.04	-24.61	150.94	0.77	0.80	0.79
D e	45	140	70	64.50	6.66	143.09	-26.18	159.02	0.91	0.95	0.90
D e	45	140	70	70.42	7.66	152.95	-27.73	171.47	1.10	1.07	0.99
D e	45	140	70	74.94	8.36	158.59	-28.60	190.33	1.26	1.15	1.06
D e	45	140	70	74.50	8.61	158.37	-28.94	193.58	1.29	1.17	1.09
D f	37	140	70	4.87	0.13	33.49	-6.29	46.63	0.04	0.04	0.04
D f	37	140	70	9.93	0.43	53.44	-9.83	62.79	0.09	0.09	0.09
D f	37	140	70	13.39	0.66	61.24	-11.70	71.52	0.13	0.13	0.13
D f	37	140	70	16.71	0.91	70.79	-13.19	78.21	0.16	0.16	0.16
D f	37	140	70	19.79	1.19	78.38	-14.54	83.88	0.20	0.20	0.20
D f	37	140	70	22.07	1.41	84.23	-15.65	87.69	0.23	0.23	0.23
D f	37	140	70	28.06	1.95	96.58	-17.56	96.88	0.29	0.30	0.30
D f	37	140	70	32.81	2.58	105.91	-19.65	105.06	0.38	0.38	0.39
D f	37	140	70	38.20	3.23	115.66	-21.35	112.12	0.46	0.47	0.48
D f	37	140	70	46.06	4.24	128.45	-23.53	123.08	0.57	0.60	0.62
D f	37	140	70	50.31	4.81	135.39	-24.62	128.93	0.63	0.69	0.69
D f	37	140	70	56.90	5.68	144.06	-26.12	137.94	0.74	0.82	0.79

D	f	37	140	70	63.23	6.63	153.82	-27.68	150.66	0.92	0.96	0.91
D	f	37	140	70	69.13	7.66	162.27	-29.19	160.51	1.16	1.10	1.01
D	f	37	140	70	75.68	8.70	171.38	-30.53	174.53	1.32	1.20	1.11
D	f	37	140	70	75.27	9.20	169.21	-31.37	173.98	1.39	1.24	1.15
D	g	51	120	70	7.87	0.33	35.01	-10.20	72.36	0.07	0.07	0.07
D	g	51	120	70	13.48	0.79	48.45	-14.24	89.08	0.13	0.13	0.13
D	g	51	120	70	15.96	1.12	54.52	-16.49	96.05	0.17	0.18	0.18
D	g	51	120	70	19.61	1.45	62.33	-18.24	104.96	0.20	0.21	0.22
D	g	51	120	70	22.45	1.82	66.24	-19.76	110.82	0.24	0.26	0.27
D	g	51	120	70	24.68	2.10	71.66	-21.03	115.92	0.27	0.29	0.31
D	g	51	120	70	29.86	2.78	81.41	-23.58	123.82	0.34	0.38	0.41
D	g	51	120	70	35.16	3.62	87.91	-25.94	133.85	0.44	0.50	0.52
D	g	51	120	70	40.18	4.50	97.89	-28.23	141.47	0.54	0.63	0.63
D	g	51	120	70	46.85	5.76	107.64	-31.16	152.80	0.72	0.78	0.77
D	g	51	120	70	51.53	6.52	114.15	-32.58	159.67	0.81	0.87	0.84
D	g	51	120	70	57.82	7.74	122.17	-34.89	170.64	0.95	1.00	0.94
D	g	51	120	70	64.32	9.00	130.62	-36.41	182.62	1.14	1.14	1.07
D	g	51	120	70	69.96	10.39	136.26	-38.79	198.97	1.36	1.27	1.18
D	g	51	120	70	75.48	11.56	143.63	-40.46	223.21	1.49	1.36	1.26
D	g	51	120	70	75.33	12.07	144.93	-41.04	223.58	1.52	1.39	1.30
D	h	45	120	80	6.42	0.24	30.89	-8.74	53.04	0.06	0.06	0.05
D	h	45	120	80	11.44	0.61	43.03	-12.59	67.71	0.12	0.12	0.12
D	h	45	120	80	14.88	0.93	49.32	-14.96	74.40	0.16	0.16	0.16
D	h	45	120	80	18.04	1.23	55.83	-16.67	79.61	0.20	0.20	0.20
D	h	45	120	80	21.26	1.58	62.55	-18.52	86.29	0.24	0.25	0.25
D	h	45	120	80	23.76	1.82	66.23	-19.44	90.94	0.27	0.28	0.29
D	h	45	120	80	28.70	2.49	75.12	-21.84	97.26	0.35	0.37	0.38
D	h	45	120	80	33.99	3.25	82.71	-24.15	105.61	0.45	0.49	0.49
D	h	45	120	80	38.94	4.09	91.17	-26.77	110.44	0.56	0.60	0.59
D	h	45	120	80	46.67	5.30	102.00	-29.31	121.22	0.72	0.76	0.73
D	h	45	120	80	50.94	6.06	108.73	-30.87	126.05	0.81	0.85	0.80
D	h	45	120	80	56.80	7.15	114.36	-32.96	135.15	0.97	0.98	0.93
D	h	45	120	80	63.76	8.44	122.38	-34.99	146.67	1.18	1.14	1.06
D	h	45	120	80	69.05	9.76	129.75	-37.03	160.69	1.39	1.28	1.20
D	h	45	120	80	74.10	10.83	135.61	-38.47	175.46	1.50	1.38	1.30
D	h	45	120	80	74.08	11.37	134.09	-39.24	177.32	1.53	1.42	1.31
D	i	45	120	60	7.53	0.41	43.03	-12.59	78.12	0.07	0.07	0.07
D	i	45	120	60	12.77	0.93	58.43	-17.48	96.70	0.13	0.13	0.14
D	i	45	120	60	16.14	1.33	67.10	-20.10	105.99	0.17	0.18	0.18
D	i	45	120	60	19.64	1.72	77.29	-22.35	114.35	0.20	0.22	0.22
D	i	45	120	60	21.79	2.15	81.84	-24.38	120.66	0.24	0.27	0.28
D	i	45	120	60	24.20	2.47	88.35	-25.79	124.38	0.27	0.30	0.32
D	i	45	120	60	29.09	3.26	101.14	-28.48	134.13	0.34	0.39	0.43
D	i	45	120	60	34.77	4.31	111.33	-31.92	145.93	0.43	0.53	0.57
D	i	45	120	60	39.83	5.30	120.43	-34.27	153.92	0.54	0.67	0.70
D	i	45	120	60	46.95	6.76	134.96	-37.69	167.85	0.72	0.85	0.85
D	i	45	120	60	51.07	7.66	140.59	-39.57	176.11	0.82	0.94	0.92
D	i	45	120	60	57.31	9.04	151.00	-42.00	188.47	0.97	1.09	1.02
D	i	45	120	60	63.48	10.51	159.46	-44.36	205.01	1.16	1.22	1.19
D	i	45	120	60	68.74	12.08	166.18	-46.76	233.61	1.51	1.40	1.34
D	i	45	120	60	75.19	13.60	175.07	-48.81	235.10	1.62	1.53	1.37
D	i	45	120	60	76.97	14.60	178.53	-50.08	233.98	1.67	1.59	1.41
D	j	57	120	70	6.67	0.24	28.51	-8.44	74.40	0.06	0.06	0.05
D	j	57	120	70	11.58	0.61	41.95	-12.20	93.35	0.11	0.11	0.11
D	j	57	120	70	14.71	0.90	46.29	-14.24	102.45	0.14	0.14	0.14
D	j	57	120	70	18.34	1.20	54.31	-15.78	111.93	0.17	0.17	0.17
D	j	57	120	70	20.72	1.51	56.91	-17.45	119.13	0.20	0.21	0.22
D	j	57	120	70	23.53	1.76	62.11	-18.46	124.66	0.22	0.23	0.24
D	j	57	120	70	27.02	2.35	70.35	-20.98	130.14	0.28	0.30	0.32
D	j	57	120	70	32.72	3.13	77.94	-23.18	144.44	0.36	0.40	0.43
D	j	57	120	70	38.12	3.89	85.09	-25.28	153.55	0.44	0.51	0.53
D	j	57	120	70	45.94	5.11	96.37	-28.00	167.66	0.58	0.67	0.67
D	j	57	120	70	49.44	5.75	102.66	-29.22	173.42	0.67	0.76	0.74
D	j	57	120	70	56.32	6.86	107.86	-31.25	187.17	0.80	0.88	0.84
D	j	57	120	70	62.14	8.07	114.80	-33.11	199.25	0.98	1.00	0.94
D	j	57	120	70	68.98	9.38	121.52	-35.16	215.13	1.20	1.12	1.06
D	j	57	120	70	76.00	10.51	129.97	-36.50	240.21	1.35	1.23	1.16
D	j	57	120	70	75.63	10.96	130.62	-37.31	249.03	1.38	1.27	1.21
D	k	45	120	70	6.89	0.31	34.80	-10.31	63.44	0.07	0.07	0.07
D	k	45	120	70	11.87	0.76	49.32	-15.03	78.30	0.12	0.12	0.12
D	k	45	120	70	15.50	1.12	58.64	-17.58	87.04	0.16	0.17	0.17
D	k	45	120	70	18.82	1.47	64.93	-19.40	92.89	0.20	0.21	0.22
D	k	45	120	70	21.79	1.88	71.87	-21.32	99.39	0.24	0.26	0.27
D	k	45	120	70	23.76	2.12	75.99	-22.82	102.55	0.26	0.29	0.31
D	k	45	120	70	28.32	2.84	87.05	-25.37	109.14	0.34	0.38	0.41
D	k	45	120	70	33.97	3.73	97.67	-27.87	118.99	0.44	0.52	0.53
D	k	45	120	70	39.00	4.60	105.69	-30.09	126.60	0.55	0.65	0.64
D	k	45	120	70	46.93	5.97	117.83	-33.35	137.57	0.73	0.81	0.79
D	k	45	120	70	50.54	6.79	123.47	-35.06	143.79	0.83	0.89	0.85
D	k	45	120	70	57.50	8.02	132.14	-37.31	153.73	0.95	1.02	0.96
D	k	45	120	70	62.78	9.31	140.16	-39.32	163.11	1.14	1.15	1.11
D	k	45	120	70	68.94	10.84	149.70	-41.70	176.86	1.37	1.31	1.24
D	k	45	120	70	74.47	12.16	155.55	-43.47	200.17	1.54	1.44	1.34
D	k	45	120	70	76.01	12.92	156.42	-44.65	201.66	1.59	1.49	1.41
D	L	37	120	70	6.75	0.32	38.70	-11.50	56.01	0.07	0.07	0.07
D	L	37	120	70	11.79	0.82	56.04	-16.72	69.01	0.12	0.13	0.12
D	L	37	120	70	15.11	1.23	64.28	-19.35	77.56	0.17	0.18	0.18
D	L	37	120	70	18.74	1.59	74.98	-21.55	83.13	0.21	0.22	0.23
D	L	37	120	70	22.25	2.06	81.41	-23.88	90.01	0.26	0.28	0.28
D	L	37	120	70	24.30	2.34	86.83	-25.09	95.21	0.29	0.31	0.32
D	L	37	120	70	28.76	3.13	97.67	-27.75	103.38	0.37	0.41	0.43
D	L	37	120	70	35.18	4.17	109.49	-31.10	112.86	0.48	0.55	0.57
D	L	37	120	70	40.62	5.13	117.83	-33.48	120.10	0.59	0.69	0.69
D	L	37	120	70	47.70	6.63	130.41	-37.01	129.21	0.76	0.87	0.84
D	L	37	120	70	52.77	7.53	136.69	-38.55	136.08	0.87	0.96	0.91
D	L	37	120	70	58.88	8.81	146.23	-40.98	143.88	1.07	1.11	1.06
D	L	37	120	70	65.23	10.37	154.47	-43.35	154.47	1.31	1.28	1.21
D	L	37	120	70	71.82	11.97	161.62	-45.84	165.06	1.54	1.42	1.34
D	L	37	120	70	76.80	13.41	168.56	-47.87	173.42	1.63	1.53	1.45
D	L	37	120	70	77.46	14.20	170.30	-48.92	173.98	1.67	1.57	1.49
E	a	57	130	80	4.20	0.09	21.57	-4.26	48.30	0.03	0.03	0.03
E	a	57	130	80	10.15	0.34	35.01	-7.07	69.85	0.08	0.08	0.08
E	a	57	130	80	12.83	0.53	40.43	-8.69	76.44	0.11	0.11	0.11
E	a	57	130	80	16.63	0.77	47.37	-9.89	86.39	0.15	0.15	0.15
E	a	57	130	80	20.11	1.03	54.96	-11.25	91.68	0.18	0.19	0.19
E	a	57	130	80	22.16	1.19	56.26	-12.10	96.79	0.20	0.21	0.21
E	a	57	130	80	28.06	1.69	64.72	-13.64	107.28	0.26	0.26	0.27
E	a	57	130	80	34.23	2.33	72.09	-15.55	117.69	0.34	0.35	0.35
E	a	57	130	80	39.21	2.89	77.72	-16.82	125.96	0.41	0.42	0.43
E	a	57	130	80	46.75	3.81	85.96	-18.77	136.17	0.53	0.56	0.56
E	a	57	130	80	51.76	4.34	89.43	-19.86	143.32	0.60	0.63	0.62
E	a	57	130	80	58.98	5.28	100.06	-21.53	152.24	0.72	0.75	0.71
E	a	57	130	80	65.80	6.31	106.34	-22.99	163.39	0.85	0.85	0.81
E	a	57	130	80	71.66	7.34	111.11	-24.49	173.61	1.00	0.95	0.91
E	a	57	130	80	75.40	7.94	115.45	-25.48	180.86	1.12	1.03	0.98
E	a	57	130	80	75.50	8.09	116.53	-25.39	181.04	1.16	1.06	1.00
E	b	45	130	70	5.11	0.16	30.89	-7.18	52.29	0.04	0.04	0.04
E	b	45	130	70	9.78	0.49	44.77	-11.02	68.46	0.10	0.10	0.10
E	b	45	130	70	13.83	0.80	57.78	-13.25	78.86	0.14	0.14	0.14
E	b	45	130	70	17.17	1.09	64.71	-15.00	85.46	0.17	0.18	0.18
E	b	45	130	70	20.83	1.47	73.39	-16.98	91.49	0.22	0.22	0.23
E	b	45	130	70	22.28	1.67	76.42	-17.89	95.95	0.24	0.25	0.26
E	b	45	130	70	27.39	2.29	86.39	-20.02	103.11	0.31	0.33	0.35
E	b	45	130	70	33.40	3.15	97.23	-22.45	113.79	0.40	0.44	0.47
E	b	45	130	70	38.59	3.90	107.21	-24.39	120.48	0.50	0.56	0.58
E	b	45	130	70	46.97	5.16	119.57	-27.36	132.18	0.67	0.73	0.73
E	b	45	130	70	50.26	5.83	124.99	-28.73	138.31	0.77	0.81	0.80
E	b	45	130	70	57.70	7.06	134.53	-30.90	148.90	0.91	0.95	0.90
E	b	45	130	70	64.57	8.38	142.98	-32.92	160.14	1.05	1.07	1.04
E	b	45	130	70	70.54	9.66	151.22	-34.85	172.77	1.25	1.23	1.16
E	b	45	130	70	77.21	11.10	158.37	-36.61	202.40	1.46	1.34	1.25
E	b	45	130	70	80.30	11.69	162.49	-37.31	200.91	1.53	1.40	1.30
E	c	37	130	60	5.26	0.23	40.22	-9.57	56.85	0.05	0.05	0.05
E	c	37	130	60	10.51	0.66	62.33	-14.21	74.31	0.10	0.11	0.11

E	c	37	130	60	13.99	1.02	74.69	-17.52	83.69	0.15	0.15	0.15
E	c	37	130	60	17.14	1.40	85.09	-19.40	90.01	0.19	0.20	0.20
E	c	37	130	60	20.76	1.87	94.20	-21.89	98.19	0.23	0.25	0.25
E	c	37	130	60	22.58	2.13	99.40	-23.18	102.83	0.26	0.28	0.29
E	c	37	130	60	27.58	2.89	111.76	-25.70	110.26	0.34	0.37	0.40
E	c	37	130	60	33.58	3.90	125.20	-28.46	122.89	0.44	0.50	0.54
E	c	37	130	60	38.63	4.86	136.91	-31.35	130.51	0.55	0.64	0.68
E	c	37	130	60	45.88	6.36	150.13	-34.92	141.65	0.72	0.83	0.84

E	c	37	130	60	49.93	7.16	158.81	-36.24	147.60	0.80	0.92	0.91
E	c	37	130	60	55.59	8.45	168.78	-38.60	157.44	0.93	1.07	0.99
E	c	37	130	60	62.41	9.98	178.97	-41.39	169.89	1.12	1.18	1.17
E	c	37	130	60	68.63	11.55	189.38	-43.58	187.45	1.32	1.38	1.30
E	c	37	130	60	75.05	13.21	198.05	-45.95	203.52	1.62	1.50	1.43
E	c	37	130	60	78.47	14.12	203.68	-46.94	205.56	1.68	1.57	1.48

Appendix B: Artificial Neural Networks

B.1 Perceptron learning process

In the biological neurons, the strength of the synapses changes based on the signal provided. In a similar way the perceptron can be trained to be able to classify patterns on the basis of a list of data. This list of data is usually called the training dataset and its classification is known in advance; the letter p will indicate the individual pattern composing the training dataset, a dataset can be composed by hundreds of patterns. The error of the neuron E_p is the difference between the desired output and the one obtained by the perceptron for the specific pattern p. In the process of training, the weights will be iteratively modified until the output of the neuron, obtained with the training dataset inputs, will coincide with the desired known output. The known patterns p will be proposed to the neuron iteratively one after the other in repetition. Each time the weights and bias of the neuron will be adjusted on the basis of a learning algorithm.

The gradient-descended strategy establishes the correction of i- weight on the basis of (B-1) (this equation is applied also to the bias, which can be considered a weight with a constant input of 1)

$$\Delta w_i = -\eta \frac{\partial E_p}{\partial w_i} \qquad \text{(B-1)}$$

Where η is a small parameter that sets the step size, usually called the *learning rate*
In the case of the perceptron the (B-1) becomes (B-2)

$$\Delta w_i = -\eta x_i^{\,p} (t^p - y^p) \qquad \text{(B-2)}$$

Where p is the training pattern of data proposed to the neuron; w_i is the weight to be modified; x_i is input that is associated to the weight w_i; y^p is the output generated by the neuron and t^p the reference true value provided by the training pattern p .

The process of training can be described as follow:

1. Initialise all the weights (w_i=0)
2. Set p=1
3. Propose pattern p of the training set to the neuron, calculate output y
4. Update the values of the weights adding the result from (B-2)

$$w_i = w_i + \Delta w_i$$

   Notice that if classification is correct Δw_i=0
5. If all the patterns have not been analysed then:

   Propose next known pattern p= (p+1) and go to step 3
6. If all the proposed patterns give Δw_i=0 then

   Stop: Training was successful

   Else go to 2

A practical example could be the training of a perceptron as the logic operator OR. Even if the concept of OR is simple from a conceptual point of view, the definition of its actual algorithm can be difficult. In Table B-1 the chart of OR is presented.

Table B-1: The logical operator OR

X1	X2	t (target)
1	1	1
0	1	1
1	0	1
0	0	0

The perceptron will therefore have two external inputs plus the constant input for the bias (i.e. 1). There will be three weights coefficients that will be updated at each iteration: the two weights of the inputs and the bias. The problem is solved with η =1, all the steps and results are presented in Table B-2.

	Inputs			target	Weights			Results		Corrections		
Pattern	X1	X2	1	t	w1	w2	bias	y	(y-t)	d w1	d w2	d bias
1	1	0	1	1	0	0	0	0	1	1	0	1
2	0	1	1	1	1	0	1	1	0	0	0	0
3	1	1	1	1	1	0	1	1	0	0	0	0
4	0	0	1	0	1	0	1	1	-1	0	0	-1
1	1	0	1	1	1	0	0	1	0	0	0	0
2	0	1	1	1	1	0	0	0	1	0	1	1
3	1	1	1	1	1	1	1	1	0	0	0	0
4	0	0	1	0	1	1	1	1	-1	0	0	-1
1	1	0	1	1	1	1	0	1	0	0	0	0
2	0	1	1	1	1	1	0	1	0	0	0	0
3	1	1	1	1	1	1	0	1	0	0	0	0
4	0	0	1	0	1	1	0	0	0	0	0	0

Table B-2: Learning process of a perceptron as OR operator

Learning on a perceptron is guaranteed, as stated by the "perceptron convergence theorem", which asserts that if a solution can be implemented on a perceptron, the learning rule will find the solution in a finite number of steps, [15].

Not all the classification problem can be solved by a perceptron, a typical example is the operator XOR; this operator can not be simulated by a single perceptron, but it can be implemented using AND, OR and NOT perceptrons in thje logic structure such as "(NOT A and B) or (A and NOT B)".

B.2 MLP as function approximators

The Multi-layer perceptron is particularly useful for the development of models whose aim is to predict the value of a (usually) continuous variable; this layout has in fact proven to be able to approximate any continuous function with a finite number of discontinuities [18].

Here a simple proof is outlined [15]; consider the case of a generic function with two inputs (x_1,x_2) and one output (y). It is known that for any given value of x_1 the function $y(x_1,x_2)$ can be approximated by a Fourier decomposition in the variable x_2 within any given (sum-of-squares) error, according to equation (B-3)

$$y(x_1,x_2) \cong \sum_s A_s(x_1)\cos(sx_2) \qquad \text{(B-3)}$$

The coefficients A are themselves functions of x1 and can be also expressed in terms of a Fourier series, equation (B-4)

$$y(x_1, x_2) \cong \sum_s \sum_l A_{sl} \cos(lx_1)\cos(sx_2) \qquad \text{(B-4)}$$

Using the standard trigonometric equation $\cos(\alpha)*\cos(\beta)=1/2*(\cos(\alpha+\beta) + \cos(\alpha-\beta))$
And inserting the values z_i where $z_{sl}=lx_1+sx_2$, $z'_{sl} = lx_1-sx$, the equation becomes a linear combination of $\cos(z_{sl})$ and $\cos(z'_{sl})$ as in (B-5)

$$y(x_1, x_2) \cong \sum_{s*l} \frac{A_{sl}}{2}(\cos(z_{sl}) + \cos(z'_{sl})) \qquad \text{(B-5)}$$

The function cos(z) itself can then be approximated to arbitrary accuracy by a linear combination of threshold step functions. In Figure B-1, it can be seen that a continuous function can be approximated by a linear superposition of threshold step functions, as shown in Figure B-1.

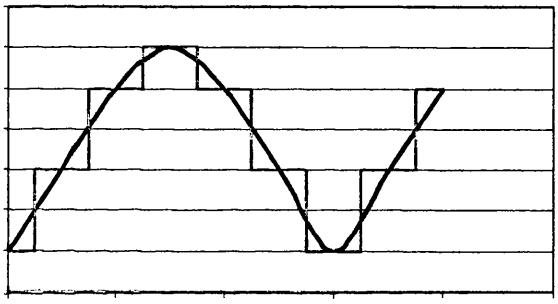

Figure B-1: Approximation of a continuous function by a linear superposition of threshold functions

The final step is the substitution of the threshold functions with a sigmoid function, which can approximate a threshold function, simply by scaling its coefficients.
Any function $y(x_1,x_2)$ can therefore be approximated arbitrary well by a linear combination of sigmoid functions whose arguments are linear combinations of the inputs. This approximation is equivalent to the multi-layer perceptron layout with its two-layer network composed by sigmoid neurons in the hidden layer and linear neurons in the output layer.
It has furthermore proved that the multi layer perceptron can approximate a function and its derivates simultaneously [15].

B.3 Training algorithms

B.3.1 Back propagation algorithm

There are different implementations of the back-propagation algorithm. In its simplest implementation, the weights and biases are updated in the direction in which the Error function decreases more rapidly: the negative of the gradient vector of the error.

$$w_{i+1} = w_i + \Delta w_i = w_i - \eta \frac{\partial E}{\partial w_i} \qquad \text{(B-6)}$$

In order to use this algorithm the error function has to be continuous and differentiable.

In presence of the MLP with K outputs and P data reference patterns, the error will become

$$E = \frac{1}{2} \sum_{p=1}^{P} \sum_{k=1}^{K} (y_k^p - t_k^p)^2 \qquad \text{(B-7)}$$

Where y will be the outputs of the network and t the target values. This is a continuous and differentiable equation; therefore the back propagation algorithm is applicable.

In order to mathematically describe the back propagation process of updating the weights, the back-propagation algorithm will be explained, for simplicity, in the incremental training style, thus removing the index p from (B-7):

$$E = \frac{1}{2} \sum_{k=1} (y_k - t_k)^2 \quad \text{and} \quad e_k = \frac{(y_k - t_k)^2}{2} \qquad \text{(B-8)}$$

Assuming:

k : index of the neurons of the output layer

j: index of the neurons of the hidden layer and index of inputs for output layer neurons

i: index of inputs of hidden layer (main inputs)

y: outputs of a neuron, y_k are the main outputs

x: inputs of a neuron

f: transfer function of a neuron

For the updating of the weights (and bias) of the output layer, (B-6) becomes:

$$w_{kj}^{I+1} = w_{kj}^{I} + \Delta w_{kj}^{I} = w_{kj}^{I} - \eta \frac{\partial e_k^{I}}{\partial w_{kj}^{I}} \qquad \text{where } I \text{ is the iteration} \tag{B-9}$$

In these neurons, the error function e is used because the output neuron is responsible only for its own output.

Now, let a be the weighted sum of the inputs, so for the output layer:

$$a_k = \sum_{j=1} w_{kj} x_{kj} = \sum_{j=1} w_{kj} y_j \tag{B-10}$$

And let's assume:

$$\delta_k = -\frac{\partial e_k}{\partial a_k} = \frac{\partial e}{\partial y_k}\frac{\partial y_k}{\partial a_k} \tag{B-11}$$

Now, expanding the derivative of the Error of (B-9), referring to (B-10),(B-11):

$$\frac{\partial e_k}{\partial w_{kj}} = \frac{\partial e_k}{\partial a_k}\frac{\partial a_k}{\partial w_{kj}} = -\delta \cdot y_j \tag{B-12}$$

Now we refer to equation (B-8) as the Error function, so

$$\frac{\partial e_k}{\partial y_k} = -(t_k - y_k) \quad \text{and} \quad \frac{\partial y_k}{\partial a_k} = f_k'(a_k) \tag{B-13}$$

So for the weights of the output layer (B-9) becomes

$$w_{kj}^{I+1} = w_{kj}^{I} + \Delta w_{kj}^{I} = w_{kj}^{I} - \eta\left(\sum_p (t_k^p - y_k^p)\right) f_k'(a_k) y_j \tag{B-14}$$

In case of linear neuron:

$$f_k'(a_k) = 1 \tag{B-15}$$

In the case of the hidden layer neurons the error function E of (B-8) is used because they are connected to all the outputs.

$$w_{ji}^{I+1} = w_{ji}^{I} + \Delta w_{ji}^{I} = w_{ji}^{I} - \eta \frac{\partial E^{I}}{\partial w_{ji}^{I}} \qquad \text{where } I \text{ is the iteration} \tag{B-16}$$

Following steps (B-9),(B-11), equation (B-17) is reached.

$$\Delta w_{ji}^{I} = \eta \delta x_j = \eta \frac{\partial E}{\partial y_j} f'(a_j) x_j \tag{B-17}$$

The problem here is the definition of the gradient of the error for the hidden neuron:

$$\frac{\partial E}{\partial y_j} = \frac{\partial \sum_k e_k}{\partial y_j} \sum_k \frac{\partial e_k}{\partial a_k} \frac{\partial a_k}{\partial y_j} = \sum_k \frac{\partial e_k}{\partial a_k} \frac{\partial \sum_{j=1} w_{kj} y_j}{\partial y_j} = \sum_k \delta_k w_{kj} \tag{B-18}$$

Therefore (B-16) becomes

$$w_{ji}^{I+1} = w_{ji}^{I} + \Delta w_{ji}^{I} = w_{ji}^{I} - \eta \sum_k \delta_k w_{kj} f'(a_j) x_j \qquad \text{where } I \text{ is the iteration} \tag{B-19}$$

Then the derivative of the sigmoid function is

$$f(a) = \frac{1}{1+e^{-a}} \quad \rightarrow \quad f'(a) = a(1-a) \tag{B-20}$$

The equations (B-20) and (B-14) are the key for the updating of the weights of the neural network. This algorithm can be applied to any feed-forward network; the only condition is that the transfer functions have to be differentiable. Due to its "gradient" nature, there is always the risk that the back-gradient algorithm will determine a local minimum instead of the optimum minimum of the function E.

Back-propagation can be improved by including a momentum, which could lead to a faster convergence.

B.3.2 Levenberg-Marquardt algorithm

The *Levenberg-Marquardt* is of particular interest; it is a quasi-Newton algorithm that has been developed to especially resolve MLP artificial neural networks.

In the quasi-Newton algorithms the weights are updated on the basis of (B-21)

$$w_{i+1} = w_i + \Delta w_i = w_i - \mathbf{A}_i^{-1} \frac{\partial E}{\partial w_i} \tag{B-21}$$

Where **A** is the Hessian matrix (second deratives) of the error function with respect to the weights. In the *Levenberg-Marquardt algorithm,*the A matrix is approximated by

$$\mathbf{A} = \mathbf{J}^T \mathbf{J} \tag{B-22}$$

Where J is the Jacobian matrix (first deratives) of the error function with respect to the weights and the gradient is computed as

$$\frac{\partial E}{\partial w} = \mathbf{J}^t \mathbf{e} \tag{B-23}$$

With **e** is the vector of the errors of the network, thus *Levenberg-Marquardt algorithm* becomes:

$$\mathbf{w}_{i+1} = \mathbf{w}_i + \Delta \mathbf{w}_i = \mathbf{w}_i - \left[\mathbf{J}^T \mathbf{J} + \mu \mathbf{I}\right]^{-1} \mathbf{J}^T \mathbf{e} \tag{B-24}$$

When μ is zero, this algorithm behaves as a simple Newton method, when μ is large it behaves as a gradient descent algorithm. The Newton method works better near an error minimum, μ therefore changes during the training process: it is decreased after each iteration and is increased only if the tentative step would produce a larger error.

B.4 Bayesian techniques

Bayesian regularisation techniques are based on the Bayes theorem, that states that the posterior density distribution of a parameter (or class) *w*, given a reference dataset D is given by:

$$p(w/D) = \frac{p(D/w)p(w)}{p(D)} \tag{B-25}$$

Where p(w) is the prior probability for w, the p(D) is a normalisation factor and p(D/w) is known as the evidence, the class conditional probability or the likelihood of D for the given parameter w.

From the application of this theorem in the definition of the parameters in the ANN, whose steps are explained in [15] [19], the following terms are derived

$$E = \beta * E_D + \alpha * E_W = \beta * \left(\frac{1}{2} \sum (t - y)^2 \right) + \alpha * \left(\frac{1}{2} \sum w^2 \right) \quad \text{(B-26)}$$

Where E is the error function to be minimised and E_D is the sum-square-error of the outputs and E_w the square sum of the weights inside the network, while β and α are the coefficients that have to be defined by the Bayesian analysis.

During the training, the values of β and α will iteratively adapt, as the weights. At each iteration, on the basis of the data provided, the training algorithm will update the weights looking for the minimisation of (B-26). After the update of the weights, a new value of the coefficient γ will be estimated on the basis of the Hessian matrix of the weights, equation (B-27). This parameter represents an indication of the quantity of weights effectively used for the modelling.

$$\gamma = W - \sum_{i=1}^{W} \frac{\alpha}{\lambda_i + \alpha} \quad \text{(B-27)}$$

Where W is the number of weights, and λ are the eigenvalues of the Hessian matrix (second derivate) of βE_D in the weights. On the basis of γ, the coefficients α and β will be updated,(B-28).

$$\alpha^{new} = \frac{\gamma}{2E_W} \qquad \beta^{new} = \frac{W - \gamma}{2E_D} \quad \text{(B-28)}$$

The best β and α are therefore iteratively defined with the weights.
Finally the local variance of the estimate can be obtained by

$$\sigma^2 = \frac{1}{\beta} + \mathbf{g}^T \mathbf{A}^{-1} \mathbf{g} \quad \text{(B-29)}$$

Where g will be the gradient of the error function in the weights, A is the Hessian matrix of the error function. The ratio 1/β will represent the output of the noise model. This variance allows plotting error bars, it can in fact be estimated that there is at least a 50% probability that the real results will fit in the range of the estimate ± σ.

Appendix C: Development of ANN for the gravure printing process

C.1 Artificial Neural Networks

Resulting Artificial neural networks presenting a MLP layout with n_x inputs, n_y outputs and n_h neurons in the hidden layer can be expressed in the mathematical form:

$$Density = L([w_2] * (S([w_1] * [x] + [b_1])) + [b_2])$$

Where

[x]= Input column vector of size (n_x)
S= Sigmoid transfer Function
L= Linear transfer Function
[w_1]=Weight matrix for hidden layer neurons of size (n_h * n_x)
[b_1]= Bias column vector for hidden layer of size (n_h)
[w_2]= Weight matrix for output layer of size (n_y * n_h)
[b_2]= Bias column vector for output layer of size (n_y)
[y]= Output column vector of size (n_y)

For the artificial neural networks developed in section 7.3:

Input vector = [Screen Angle, Screen Ruling, Stylus Angle, Volume]
Output vector = [Optical Colour Density]

The size of the hidden layer and the obtained values of the weights and bias will depend on the design choice and on the different performed training. Three different combinations were explored, the values of the obtained weights and biases are here presented.

C.1.1 Levenberg-Marquardt MLP design with 8 hidden neurons

$n_{h=8}$

w_1				b_1
-0.005	0.040	-0.002	-0.020	-1.320
-0.008	0.089	-0.029	0.184	-11.212
-0.007	-0.031	0.208	0.290	-24.259
0.060	0.006	0.051	0.014	-6.230
0.027	-0.103	-0.066	-0.294	19.418
0.002	-0.032	0.000	-0.128	5.779
0.049	-0.004	0.136	0.136	-12.995
0.003	0.013	-0.007	0.829	-23.658

w_2^T	b_2
-0.493	-0.337
0.121	
0.054	
-0.048	
-0.090	
-0.641	
0.029	
0.790	

C.1.2 8 neurons Bayesian regularisation MLP design

$n_h=8$

w_1				b_1
0.013	-0.073	-0.007	-0.155	10.175
0.001	-0.040	0.015	-0.079	4.351
0.002	0.030	-0.089	0.112	-3.078
0.003	-0.049	0.014	-0.122	5.942
0.053	-0.077	-0.021	-0.003	1.418
0.029	-0.036	0.004	-0.047	1.164
-0.008	0.023	0.011	-0.056	0.044
0.005	0.028	0.030	0.080	-5.300

w_2^T	b_2
-0.414	-0.070
0.864	
0.133	
-0.575	
0.108	
-0.382	
-0.832	
0.355	

C.1.3 12 neurons Bayesian regularisation MLP design

n_h=12

w_1				b_1
-0.014	-0.016	-0.023	-0.085	5.820
-0.018	0.032	-0.002	0.038	-1.642
0.039	-0.073	-0.048	-0.014	4.790
0.000	-0.006	-0.010	0.077	-0.963
0.009	-0.055	-0.013	-0.146	8.050
0.007	0.015	0.080	-0.062	-2.293
-0.004	0.061	0.006	0.198	-9.953
-0.014	0.052	0.058	0.007	-5.017
-0.011	-0.037	-0.048	-0.091	7.607
0.028	-0.035	0.003	0.008	0.004
-0.024	-0.002	-0.063	-0.010	6.125
0.001	-0.028	-0.008	-0.119	6.523

w_2^T	b_2
1.042	-0.103
0.898	
-0.319	
1.266	
0.988	
0.147	
0.566	
-0.398	
-0.511	
0.675	
-0.515	
-1.136	